

Confinement physics for a steady state net  
electric burning spherical tokamak

Bhavin Patel

Doctor of Philosophy

University of York

Physics

January 2021

## Abstract

Spherical tokamaks have many desirable properties that make them a suitable candidate for a compact fusion reactor. Such a device could accelerate the timeline of fusion and reduce capital costs, allowing fusion to have a more significant impact on the world. The feasibility of a compact spherical tokamak able to generate net electricity needs to be examined as well as the modelling tools currently available. Extrapolating to reactor relevant conditions requires a great deal of trust in these models.

This work begins by identifying steady state plasma equilibria and applying empirical limits to characterise the available parameter space for a given machine design and scale. This is done with a consistent calculation of the neoclassical currents, allowing for the auxiliary current drive requirements to be determined. A baseline scenario was identified with a major radius of 2.5 m and fusion power of 1.1 GW. An important result found is that a minimum current drive efficiency is required given the empirical limits used. Neutral beam injection was found to have a sufficient current drive efficiency, with 94 MW of power needed to drive all the required current. The validity of reduced physics neutral beam models was also examined and it was found that reasonable predictions were made provided the beams were aligned with the magnetic field.

The performance of a tokamak is generally limited by the turbulent transport so the linear gyrokinetic stability of a baseline ST reactor plasma scenario was investigated. The baseline equilibrium showed some desirable properties as the electron scale turbulence was found to be stable. In the ion scale, kinetic ballooning modes and micro-tearing modes were found to co-exist on multiple flux surfaces. Through exploring the drives of these modes it was possible to optimise the equilibrium to minimise their growth rates. Moreover, the credibility of quasi-linear transport models was explored with a new tool developed that is better able to capture the instabilities in this regime, though further development is still needed.

# Contents

<b>Abstract</b>	<b>1</b>
<b>Contents</b>	<b>2</b>
<b>List of Tables</b>	<b>6</b>
<b>List of Figures</b>	<b>8</b>
<b>Acknowledgements</b>	<b>16</b>
<b>Declaration</b>	<b>18</b>
<b>1 Introduction</b>	<b>19</b>
1.1 Fusion’s place in the energy-mix . . . . .	19
1.2 Fusion on Earth . . . . .	21
1.2.1 Tokamaks . . . . .	22
1.2.2 BurST - Burning Spherical Tokamak . . . . .	23
<b>2 Steady state modelling in Tokamaks</b>	<b>25</b>
2.1 Plasma equilibrium . . . . .	26
2.1.1 Grad-Shafranov equation . . . . .	26
2.2 Sources of current . . . . .	27
2.2.1 Neoclassical Currents . . . . .	27
2.2.2 Auxiliary Current . . . . .	30
2.2.3 Total current . . . . .	32
2.3 Transport processes . . . . .	32
2.3.1 Magneto-hydrodynamic stability . . . . .	33
2.3.2 Neoclassical Transport . . . . .	34
2.3.3 Anomalous transport . . . . .	34

2.3.4	Confinement scaling laws . . . . .	34
2.4	Gyrokinetic theory . . . . .	36
2.4.1	Linear gyrokinetic theory . . . . .	36
2.4.2	Local flux tube and ballooning transformation . . . . .	41
2.4.3	Sheared flow . . . . .	43
2.4.4	Non-linear gyrokinetics . . . . .	44
2.5	Quasi-linear theory . . . . .	45
2.5.1	Quasi-linear approximation . . . . .	46
2.6	Summary . . . . .	47
<b>3</b>	<b>Available physics models</b>	<b>48</b>
3.1	Equilibrium code - SCENE . . . . .	48
3.1.1	Global parameters . . . . .	48
3.1.2	Kinetic profiles . . . . .	49
3.1.3	Bootstrap current . . . . .	51
3.1.4	Current profile . . . . .	52
3.2	NBI codes - NUBEAM, NBeams and RABBIT . . . . .	53
3.2.1	NUBEAM . . . . .	53
3.2.2	NBeams . . . . .	54
3.2.3	RABBIT . . . . .	57
3.3	Gyrokinetic codes - GS2 & CGYRO . . . . .	58
3.4	Quasi-linear codes - TGLF & QLGYRO . . . . .	58
3.4.1	TGLF eigensolver . . . . .	58
3.4.2	TGLF saturation rule . . . . .	60
3.4.3	QLGYRO . . . . .	62
3.5	Summary . . . . .	63
<b>4</b>	<b>Plasma scenarios for a net electric ST</b>	<b>64</b>
4.1	Creating a baseline equilibrium . . . . .	65
4.1.1	Minimum fusion power . . . . .	65
4.1.2	Minimise auxiliary power . . . . .	66
4.1.3	Size of the device . . . . .	67
4.1.4	Aspect ratio . . . . .	68
4.1.5	Plasma shaping . . . . .	68
4.1.6	Kinetic profiles . . . . .	70

4.1.7	Auxiliary current profile . . . . .	72
4.1.8	Plasma current . . . . .	73
4.1.9	Auxiliary power . . . . .	74
4.2	Different operating scenarios . . . . .	74
4.2.1	Baseline scenario . . . . .	74
4.2.2	Operating temperature . . . . .	77
4.3	Higher toroidal field - superconducting centre column . . . . .	82
4.4	Summary . . . . .	87
<b>5</b>	<b>Identifying neutral beam injection configurations</b>	<b>89</b>
5.1	On axis beam . . . . .	90
5.1.1	Benchmark of NBeams and RABBIT . . . . .	91
5.1.2	Core beam penetration . . . . .	95
5.2	Off axis beam . . . . .	98
5.2.1	Field-aligned beam . . . . .	102
5.3	Temperature/Density dependence on $\eta_{\text{NBI}}$ . . . . .	107
5.4	Final beam configuration . . . . .	109
5.4.1	Heating profiles . . . . .	110
5.5	Summary . . . . .	111
<b>6</b>	<b>Optimisation of equilibrium parameters using linear gyrokinetics</b>	<b>113</b>
6.1	Identifying the relevant micro-instabilities in BurST . . . . .	116
6.1.1	Inclusion of different fields . . . . .	116
6.1.2	Co-existing KBM and MTM . . . . .	121
6.2	Routes to stabilise long wavelength turbulence in the core . . . . .	123
6.2.1	Impact of flow shear . . . . .	123
6.2.2	Impact of kinetic profiles . . . . .	124
6.2.3	Impact of magnetic equilibrium . . . . .	131
6.2.4	Impact of higher toroidal field . . . . .	136
6.2.5	Summary . . . . .	137
6.3	Routes to stabilise intermediate wavelength MTMs in the core . . . . .	139
6.3.1	Impact of flow shear . . . . .	139
6.3.2	Impact of kinetic profiles . . . . .	140
6.3.3	Impact of magnetic equilibrium . . . . .	142
6.3.4	Impact of higher toroidal field . . . . .	143

6.3.5	Summary . . . . .	144
6.4	Cause of short wavelength mode stability . . . . .	145
6.4.1	Impact of kinetic profiles . . . . .	145
6.4.2	Impact of magnetic equilibrium . . . . .	146
6.4.3	Impact of higher field . . . . .	148
6.4.4	Summary . . . . .	148
6.5	Stability of a deep core flux surface . . . . .	149
6.5.1	Stability at different scales . . . . .	149
6.6	Stability of an edge flux surface . . . . .	151
6.6.1	Stability at different $k_y$ . . . . .	151
6.6.2	Routes to stabilise short-intermediate wavelength MTMs in the edge . . . . .	152
6.6.3	Impact of higher toroidal field . . . . .	156
6.7	Equilibrium optimised for core turbulent transport . . . . .	157
6.8	Summary . . . . .	160
<b>7</b>	<b>Assessment of quasi-linear transport models for a high <math>\beta</math> ST</b>	<b>162</b>
7.1	Need for QLGYRO . . . . .	163
7.2	Nonlinear BurST simulations . . . . .	165
7.3	GA-STD - ITG turbulence . . . . .	169
7.3.1	Parameter scans around GA-STD . . . . .	172
7.4	MAST - ITG turbulence . . . . .	174
7.4.1	Summary . . . . .	179
7.5	NSTX - MTM turbulence . . . . .	179
7.5.1	Without flow shear . . . . .	181
7.5.2	With flow shear . . . . .	183
7.6	Summary . . . . .	191
<b>8</b>	<b>Summary and Discussion</b>	<b>194</b>
	<b>References</b>	<b>200</b>

# List of Tables

4.1	Comparison of different exhaust relevant parameters for future tokamak designs. SND corresponds to single null divertor and DND to double null divertor.	68
4.2	Basic plasma parameters for this baseline scenario and the reasoning behind them.	76
4.3	Outline for STPP centre column designs, reproduced from [134].	83
4.4	Comparison of the BurST centre column design when using an aluminium conductor and a CORC REBCO superconductor.	84
5.1	Comparison of NBeams, NUBEAM and RABBIT's prediction for the integrated currents and $\eta_{\text{shield}}$ with an 8MW, 1MeV beam with $R_t = 3.1\text{m}$	94
5.2	Comparison of NBeams, NUBEAM and RABBIT's prediction for the integrated currents, $\eta_{\text{shield}}$ and $\eta_{\text{NBI}}$ with a 90MW, 500keV beam with $R_t = 3.8\text{m}$ parallel to the horizontal plane.	101
5.3	Comparison of NBeams, NUBEAM and RABBIT's prediction for the integrated currents, $\eta_{\text{shield}}$ and $\eta_{\text{NBI}}$ with a 90MW, 500keV field-aligned beam with $R_t = 3.8\text{m}$	104
5.4	Break down of the power deposition from the NBI and $\alpha$ heating to the different species in BurST	111
6.1	Normalising quantities used in CGYRO and this thesis	114
6.2	Plasma and Miller parameters for 3 flux surfaces, $\rho_\psi = 0.3, 0.5$ & $0.85$ for the equilibrium in Table 4.2.	116
6.3	Basic plasma parameters for the optimised scenario	158
6.4	Plasma and Miller parameters for the $\rho_\psi = 0.5$ surface of the optimised equilibrium.	158
7.1	Miller and plasma parameters for GA-STD case	169

7.2	Electrostatic energy flux prediction made by nonlinear CGYRO, QLGYRO and TGLF for the GA-STD case. . . . .	170
7.3	Experimental Miller and plasma parameters for MAST #27274 at $r/a = 0.8$ [84]. Note simulations conducted here enforced $a/L_{Te} = a/L_{Ti}$ and were performed without flow shear. . . . .	174
7.4	Experimental Miller and plasma parameters for NSTX shot #120968 at $r/a = 0.6$ [168]. . . . .	180
7.5	Comparison of simulation domains in [196] and the CGYRO domain used for the NSTX simulation. . . . .	181
7.6	Electromagnetic flutter electron energy flux predictions for the NSTX case without flow shear. The GYRO results are taken directly from [196] . . . . .	181
7.7	Electromagnetic flutter electron energy flux predictions for the NSTX case with flow shear. The GYRO result is taken directly from [196] . . . . .	185

# List of Figures

1.1	Illustration of the tokamak design. A combination of the toroidal (red) and poloidal (blue) fields generates a helical field that can cancel out the average drifts created by magnetic geometry. Taken with permission from [28] . . . .	22
2.1	Illustration of the passing particles that perform a full poloidal orbit and the trapped particles that are trapped on the outboard low field side. Taken with permission from [28] . . . . .	30
2.2	Guiding centre co-ordinates shown can describe the position of a particle with $\rho_L$ showing the direction of the Larmor radius vector, and $\gamma$ showing the gyro-phase. Taken with permission from [28] . . . . .	37
3.1	Comparing the bootstrap prediction made by different neoclassical models for a high $\beta$ ST reactor. . . . .	52
3.2	Illustration of how SCENE fills in the toroidal current hole by using the bootstrap current profile where $\text{psic} = 0.025$ . . . . .	53
4.1	4 different scenarios (outlined in the text) showing the impact on $l_i$ , showing a) $p'$ and b) $J_{\text{aux}}$ . . . . .	69
4.2	Comparison of the BurST plasma boundary to the JET, ITER and DEMO boundaries. . . . .	70
4.3	Impact of increasing $\zeta_2$ on a) $J_{\text{aux}}$ (thus the extent of off axis current drive) and on b) $q$ . . . . .	72
4.4	A scan in total $I_p$ showing a) a breakdown of the contributions of the different pressure driven currents and the external current and b) $H_{98}$ and $H_{\text{Petty}}$ . Note this was done at fixed $P_{\text{aux}} = 50\text{MW}$ and $P_{\text{fus}} = 1.1\text{GW}$ . . . . .	73
4.5	a) Flux surfaces and b) electron density and temperature profiles of the baseline equilibrium. . . . .	75
4.6	a) Density and b) temperature profiles examined at fixed $P_{\text{fus}} = 1.1\text{GW}$ . . . .	77

4.7	Impact of changing $T_{e0}$ at fixed $P_{\text{fus}} = 1.1\text{GW}$ , showing how a) $P_{\text{aux}}$ , b) $H_{98}$ and $H_{\text{Petty}}$ change when $\eta_{\text{NBI}} = 0.4\text{A m}^{-2}\text{W}^{-1}$ is assumed. . . . .	78
4.8	Contour plots for a 2D scan changing $I_p$ and $T_{e0}$ at fixed $P_{\text{fus}} = 1.1\text{GW}$ , showing the variation of a) $P_{\text{aux}}$ , b) $H_{98}$ c) $H_{\text{Petty}}$ , d) $f_{\text{GW}}$ and e) $\beta_N$ . . . . .	79
4.9	Available parameter space if the following restrictions are imposed: $P_{\text{aux}} < 100\text{MW}$ , $f_{\text{GW}} < 1.0$ , and a) $H_{98} < 1.6$ and b) $H_{\text{Petty}} < 1.0$ assuming $\eta_{\text{NBI}} = 0.4\text{A m}^{-2}\text{W}^{-1}$ . The arrows indicate the direction which is within the imposed limit. . . . .	81
4.10	Contour plots for a 2D scan changing $I_p$ and $T_{e0}$ at fixed $P_{\text{fus}} = 1.1\text{GW}$ , showing the necessary a) $P_{\text{aux}}$ and b) $H_{98}$ when $\eta_{\text{NBI}} = 0.2\text{A m}^{-2}\text{W}^{-1}$ is assumed. . . . .	82
4.11	Available parameter space if the following restrictions are imposed: $P_{\text{aux}} < 100\text{MW}$ , $H_{98} < 1.6$ and $f_{\text{GW}} < 1.0$ assuming $\eta_{\text{NBI}} =$ a) 0.3 and b) $0.2\text{A m}^{-2}\text{W}^{-1}$ . The arrows indicate the direction which is within the imposed limit. . . . .	82
4.12	Contour plots for a 2D scan changing $I_p$ and $T_{e0}$ at fixed $P_{\text{fus}} = 1.1\text{GW}$ with $I_{\text{rod}} = 50\text{MA}$ showing the variation of a) $P_{\text{aux}}$ , b) $H_{98}$ c) $H_{\text{Petty}}$ and d) $\beta_N$ when $\eta_{\text{NBI}} = 0.4\text{A m}^{-2}\text{W}^{-1}$ is assumed. . . . .	85
4.13	Available parameter space for the superconducting design if the following restrictions are imposed: $P_{\text{aux}} < 100\text{MW}$ , $H_{98} < 1.6$ and $f_{\text{GW}} < 1.0$ assuming $\eta_{\text{NBI}} =$ a) 0.4 b) 0.2 and c) $0.15\text{A m}^{-2}\text{W}^{-1}$ . The arrows indicate the direction which is within the imposed limit. . . . .	87
5.1	NBeams prediction for the current density for an 8MW 1MeV beam with $R_t = 3.1\text{m}$ to drive the on axis current. The magnetic axis was at $R_0 = 3.15\text{m}$ Shown as a function of $\sqrt{\rho\psi}$ . . . . .	91
5.2	NUBEAM prediction for the marker deposition as seen from a) above and b) as a poloidal cross section for an 8MW 1MeV beam with $R_t = 3.1\text{m}$ oriented in the horizontal plane. . . . .	92
5.3	Comparison of NBeams, NUBEAM and RABBIT's prediction for the a) initial deposition, b) orbit average deposition of a 8MW, 1MeV beam with $R_t = 3.1\text{m}$ . Note that NBeams doesn't perform an orbit average so $S_0 = S_{av}$ . . . . .	92
5.4	Comparison of NBeams, NUBEAM and RABBIT's prediction for the a) fast ion density, b) unshielded current and c) shielded current profile with a 8MW, 1MeV beam with $R_t = 3.1\text{m}$ . . . . .	94

5.5	a) $J_{\text{NBI}}$ b) power deposition with an 8MW 1MeV beam for a range of different core temperatures. The auxiliary power required to reach the necessary current density in the core is shown in c) . . . . .	96
5.6	Available parameter space if the following restrictions are imposed: $P_{\text{aux}} < 100\text{MW}$ , $H_{98} < 1.6$ , $f_{\text{GW}} < 1.0$ and $\langle n_{e20} \rangle < 1.65$ and $P_{\text{fus}} = 1.1\text{GW}$ . Here $\eta_{\text{CD}} = 0.4\text{A m}^{-2}\text{W}^{-1}$ has been assumed and the arrows indicate the direction within the limit. . . . .	97
5.7	NBeams current drive prediction for an 90MW 500keV beam to drive the off axis current along with the required current as specified in SCENE. . . . .	98
5.8	NUBEAM prediction for the marker deposition as seen from a) above and b) as a poloidal cross section for an 90MW 500keV beam with $R_t = 3.8\text{m}$ oriented in the horizontal plane. . . . .	99
5.9	Comparison of NBeams, NUBEAM and RABBIT's prediction for the beam's a) initial deposition, b) orbit average deposition with a 90MW, 500keV beam with $R_t = 3.8\text{m}$ . Note for NBeams doesn't perform an orbit average so $S_0 = S_{av}$ . . . . .	99
5.10	Comparison of NBeams, NUBEAM and RABBIT's prediction for the a) fast ion density, b) unshielded current and c) shielded current with a 90MW, 500keV beam with $R_t = 3.8\text{m}$ . . . . .	100
5.11	Fast ion distribution function for a) NBeams b) NUBEAM and c) RABBIT at $\sqrt{\rho_\psi} = 0.74$ for the off axis beam aligned with the horizontal plane. . . . .	102
5.12	NUBEAM prediction for the marker deposition as seen from a) above and b) as a poloidal cross section for a 90MW 500keV beam with $R_t = 3.8\text{m}$ angled at $45^\circ$ to the horizontal plane. . . . .	103
5.13	NUBEAM and RABBIT prediction for a) initial and b) orbit averaged deposition with a 90MW 500keV beam angled at $45^\circ$ such that it is aligned with the magnetic field. Note NBeams is included but cannot model angled beams. . . . .	104
5.14	NUBEAM and RABBIT prediction for the a) fast ion density, b) unshielded current and c) shielded current with a 90MW 500keV beam angled at $45^\circ$ such that it is aligned with the magnetic field. Note NBeams is included but cannot model angled beams. . . . .	105
5.15	Fast ion distribution function for a) NUBEAM and b) RABBIT at $\sqrt{\rho_\psi} = 0.74$ with a beam aligned to the magnetic field. . . . .	106
5.16	$\eta_{\text{NBI}}$ for an angled 90MW, 500keV beam for a) a scan in $\langle n_{e20} \rangle$ at fixed $\langle T_e \rangle = 14.8\text{keV}$ and b) a scan in $\langle T_e \rangle$ at fixed $\langle n_{e20} \rangle = 1.54\text{m}^{-3}$ predicted by NUBEAM. . . . .	107

5.17	a) $\eta_{\text{NBI}} \frac{T_{\text{ref}}}{\langle T_e \rangle}$ and b) $\eta_{\text{NBI}} \sqrt{\frac{T_{\text{ref}}}{\langle T_e \rangle}}$ for an angled 90MW, 500keV beam for a scan in $\langle T_e \rangle$ at fixed $\langle n_{e20} \rangle = 1.54\text{m}^{-3}$ predicted by NUBEAM. Here $T_{\text{ref}} = 15\text{keV}$ .	108
5.18	Available parameter space if the following restrictions are imposed: $P_{\text{aux}} < 100\text{MW}$ , $H_{98} < 1.6$ , $f_{\text{GW}} < 1.0$ and $\langle n_{e20} \rangle < 1.65$ and $P_{\text{fus}} = 1.1\text{GW}$ . Here $\eta_{\text{CD}}^* = 0.34\text{A m}^{-2} \text{W}^{-1}$ has been assumed and the arrows indicates the direction that lies within the limit imposed.	108
5.19	Comparing the a) initial specified $J_{\text{aux}}$ profile and the b) NUBEAM matched $J_{\text{aux}}$ to the NUBEAM predictions of the final beam configuration.	109
5.20	Heating profiles for the a) ions and b) electrons from the NBI and Fusion $\alpha$ 's in the BurST scenario.	110
6.1	Miller fit shown for $\rho_\psi = 0.5$ surface showing the a) flux surface contour and b) the poloidal field.	116
6.2	Impact of including different fields on the linear micro-instability predictions by GS2 for the $\rho_\psi = 0.5$ surface of the baseline equilibrium. Note the log scale.	117
6.3	Eigenfunction for the dominant fully electromagnetic mode at $k_y =$ a) 0.1, b) 0.35, and c) 4.2 in the baseline equilibrium at $\rho_\psi = 0.5$ .	120
6.4	a) Linear spectra of the dominant odd and even modes for $k_y = 0.1 \rightarrow 1.0$ . The hollow marker denotes an even parity eigenfunctions and a filled marker an odd eigenfunction. b) Dominant odd eigenfunction at $k_y = 0.35$ .	122
6.5	a) $\theta_0$ scan for $k_y = 0.35$ showing the narrow nature of the KBM and the unaffected MTMs. b) The MTM eigenfunction when $\theta_0 = \pi$ . c) Effective growth rate when including flow shear where the vertical black line represents the diamagnetic flow shear $\gamma_{\text{dia}}$ .	124
6.6	a) Examining the impact of plasma $a/L_{Te}$ when $k_y = 0.35$ . The dominant even (KBM) and odd (MTM) instabilities are shown, with the KBM demonstrating much stiffer behaviour. Note the log scale in $\gamma$ . The dashed line shows the analytic prediction $\omega_{\text{MTM}}^{\text{CR}}$ defined in the text. b) Eigenfunction of for the ion direction mode (filled green stars) for $a/L_{Te} = 7.0$ ; despite being odd parity, the mode is not tearing as $C_{\text{tear}} = 0.0$ .	126
6.7	Examining the impact of plasma $a/L_{Ti}$ when $k_y = 0.35$ . The dominant even (KBM) and odd (MTM) instabilities are shown, with the KBM demonstrating much stiffer behaviour. The oKBM is again found at high $a/L_{Ti}$ .	127

6.8	Examining the impact of $a/L_n$ when $k_y = 0.35$ . The dominant even (KBMs and TEMs) and odd (MTM) instabilities are shown, with the KBM demonstrating much stiffer behaviour. . . . .	128
6.9	a) A scan was performed at fixed $a/L_p$ where the contribution of $a/L_n$ was varied for $k_y = 0.35$ . $a/L_{Te} = a/L_{Ti}$ was enforced. . . . .	129
6.10	a) Impact of collision frequency showing the dominant odd and even parity mode for different values of $\nu_{ee}$ when $k_y = 0.35$ . Note the linear scale here. b) the eigenfunction when $\nu_{ee} = 0.14c_s/a$ . . . . .	130
6.11	Examining the impact of $Z_{\text{eff}}$ on the KBMs and MTMs for $k_y = 0.35$ and $\nu_{ee} = 0.14c_s/a$ . . . . .	131
6.12	Examining the impact of a) $\beta_{e,\text{unit}}$ at fixed $\beta'_{e,\text{unit}}$ and b) $\beta'_{e,\text{unit}}$ at fixed $\beta_{e,\text{unit}}$ on the linear micro-instabilities at $k_y = 0.35$ . . . . .	132
6.13	The impact $\beta'_{e,\text{unit}}$ has on $\omega_{\nabla B}$ and $\omega_{\text{curv}}$ . The $\nabla B$ drift is negative for the high $\beta'$ cases when $ \theta  < \pi$ , which is stabilising for ballooning modes. . . . .	133
6.14	Changing $\beta_{e,\text{unit}}$ and $\beta'_{\text{unit}}$ consistently. It can be seen that there is a smooth transition between the ITG at $\beta_{e,\text{unit}} = 0$ to the equilibrium $\beta'_{e,\text{unit}} = 0.012$ . . . . .	134
6.15	$\hat{s} -  \beta' $ diagram showing how the the ideal ballooning stability boundary moves with $q$ . The reference equilibrium value of $\hat{s}$ and $ \beta'_{e,\text{unit}} $ is shown by the magenta cross and has $q = 4.3$ (green curve). . . . .	135
6.16	Dominant even eigenvalues when changing a) $q$ and b) $\hat{s}$ for $k_y = 0.35$ . . . . .	135
6.17	Dominant odd eigenvalues when changing a) $q$ (at $\nu_{ee} = 0.14c_s/a$ ) and b) $\hat{s}$ for $k_y = 0.35$ . . . . .	136
6.18	Examining the impact of a higher field device by increasing $I_{\text{rod}}$ for $k_y = 0.35$ at $\rho_\psi = 0.5$ . . . . .	137
6.19	a) $\theta_0$ scan of the dominant mode at $k_y = 4.2$ , b) eigenfunction for the inboard iMTM and c) effective growth rate with $E \times B$ shear. The vertical black line shows $\gamma_{\text{dia}}$ . . . . .	140
6.20	Examining the impact of a) $a/L_{Te}$ and b) $a/L_n$ on the MTMs at $k_y = 4.2$ . . . . .	141
6.21	Examining the impact of $\nu_{ee}$ on the MTMs at $k_y = 4.2$ . . . . .	141
6.22	Examining the impact of changing a) $\beta_{e,\text{unit}}$ at fixed $\beta'_{e,\text{unit}}$ and b) $\beta'_{e,\text{unit}}$ at fixed $\beta_{e,\text{unit}}$ and c) $\beta_{e,\text{unit}}$ and $\beta'_{e,\text{unit}}$ together on the MTMs at $k_y = 4.2$ . . . . .	142
6.23	Impact of a) $q$ and b) $\hat{s}$ on the MTMs at $k_y = 4.2$ . . . . .	143
6.24	Examining the impact of a higher field device by increasing $I_{\text{rod}}$ on the MTMs for $k_y = 4.2$ . . . . .	144

6.25	a) Growth rate spectrum for high values of $k_y$ at different $a/L_{Te}$ . The equilibrium value was $a/L_{Te} = 2.77$ . b) Eigenfunctions for $k_y = 35$ when $a/L_{Te} = 7.0$ .	145
6.26	Impact of a) $\beta_{e,\text{unit}}$ and b) $\beta'_{e,\text{unit}}$ at different $a/L_{Te}$ with $k_y = 35$ .	146
6.27	Impact of a) $q$ and b) $\hat{s}$ with different $a/L_{Te}$ at $k_y = 35$ .	147
6.28	Critical $a/L_{Te}$ threshold for various a) $q$ and b) $\hat{s}$ at $k_y = 35$ .	147
6.29	Examining the impact of $I_{\text{rod}}$ on the ETG modes for 3 higher temperature gradients at $k_y = 35$ .	148
6.30	a) Dominant odd and even mode for the $\rho_\psi = 0.3$ surface of the baseline equilibrium.	149
6.31	Eigenfunctions found for the a) KBM at $k_y = 0.35$ b) MTM at $k_y = 0.35$ c) MTM at $k_y = 4.2$ for the $\rho_\psi = 0.3$ surface of the baseline equilibrium.	150
6.32	a) Dominant odd and even modes for $\rho_\psi = 0.85$ and b) Eigenfunction of the MTM mode when $k_y = 1.05$ .	151
6.33	Impact of $\theta_0$ on the MTM seen at $k_y = 1.05$ when $\rho_\psi = 0.85$ .	152
6.34	Impact of a) $a/L_{Te}$ and b) $a/L_n$ on MTM seen at $k_y = 1.05$ when $\rho_\psi = 0.85$ .	153
6.35	Impact of $\nu_{ee}$ on MTM seen at $k_y = 1.05$ when $\rho_\psi = 0.85$ .	154
6.36	Impact of a) $\beta_{e,\text{unit}}$ at fixed $\beta'_{e,\text{unit}}$ and b) $\beta'_{e,\text{unit}}$ at fixed $\beta_{e,\text{unit}}$ and c) consistent $\beta_{e,\text{unit}}$ and $\beta'_{e,\text{unit}}$ for the MTM seen at $k_y = 1.05$ when $\rho_\psi = 0.85$ .	155
6.37	Impact of a) $q$ and b) $\hat{s}$ on MTM seen at $k_y = 1.05$ when $\rho_\psi = 0.85$ .	156
6.38	Impact of $I_{\text{rod}}$ on MTM seen at $k_y = 1.05$ when $\rho_\psi = 0.85$ .	156
6.39	Dominant odd and even mode for the $\rho_\psi = 0.5$ surface of the optimised equilibrium without flow shear outlined in Table 6.4.	159
6.40	Effective growth rate for the $\rho_\psi = 0.5$ surface of the optimised equilibrium with diamagnetic levels of flow shear.	160
7.1	Linear spectra of the fully electromagnetic dominant mode predicted by GS2, CGYRO, and TGLF for the BurST baseline equilibrium.	164
7.2	a) Time trace of the different flux components for the BurST equilibrium, with the electron flutter flux dominating the spectrum, indicative of MT transport. b) Zoomed in on the other fluxes. Note that this simulation has not saturated.	166
7.3	$k_x$ spectrum of $\phi$ summed over $k_y$ at $\theta = 0$ . A build up of potential is seen at the highest $k_x$ , suggesting insufficient radial resolution to properly capture the dissipative damping mechanism.	167

7.4	$k_x$ spectrum of $\phi$ with a) 384 $k_x$ modes and $L_x = 65\rho_s$ b) increased collisionality of $\nu_{ee} = 0.05c_s/a$ and c) increased $\hat{s} = 1.5$ . . . . .	168
7.5	Time trace of the flux components of the GA-STD case. . . . .	170
7.6	Electrostatic energy flux spectrum prediction by CGYRO, QLGYRO and TGLF as a function of $k_y$ for the GA-STD case. . . . .	171
7.7	a) Quasi-linear weights $w^\phi$ and b) saturated potential $ \Phi $ prediction by CGYRO, QLGYRO and TGLF for the GA-STD case. . . . .	172
7.8	Total electrostatic energy flux prediction by CGYRO, QLGYRO and TGLF when scanning through a) $a/L_T$ b) $R_{\text{maj}}/a$ and c) $\kappa$ for the GA-STD case. . .	173
7.9	Total electrostatic energy flux prediction by CGYRO, QLGYRO and TGLF as a function of $a/L_T$ for the MAST #27274 equilibrium. . . . .	175
7.10	Quasi-linear weights $w^\phi$ prediction by CGYRO, QLGYRO and TGLF for the MAST #27274 equilibrium when a) $a/L_T = 2.0$ and b) $a/L_T = 5.2$ . . . . .	176
7.11	Saturated potential $ \Phi $ prediction by CGYRO, QLGYRO and TGLF for the MAST equilibrium when a) $a/L_T = 2.0$ and b) $a/L_T = 5.2$ . . . . .	177
7.12	$k_{x,\text{rms}}$ prediction by CGYRO, QLGYRO and TGLF for the MAST #27274 equilibrium when a) $a/L_T = 2.0$ and b) $a/L_T = 5.2$ . . . . .	178
7.13	Effective growth rate $\gamma_{\text{eff}}$ prediction by CGYRO, QLGYRO and TGLF for the MAST #27274 equilibrium when a) $a/L_T = 2.0$ and b) $a/L_T = 5.2$ . . . . .	178
7.14	Saturated zonal flow $V_{\text{ZF}}$ prediction by CGYRO, QLGYRO and TGLF for the MAST #27274 equilibrium as a function of $a/L_T$ . . . . .	179
7.15	Time trace of the flux components prediction by CGYRO for the NSTX #120968 equilibrium without flow shear. . . . .	182
7.16	a) $k_x$ spectrum of $\phi$ where no build up at high $k_x$ is seen. b) $k_x$ spectrum of $A_{\parallel}$ with no build up seen, but it is very peaked at $k_x = 0$ . c) Time trace of $A_{\parallel}$ for the lowest $k_y$ , with the lowest $k_y$ in the “runaway” phase, especially beyond $t = 600a/c_s$ . . . . .	183
7.17	NSTX MTM simulation with flow shear showing the a) time trace for the heat flux, b) $k_y$ spectrum of $A_{\parallel}$ and c) the $k_y$ magnetic flutter heat flux spectrum. . . . .	184
7.18	Eigenvalues comparing QLGYRO to TGLF when using a range of a) $0.3 \rightarrow 1.65$ (default setting) and b) $0.3 \rightarrow 0.5$ for the initial guesses of $\theta_w$ . . . . .	186
7.19	Quasi-linear weights prediction by CGYRO, QLGYRO and TGLF when using $\phi$ as the normalising field for all 3 codes. . . . .	187

7.20	a) $R_{A_{  }}^{\phi}$ which shows the ratio of $\phi$ and $A_{  }$ . b) Modified quasi-linear weight $w^{A_{  }}R_{A_{  }}^{\phi}$ prediction by CGYRO, QLGYRO and TGLF. . . . .	188
7.21	Simulation where $A_{  }$ is turned off in the non-linear term illustrating a) $R_{A_{  }}^{\phi}$ which shows the ratio of $\phi$ and $A_{  }$ . b) Modified quasi-linear weight $w^{A_{  }}R_{A_{  }}^{\phi}$ predictions by CGYRO, QLGYRO and TGLF. . . . .	189
7.22	Saturated potential of the nonlinear CGYRO run showing a) $ \Phi $ and the QLGYRO prediction. b) shows the saturated $ \mathbf{A}_{  } $ predicted by CGYRO. . . . .	190
7.23	Effective growth rate using $A_{  }$ predicted by CGYRO. It displays a similar functional form to the TGLF equivalent and suggests there is a saturation mechanism. . . . .	191

# Acknowledgements

The work presented in this thesis would not have been possible without the many people who have supported me throughout my PhD. My supervisors, Prof. Howard Wilson, Dr. David Dickinson and Dr. Colin Roach have pushed me to become a better scientist. The breadth of their combined knowledge continues to astound me as I often spent many meetings just trying to keep up with them. I hope to one day match their level of excellence in this field. I was also lucky to collaborate with many people around the globe and would like to thank Gary Staebler, Walter Guttenfelder and Markus Weiland for their contributions to this work.

I owe my sanity to both the friends I've known since childhood and to the ones I've made on this course. The annual Christmas carnage trip with my fellow PhD students have made some of the most memorable weekends of my life and I can honestly say that those weekends changed me. I look forward to all the future hot tub moments. It definitely feels like I've been through hell and back with all of these friends and getting through the day to day was only possible with the help of the "Covfefe" and "Yorkies" gang.

To all the friends I made before my PhD, I thank you for bearing with my inability to keep in touch. I've had the weirdest conversations with the "Toad venom group", and want to thank the "Cool group" for all the holidays we've gone on together. My mandir boys kept me grounded throughout my entire educational life and gave me the mental fortitude to handle a PhD, for which I am eternally grateful and only slightly resentful.

The views and opinions expressed herein do not necessarily reflect those of the European Commission. This work was supported by the Engineering and Physical Sciences Research Council [EP/L01663X/1, EP/R034737/1, EP/T012250/1]. This work used the ARCHER UK National Supercomputing Service (<http://www.archer.ac.uk>). We acknowledge the CINECA award under the ISCRA initiative, for the availability of high performance computing resources

and support. This research used resources of the National Energy Research Scientific Computing Center (NERSC), a U.S. Department of Energy Office of Science User Facility located at Lawrence Berkeley National Laboratory, operated under Contract No. DE-AC02-05CH11231.

*I find myself incredibly lucky to have parents and a sister who have supported me in all my endeavours and I can unequivocally say that I would not be where I am today without them. Finally to Surabhi, I have not met a person who can drive me insane quite like you do but also keep me from falling apart. You've made me a better version of myself and I've cherished getting to share this experience with you.*

# Declaration

I declare that this thesis is a presentation of original work and I am the sole author. This work has not previously been presented for an award at this, or any other, University. All sources are acknowledged as references.

Components of Chapter 1 have been published in the following articles:

- HR Wilson, IT Chapman, T Denton, AW Morris, BS Patel, GM Voss, C Waldon, and the STEP Team, “STEP—on the pathway to fusion commercialization, Commercialization of Fusion - Chapter 8”, *IOP Publishing* (2020) 8, 1-18.
- TEG Nicholas, TP Davis, F Federici, J Leland, BS Patel, C Vincent, & SH Ward “Re-examining the role of nuclear fusion in a renewables-based energy mix”, *Energy Policy* 149 (2020), 112043.

Components of Chapters 3 and 7 have been published in the following articles:

- GM Staebler, J Candy, EA Belli, JE Kinsey, N Bonanomi, & BS Patel, “Geometry dependence of the fluctuation intensity in gyrokinetic turbulence”, *Plasma Physics and Controlled Fusion* 63.1 (2020), 015013

Components of Chapters 3 and 7 have been published in the following conference proceedings

- BS Patel, D Dickinson, F Koechl, CM Roach, GM Staebler, & HR Wilson, “Optimising TGLF for a Q=10 Burning Spherical Tokamak”, *46th EPS Conference on Plasma Physics*, EPS 2019. European Physical Society (EPS)

# Chapter 1

## Introduction

### 1.1 Fusion’s place in the energy-mix

Fusion energy has long been considered as a potential solution to the world’s long term energy needs. Historically human progression has been closely correlated with energy usage [1, 2] and energy demand is expected to increase significantly in the near future. In 2019 approximately 167 000 TW h of energy was consumed, of which 80% was comprised of fossil fuels such as oil, coal and gas with the remaining being filled with renewables and nuclear [3]. For scale, this corresponds to 19 000 GW<sub>e</sub> plants running throughout the year. However, this now must be examined in the context of rising CO<sub>2</sub> emissions, which has led to the suggestion by many scientists that complete de-carbonisation must be achieved as rapidly as possible [4].

On paper, fusion aligns well with this goal as it is a low carbon source with an abundance of primary fuels (deuterium and lithium) potentially lasting thousands of years. However, fusion is not commercially available and there has not yet been a demonstration of net energy gain, let alone net electricity.

ITER, a major milestone of the EUROfusion roadmap, is expected to be constructed by 2025. It is an international project involving over 35 countries and by 2035 is expected to generate ten times the auxiliary power used, a crucial step in the fusion timeline. It will be the first reactor to demonstrate a scenario where more power is generated by the plasma than is put into the plasma, which is termed “energy break-even”. Once ITER has achieved this “full powered” regime, the construction of DEMO will begin, which will be a fully operational power plant capable of generating electricity in the 2050s-60s at the earliest [5]. However, this is a first of a kind plant, and it will take time for fusion to become a significant fraction of the energy-mix.

Similar to historical growth of fission<sup>1</sup>, solar and wind are currently experiencing an exponential growth phase where their installed power doubles approximately every 3 years. This exponential growth is expected to continue until the supply reaches approximately 10% of its final penetration. After this point the construction is expected to transition to a linear growth [6]. Applying this premise to fusion and assuming DEMO generates 1 GW<sub>e</sub> by 2060; fusion will begin to make a significant contribution to the energy-mix by the end of the century. This exponential phase is often labelled as the “valley of death” for product development and requires solid financial backing to cross. During this exponential growth if the installed doubling time is shorter than the economic payback time then fusion as an industry will be a net financial sink and thus requires significant investment, until the aforementioned linear phase is reached where revenue begins to be generated [6, 7]. Furthermore, the long build times and high capital costs limit the innovation cycle meaning N<sup>th</sup>-of-a-kind development takes significantly longer.

However, the urgency invoked by anthropogenic climate change means that the energy-mix fusion will be entering will likely look very different to the current one. The IPCC report recommends that net-zero CO<sub>2</sub> emissions should be reached by 2050 to mitigate the worst effects of climate change. When this is actually achieved is a complicated question, but several reports predict varying penetrations of renewable energy in a net zero scenario, with 100% renewables being theoretically possible with developed infrastructure, energy storage and demand side management [8–10]. However, this necessitates a large amount of over-capacity given the intermittency issues of variable renewable energy sources (vRES) like wind and photo-voltaics. Energy storage systems help mitigate the intermittency issue of vRES but cannot completely substitute “firm” sources like nuclear or gas with carbon capture and storage (CCS) at a reasonable cost estimate [11]. Furthermore, vRES tends to be energy sparse, so situations where land is valuable or energy demand is dense (mega-cities), high fractions of vRES may not be feasible [12, 13]. The penetration of vRES in a net zero scenario has many factors when being calculated, but least cost analysis has found it may vary between 30-80% [11, 14]. Other energy sources will need to fill in the gap left by renewables, with flexibility being a desirable property [15]. When including “firm” sources, the overall costs drops [9, 16, 17].

By the end of the 21<sup>st</sup> century, it is highly likely that renewables will form a significant fraction of the total energy-mix. Given the current fusion timeline, it is unlikely that fusion will play any significant role in the path to net zero carbon emissions, but will be relevant as

---

<sup>1</sup>Pre-Chernobyl

a post-carbon technology as energy demand continues to increase.

Fusion will likely complement with other low carbon firm sources such as fission and gas+CCS and their relative merits need to be compared, which will vary in different situations and geographical locations. Compared to fission, fusion has several advantages with its inherent safety, fuel abundance, non-proliferation and its lack of high-level radioactive waste<sup>2</sup>. It should be noted that some waste materials from the current DEMO design will still be classified as intermediate level waste after 100 years due to material impurities and will require geologic disposal, similar to fission [18]. Fusion will likely be economically similar to current fission with large capital costs and minimal operating and fuel costs but potentially reduced decommissioning costs. As the overnight costs<sup>3</sup> of fission increases, its penetration into the energy-mix is expected to reduce such that above 6200 £/kW<sub>e</sub>, some anticipate that it will play a minimal part of the total energy-mix [9, 19]. However, this is highly dependent on many assumptions from geography to competing technologies and political factors. For example, if the overnight costs of gas+CCS drops from the previously assumed 1270 £/kW<sub>e</sub> to 775 £/kW<sub>e</sub>, then fission needs to be below 3500 £/kW<sub>e</sub> to remain competitive. Fusion will likely face a similar fate, and current estimates for the DEMO<sup>4</sup> are 6600 £/kW<sub>e</sub> [20]. This assumed “first-of-a-kind” costs which may lower over time by 25 – 40% if a single design is developed [21, 22]. If fusion is not competitive<sup>5</sup> with these sources, it will likely need a niche to fill or become a post-fission/CCS technology [23, 24].

If the fusion timeline can be accelerated and the capital cost reduced via a more compact device, then the impact fusion will have on the energy-mix will be increased. This work aims to explore the physics associated with a compact high performance reactor that can generate net electricity on a shorter timescale.

## 1.2 Fusion on Earth

Currently, the only place fusion occurs naturally in significant amounts is in stars. Here hydrogen is gravitationally confined and heated to high enough temperatures that the ions are able to fuse together releasing a significant amount of energy. Due to the incredibly long confinement time in the sun ( $\sim 10^6$  yrs), the core temperature of the sun only needs to be at  $\mathcal{O}(10^6)$  K, well below the peak of the reaction rate for proton-proton fusion. Terrestrial fusion

---

<sup>2</sup>Though fusion may have to compete against GEN IV fission reactors where its advantages are fewer.

<sup>3</sup>Calculated by dividing the capital expenditure by the net electrical power of the plant.

<sup>4</sup>This assumed no development of fusion technologies is required.

<sup>5</sup>Once again this is highly dependant on multiple factors as cost isn't the only consideration

does not have this luxury. Deuterium and tritium are the main candidates for the fusion reaction due to their high reaction rate at lower temperatures, the products of which are a 3.5 MeV helium nucleus and 14.1 MeV neutron [25, 26].

### 1.2.1 Tokamaks

There have been many attempts to utilise this mechanism on earth as an energy source. Due to limitations on the confinement time, the hydrogen isotopes need to be at  $\mathcal{O}(10^8)\text{K}$  [27] which is well beyond the capability of any material to contain. Some fusion reactor designs utilise the fact that at fusion relevant temperatures, deuterium and tritium become fully ionised, forming a plasma. This has led to several designs which magnetically confine the plasma to harness fusion energy. One route initially attempted is to use a purely toroidal magnetic configuration, which would be able to confine the plasma in a doughnut-like shape, as shown by the red lines in Figure 1.1. The strategy here was that particles within the plasma would be able to freely travel along the magnetic field line in the toroidal direction  $\varphi$ , but be confined in the planes perpendicular to it. This magnetic configuration can be achieved with a vertical current  $I_{\text{rod}}$  along the symmetry axis, the strength of which scales like  $1/R$ .

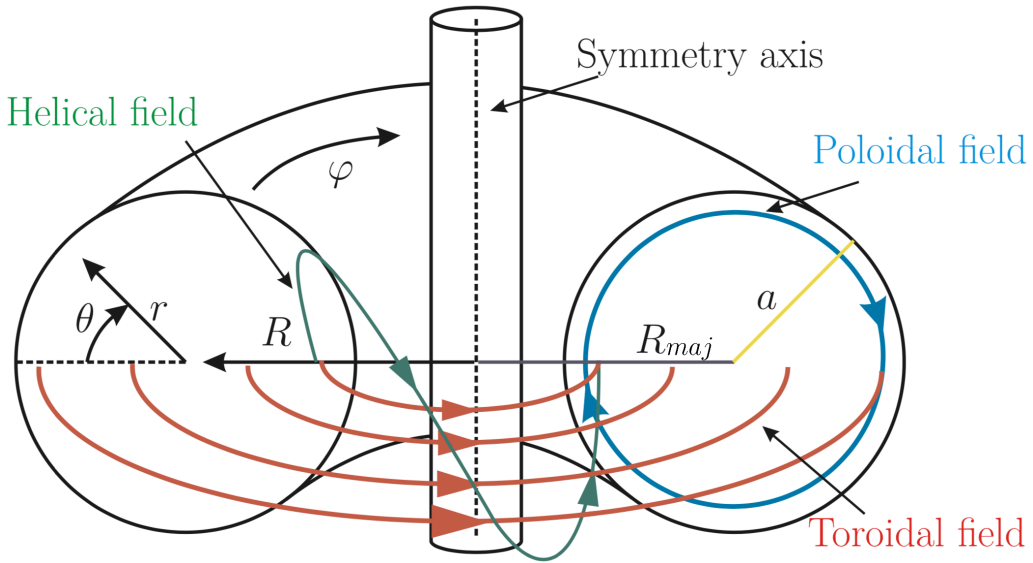


Figure 1.1: Illustration of the tokamak design. A combination of the toroidal (red) and poloidal (blue) fields generates a helical field that can cancel out the average drifts created by magnetic geometry. Taken with permission from [28]

However, due to the curvature and gradient of this magnetic configuration, there exists a vertical drift for all plasma species,  $v_{\text{curv}}$  and  $v_{\nabla B}$  where the sign of the velocity is dependent on the particle's charge [26]. This charge separation sets up a vertical electric field which in

turn creates a radial velocity  $v_{E \times B}$ , causing all the particles to drift out of the plasma. This design alone was found to be insufficient at confining the plasma for a significant period of time. This was overcome by including a poloidal magnetic field, shown with the blue line in Figure 1.1, that allows particles to short circuit the electric field preventing the generation of a  $v_{E \times B}$ . A toroidal current can be used to generate this poloidal field. A solenoid is wrapped around the symmetry axis and by ramping up its current, a toroidal current,  $I_p$ , is induced in the plasma via transformer action. Figure 1.1 illustrates the different components of the fields along with the different dimensions. In this design there are closed field lines meaning that particles are not able to easily escape, which effectively isolates the plasma from any material. This design is known as a tokamak and has proven to be the most successful fusion reactor so far, forming the basis for ITER and DEMO.

The triple product, defined as the product of the fuel density  $n$ , temperature  $T$ , and confinement time  $\tau_E$ , is often used as a figure of merit for fusion. For the fusion reaction to become self-sustaining, which is defined as “ignition”, a D-T reactor must satisfy [26]

$$nT\tau_E \geq 3.1 \times 10^{21} \text{keV s m}^{-3} \quad (1.1)$$

Tokamaks have achieved the highest triple product with both JET and JT60-U reporting  $nT\tau_E > 1 \times 10^{21} \text{keV s m}^{-3}$  [29, 30]. The limiting factor on  $\tau_E$  is typically turbulence, which causes significant transport, without which the commercialisation of fusion would likely have already occurred. The general strategy has been to increase  $\tau_E$  by increasing the size or magnetic field of the reactor [31, 32].

### 1.2.2 BurST - Burning Spherical Tokamak

The aspect ratio of a tokamak is defined as  $A = R_{\text{maj}}/a$ , and the inverse aspect ratio as  $\varepsilon = a/R_{\text{maj}}$ . Conventional tokamaks have  $\varepsilon \sim 1/3$ , with both ITER and DEMO being designed with a conventional aspect ratio. Spherical tokamaks (STs) will have  $\varepsilon$  closer to 1. In a conventional tokamak the toroidal field  $B_\varphi$  is significantly larger than the poloidal field  $B_\theta$ , but for STs, they can be comparable.

ST designs have accessed high confinement regimes, and have achieved the highest plasma pressures for a given magnetic field of any tokamak design [33–35], increasing the achievable fusion power density. Furthermore, they have been shown to have improved stability properties and capability for a higher bootstrap current [36–39] which will be discussed in more detail in later chapters. These properties make STs a perfect candidate for examining

an accelerated path to a compact fusion device. This strategy is being explored by public and private institutions such as the STEP program by CCFE [40] and the ST40 by Tokamak Energy [41]. Furthermore, the SPARC program by Commonwealth Fusion Systems examines the feasibility of a high field, net energy, compact conventional tokamak to accelerate the path to fusion [32].

This work will look at the feasibility of an ST that will generate net electricity which will be called BurST, standing for Burning Spherical Tokamak. Chapter 2 will examine various areas of relevant physics necessary for modelling a steady state scenario and Chapter 3 will examine some of the modelling tools currently available. Different steady state scenarios will be examined and the current drive requirement will be determined in Chapter 4. In Chapter 5, neutral beam modelling will be used to find a viable non-inductive configuration and the validity of reduced neutral beam models will be determined. Chapter 6 examines the drivers of turbulent modes that occur in this BurST case and in Chapter 7, the first steps are taken to develop a quasi-linear turbulent transport suitable in a BurST regime. Finally, Chapter 8 summarises the results of this work.

## Chapter 2

# Steady state modelling in Tokamaks

This chapter will focus on some of the relevant physics needed for the steady state modelling of a BurST reactor design. It should be noted that the ramp up/ramp down of the plasma is not examined here but is crucial to understand. Once a suitable flattop scenario has been designed it will be necessary to understand if it is even possible to reach such a regime, but that is outside the scope of this work.

First, any plasma design must satisfy force balance such that it is consistent with the Grad-Shafranov equation. To solve the Grad Shafranov equation, it will be shown that knowledge of the current profile is necessary so the different sources of current, both neoclassical and auxiliary, will be discussed. Furthermore, knowledge of the pressure profile is also required. The density and temperature profiles are determined by the fuelling and heating systems and the different transport mechanisms that arise in a tokamak plasma. To model a steady state scenario requires an appropriate physics model for each of these different areas. When these are combined, they form an integrated modelling suite.

This chapter will be laid out as follows

- Section 2.1: Derivation of the Grad-Shafranov equation
- Section 2.2: Examination of the different sources of current
- Section 2.3: Examination of the different sources of transport
- Section 2.4: Derivation of the gyrokinetic equation
- Section 2.5: Examination of quasi-linear theory
- Section 2.6: Summary

## 2.1 Plasma equilibrium

The first step of designing a tokamak is to generate a consistent plasma equilibrium which requires a solution to the Grad-Shafranov equation.

### 2.1.1 Grad-Shafranov equation

Due to the toroidal symmetry of a tokamak, as shown in Figure 1.1, the plasma is composed of nested toroidal magnetic surfaces. The plasma must satisfy force balance

$$\vec{J} \times \vec{B} = \vec{\nabla} p \quad (2.1)$$

where  $p$  is the plasma pressure and  $\vec{J}$  is the current density. From this it is clear that  $\vec{B} \cdot \vec{\nabla} p = \vec{J} \cdot \vec{\nabla} p = 0$ , so the directions of the magnetic field and current density must lie on surfaces of constant pressure. A flux surface co-ordinate,  $\psi$ , can be defined as:

$$\psi = \int_0^V dV \vec{B} \cdot \vec{\nabla} \theta \quad (2.2)$$

where  $\theta$  is parameter along the surface. Given that  $\psi$  satisfies  $\vec{B} \cdot \vec{\nabla} \psi = 0$ , the pressure can be written as  $p = p(\psi)$ . When combined with the toroidal symmetry (in a right-handed co-ordinate system), the poloidal field is related to  $\psi$  by the following [26]

$$\vec{B}_\theta = \vec{\nabla} \psi \times \vec{\nabla} \varphi \quad (2.3)$$

where  $\varphi$  is the toroidal angle, as shown in Figure 1.1. Due to symmetry between  $\vec{B}$  and  $\vec{J}$ , an analogous flux function,  $f(\psi)$ , exists that is related to the poloidal current density. A similar equation can be written for the poloidal current

$$\vec{J}_\theta = \vec{\nabla} f(\psi) \times \vec{\nabla} \varphi \quad (2.4)$$

Equation 2.4 must be consistent with Ampère's Law from which it follows that:

$$f = \frac{RB_\varphi}{\mu_0} \quad (2.5)$$

It is possible to re-write Equation 2.1 as:

$$\vec{J}_\theta \times \vec{B}_\varphi + \vec{J}_\varphi \times \vec{B}_\theta = \vec{\nabla} p \quad (2.6)$$

Substituting Equations 2.3, 2.4 and 2.5 into 2.6 results in

$$-\frac{B_\varphi}{R}\vec{\nabla}f + \frac{J_\varphi}{R}\vec{\nabla}\psi = \vec{\nabla}p \quad (2.7)$$

This can be re-written in terms of  $\psi$  as

$$\vec{\nabla}f = \frac{df}{d\psi}\vec{\nabla}\psi, \quad \vec{\nabla}p = \frac{dp}{d\psi}\vec{\nabla}\psi$$

resulting in the following equation for the toroidal components of the current density:

$$J_\varphi = \frac{\mu_0}{R}ff' + Rp' \quad (2.8)$$

where the prime  $'$  denotes a derivative with respect to  $\psi$ .  $J_\varphi$  can also be written in terms of  $\psi$  using the toroidal component of Ampère's Law

$$\mu_0\vec{J}_\varphi = \vec{\nabla} \times \vec{B}_\theta \quad (2.9)$$

Comparing this with Equation 2.3 for  $\vec{B}_\theta$ , the Grad-Shafranov equation can be derived, shown in Equation 2.10 [26]. This can then be solved for  $\psi$ , given the boundary of the plasma and the form of  $p(\psi)$  and  $f(\psi)$ .

$$R\frac{1}{\partial R}\frac{1}{R}\frac{\partial\psi}{\partial R} + \frac{\partial^2\psi}{\partial Z^2} = -\mu_0R^2p' - \mu_0^2ff' \quad (2.10)$$

## 2.2 Sources of current

Solving the Grad-Shafranov equation requires knowledge about all the current within the plasma. There are two types of current that need to be examined, the self generating neoclassical currents and the externally driven currents. A self-consistent form for  $f(\psi)$  in terms of  $p(\psi)$  can be calculated by combining expressions for these neoclassical currents with externally driven currents.

### 2.2.1 Neoclassical Currents

In tokamaks there are mechanisms for the plasma to generate toroidal current via the plasma pressure gradient. These self-driven currents, such as the bootstrap current, can become a large fraction of the total current so quantifying their contribution is essential when designing an equilibrium.

There are 3 neoclassical currents that are necessary to model: the diamagnetic current, the Pfirsch-Schlüter current and the bootstrap current.

## Diamagnetic current

The diamagnetic current,  $\vec{J}_{\text{dia}}$ , arises from force balance and is the component of the current that is perpendicular to the magnetic field. It can be obtained by taking the cross product of Equation 2.1 with  $\vec{B}$  to give:

$$\vec{J}_{\text{dia}} = \frac{\vec{B} \times \vec{\nabla} p}{B^2} \quad (2.11)$$

Given that

$$\vec{B} = \mu_0 f(\psi) \vec{\nabla} \varphi + \vec{\nabla} \psi \times \vec{\nabla} \varphi \quad (2.12)$$

the diamagnetic contribution can be written in the form

$$\vec{J}_{\text{dia}} = \frac{p'}{B^2} \left( R^2 B^2 \vec{\nabla} \varphi - \mu_0 f \vec{B} \right) \quad (2.13)$$

## Pfirsch-Schlüter Current

The Pfirsch-Schlüter current arises due to the diamagnetic current not being divergence free. The diamagnetic current on its own would therefore result in an electrostatic potential due to the build-up of charge on the field line. The resulting electric field drives a current parallel to the magnetic field, known as the Pfirsch-Schlüter current.

$$\vec{J}_{\text{ps}} = J_{\text{ps}} \frac{\vec{B}}{B} \quad (2.14)$$

The combination of this and the diamagnetic current should be divergence free. Taking the divergence of  $\vec{J}_{\text{dia}}$  and noting the toroidal symmetry:

$$\vec{\nabla} \cdot \vec{J}_{\text{dia}} = -\mu_0 f p' (\vec{B} \cdot \vec{\nabla}) \left( \frac{1}{B^2} \right) \quad (2.15)$$

Taking the divergence of  $\vec{J}_{\text{ps}}$ , the following must be satisfied:

$$\vec{B} \cdot \vec{\nabla} \left( \frac{J_{\text{ps}}}{B} \right) = \mu_0 f p' (\vec{B} \cdot \vec{\nabla}) \left( \frac{1}{B^2} \right) \quad (2.16)$$

This can be integrated and results in:

$$\vec{J}_{\text{ps}} = \frac{\mu_0 f p'}{B^2} \vec{B} + K(\psi) \vec{B} \quad (2.17)$$

where the  $K(\psi)$  arises as a constant of integration. When the diamagnetic current attempts to build up electrostatic potential, it would not do so uniformly. These local potentials drive the Pfirsch-Schlüter current hence the current must obey the parallel Ohm's law meaning:

$$\eta \vec{J}_{\text{ps}} = \vec{E}_{\text{ps}} = \frac{B_\theta}{B} E_\theta + \frac{B_\varphi}{B} E_\varphi \quad (2.18)$$

From this, it is possible to determine the value of  $K$ . For a steady state toroidal magnetic field Faraday's Law states

$$\oint E_\theta dl = 0 \quad (2.19)$$

which means that  $\oint J_{\text{ps}} B / B_\theta dl = 0$  (assuming  $\eta$  is a function of  $\psi$ ). This results in

$$\vec{J}_{\text{ps}} = \frac{\mu_0 f p'}{B^2} \left( 1 - \frac{B^2}{\langle B^2 \rangle_F} \right) \vec{B} \quad (2.20)$$

where the  $\langle \dots \rangle_F$  denotes a flux surface average defined as

$$\langle \dots \rangle_F = \frac{\oint \dots \frac{dl}{B_\theta}}{\oint \frac{dl}{B_\theta}} \quad (2.21)$$

### Bootstrap current

In a tokamak, particles with a sufficiently high pitch angle are trapped and perform “banana” shaped orbits in the region of low magnetic field, as shown in Figure 2.1. These banana orbits have a finite width,  $\Delta_b$ , and in the presence of a pressure gradient drive an additional equilibrium current that supplements the diamagnetic current. A transfer of momentum to predominantly the passing ions amplifies this current, which is known as the bootstrap current. This mechanism becomes ineffective in a collisional plasma as the particles are de-trapped before they can complete a full orbit. The bootstrap current differs from the Pfirsch-Schlüter and diamagnetic currents in that it is collisionality dependent, being the largest in a low collisionality regime,  $\nu_* = \nu_s / \varepsilon \omega_b < 1$  where

$$\nu_s = \frac{\sqrt{2} \pi n_s Z_s^4 e^4 \ln(\Lambda)}{\sqrt{m_s} T_s^{3/2}} \quad (2.22)$$

$$\omega_b = \frac{\varepsilon^{1/2} v_{\text{th}}}{Rq} \quad (2.23)$$

The bootstrap current must be divergence free and will be parallel to the magnetic field. The bootstrap current can be written as

$$\vec{J}_{\text{bs}} = \frac{\langle \vec{J}_{\text{bs}} \cdot \vec{B} \rangle_F}{\langle B^2 \rangle_F} \vec{B} \quad (2.24)$$

where neoclassical theory provides an expression for  $\langle \vec{J}_{\text{bs}} \cdot \vec{B} \rangle_F$ .

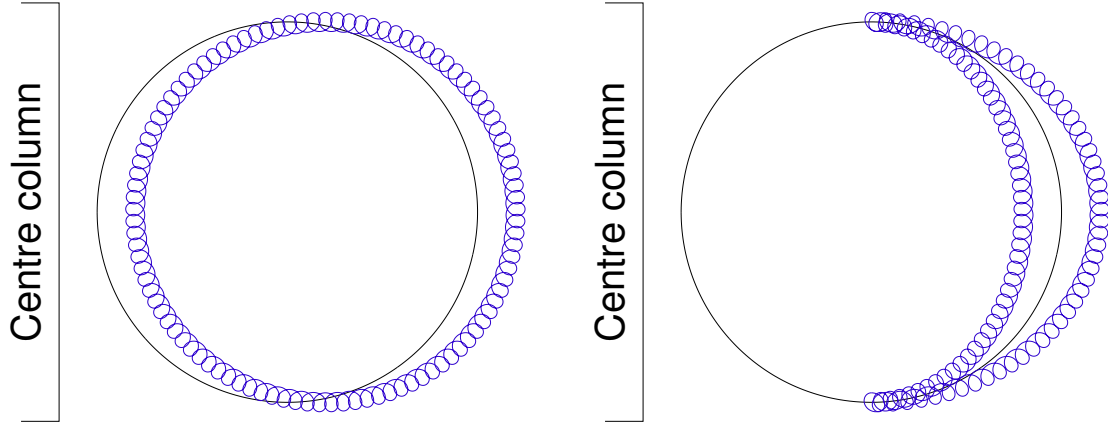


Figure 2.1: Illustration of the passing particles that perform a full poloidal orbit and the trapped particles that are trapped on the outboard low field side. Taken with permission from [28]

### 2.2.2 Auxiliary Current

Another form of toroidal current is one driven externally, which can be inductive or non-inductive.

Ohmic current is a form of inductive current drive commonly used in tokamaks. A solenoid can be wrapped around the centre column shown in Figure 1.1. By ramping the current in the solenoid, the toroidal magnetic field is generated via transformer action. This is especially useful for plasma start up. However, this cannot be relied upon for a steady state scenario as it is not possible to ramp up the current in a solenoid indefinitely. Steady state operating scenarios therefore require fully non-inductive current drive systems and scenario development must be balanced with the limits of these sources.

Non-inductive forms of current drive include neutral beam injection (NBI) where highly energetic neutral particles are fired into the plasma that provide heating and drive current, and radio-frequency (RF) injection where microwaves and radio wave are injected into the plasma which resonate with the different particle species in the plasma, generating heat and current. The heating provided by both of these systems impacts the temperature of the core plasma.

#### Radio-frequency injection

Electromagnetic waves have been used extensively in tokamaks to heat and drive current in the plasma [42]. There are a range of different frequencies that can be injected into the plasma which impact the deposition process.

Ion cyclotron current drive (ICCD) is an example where the frequency of the wave is  $\omega_{RF} \sim$

$\Omega_i = \frac{Z_i e B}{m_i c}$ . This is typically around 30 MHz to 120 MHz and here the wave resonates directly with the ions. There also exists electron cyclotron current drive (ECCD) where the wave oscillates at  $\omega_{RF} \sim \Omega_e = \frac{eB}{m_e c}$  typically around 100 GHz to 200 GHz. This equivalently directly interacts with the electrons. In between these two is lower hybrid current drive (LHCD) which tends to operate around 1 GHz to 10 GHz.

In general spherical tokamaks operate at low field and high density, which results in density cut-offs preventing access to the core plasma for most frequencies [43]. However, ECCD offers a potential solution at the highest field as the frequency is sufficiently high to penetrate into the core. Electron Bernstein waves are electrostatic and are not limited by density cut-offs; they are very successful in driving current in STs, though they lack the flexibility of ECCD and the physics is not as developed [44]. RF methods are advantageous in that they require small ports, are able to run for long periods of time and can be steered. Furthermore, it offers a method for plasma start-up.

### Neutral Beam Injection

NBI is the other main form of current drive that has been very successful in tokamaks. Energetic neutral particles are injected into the plasma, getting ionised and providing fuelling, heating and current. NBI systems have achieved the highest current drive efficiency of any system but require very large ports and are difficult to engineer [45]. NBI also has accessibility issues as the penetration depth of a beam goes as  $\lambda_{NB} \propto \frac{(E_b/A_a)^{1/2}}{n_e a}$ . Here  $A_b$  corresponds to the mass of the injected neutral,  $E_b$  is the energy and  $n_e$  is the electron density. Reactor relevant plasmas require a high density, meaning high beam energies will be required to penetrate into the core of the plasma. For ITER, a 1 MeV beam is necessary for core access [46]. These beams are generated by accelerating ions to the required energy which are then neutralised and injected into the plasma. However at energies above 120 keV, the neutralisation efficiency of positive ion sources drops substantially such that they are no longer feasible. Neutralisation of negative ions ( $D^-$ ) remain at an acceptable level of  $\sim 56\%$  and are to be used in ITER [47].

### Current drive efficiency

A measure for the current drive efficiency of these systems can be made using the following metric

$$\eta_{\text{CD}} = \frac{I_{\text{aux}} \langle n_{e20} \rangle R_{\text{maj}}}{P_{\text{aux}}} \quad (2.25)$$

where  $\langle n_{e20} \rangle$  is the volume average density in units of  $\times 10^{20} \text{m}^{-3}$ ,  $I_{\text{aux}}$  is the externally driven current in A and  $P_{\text{aux}}$  is the auxiliary power of the current drive system in W.  $\eta_{\text{CD}}$  represents the current drive efficiency of a particular system. The NBI system on ITER was designed with a  $\eta_{\text{NBI}} = 0.4 \text{A m}^{-2} \text{W}^{-1}$  [48]. More recent studies have found this could be as high as  $\eta_{\text{NBI}} = 0.55 \text{A m}^{-2} \text{W}^{-1}$  [49, 50]. RF methods typically can vary in their efficiency, with LHCD expected to have an efficiency of  $\eta_{\text{LHCD}} = 0.24 \text{A m}^{-2} \text{W}^{-1}$  on ITER [51]. ECCD had a slightly lower prediction for ITER with  $\eta_{\text{ECCD}} = 0.2 \text{A m}^{-2} \text{W}^{-1}$ .

This thesis will focus on using neutral beam injection to drive the external current as the higher current drive efficiency will allow for a lower auxiliary power. This will be examined in further detail in Chapter 5.

Similar to the bootstrap current, a steady state auxiliary current will be divergence free and parallel to the magnetic field so can be written as.

$$\vec{J}_{\text{aux}} = \frac{\langle \vec{J}_{\text{aux}} \cdot \vec{B} \rangle_F}{\langle B^2 \rangle_F} \vec{B} \quad (2.26)$$

### 2.2.3 Total current

Summing Equations 2.13, 2.20, 2.24 and 2.26 the total current is given by

$$\vec{J} = \frac{\langle \vec{J}_{\text{aux}} \cdot \vec{B} \rangle_F}{\langle B^2 \rangle_F} \vec{B} + \frac{\langle \vec{J}_{\text{bs}} \cdot \vec{B} \rangle_F}{\langle B^2 \rangle_F} \vec{B} + p' \left( R^2 \vec{\nabla} \varphi - \frac{\mu_0 f}{\langle B^2 \rangle_F} \vec{B} \right) \quad (2.27)$$

Taking the toroidal component of it is possible to get an expression for  $f f'$  by substituting in Equation 2.8 to get

$$f f' = \frac{\langle \vec{J}_{\text{aux}} \cdot \vec{B} \rangle_F}{\langle B^2 \rangle_F} f + \frac{\langle \vec{J}_{\text{bs}} \cdot \vec{B} \rangle_F}{\langle B^2 \rangle_F} f - \frac{\mu_0 f^2 p'}{\langle B^2 \rangle_F} \quad (2.28)$$

## 2.3 Transport processes

The confinement of a tokamak is dictated by the transport processes within it, which directly impacts the density and temperature profiles. To consistently calculate the steady state temperature profile would require full knowledge of all the sources and sinks of heat in a tokamak. This kind of analysis is routinely conducted with tools such as TRANSP [52], JETTO [53] and TGYRO [54]. The crucial question is whether the models being used to quantify the sources and sinks are valid for spherical tokamak plasma equilibrium like BurST.

### 2.3.1 Magneto-hydrodynamic stability

The most violent instabilities are generally magneto-hydrodynamic (MHD) modes, driven by gradients in current and pressure [26]. Any steady state reactor will need to avoid these modes as they can lead to significant particle and heat transport as well as disruptions. Given the nature of these modes they are usually affected by plasma parameters like  $\beta = \frac{p}{B^2/2\mu_0}$  and the safety factor  $q$  defined as [35, 55]

$$q = \frac{d\psi_t}{d\psi} \quad (2.29)$$

$$\psi_t = \int_0^V dV \vec{B} \cdot \nabla \varphi \quad (2.30)$$

Many common MHD modes occur at rational surfaces when  $q = m/n$  where  $m$  and  $n$  are the poloidal and toroidal mode numbers respectively. Examples of this are sawteeth which occur at the  $q = 1$  surface and neoclassical tearing modes (NTMs) which occur at other rational surfaces. The 2/1 and 3/2 NTM modes are commonly observed in tokamaks leading to flattened temperature profiles [56]. Both of these modes degrade the performance of tokamaks and should be avoided if possible [57, 58].

Fundamentally, MHD stability codes such as ELITE [59] and MISHKA [60] examine how perturbations change the total energy in the system. If the perturbation lowers the energy, then it is considered unstable. Examining the MHD stability is outside the scope of this work, but some “best practices” will be utilised in the design.

Careful tailoring of the  $q$  profile can avoid these instabilities by having  $q_{\min} > 2$  which has also been shown to increase the maximum  $\beta_N = \beta \frac{aB_\varphi}{I_p}$  in units of % m T MA<sup>-1</sup> [61]. Though it is less common, the 5/2 NTM could still form in this regime so  $q_{\min}$  should be pushed higher if possible.

There is evidence that reverse shear configurations can lead to internal transport barriers and high  $\beta$  plasmas [62]. However, studies have shown that resistive interchange modes are driven unstable in high  $\beta$  reverse shear designs [63], limiting core pressure peaking. Furthermore, there is evidence of double tearing modes forming in reverse shear regimes leading to disruptions [64]. With careful analysis using an MHD code it may be possible to avoid these issues, but as that is outside the scope of this work it was decided to keep  $q$  monotonic for simplicity.

### 2.3.2 Neoclassical Transport

Neoclassical transport arises from a combination of particle collisions and the magnetic geometry of a tokamak meaning it is an unavoidable level of transport. The mechanism that drives the bootstrap current is also the cause of this neoclassical transport. As mentioned previously some particles can be trapped on the low field side of the tokamak performing banana shaped orbits. When  $\nu_* < 1$ , the tokamak will be in the banana regime of transport such that whenever a trapped particle is scattered out of their orbit, the particle is displaced by  $\Delta_b$ . A reactor must operate at high temperatures to achieve sufficient fusion power which reduces the collision frequency sufficiently that it will be in this banana regime, with ITER having  $\nu_* < 0.1$  [65].

To solve for this type of transport, the drift-kinetic equation is solved [66] and models such as NCLASS [67] and NEO [68] have been developed to examine this. NCLASS doesn't contain the full ion-electron coupling which can have an impact at high collisionality regimes, but for the equilibria being examined here either code should be sufficient [69].

### 2.3.3 Anomalous transport

Experimental fluxes tend to be significantly larger than the predictions made by neoclassical theory, where electron transport can be up to 2 orders of magnitude larger [70]. This “anomalous” transport is the main focus of this thesis as it will likely be the dominant source of heat loss. It is largely believed that the source of this anomalous transport is turbulent diffusion via small fluctuations [71]. This turbulence is believed to arise from nonlinear interactions as a consequence of micro-instabilities driven by kinetic gradients. Gyrokinetic theory has been developed to model these fluctuations. Nonlinear simulations are often computationally expensive, but insight can usually be gained about the turbulent properties from linear theory [72, 73]. This thesis will examine the turbulent characteristics of a high  $\beta$  ST using linear gyrokinetic theory. There are, however, simpler models that attempt to globally quantify all the transport.

### 2.3.4 Confinement scaling laws

The simplest transport model uses global plasma parameters to quantify the quality of confinement. The steady state global energy confinement can be characterised by  $\tau_E = \frac{W}{P_{\text{heat}}}$  where  $W$  is the total thermal energy content of the plasma and  $P_{\text{heat}}$  is the total heating power given by the sum of the auxiliary heating  $P_{\text{aux}}$  and the  $\alpha$  heating  $P_\alpha$ . Empirical predictions

exist that attempt to quantify this global confinement property. They have been generated from data across several different tokamaks and involve examining large databases of shots and performing regression analysis to create a scaling law. One of the most commonly used scaling laws is the ITER98 ELMy H mode scaling [74], where a prediction for the confinement time is given by

$$\tau_E^{\text{IPB98}(y,2)} = 0.0562 I_p^{0.93} B^{0.15} \bar{n}^{0.41} P_{\text{heat}}^{-0.69} R^{1.97} \kappa^{0.78} \varepsilon^{0.58} M^{0.19} \quad (2.31)$$

Here  $\bar{n}$  corresponds to the line average electron density,  $\kappa$  is the plasma elongation and  $M$  is the mass of the hydrogen isotope. When comparing a quality of confinement relative to this scaling law,  $H_{98} = \tau_E / \tau_E^{\text{IPB98}(y,2)}$  is used. This has been reasonably successful in predicting the quality of confinement for existing tokamaks. Yet other confinement scaling laws exist that also have a reasonable agreement with the data but look quite different and extrapolate to future tokamaks in different ways. An example is the Petty scaling law given by [75]

$$\tau_E^{\text{Petty}} = 0.052 I_p^{0.75} B^{0.30} \bar{n}^{0.32} P_{\text{heat}}^{-0.47} R^{2.0} \kappa^{0.88} \varepsilon^{0.84} M^{0.0} \quad (2.32)$$

This has shown to be equivalently successful in modelling the data [76] but has significantly different consequences on reactor design, especially in STs. This becomes clearer when examining the dimensionless forms of these confinement times.

$$\Omega_i \tau_E^{\text{IPB98}(y,2)} \propto \rho_*^{2.7} \beta^{-0.9} \nu_*^{-0.01} q^{-3.0} \kappa^{3.3} \varepsilon^{0.73} M^{0.96} \quad (2.33)$$

$$\Omega_i \tau_E^{\text{Petty}} \propto \rho_*^{3.0} \beta^{0.0} \nu_*^{-0.3} q^{-1.1} \kappa^{2.2} \varepsilon^{-0.8} M^{0.5} \quad (2.34)$$

From these two equations it is clear that the dependencies on critical parameters such as  $\beta$ ,  $\nu_*$  and  $\varepsilon$  vary significantly. Further analysis using NSTX data found an even stronger dependence on collisionality where  $\Omega_i \tau_E \propto \nu_*^{-0.95}$  [77]. Yet some MAST data was found to be more consistent with the ITER98 scaling [78]. Furthermore, these scaling laws don't include all plasma parameters that may be relevant. For example, the plasma triangularity,  $\delta$ , is not included in these laws, but has been shown to have impact on the anomalous transport on TCV [79]. Moreover, the transition from a carbon to a metal wall on JET also had a significant impact on the confinement [80].

These scaling laws may be used as approximate guidelines for the confinement of a future reactor but more rigorous physics-based tools must be used to gain confidence in these designs.

## 2.4 Gyrokinetic theory

It is necessary to have a model that describes the turbulent behaviour, often thought to be caused by fluctuations in the electromagnetic fields and plasma parameters [71]. This is possible using the Vlasov equation shown below

$$\frac{\partial f_s}{\partial t} + \vec{v} \cdot \vec{\nabla} f_s + \frac{d\vec{v}}{dt} \cdot \frac{\partial f_s}{\partial \vec{v}} = C[f_s] \quad (2.35)$$

where  $f_s$  is the distribution function describing a given species  $s$ .  $C[f_s]$  represents a collision operator between alike and different species and the acceleration is given by the Lorentz force equation

$$\frac{d\vec{v}}{dt} = \frac{q}{m_s} [\vec{E} + \vec{v} \times \vec{B}]$$

Solving this directly is not computationally tractable as it is a 6D problem and would require huge ranges of scales in both length and time to capture all of the physics, from the fast gyrating electrons to the slower motion of the thermal ions. To overcome this issue several physically motivated assumptions are made that greatly simplify the problem.

### 2.4.1 Linear gyrokinetic theory

It is assumed that the distribution function can be split into two parts, a background equilibrium value  $f_0$  and a small perturbation  $\epsilon f_1$

$$f_s = f_0 + \epsilon f_1 + O(\epsilon^2) \quad (2.36)$$

where  $\epsilon \ll 1$  is assumed, meaning the perturbations are small compared to the background equilibrium. This is also applied to the background fields  $\vec{E}$  and  $\vec{B}$ . Subscripts will be used to denote an expansion in  $\epsilon$  and solving for  $f_1$  is known as  $\delta f$  gyrokinetics. Applying this expansion to Equation 2.35 results in the following  $0^{th}$  and  $1^{st}$  order equations

$$\frac{\partial f_0}{\partial t} + \vec{v} \cdot \vec{\nabla} f_0 + \frac{q}{m_s} \left[ \vec{E}_0 + \vec{v} \times \vec{B}_0 \right] \cdot \frac{\partial f_0}{\partial \vec{v}} = C[f_0] \quad (2.37)$$

$$\frac{\partial f_1}{\partial t} + \vec{v} \cdot \vec{\nabla} f_1 + \frac{q}{m_s} \left[ \vec{E}_1 + \vec{v} \times \vec{B}_1 \right] \cdot \frac{\partial f_0}{\partial \vec{v}} + \frac{q}{m_s} \left[ \vec{E}_0 + \vec{v} \times \vec{B}_0 \right] \cdot \frac{\partial f_1}{\partial \vec{v}} = C[f_1] \quad (2.38)$$

It is assumed that the background quantities evolve on a slow transport timescale compared to the fluctuations such that  $\partial f_0 / \partial t = 0$  and we also neglect equilibrium flows.

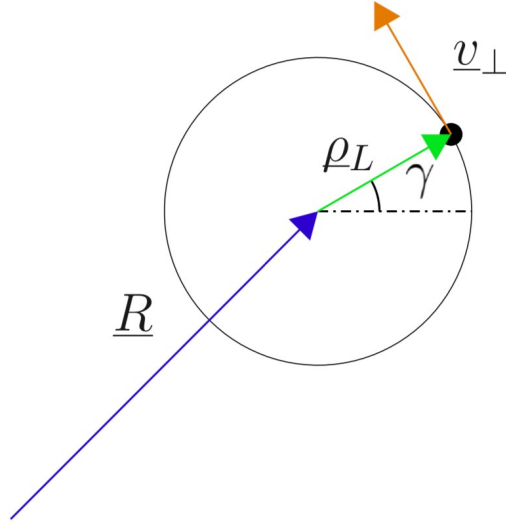


Figure 2.2: Guiding centre co-ordinates shown can describe the position of a particle with  $\rho_L$  showing the direction of the Larmor radius vector, and  $\gamma$  showing the gyro-phase. Taken with permission from [28]

### Gyromotion

Particles confined by a magnetic field perform circular orbits around the magnetic field line with a frequency  $\omega_c = qB/m$  and radius  $\rho_L = \frac{mv_\perp}{qB}$ , known as the gyrofrequency and Larmor radius respectively.

By transforming to a co-ordinate system where the gyro-motion is more explicit, the velocity derivative can be more easily handled. An orthogonal set of co-ordinates are defined  $(\vec{b}, \vec{e}_\gamma, \vec{e}_\rho)$  which point along the local magnetic field, in the direction of the gyro-phase angle and along the Larmor radius respectively, as shown in Figure 2.2. Here,  $\vec{e}_\rho = \vec{b} \times \vec{v}_\perp / v_\perp$ . The velocity can then be written as

$$\vec{v} = v_\perp \vec{e}_\gamma + v_\parallel \vec{b} \quad (2.39)$$

where  $\gamma$  represents the direction of the gyro-phase angle. This can also be written in terms of  $(\varepsilon, \mu, \gamma)$ - space or  $(\varepsilon, \lambda, \gamma)$ - space where  $\varepsilon = v^2/2$  is the energy,  $\mu = v_\perp^2/2B$  is the magnetic moment and  $\lambda = \mu/\varepsilon$  is the pitch angle. Here  $\mu$  will be used such that the velocity gradient is

$$\frac{\partial}{\partial v} = \vec{v} \frac{\partial}{\partial \varepsilon} + \frac{\vec{v}_\perp}{B} \frac{\partial}{\partial \mu} + \frac{\vec{v}_\perp \times \vec{b}}{v_\perp^2} \frac{\partial}{\partial \gamma} \quad (2.40)$$

This allows for Equation 2.38 to be written as

$$\left[ \frac{\partial}{\partial t} + \vec{v} \cdot \vec{\nabla} + \omega_c \frac{\partial}{\partial \gamma} \right] f_1 = -\frac{q}{m} \left[ \vec{E}_1 \cdot \left( \vec{v} \frac{\partial}{\partial \varepsilon} + \frac{\vec{v}_\perp}{B} \frac{\partial}{\partial \mu} + \frac{\vec{v}_\perp \times \vec{b}}{v_\perp^2} \frac{\partial}{\partial \gamma} \right) + \frac{(\vec{v}_\parallel \times \vec{B}_1) \cdot \vec{v}_\perp}{B} \frac{\partial}{\partial \mu} + \left( \vec{B}_{1\parallel} - \frac{v_\parallel \vec{v}_\perp \cdot \vec{B}_{1\perp}}{v_\perp^2} \right) \frac{\partial}{\partial \gamma} \right] f_0 \quad (2.41)$$

where  $E_0$  has been neglected as  $E_0/v_{\text{th}}B_0 \sim \rho_L/a$  which is assumed to be small as outlined in the next section.

### Gyrokinetic ordering for perturbations

To further simplify the problem several assumptions are made about the relative size of different terms within the system. These are physically motivated utilising the geometry of tokamaks. The gyrokinetic ordering assumptions are as follows

$$\frac{k_\parallel}{k_\perp} \sim \frac{\Omega}{\omega_c} \sim \frac{E_0}{B_0 v_{\text{th}}} \sim \frac{\rho_L}{a} = \delta \ll 1 \quad (2.42)$$

The first term arises from particles being able to freely travel along the field line but can only travel slowly across them via drifts and collisions, resulting in long wavelengths parallel to the field and short perpendicular to the field. This describes the anisotropy of the turbulence. The second term states that gyro-motion occurs on a much shorter time scale compared to the period of the mode, creating temporal separation. The third term is stating that the background electric field is smaller compared to the magnetic field. Finally,  $\rho_L$  is assumed to be much smaller than the size of the device such that across a gyro-orbit the equilibrium changes are small, creating spatial separation.

### Eikonal representation

An eikonal representation for the perturbed quantities can be used here where

$$f_1 = f_1(\vec{r}, \vec{v}) e^{(i\vec{k} \cdot \vec{r} - i\Omega t)} \quad (2.43)$$

$\vec{r}$  represents the position. This allows for the larger scale perturbation, contained in the  $f_1(\vec{r}, \vec{v})$ , to be separated from the smaller scale which are contained in the exponential. This representation allows for  $\vec{\nabla}_\parallel \sim k_\parallel$  and  $\vec{\nabla}_\perp \sim k_\perp$  such that  $\vec{\nabla}_\parallel / \vec{\nabla}_\perp \sim \delta$ .  $\Omega$  can be split into its real and imaginary components  $\Omega = \omega + i\gamma$ , which corresponds to the mode frequency and growth rate respectively.

### Ordered Linear Vlasov equation

Using the ordering as described above with an eikonal representation, it is possible to further separate out the Vlasov equation by expanding in  $\delta$ . Superscripts will be used to denote this. Looking at the LHS of Equation 2.41 the operator can be split up as follows

$$\left[ \frac{\partial}{\partial t} + \vec{v} \cdot \vec{\nabla} + \omega_c \frac{\partial}{\partial \gamma} \right] f_1 = \left( L^1 + L^\delta \right) f_1 \quad (2.44)$$

where

$$L^1 = v_\perp \cdot \vec{\nabla}_\perp + \omega_c \frac{\partial}{\partial \gamma} \sim 1 \quad (2.45)$$

$$L^\delta = \frac{\partial}{\partial t} + \vec{v}_\parallel \cdot \vec{\nabla}_\parallel \sim \delta \quad (2.46)$$

Similarly the RHS can be ordered using the perturbed fields,  $\vec{E}_1$  and  $\vec{B}_1$  as expressed in terms of the potentials given that  $\vec{E} = -\vec{\nabla}\phi - \frac{\partial \vec{A}}{\partial t}$  and  $\vec{B} = \vec{\nabla} \times \vec{A}$ .

Assuming  $\vec{E}_1 = \vec{E}_1^1 + \vec{E}_1^\delta$  and  $\vec{B}_1 = \vec{B}_1^1 + \vec{B}_1^\delta$ , it is shown in [28] that the RHS of Equation 2.41 will take the form

$$\begin{aligned} -\frac{q}{m} \left[ \vec{E}_1 \cdot \left( \vec{v} \frac{\partial}{\partial \varepsilon} + \frac{\vec{v}_\perp}{B} \frac{\partial}{\partial \mu} + \frac{\vec{v}_\perp \times \vec{b}}{v_\perp^2} \frac{\partial}{\partial \gamma} \right) + \frac{(\vec{v}_\parallel \times \vec{B}_1) \cdot \vec{v}_\perp}{B} \frac{\partial}{\partial \mu} \right. \\ \left. + \left( \vec{B}_{1\parallel} - \frac{v_\parallel \vec{v}_\perp \cdot \vec{B}_{1\perp}}{v_\perp^2} \right) \frac{\partial}{\partial \gamma} \right] f_0 = \left( M^1 + M^\delta \right) f_0 \end{aligned} \quad (2.47)$$

where

$$M^1 = \frac{q}{m} \left[ v_\perp \cdot \vec{\nabla}_\perp \phi_1 \left( \frac{\partial}{\partial \varepsilon} + \frac{1}{B} \frac{\partial}{\partial \mu} \right) - \vec{v}_\perp \cdot \vec{\nabla}_\perp A_{1\parallel} \frac{v_\parallel}{B} \frac{\partial}{\partial \mu} \right] \quad (2.48)$$

$$\begin{aligned} M^\delta = -\frac{q}{m} \left[ \vec{E}_1^\delta \cdot \left( \vec{v} \frac{\partial}{\partial \varepsilon} + \frac{\vec{v}_\perp}{B} \frac{\partial}{\partial \mu} \right) + \vec{E}_1^1 \cdot \frac{\vec{v}_\perp \times \vec{b}}{v_\perp^2} \frac{\partial}{\partial \gamma} \right. \\ \left. + \frac{(\vec{v}_\parallel \times \vec{B}_1^\delta) \cdot \vec{v}_\perp}{B} \frac{\partial}{\partial \mu} + \left( \vec{B}_{1\parallel}^1 - \frac{v_\parallel \vec{v}_\perp \cdot \vec{B}_{1\perp}^1}{v_\perp^2} \right) \frac{\partial}{\partial \gamma} \right] \end{aligned} \quad (2.49)$$

Thus Equation 2.41 can be written in terms of expansion in  $\delta$  as follows

$$\left( L^1 + L^\delta \right) (f_1^1 + f_1^\delta) = \left( M^1 + M^\delta \right) (f_0^1 + f_0^\delta) \quad (2.50)$$

where  $f_0^1$  is assumed to be a Maxwellian distribution.

## Leading order Vlasov Equation

Taking the leading order terms from Equation 2.50 gives  $L^1 f_1^1 = M^1 f_0^1$ . It is possible to split the distribution function where  $f_1^1 = \bar{f}_1^1 + \tilde{f}_1^1$  where  $\bar{f}_1^1$  is independent of  $\gamma$  and  $\tilde{f}_1^1$  oscillates in  $\gamma$ . Examining the gyrophase-independent terms of this equations leads to

$$\bar{f}_1^1 = \frac{q}{m} \left[ \phi_1 \left( \frac{\partial}{\partial \varepsilon} + \frac{1}{B} \frac{\partial}{\partial \mu} \right) - \frac{v_{\parallel} A_{1\parallel}}{B} \frac{\partial}{\partial \mu} \right] f_0^1 \quad (2.51)$$

which leaves the gyrophase-dependent term as

$$\omega_c \frac{\partial}{\partial \gamma} \left[ \tilde{f}_1^1 e^{(i\vec{k}\cdot\vec{x})} \right] = 0 \quad (2.52)$$

which has the solution of

$$\tilde{f}_1^1 = g(\vec{x}, \varepsilon, \mu) e^{(i\vec{k}\cdot\vec{x})} \quad (2.53)$$

where  $g$  is independent of  $\gamma$ . This is often referred to as the non-adiabatic part of the distribution function. Therefore the leading order has the following solution

$$f_1^1 = \frac{q}{m} \left[ \phi_1 \left( \frac{\partial}{\partial \varepsilon} + \frac{1}{B} \frac{\partial}{\partial \mu} \right) - \frac{v_{\parallel} A_{1\parallel}}{B} \frac{\partial}{\partial \mu} \right] f_0^1 + g(\vec{x}, \varepsilon, \mu) e^{(i\vec{k}\cdot\vec{x})} \quad (2.54)$$

## First order Vlasov equation

For the first order terms we have

$$L^1 f_1^\delta + L^\delta f_1^1 = M^1 f_0^\delta + M^\delta f_0^1 \quad (2.55)$$

This can be re-written as

$$\frac{\partial}{\partial \gamma} [f_1^\delta e^{(i\vec{k}\cdot\vec{x})}] + \frac{e^{(i\vec{k}\cdot\vec{x})}}{\omega_c} L^\delta f_1^1 = \frac{e^{(i\vec{k}\cdot\vec{x})}}{\omega_c} (M^1 f_0^\delta + M^\delta f_0^1) \quad (2.56)$$

It is possible to remove the  $f_1^\delta$  from this equation by performing an average over the gyrophase, leaving an equation for  $g$ . A gyro-average will be represented by  $\langle h \rangle_G = \frac{1}{2\pi} \int_0^{2\pi} h d\gamma$ .

Applying this to Equation 2.56 gives

$$\left\langle \frac{e^{(i\vec{k}\cdot\vec{x})}}{\omega_c} L^\delta f_1^1 \right\rangle_G = \left\langle \frac{e^{(i\vec{k}\cdot\vec{x})}}{\omega_c} (M^1 f_0^\delta + M^\delta f_0^1) \right\rangle_G \quad (2.57)$$

Assuming that  $f_0^1$  is independent from  $\mu$ , it is possible to re-write Equation 2.57 as the linear electromagnetic gyrokinetic equation [81].

$$\left[ \frac{\partial}{\partial t} + (v_{\parallel} \vec{b} + \vec{v}_D) \cdot \vec{\nabla} \right] g = - \left[ \frac{\vec{\nabla} f_0^1}{B} \cdot \vec{b} \times \vec{\nabla}_{\perp} + \frac{q}{m} \frac{\partial f_0^1}{\partial \varepsilon} \frac{\partial}{\partial t} \right] \left[ (\phi_1 - v_{\parallel} A_{1\parallel}) J_0(k_{\perp} \rho_L) + \frac{v_{\perp}}{k_{\perp}} B_{1\parallel} J_1(k_{\perp} \rho_L) \right] \quad (2.58)$$

Here  $J_0$  and  $J_1$  are the  $0^{th}$  and  $1^{st}$  order Bessel functions respectively which arises from the gyro-averaging.  $\vec{v}_D$  represent the magnetic drifts and is defined as below

$$\vec{v}_D = \frac{1}{\Omega} \vec{b} \times \left( v_{\parallel}^2 \vec{b} \cdot \vec{\nabla}_{\perp} \vec{b} + \frac{v_{\perp}^2}{2B} \vec{\nabla}_{\perp} B \right) \quad (2.59)$$

We can define a total electromagnetic potential as  $\chi = (\phi_1 - v_{\parallel} A_{1\parallel}) J_0(k_{\perp} \rho_L) + \frac{v_{\perp}}{k_{\perp}} B_{1\parallel} J_1(k_{\perp} \rho_L)$ . These equations can then be closed using Maxwell's equations [82].

## 2.4.2 Local flux tube and ballooning transformation

To fully utilise the scale separation, gyrokinetic codes can model a small region of the plasma known as a flux tube where it is assumed that the length scale of the perturbations is significantly small compared to the simulation domain such that they cannot ‘see’ the edge of the box. There are limitations in using this model as the Larmor radius can be relatively large, especially in spherical tokamaks due to the lower magnetic field. This can result in ‘local’ simulations that span the whole minor radius of the device [83, 84], which is questionable. The solution to this is to use a global gyrokinetic code where equilibrium profiles can vary across the simulation domain. This work will focus on local simulations due to constraints with computational resources, but acknowledges that future work should examine global effects. In the flux tube, two local perpendicular co-ordinates  $x$ , the radial direction, and  $y$  the bi-normal can be defined as follows [85, 86]

$$x = \frac{q_0}{B_0 r_0} (\psi - \psi_0) \quad (2.60)$$

$$y = \frac{r_0}{q_0} (\alpha - \alpha_0) \quad (2.61)$$

The subscript 0 corresponds to a quantity's value at the centre of the box and  $\alpha$  is the field aligned co-ordinate defined as

$$\alpha = \varphi - \int^{\theta} q_* d\theta \quad (2.62)$$

where  $q_* = \frac{\vec{B} \cdot \vec{\nabla} \phi}{B \cdot \vec{\nabla} \theta}$  such that  $q = \frac{1}{2\pi} \oint q_* d\theta$  [87]. This can also be written as  $\alpha = \varphi - q\theta - \nu$ , where  $\nu$  is periodic in  $\varphi$  and  $\theta$ .  $q$  can be Taylor-expanded giving  $q(x) = q_0 - xq'$  where the  $'$  denotes a derivative with respect to  $x$ .

The local approximation is utilised when the Larmor orbit length scale is small compared to the equilibrium length scale, equivalent to  $\rho_* = \rho_L/a \ll 1$ . This assumes that neighbouring rational surfaces experience approximately the same equilibrium properties. This is characterised by assuming the radial separation between rational surfaces,  $d = 1/nq'$  is small. Equivalently this is true when  $n$ .

This scale separation indicates that an eikonal representation may be advantageous. An eikonal representation for a perturbation, e.g. the potential, is used where

$$\phi(x, y, \theta) = A(x, y, \theta)e^{-in\alpha} \quad (2.63)$$

$A(x, y, \theta)$  represents the slowly varying amplitude of the function and the exponential describes the rapid perpendicular variation, which aligns with the gyrokinetic ordering. The toroidal variation can be described by  $n$  and any explicit dependence on  $\varphi$  and  $\nu$  can be absorbed into  $\varphi$  by defining an alternative toroidal co-ordinate  $\zeta = \varphi - \nu$ . To recover the dependence on  $\zeta$ , the terms can be multiplied by  $e^{in\zeta}$ .  $\phi(x, y, \theta)$  needs to be periodic in  $\theta$ , therefore the following constraint must be satisfied

$$A(x, y, \theta + 2\pi) = A(x, y, \theta)e^{inq'2\pi} \quad (2.64)$$

A similar constraint must also apply to the radial derivative where

$$A'(x, y, \theta + 2\pi) - A'(x, y, \theta)e^{inq'2\pi} = inq'2\pi A(x, y, \theta) \quad (2.65)$$

An eikonal representation requires  $A'/A \ll 1$  which cannot be satisfied except when  $nq'$  is small. Therefore this periodicity constraint cannot be met in tokamaks with finite magnetic shear. However this is in direct contradiction to the local approximation.

Ballooning theory handles this by Fourier transforming  $\phi$  from a periodic  $\theta$  domain from  $-\pi \rightarrow \pi$  to an infinite domain around an initial ballooning angle  $\theta_0$  using a Poisson summation.  $\theta_0$  sets where the radial wavenumber is zero. When performing this ballooning transform, the eigenvalues are preserved, allowing for the periodicity constraint to be overcome [88]. This allows for an eikonal representation of  $\phi$  in ballooning space such that the amplitudes can be written as

$$\phi = \hat{\phi}(x, y, \theta)e^{-inS} \quad (2.66)$$

Where  $S$  is typically written as [87, 89]

$$S = \alpha + q\theta_0 \quad (2.67)$$

which is a constant along a field line and varies slowly with  $x$ . To recover the real space equivalent, an infinite number of copies of Equation 2.66 can be summed together, where each copy is separated by  $2\pi$  in  $\theta$ . This is equivalent to a Poisson summation and ensures a periodic function is returned.

Comparing Equation 2.66 with the Fourier space derivatives it can be shown that

$$\partial_y \rightarrow -ik_y = -i\frac{nq}{r} \quad (2.68)$$

$$\partial_x \rightarrow -ik_x = -inq'(\theta - \theta_0) \quad (2.69)$$

This shows that  $nq' = k_y\hat{s}$  where  $\hat{s} = \frac{r}{q}\frac{\partial q}{\partial r}$ , such that  $k_x = k_y\hat{s}(\theta - \theta_0)$ .

### 2.4.3 Sheared flow

$E \times B$  sheared flow can have a significant impact on transport, and is thought to be one of the main causes of transport barriers via the suppression of turbulence [90, 91]. The inclusion of a sheared flow will modify the gyrokinetic equation such that the eikonal  $S$  becomes time-dependent [85]. This in turn will cause the ballooning angle to have a time-dependence such that the mode will begin to poloidally convect around the flux surface. This will move the mode from the bad curvature side to the good curvature side, potentially stabilising the mode. It is possible to find an effective growth rate by averaging the mode's growth over several oscillations around the flux surface, known as a Floquet period [83]. There may be cases where a different mode is dominant at different  $\theta_0$ , such that there are two competing modes during a Floquet period. It is not clear whether it is necessary to follow the instantaneous growth of each individual mode or the dominant mode [92].

The pressure gradient can drive a diamagnetic flow shear,  $\gamma_{\text{dia}}$ . This is calculated by examining the radial force balance equation for ions and can be shown to be as follows in the absence of a toroidal ion velocity [93].

$$\gamma_{\text{dia}} = \left(\frac{\partial\psi}{\partial\rho}\right)^2 \frac{1}{B} \left(\frac{(p')^2}{n_i e p (1 + \eta_i)} - \frac{p''}{n_i e}\right) \quad (2.70)$$

where  $\eta_i = n_i T_i' / n_i' T_i$ .

#### 2.4.4 Non-linear gyrokinetics

So far it has been assumed that the fluctuations are infinitesimal, independent and non-interacting. But an unstable mode will continue to grow to a point where this is no longer valid. This can be overcome by including nonlinear interactions between perturbed quantities in the gyrokinetic equations, by assuming perturbations grow to an amplitude such that  $f_1/f_0 \sim \delta$ . Doing this introduces another term in Equation 2.58, which will be the nonlinear interaction term. This will allow for different toroidal harmonics to interact allowing for the fluctuations to saturate. This is critical to determine the magnitude of the particle and heat fluxes which is the ultimate goal of gyrokinetics. Utilising this along-side the previous derivation leads to the following nonlinear electromagnetic gyrokinetic equation

$$\left[ \frac{\partial}{\partial t} + (v_{\parallel} \vec{b} + \vec{v}_D) \cdot \vec{\nabla} \right] g = - \left[ \frac{\vec{\nabla} f_0^1}{B} \cdot \vec{b} \times \vec{\nabla}_{\perp} + \frac{q}{m} \frac{\partial f_0^1}{\partial \varepsilon} \frac{\partial}{\partial t} + N \right] \chi \quad (2.71)$$

The non-linearity is described by

$$N = \frac{\vec{\nabla} g}{B} \cdot \vec{b} \times \vec{\nabla}_{\perp} \quad (2.72)$$

This allows us to define an effective velocity from the total electromagnetic potential as

$$\delta v_{\chi} = \frac{\vec{b} \times \vec{\nabla}_{\perp} \chi}{B} \quad (2.73)$$

Remembering that  $\chi = (\phi_1 - v_{\parallel} A_{1\parallel}) J_0(k_{\perp} \rho_L) + \frac{v_{\perp}}{k_{\perp}} B_{1\parallel} J_1(k_{\perp} \rho_L)$ , the term with  $\phi$  corresponds to  $E \times B$  advection (electrostatic). The  $A_{\parallel}$  term describes motion along the perturbed field line (magnetic flutter) and the  $B_{\parallel}$  term describes  $\nabla B$  drift arising from the perturbed field line (compressional  $B$ ). In spectral co-ordinates this will have dimensions of  $\chi(k_x, k_y, \theta)$ .

The particle, heat and momentum fluxes can now be calculated. A general flux  $F$  for a species,  $s$  from a field  $\chi$  is given by [82]

$$\vec{F}_s^{\chi} = \int d^3 \vec{v} \delta v_{\chi} M_{F,s}^* \quad (2.74)$$

where  $M_{F,s}$  generates the appropriate moment of the non-adiabatic distribution function  $g$ . For particle transport  $M_{\Gamma,s}$  needs to generate  $\delta \tilde{n}_s$  and for heat transport  $M_{Q,s}$  must generate  $\delta \tilde{E}_s$  such that

$$\delta \tilde{n}_s = \int d^3 \vec{v} g \rightarrow M_{\Gamma,s} = g \quad (2.75)$$

$$\delta\tilde{E}_s = \int d^3\vec{v} \frac{m_s v^2}{2} g \rightarrow M_{Q,s} = \frac{m_s v^2}{2} g \quad (2.76)$$

The interpretation of this form is that the transported quantity is advected by the fluctuating potentials. Assuming the eikonal representation for the fields and by taking both time and flux surface averages it can be shown that the radial components of the particle and heat flux are given by [94]

$$\Gamma_s^\chi(k_y) = \langle \vec{\Gamma}_s^\chi(k_y) \cdot \vec{\nabla} \rho_L \rangle_F = \text{Re} \left[ \int d^3\vec{v} \sum_{k_x} \left\langle \frac{ik_y \chi \cdot M_{\Gamma,s}^*}{B} \right\rangle_F \right] \quad (2.77)$$

$$Q_s^\chi(k_y) = \langle \vec{Q}_s^\chi(k_y) \cdot \vec{\nabla} \rho_L \rangle_F = \text{Re} \left[ \int d^3\vec{v} \sum_{k_x} \left\langle \frac{ik_y \chi \cdot M_{Q,s}^*}{B} \right\rangle_F \right] \quad (2.78)$$

This indicates the importance of the phase difference between the fields and the transported quantity, such that when there is no phase difference there will be no transport.

It should be noted that to maintain quasi-neutrality it is necessary that the following hold

$$\sum_s q_s \Gamma_s^\chi(k_y) = 0 \quad (2.79)$$

However, examining the magnetic flutter transport it can be seen that it is proportional to  $v_{||}$ . Given that  $v_{||,e} > v_{||,i}$ , this would initially suggest that this transport should not be ambi-polar. However, the adiabatic response of the electrostatic potential ensures that the particle flux remains ambi-polar<sup>1</sup>, which is built into gyrokinetic theory via its closure. This means that the magnetic flutter particle transport will be set by the ion response [95].

## 2.5 Quasi-linear theory

The ultimate aim of gyrokinetics is to calculate the turbulent transport in a reactor. Once there is a trusted tool for this, the confidence in any future reactor design will increase significantly. Nonlinear gyrokinetics has been shown to match experimental fluxes [84, 96, 97]<sup>2</sup> but it comes at a large computational cost. A single flux evaluation for a single flux surface in a transport solver may require anywhere in between 10,000  $\rightarrow$  500,000 CPUh. 1.5D transport analysis requires several flux surfaces to be modelled over at least a single confinement time, meaning it is not feasible to use nonlinear gyrokinetics in a transport solver. We must turn to reduced physics models.

<sup>1</sup>This is true as long as the timescale on which the electrostatic potential builds up is faster than the mode frequency. This is violated in certain cases, an example of which are runaway electrons.

<sup>2</sup>Large uncertainties on both the inputs and outputs leads to less confidence in these predictions.

### 2.5.1 Quasi-linear approximation

Quasi-linear (QL) theory offers a tool that may allow for fast predictions of transport using information from the linear physics. One of the main premises of quasi-linear turbulent transport is that the relative phase of the fields and fluctuating quantities does not change significantly between linear and nonlinear simulations. This aligns with the assumption that the fluctuating quantities are small relative to the background quantities, meaning the linear fluctuations aren't "washed out" by the nonlinear interaction. This has been shown to be true for marginal stability in the low  $k_y$  region which normally dominates the transport [98]. This is captured by the quasi-linear weights defined as

$$w_s^\chi(k_y) = \frac{Q_s^\chi(k_y)}{|\Phi(k_y)|^2} \quad (2.80)$$

where the superscript denotes the field and subscript the species.  $\Phi$  is the normalised electrostatic potential given by

$$|\Phi(k_y)|^2 = \left( \frac{ae}{\rho_L T_e} \right)^2 \sum_{k_x} \langle |\tilde{\phi}|^2 \rangle_F \quad (2.81)$$

QL theory assumes these weights do not significantly change between linear and nonlinear simulations such that the quasi-linear weight can be approximated using

$$w_s^\chi(k_y) \approx \frac{1}{|\Phi^L|^2} Re \left[ \int d^3\vec{v} \sum_{k_x} \left\langle \frac{ik_y \chi^L \cdot M_{Q,s}^{*L}}{B} \right\rangle_F \right] \quad (2.82)$$

where the superscript  $L$  denotes a linear result. Comparing this to nonlinear data allows for the validity of using the linear response to be tested. By using the appropriate field from  $\chi$ , the electrostatic and electromagnetic components of flux are determined. This determines the relative phase of the fluctuations, but the intensity of the fluctuations can't be directly determined through the linear physics.

The second major premise is that the intensity of the saturated electrostatic potential,  $\bar{\Phi}(k_y)$ , can be determined through understanding the saturation mechanism and a database of nonlinear gyrokinetic data to correctly normalise the amplitude. This will be examined in detail in Section 3.4.2. In general, the electrostatic potential is used, but in principle any of the fields could be used. In scenarios where magnetic transport is dominant, a model may be necessary for the the saturated magnetic fluctuation [99].

The validity of the quasi-linear approximation can thus be tested in two ways. Firstly, do the quasi-linear weights accurately capture the nonlinear phase differences? Secondly, does

the saturation model capture the amplitudes of fluctuations in the nonlinear saturated state? Quasi-linear models are constantly improving [100, 101] and currently provide the best option for reduced physics-based modelling of turbulent transport, and increase confidence in predictive scenarios of devices like ITER or BurST.

## 2.6 Summary

This chapter has gone through several different areas of physics that are necessary for the modelling of a steady state reactor. A plasma equilibrium must satisfy the Grad-Shafranov equation. To consistently solve this equation requires information about the current and pressure profile. The neoclassical currents were discussed along with the relevant equations that govern them. Furthermore, the major options for the auxiliary current drive, RF and NBI, were discussed. The different sources of transport that determine the pressure profile; MHD, neoclassical and anomalous, were examined. In particular the gyrokinetic equation, which can be used to model the anomalous transport, was derived. Finally, the premise of quasi-linear gyrokinetic theory was discussed.

This thesis will examine different plasma equilibria that are relevant for a BurST regime, where the neoclassical current are consistently calculated. Basic assumptions will be made about the confinement using scaling laws. The auxiliary current will be examined in more detail, using NBI codes to examine what is feasible. The confinement will also be examined by using linear gyrokinetics to diagnose the nature of turbulence to be expected in a BurST regime and potential route to improved confinement. Finally, to make the turbulent transport modelling more tractable in a transport solver, this thesis will examine the validity of quasi-linear models in the high  $\beta$  ST regime, by comparing the predictions of these models to nonlinear simulations. The next chapter will examine in more detail the codes that will be used to do this.

## Chapter 3

# Available physics models

This chapter will focus on the models to be used for designing this reactor. This thesis will utilise the following codes, each of which will be described in detail.

- Section 3.1: SCENE - Grad-Shafranov solver
- Section 3.2: NUBEAM/NBeams/RABBIT - NBI models
- Section 3.3: GS2/CGYRO - Gyrokinetic solver
- Section 3.4: TGLF/QLGYRO - Quasi-linear transport models

### 3.1 Equilibrium code - SCENE

SCENE [102] is a fixed boundary equilibrium solver providing solutions for the Grad-Shafranov equation whilst self consistently calculating the neoclassical currents. To accurately determine the neoclassical currents requires a consistent equilibrium, but an equilibrium requires information about the neoclassical currents. SCENE handles this using an iterative approach where an initial guess of  $f(\psi)$  is made and the user specifies  $p(\psi)$ . From these inputs Equation 2.10 is solved to find  $\psi(R, Z)$ . The neoclassical currents can then be calculated from the equilibrium and, along with the user specified auxiliary current profile, is plugged into the right hand side of Equation 2.28. The initial and final  $ff'$  will generally differ so the equilibrium is then run with newly calculated profile until  $ff'$  converges to within a specified tolerance.

#### 3.1.1 Global parameters

In SCENE, the following global plasma parameters are specified by the user.

- Rod current -  $I_{\text{rod}}$
- Total plasma current -  $I_{\text{p}}$
- Total auxiliary power -  $P_{\text{aux}}$
- Plasma boundary

$I_{\text{rod}}$  will set the vacuum toroidal field and is limited by engineering constraints on the centre column.  $I_{\text{p}}$  impacts the confinement assumption and will determine the amount of auxiliary current that needs to be driven.  $P_{\text{aux}}$  is also specified, but doesn't impact the Grad-Shafranov solver. It is used to calculate the scaling law predictions,  $H_{98}$  and  $H_{\text{Petty}}$ , effectively setting the confinement assumption though it could be derived from the auxiliary current drive requirements. SCENE does not perform any transport analysis so when specifying these parameters, the user is assuming that this  $P_{\text{aux}}$  is sufficient to maintain the profiles. A Miller parameterisation is used for the plasma boundary [103]. SCENE does not model the X-points in the plasma, so the boundary is more similar to the  $\rho_{\psi} = \psi/\psi_{\text{LCFS}} = 0.95$  surface. The feasibility of any boundary would need to be confirmed with a free boundary code, which provides the requirements of the PF coils.

### 3.1.2 Kinetic profiles

In SCENE there are 2 types of ions that are specified, a main ion species and an impurity species. For a D-T plasma, a single main ion species with mass  $2.5m_p$  is specified which is assumed to be a 50:50 DT mix. The kinetic profiles of the separate plasma species are then inputs to SCENE. In reality the kinetic profile is determined by the heat and particle sources and transport processes so whether the specified pressure profile is feasible is an important, but separate question. In SCENE, there are several options for parameteric profiles, and this work will utilise the forms outlined as follows<sup>1</sup>.

#### Temperature profile

The absolute temperature profile of each species is specified. The profiles are specified as functions of  $X_{\psi} = 1 - \rho_{\psi}$ , going from  $X_{\psi} = 1$  in the core to  $X_{\psi} = 0$  at the edge. The temperature profile for each species is of the following form.

---

<sup>1</sup>In SCENE this is specified with the flag `IPSW` and this work corresponds to `IPSW = 19`, though there are many more available [102]

$$T_s(\psi) = T_{\text{edge}} + (T_0 - T_{\text{edge}})(X_\psi^{\tau_0} + \alpha_T(X_\psi^{\tau_0} - X_\psi^{\tau_1})) \quad (3.1)$$

where

$$T_{\text{edge}} = T_a + (T_{\text{ped}} - T_a)\tanh(T_{\text{grad}}X_\psi) \quad (3.2)$$

$T_a$  sets the temperature at the plasma boundary,  $T_{\text{ped}}$  sets the pedestal height,  $T_{\text{grad}}$  sets pedestal gradient and  $T_0$  sets the core temperature. The pedestal profile is set by a *tanh* function, which is common to do [104].  $\tau_0$  sets the power in a purely parabolic profile.  $\alpha_T$  and  $\tau_1$  act to flatten the core temperature profile. This allows for some additional flexibility in the shape of the temperature profile.

### Density/Pressure profile

In SCENE the profile shape of the density is specified, from which the pressure is calculated<sup>†</sup>. The absolute value of the density is part of the iteration. The profile has the following form

$$n_s(\psi) = n_{\text{edge}} + n_0 \left[ (1 + X_\psi)^{\eta_0} - (1 + \eta_0 X_\psi) \right] \quad (3.3)$$

$$n_{\text{edge}} = n_a + (n_{\text{ped}} - n_a)\tanh(n_{\text{grad}}X_\psi) \quad (3.4)$$

Once again a *tanh* function is used to set the pedestal.  $n_a$  sets the relative density at the plasma boundary,  $n_{\text{ped}}$  sets the relative density at the pedestal top,  $n_{\text{grad}}$  sets density pedestal gradient and  $n_0$  sets the core density. Here  $\eta_0$  acts to add density peaking where  $\eta_0 = 1$  corresponds to a flat density profile.

The absolute density is modified in SCENE by an input called **bpol**. This effectively sets the ratio of the  $p'$  and  $ff'$  term in Equation 2.10 such that the following is solved

$$R \frac{1}{\partial R} \frac{1}{R} \frac{\partial \psi}{\partial R} + \frac{\partial^2 \psi}{\partial Z^2} = -\mu_0 \left( [\text{bpol}] R^2 p' + [1 - \text{bpol}] \frac{ff'}{\mu_0} \right) \quad (3.5)$$

Increasing **bpol** increases the total contribution of  $p'$ , which in turn increases the density. It is essentially a measure of poloidal beta  $\beta_\theta = \frac{p}{B_\theta/2\mu_0}$ .

---

<sup>†</sup>It is also possible to specify the pressure profile from which the density is calculated.

### 3.1.3 Bootstrap current

Calculating the bootstrap current requires neoclassical theory calculations and has been examined in many regimes, from aspect ratio dependence to different collisionality scales. The work here utilises the Hirshman Sigmar formalism [105], which accounts for collisionality and impurity effects. There are more recent derivations of the bootstrap current done by Sauter *et al* [106], NCLASS and NEO that may have an impact on the total current. Though it has previously been seen that these two codes agree at low collisionality [69]. The validity of the Hirshman-Sigmar formalism has been examined previously and in the banana regime has shown to agree with the Sauter model<sup>†</sup> [107].

The model for the bootstrap current has the following form

$$\langle \vec{J} \cdot \vec{B} \rangle = \left[ L_{31} \frac{p'_e}{p_e} + \frac{L_{31} T_i}{Z_i T_e} \left( \frac{p'_i}{p_i} + \alpha_i \frac{T'_i}{T_i} \right) + L_{32} \frac{T'_e}{T_e} \right] \quad (3.6)$$

where the definitions  $L_{31}$ ,  $L_{32}$  and  $\alpha_i$  can be found in [102].

It is crucial to ensure that the bootstrap model being used is valid as this will impact the auxiliary current drive requirements greatly. The difference between an  $f_{bs}$  of 80% and 90%, for example, is a factor of two difference in the required driven current. Here the Hirshman-Sigmar model is compared to the Sauter, NCLASS and NEO models for  $\langle \vec{J} \cdot \vec{B} \rangle$ .

Figure 3.1 shows how the Hirshman-Sigmar, NCLASS and Sauter models are in good agreement when  $\rho_\psi < 0.8^\ddagger$ . These models overestimate the total bootstrap compared to NEO. Furthermore, in the pedestal the agreement is quite poor between the codes. The sharp gradients make the pedestal more difficult to resolve and the high  $\nu^*$  results in uncertain transitions to other collisionality regimes. This work will continue to use the Hirshman-Sigmar model as it matches both the Sauter and NCLASS models well in the core but future work could examine the impact of utilising different models in more detail.

---

<sup>†</sup>In the plateau region of transport it was found that this formalism was only valid at high aspect ratio, but as discussed previously this work will only examine equilibria in the banana regime.

<sup>‡</sup>The details for this equilibrium are outlined in Table 4.2

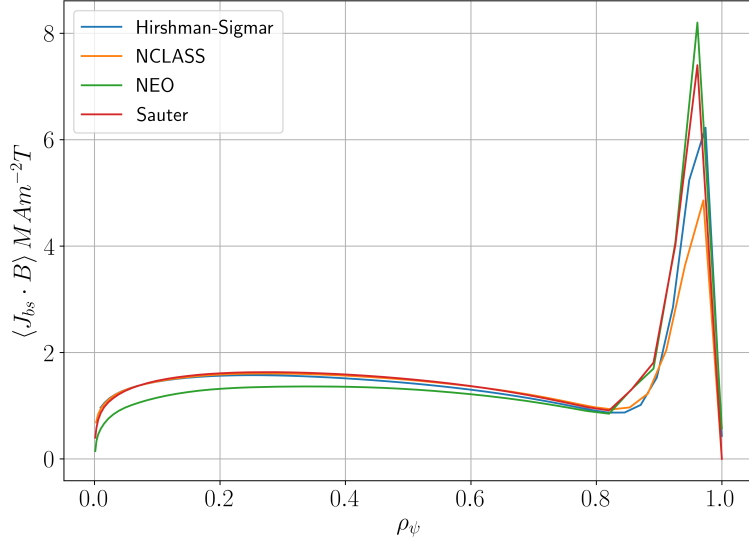


Figure 3.1: Comparing the bootstrap prediction made by different neoclassical models for a high  $\beta$  ST reactor.

### 3.1.4 Current profile

In SCENE the auxiliary current profile is another user input<sup>‡</sup>. The current profile takes the following form

$$J_{\text{aux}}(\psi) = \alpha_0 (X_\psi)^{\zeta_0} + \alpha_1 \left[ X_\psi^{\zeta_1} (1 - X_\psi)^{\zeta_2} \right] \quad (3.7)$$

The first term sets the current profile in the core and the second term allows for current peaked off axis. Increasing  $\zeta_1$  pulls the current towards the core and  $\zeta_2$  pushes it towards the edge. The ratio of  $\zeta_1/(\zeta_1 + \zeta_2)$  sets the position of the peak of the off-axis current and their difference sets the width. The absolute value of the auxiliary current is a result of the iteration as the neoclassical currents are first calculated, and then the auxiliary current scaled such that the total current is equal to  $I_p$ . This is one of the most important outputs of SCENE, as the total auxiliary current  $I_{\text{aux}}$ , will impact the amount of auxiliary power needed for BurST.

At the magnetic axis,  $\varepsilon \rightarrow 0$ , meaning there will be no bootstrap current. If  $\alpha_0 = 0$ , then there will be a current hole at the plasma core leading to  $q_0 \rightarrow \infty$ . To allow for convergence SCENE has been designed to automatically fill in the current hole such that the current is flat around  $\psi = 0$ . To do this SCENE will calculate the bootstrap current at a user specified flux

<sup>‡</sup>It is also possible to specify the total current profile as opposed to the auxiliary current profile. There is no need for an iteration here as this exactly specifies  $ff'$ . This is less useful than the former method of running SCENE as usually the user will have more information about the auxiliary current drive profile rather than the total current profile.

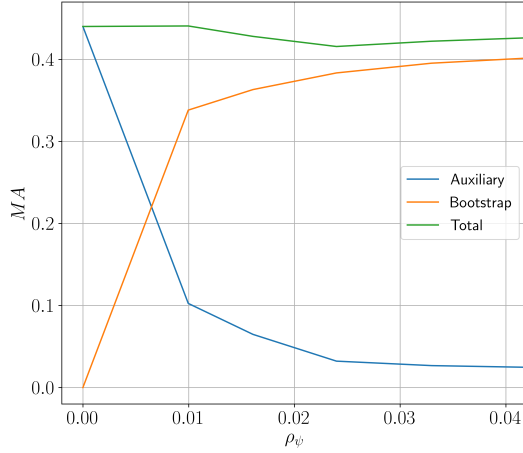


Figure 3.2: Illustration of how SCENE fills in the toroidal current hole by using the bootstrap current profile where  $\rho_{\text{psic}} = 0.025$

surface  $\rho_{\text{psic}}$  and ensures the total current is at least at that level using the auxiliary current, as shown in Figure 3.2.

A more detailed summary of the SCENE inputs can be found in [102]. SCENE is used to explore the physics and engineering limits of an ST reactor design.

## 3.2 NBI codes - NUBEAM, NBeams and RABBIT

It is necessary to determine if the  $J_{\text{aux}}$  specified in SCENE is feasible to drive and what kind of system is required to do so. Neutral beam injection will be used as the current drive system of choice and this work will focus on comparing 3 different codes for NBCD simulations NUBEAM [108], NBeams [109] and RABBIT [110].

### 3.2.1 NUBEAM

NUBEAM is a Monte-Carlo code that does full orbit tracking of the fast ions as they slow down. It has been successful in NBI modelling for several different tokamaks including NSTX [111], JET [112] and DIII-D [113]. Depending on the number of Monte Carlo particles used, a NUBEAM simulation can require 100-1000 CPUh to model a single slowing down time.

The fast ion distribution function is represented numerically by several markers that represent an ensemble of physical particles. The trajectories of these markers are followed through the plasma, including modelling of

- Electron impact ionisation

- Thermal ion impact ionisation and charge-exchange
- Impurity ion impact ionisation and charge exchange
- Impact ionisation and charge exchange with slowing down fast ions

This allows for a complete model of the deposition and slowing down of the neutral beam particles. Large scale instabilities, ripple effects, finite Larmor radius effects and anomalous diffusion are all included in the physics model. NUBEAM is capable of modelling multiple beamlines with full beamline geometries. The main drawback with NUBEAM is the computational cost as to reduce the noise of the simulation by a factor of  $N$  requires  $N^2$  more markers. NUBEAM is used to benchmark the reduced physics codes NBeams and RABBIT.

### 3.2.2 NBeams

NBeams is a simple real-time capable code, where the distribution function for the fast ions is assumed to be a solution of the Fokker-Planck equation shown below

$$\frac{df_b}{dt} + \vec{v} \cdot \nabla f_b + \frac{q}{m} \left( \vec{E} + \vec{v} \times \vec{B} \right) \cdot \frac{\partial f_b}{\partial \vec{v}} = C(f_b) + S \quad (3.8)$$

where  $f_b$  is the beam fast ion distribution function,  $C$  is a collision operator and  $S$  is a source term. NBeams utilises the steady state solution of this equation so the first term on the left hand side is set to 0. By assuming  $\vec{E} = 0$  and that the beam distribution is axisymmetric around the magnetic field, the third term of Equation 3.8 can also be set to 0.

A Landau collision operator is used and assumes that  $v_{i,th} < v_b < v_{e,th}$  [114]. This is true as long as the energy of the beam  $E_b$  is greater than  $T_i$  but not a factor of  $m_i/m_e$  larger than  $T_e$ . The collision operator has the following form

$$C(f_b) = \frac{1}{\tau_s v^3} \left[ v \frac{\partial}{\partial v} (v^3 + v_c^3) f_b + Z_{\text{eff}} \frac{v_c^3}{2} \frac{\partial}{\partial \xi} (1 - \xi^2) \frac{\partial f_b}{\partial \xi} \right] \quad (3.9)$$

where  $v_c$  corresponds to the critical energy for slowing down given by

$$v_c = \left( \frac{3\sqrt{\pi} m_e Z_b}{4m_b} \right)^{1/3} \quad (3.10)$$

$\tau_s$  is the Spitzer slowing down time given by

$$\tau_s = \frac{m_b^3 v_c^3}{4\pi e^2 Z_b^2 Z_i n_e L n \Lambda} \quad (3.11)$$

$\xi$  is the pitch angle. The first term represents the slowing down of the beam, where the  $v^3$  component represents the drag on the fast ions from the electrons and the  $v_c^3$  component is

the drag from the background ions. When  $v = v_c$  the energy transfer from the fast ions to electrons is the same as to the background ions. The second terms represents the pitch angle scattering of the beam, which only becomes significant when  $v < v_c$ .

The steady state equation then becomes

$$\frac{1}{\tau_s v^3} \left[ v \frac{\partial}{\partial v} (v^3 + v_c^3) f_b + Z_{\text{eff}} \frac{v_c^3}{2} \frac{\partial}{\partial \xi} (1 - \xi^2) \frac{\partial f_b}{\partial \xi} \right] + S(v, \xi) = 0 \quad (3.12)$$

If the source term  $S$  is taken to be delta function in energy and pitch  $S = \frac{S_0}{v^2} \delta(v - v_b) \delta(\xi - \xi_b)$  then the solution is in the form of an infinite sum of Legendre polynomials [115]

$$f_b(v, \xi) = \frac{S_0 \tau_s}{v^3 + v_c^3} \sum_{l=0}^{\infty} \frac{2l+1}{2} P_l(\xi) P_l(\xi_b) \left[ \left( \frac{v^3}{v_b^3} \right) \left( \frac{v_b^3 + v_c^3}{v^3 + v_c^3} \right) \right]^{\frac{1}{6} l(l+1) Z_{\text{eff}}} \quad (3.13)$$

where  $S_0$  is the fast ion source,  $P_l(\xi)$  are Legendre polynomials and  $\xi_b$  is the birth pitch. NBeams assumes that fast ions stay on the flux surface they are born and that they have a single birth pitch. It is not able to account for orbit effects. Furthermore, it assumes a purely toroidal field when calculating the birth pitch, which can lead to an overestimation as the poloidal field can be significant in an ST.

To calculate the source term  $S_0$ , NBeams uses a pencil-beamlet technique as outlined in [109, 116]. NBeams models several beamlets together to form a beam with a specified gaussian width.

To calculate other useful beam quantities, such as fast ion density and current, moments of  $f_b$  need to be taken. The fast ion density defined as

$$n_b = \int_0^{\infty} dv \int_{-1}^{+1} d\xi v^2 f_b(v, \xi) \quad (3.14)$$

It should be noted that Legendre polynomials have the following behaviour

$$\int_{-1}^{+1} d\xi P_n(\xi) P_m(\xi) = \frac{2}{2n+1} \delta_{nm} \quad (3.15)$$

And as  $P_0(\xi) = 1$ , the pitch angle component of Equation 3.13 can written as

$$\sum_{l=0}^{\infty} \int_{-1}^{+1} P_0(\xi) P_l(\xi) d\xi \quad (3.16)$$

only the  $l = 0$  term in Equation 3.13 contributes to the fast ion density moment resulting in

$$n_b = \int_0^{\infty} dv v^2 \frac{S_0 \tau_s}{2(v^3 + v_c^3)} = \frac{S_0 \tau_s}{3} \ln \left[ \frac{1 + (v_b/v_c)^3}{1 + (v_{th}/v_c)^3} \right] \quad (3.17)$$

Similarly the fast ion current is defined as

$$J_{\text{fast}} = \int_0^\infty dv \int_{-1}^{+1} d\xi v^3 \xi f_b(v, \xi) \quad (3.18)$$

$P_1(\xi) = \xi$  so here only the  $l = 1$  term survives the integration such that

$$J_{\text{fast}} = S_0 \tau_s \xi_b \int_0^\infty dv \frac{v^3}{v^3 + v_c^3} \left[ \left( \frac{v^3}{v_b^3} \right) \left( \frac{v_b^3 + v_c^3}{v^3 + v_c^3} \right) \right]^{\frac{Z_{\text{eff}}}{3}} \quad (3.19)$$

This term is calculated numerically.  $J_{\text{fast}}$  is generally known as the unshielded current. This, however, is not the total current that gets driven. The electrons act as a drag on the fast ions, which partially cancels out the total current. The total neutral beam current is given by

$$J_{NB} = \eta_{\text{shield}} J_{\text{fast}} \quad (3.20)$$

Several different models exist for  $\eta_{\text{shield}}$  that include impurity and neoclassical effects. NBeams has implemented the following model for the shielding

$$\eta_{\text{shield}} = 1 - \frac{Z}{Z_{\text{eff}}} [1 - L_{31}] \quad (3.21)$$

where  $L_{31}$  is derived from neoclassical theory and accounts for the impact of trapped electrons as they cannot contribute as much to this electron return current. A model for  $L_{31}$  is based off of [117]

$$L_{31} \approx \left( 1.55 + \frac{0.85}{Z_{\text{eff}}} \right) \sqrt{\varepsilon} - \left( 0.20 + \frac{1.55}{Z_{\text{eff}}} \right) \varepsilon \quad (3.22)$$

This was found to be valid for  $\varepsilon < 0.2$  meaning it will only be valid for the very core of an ST. It should be noted that with this model as  $\varepsilon \rightarrow 0$ , which corresponds to the core of the reactor, this shielding term becomes stronger. If the plasma had no impurities, i.e.  $Z_{\text{eff}} = 1$ , then this would completely cancel out the fast ion current.

The power deposition can be directly calculated from the source term

$$p_b = (1 - f_{\text{shine}}) S_0 E_b \quad (3.23)$$

where  $f_{\text{shine}}$  is the beam shine-through fraction

## Limitations

This model for the distribution function doesn't account for first orbit effects, charge exchange losses or a high energy tail. The importance of the orbit effects will be examined as we move

forward. The pencil-beamlet model used cannot model the detailed optics of an injection system such as beam divergence or angling.

### 3.2.3 RABBIT

RABBIT is also a real time capable code, utilising the same distribution function as NBeams, but does not assume that the source term is singular in pitch as it will change over the fast ions orbit, especially for trapped particles. RABBIT attempts to account for this first orbit effect by modelling and averaging the deposition over the first orbit. The source term is thus defined as

$$S = \frac{S_{av}}{v^2} \delta(v - v_b) K(\xi) \quad (3.24)$$

where  $S_{av}$  has been adjusted to account for the radial spread due to width of the banana orbit.  $K(\xi)$  represents the broadened pitch distribution and has been normalised such that  $\int d\xi K(\xi) = 1$ . It only tracks the first orbit so cannot account for orbit effects whilst slowing down.

This results in a slightly modified solution for the distribution function

$$f_b(v, \xi) = \frac{S_{av} \tau_s}{v^3 + v_c^3} \sum_{l=0}^{\infty} \frac{2l+1}{2} P_l(\xi) K_l \left[ \left( \frac{v^3}{v_b^3} \right) \left( \frac{v_b^3 + v_c^3}{v^3 + v_c^3} \right) \right]^{\frac{1}{6} l(l+1) Z_{\text{eff}}} \quad (3.25)$$

where

$$K_l = \int d\xi K(\xi) P_l(\xi) \quad (3.26)$$

The fast ion density, current and power are then calculated in the same way as NBeams. RABBIT has been successfully bench-marked against NUBEAM for DIII-D [110], but orbit effects could be significant for an ST as a trapped particle's pitch will change sign, lowering the average pitch. This would have an impact on the total current prediction. RABBIT uses a different model for  $L_{31}$  based off of the Sauter model [106], which is also the model used by NUBEAM.

NUBEAM will be used to benchmark NBeams and RABBIT, as well as to identify a neutral beam configuration that can drive the auxiliary current in BurST.

### 3.3 Gyrokinetic codes - GS2 & CGYRO

Several codes exist which solve the  $\delta f$  gyrokinetic equation and there exists work that has bench-marked these codes against each other [118]. Cross-code validation is important, especially when designing a future reactor, as it will give greater confidence in the conclusions drawn from the micro-stability analysis. This type of validation won't ensure that experimental data can be accurately captured with gyrokinetics, just that the equations are being solved correctly. This work will focus on 2 codes, GS2<sup>§</sup> [85] and CGYRO<sup>¶</sup> [119] and compare their linear predictions for BurST. Linearly, both GS2 and CGYRO are initial value solvers for the electromagnetic gyrokinetic equation<sup>||</sup>. These codes will calculate the eigenfunctions and frequency of the dominant instability for a given  $k_y$  on a flux surface of a plasma equilibrium. Nonlinearly, they can return the saturated fluxes arising from the coupled micro-instabilities. Both of these codes will be used to examine the turbulent characteristics of a BurST plasma. Going through the algorithms in detail is quite an involved process and will not be examined here, but details can be found in [85] for GS2 and [119] for CGYRO.

### 3.4 Quasi-linear codes - TGLF & QLGYRO

Several quasi-linear transport models exist, such as Qualikiz [120] and TGLF [73], that use reduced physics models to speed up the calculation time of turbulent fluxes. They have proven to be successful modelling experimental profiles of conventional tokamaks like DIII-D [121] and JET [101] and there has even been success in modelling MAST [90, 121]. This thesis will focus on the TGLF model as Qualikiz uses a small inverse-aspect ratio expansion which is not appropriate for most of an ST.

TGLF has two main components, a gyro-Landau fluid eigensolver to find the quasi-linear weights, and a nonlinear saturation rule<sup>\*\*</sup>.

#### 3.4.1 TGLF eigensolver

The eigensolver in TGLF solves the gyro-Landau fluid equations where velocity moments of the gyrokinetic equation are taken, with a closure that attempts to retain the kinetic effects [73]. TGLF solves for 15 different moments, 12 for passing and 3 for trapped particles using a Miller equilibrium model. It represents the eigenfunctions using up to 32 Hermite polynomials.

---

<sup>§</sup>This work uses the GS2 v8.0.4 in the git commit 57e36c0.

<sup>¶</sup>This work uses the CGYRO version in the git commit 23f62b6.

<sup>||</sup>GS2 can be run as an eigensolver to examine sub-dominant modes

<sup>\*\*</sup>This work uses the TGLF version in the git commit 07e4f94

A heuristic approach was taken when TGLF was developed to reduce the difference in linear growth rates of from gyrokinetic simulations. This led to several fitting parameters which have been tuned to low  $\beta$  DIII-D like equilibria as this was the database from which the saturation model was developed. Its validity must be examined in a BurST like regime. It has previously been found that TGLF does not accurately capture nonlinear simulations when including  $\delta B_{\parallel}$ , which can be important in high  $\beta$  regimes [122]. Some of the fitted parameters may need to be re-tuned for a ST regime [123]. TGLF does not split the distribution function into trapped and passing particles, but rather splits the particle populations into Landau resonating and Landau averaging groups. TGLF makes some assumptions to find the boundary between the Landau resonating and averaging populations.

For a particle to be able to resonate with a wave, its parallel velocity must satisfy  $v_{\parallel} \approx \omega/k_{\parallel}$ . For trapped particles, the sign of  $v_{\parallel}$  changes so it is possible for them to average out the Landau resonance. If a trapped particle's parallel velocity changes sign within a half period of the wave, it can average out the resonance, which corresponds to  $\omega < v_{\parallel}/Rq$ . Combining these conditions together results in  $Rqk_{\parallel} < 1$ . TGLF uses this condition to split its particles, however  $k_{\parallel}$  is not known *a priori*. TGLF handles this by assuming  $Rq|k_{\parallel}| = 1/(\sqrt{2}\alpha_{LA}\theta_w)$  where  $\theta_w$  is the Gaussian width of the mode in radians and  $\alpha_{LA}$  is a fitting parameter.

This method still requires prior knowledge about  $\theta_w$ . TGLF manages this by running the eigensolver for a range of widths with at least 2 Hermite polynomials. It selects the width that generates the largest growth rate and will re-run the eigensolver with all the requested polynomials using the width previously found [73]. The default range of widths chosen was to be from  $\theta_w = 0.3 \rightarrow 1.65$  which was selected by choosing widths relevant to low  $\beta$  conventional aspect ratio tokamaks. It is also possible to set a fixed width, though this requires the user to make an educated guess for it.

$\alpha_{LA}$  was selected by matching the growth rate between TGLF and several linear GKS [124] simulations. These simulations were again of a low  $\beta$  conventional aspect ratio device and did not include scans in aspect ratio, shaping or  $\beta$ , so it cannot capture the behaviour of these parameters.

This work will examine the validity of the TGLF eigensolver in describing ST equilibria by comparing it to linear CGYRO/GS2 simulations. However, improving the TGLF eigensolver is outside of the scope of this work. Another approach that has been taken is to use a neural network to get the linear properties from a large database of linear simulations [125, 126], which can be faster than using an eigensolver. If the parameter space used to train the neural network is sufficiently large, then the predictions can be valid over a wide range of tokamak

regimes. This offers an alternative route to obtaining the linear properties.

### 3.4.2 TGLF saturation rule

The second major part of any quasi-linear theory is the saturation model. TGLF attempts to model the saturated state of the 3D potential fluctuation  $\Phi(k_x, k_y, \theta)$  where  $k_x$  and  $k_y$  are normalised by  $\rho_s$ . There is evidence that the zonal fluctuations ( $k_y = 0$ ) of the distribution function are closely linked to the saturated level of ion scale turbulence [127]. TGLF utilises this by assuming that the zonal flow advects the mode which directly leads to dissipation as it couples unstable low  $k_x$  modes to the higher dissipative  $k_x$  modes at the same  $k_y$ . Furthermore, this mechanism is able to saturate at both electron and ion scales as the zonal flow mixing rate for each mode is given by  $\gamma_{ZF} = k_y V_{ZF}$  where [128]

$$V_{ZF} = \frac{1}{2} \sqrt{\sum_{k_x} k_x^2 \Phi^2(k_x, k_y = 0, \theta = 0)} \quad (3.27)$$

$$\Phi(k_x, k_y, \theta) = \frac{e|\phi|}{T_e} \frac{a}{\rho_n} \quad (3.28)$$

The zonal flow will saturate the turbulence when the zonal flow mixing rate competes with the linear growth rate  $\gamma$ . This leads to the approximation that

$$V_{ZF} \approx \text{MAX}[\gamma/k_y] = \frac{\gamma_{\text{max}}}{k_{y,\text{max}}} \quad (3.29)$$

where  $\gamma_{\text{max}}$  and  $k_{y,\text{max}}$  are the values of the normalised growth rate and bi-normal wavenumber at the peak value of  $\gamma/k_y$ . This results in an effective growth rate across the  $k_y$  spectrum given by  $\gamma_{\text{eff}} = c_0 \gamma_{\text{max}}$ . It is necessary for  $\gamma_{\text{eff}} \rightarrow 0$  as  $k_y \rightarrow 0$ , so for  $k_y < k_{y,\text{max}}$ , it was found that for a simple GA-STD case that  $\gamma_{\text{eff}} = c_0 \gamma$  worked well in this region.  $c_0$  is a fitting parameter determined by minimising the difference between the heat flux predictions made by TGLF and nonlinear CGYRO simulations and it was found that<sup>††</sup>

$$c_0^2 = \frac{294.24\varepsilon}{a/L_p} \quad (3.30)$$

where the 294.24 is another fitted parameter used to minimise the difference between TGLF prediction of the heat flux and the nonlinear gyrokinetic simulation.

A full model for the effective growth rate is given by

---

<sup>††</sup> $c_0$  was determined by examining  $a/L_T$  and  $R/a$  scans around the GA-STD, discussed in Chapter 7

$$\gamma_{\text{eff}} = c_0 \gamma \text{ for } k_y < k_{y,\text{max}} \quad (3.31)$$

$$= c_0 \gamma_{\text{max}} \text{ for } k_y \geq k_{y,\text{max}} \quad (3.32)$$

When including flow shear, this maximum growth rate is then modified by a ‘‘quench’’ rule defined as

$$\gamma_{\text{max}} \rightarrow \text{MAX}(\gamma_{\text{max}} - 0.3\gamma_{E \times B}, 0) \quad (3.33)$$

where the 0.3 was found from comparisons to nonlinear simulations of an  $E \times B$  scan around a conventional aspect ratio low  $\beta$  tokamak.

TGLF uses a mixing length argument to determine the peak of the potential, which has had success in comparisons to nonlinear data [128], but has obvious limitations such as cases where there is a Dimits shift [129, 130]. In TGLF the potential takes the following form

$$|\Phi(k_x = 0, k_y, \theta = 0)|^2 = \left( \frac{\gamma_{\text{eff}}}{k_{x,\text{rms}} k_y} \right)^2 \quad (3.34)$$

$k_{x,\text{rms}}$  is the root mean square of the potential in  $k_x$ , that would be obtained from a nonlinear simulation using

$$k_{x,\text{rms}} = \sqrt{\frac{\sum_{k_x} k_x^2 |\Phi(k_x, k_y, \theta = 0)|^2}{\sum_{k_x} |\Phi(k_x, k_y, \theta = 0)|^2}} \quad (3.35)$$

TGLF uses a model for  $k_{x,\text{rms}}$  which was created by fitting to nonlinear CGYRO simulations of an electrostatic conventional aspect ratio tokamak [100].

$$k_{x,\text{rms}}^{\text{model}} = \frac{B_{\text{unit}}}{B_{\text{norm}}} \frac{c_1 k_{y,\text{max}}}{|\nabla r|_0} \text{ for } k_y < c_1 k_{y,\text{max}} \quad (3.36)$$

$$= \frac{B_{\text{unit}}}{B_{\text{norm}}} \left( \frac{c_1 k_{y,\text{max}}}{|\nabla r|_0} + c_2 (k_y - c_1 k_{y,\text{max}}) G_q(0) \right) \text{ for } k_y \geq c_1 k_{y,\text{max}} \quad (3.37)$$

where  $G_q(\theta) = \frac{rB}{qRB_\theta} = \frac{B}{B_{\text{unit}}|\nabla r|}$ .  $G_q$  is a shaping factor that reduces to 1 for a large aspect ratio circular plasma.  $B_{\text{unit}}$  is defined as

$$B_{\text{unit}} = \frac{q}{r} \frac{\partial \psi}{\partial r} \quad (3.38)$$

which is a flux surface quantity.

TGLF assumes that the potential has a Lorentzian form in  $k_x$  and the  $\theta$  dependence can be derived from geometric factors. The final model for the 3D intensity is given by

$$\langle |\Phi(k_y)|^2 \rangle = \langle G^2(\theta) \rangle_F \left( \frac{\gamma_{\text{eff}}}{k_{x,\text{rms}} k_y} \right)^2 \quad (3.39)$$

where  $G^2(\theta)$  is comprised of several geometrical factors and describes the  $\Phi$  dependence on  $\theta$  from nonlinear simulations. The full details of  $G^2(\theta)$  can be found in Staebler *et al* [100], but it was also found by examining nonlinear CGYRO simulations and required another fitting parameter  $c_3$ .

$c_0, c_1, c_2, c_3$  are all determined by making comparison to nonlinear simulations that involved scans in  $\Delta = \frac{\partial R_0}{\partial r}$ ,  $\kappa$  and  $\nu_{ee}$ . A previous saturation rule [73] included scans in  $a/L_T$ ,  $q$  and  $\hat{s}$ , but were all for an electrostatic, conventional aspect ratio, collisionless plasmas. Given that these parameters were defined using a dataset far away from a BurST regime, their validity must be examined further.

### 3.4.3 QLGYRO

As mentioned previously, the TGLF eigensolver may not be suited for high  $\beta$  ST regime, so a new tool, called QLGYRO, was developed that combines the initial value solver from CGYRO<sup>††</sup> and the TGLF saturation rule. This will ensure that the linear physics is being described accurately and will allow for a more direct diagnosis of shortcomings in the quasi-linear assumption.

The quasi-linear weights, introduced in Section 2.5.1, are calculated by QLGYRO for a user-specified range of  $k_y$ . Once these are known, the saturation rule can be quickly calculated to estimate the fluxes. This does come at a computational cost as for each  $k_y$ , the TGLF eigensolver requires a CPU-second to run but initial value CGYRO can require  $\sim 100$  CPUh. Nevertheless, this is still significantly more tractable than a nonlinear simulation which may require over 100,000 CPUh.

QLGYRO allows for each of the  $k_y$  to be run in parallel allowing for efficient scaling with the number of processors. For example, if a 1.5D transport analysis required 10 radial positions and each radial position needed 16 bi-normal wavenumbers, then all 160  $k_y$  could be run in parallel, with the bottleneck being the slowest linear run to converge.

In a perfect system, all the  $k_y$  would converge at the same time but this is not generally true as some modes will take much longer to converge than others, especially near marginality. Thus if all the  $k_y$  were run at the same time then many processors would be sitting idle waiting for the slowest to converge  $k_y$ . So QLGYRO has been set up such that it possible to run any

---

<sup>††</sup>It is also possible to employ GYRO as well and in principle any linear gyrokinetic solver could be used

number of  $k_y$  in parallel asynchronously. This is done by splitting up the total number of processors into smaller groups, where each group can simulate a single  $k_y$  independent of the other groups. It is possible to split the total number of processors into any integer divisor number of groups. For example, if 256 processors are available, then it is possible to split this into; 4 groups of 64 processors, 8 groups of 32 processors, 16 groups of 16 processors etc.

Once a particular group of processors has completed their  $k_y$ , QLGYRO will check for the next  $k_y$  that needs to be run and proceed with that. Thus if one particular  $k_y$  takes very long to converge then the other processor groups will proceed ahead, minimising the amount of time spent idle, resulting in a more efficient use of processors. Once all the eigenvalues have been calculated the saturation rule is applied and the nonlinear fluxes are returned. This approach would allow for “multi-scale” simulations to be run in a more reasonable time. The predictions made by QLGYRO will be examined in Chapter 7.

### 3.5 Summary

This chapter discussed the different codes and models that will be utilised to analyse the steady state scenario for BurST.

SCENE will be used as a Grad-Shafranov solver to examine different regimes BurST may operate in. Different physics and engineering constraints will be examined as well as the viability of different operating regimes. NUBEAM will be used to identify a neutral beam configuration that is able to drive the required auxiliary current profile and will be used to benchmark the reduced physics codes, NBeams and RABBIT. GS2/CGYRO will be used to examine the types of linear instabilities that will arise in BurST, identifying the major drivers of these and possible routes to reduce the impact of turbulent transport. The validity of TGLF and QLGYRO will be examined with preliminary results on the turbulence transport arising in BurST.

## Chapter 4

# Plasma scenarios for a net electric ST

This work aims to design a spherical tokamak reactor plasma that fulfils the following requirements

- Put net energy onto the grid
- Minimise the auxiliary power requirements
- Minimise the size of the device
- Have a steady state scenario

Achieving net energy is quantified by  $P_{\text{net}} > 0$ , which is the difference between the total electrical power produced,  $P_{\text{gross}}$  and the total electrical power consumed by the plant  $P_{\text{plant}}$ . These requirements have driven the design of the plasma equilibrium, which is the core of any fusion device. They are all inherently linked so it is necessary to consider how optimising for one criterion impacts on the others. To generate a  $P_{\text{net}} > 0$  device, a starting point equilibrium was generated from which different parameter scans could be conducted to optimise the device. This thesis will aim to generate an optimised equilibrium for current drive using SCENE whilst making assumptions about the confinement through the  $H_{98}$  scaling. This confinement assumption can be tested with more rigorous transport models. If the total heating power and profile are not compatible then the equilibrium can be modified to optimise the performance. The layout of this chapter is as follows

- Section 4.1: Develop a baseline scenario for a net electric ST
- Section 4.2: Examine the impact of different operating temperatures, densities and currents

- Section 4.3: Examine the impact of a higher toroidal field
- Section 4.4: Summary

## 4.1 Creating a baseline equilibrium

### 4.1.1 Minimum fusion power

There already exist conceptual designs of reactor relevant spherical tokamaks that have become the basis of this work, such as the Spherical Tokamak Power Plant (STPP) [33, 37] which had a major radius of  $R_{\text{maj}} = 3.4$  m. The aim of this device was to have  $P_{\text{net}} > 1000$  MW. STPP was designed to generate a fusion power of  $P_{\text{fus}} = 3300$  MW. Furthermore, heat is generated in the tritium breeding blankets due to the breeding reaction being exothermic\*, contributing a further  $P_{\text{blanket}} = 800$  MW, giving a total thermal power of  $P_{\text{thermal}} = 4100$  MW. The gross electrical power can be calculated from the thermal power using the total steam cycle efficiency  $\eta_{\text{eff}} = P_{\text{gross}}/P_{\text{thermal}}$ . STPP was designed with  $\eta_{\text{eff}} = 41\%$  resulting in  $P_{\text{gross}} = 1700$  MW. The plant was expected to have  $P_{\text{plant}} = 500$  MW resulting in  $P_{\text{net}} = 1200$  MW.

On the other end of the scale exists the Components Test Facility (CTF), a spherical tokamak with a  $R_{\text{maj}} = 0.85$  m. The purpose of this device was to create fusion relevant neutrons for components testing. Given the different goal, it was designed to be a  $Q = P_{\text{thermal}}/P_{\text{aux}} \sim 1$  device, with  $P_{\text{thermal}} = 50$  MW, and  $P_{\text{aux}} = 44$  MW [131–133]. Overall, CTF consumed more power than it generated as  $P_{\text{plant}} = 380$  MW.

The important question becomes “what is the minimum fusion power required to generate  $P_{\text{net}} > 0$ ?” In all likelihood the device is going to lie somewhere between CTF and STPP, so these two design have been used as a lower and upper bound for BurST. Naively, looking at STPP’s power consumption of 500 MW indicates that with an  $\eta_{\text{eff}} = 41\%$ ,  $P_{\text{thermal}} > 1200$  MW is needed. Assuming the ratio of  $P_{\text{fus}}/P_{\text{blanket}}$  is approximately the same as STPP suggests that  $P_{\text{fus}} > 980$  MW is necessary for net electricity. Applying this same reasoning to CTF, with its operating power of 380 MW, suggests a minimum of  $P_{\text{thermal}} = 930$  MW and  $P_{\text{fus}} = 750$  MW. It should be noted that CTF did make less ambitious confinement assumptions compared to STPP.

It is clear from this logic that reducing  $P_{\text{plant}}$  is crucial in ensuring that net energy is achieved. By modifying design choices it may be possible to reduce this. For example, CTF used a copper TF and PF coils, which had resistive power losses of 223 MW. Turning to a supercon-

---

\*Assuming enriched Li-6 is used. If Li-7 is used then this reaction is actually endothermic

ducting system would remove this issue reducing the power required, though there are other considerations that arise due to the additional complexities such as the shielding needed to protect the superconductor and the increased cost [134].

An example of this is the ST pilot plant [135], where the TF and PF coils were both superconducting. They found that with a  $P_{\text{fus}} = 1000\text{MW}$  device at  $\eta_{\text{eff}} = 30\%$ , more electrical power would be produced than is consumed, defined as  $Q_{\text{eng}} > 1$ . When the thermal efficiency was increased to 45% it was possible for it to go as low as  $P_{\text{fus}} = 650\text{MW}$  whilst maintaining  $Q_{\text{eng}} > 1$ . This will be examined further in Section 4.3.

A rigorous power cycle study would be required to calculate the net energy of any particular device, but the above argument justifies an assumption that  $P_{\text{fus}} > 1000\text{MW}$  should ensure that  $P_{\text{net}} > 0$  is satisfied.

#### 4.1.2 Minimise auxiliary power

The auxiliary power systems of a tokamak can have a large impact on the required fusion power as the amount of electrical power needed to generate a given  $P_{\text{aux}}$  can be 3-4 times higher than  $P_{\text{aux}}$  itself. This is due to efficiency losses in generating the neutral beams or RF waves. For example, CTF required 157MW of electrical power to generate a  $P_{\text{aux}} = 44\text{MW}$  [131]. This highlights the benefits of reducing  $P_{\text{aux}}$ . The logic outlined in the previous section should be valid provided  $P_{\text{plant}} < 400\text{MW}$ , suggesting that a net electric device with  $P_{\text{fus}} \sim 1000\text{MW}$  can have a maximum of  $P_{\text{aux}} \sim 100\text{MW}$ .

Auxiliary power systems in tokamaks generally have 3 main uses, heating, current drive and plasma control. This work will focus on the first two and attempt to minimise the power needed here.

It is crucial to maximise the bootstrap current to reduce the load on the auxiliary current drive systems. This can be a significant fraction of  $I_p$  and in the STPP design it was as high as 90%. An approximate scaling for the bootstrap current,  $I_{\text{bs}}$ , is given by Wilson *et al* [37]

$$f_{\text{bs}} = \frac{I_{\text{bs}}}{I_p} \propto \beta_N \frac{I_{\text{rod}}}{I_p} h(\kappa) \quad (4.1)$$

where  $h(\kappa)$  is a function of elongation, approximately linear in  $\kappa$ . A low aspect ratio naturally permits operation at higher elongations, with elongations around 3 possible [39]. This is consistent with NSTX data which has an aspect ratio of  $A = 1.45$ , where it was found that the upper bound on the X-point elongation was given by [136]

$$\kappa_X = 3.4 - l_i \quad (4.2)$$

where  $l_i$  is the internal inductance defined as

$$l_i = \frac{L^2}{2\pi\mu_0^2 I_p^2 V} \oint_V B_\theta dV \quad (4.3)$$

where  $L$  is the poloidal circumference of the last closed flux surface. NSTX would reach  $l_i \approx 0.4$ , suggesting elongations close to 3 are possible. This leads to designs where the internal inductance is minimised, which corresponds to moving current off axis. This is doubly beneficial as it will also raise the safety factor on axis,  $q_0$ , helping to avoid instabilities such as sawteeth and NTMs, but will require careful tailoring of the current profile. It will also be beneficial for ideal ballooning stability as will be shown in Chapter 6.

### 4.1.3 Size of the device

There are two major plasma parameters that determine the radial build of a reactor,  $R_{\text{maj}}$  and  $A$ . One important factor impacting the size of the device is the exhaust. Materials can withstand at most  $10\text{MW m}^{-2}$  of heat flux [137]. A crude, but useful, metric to examine the exhaust problem is  $P_{\text{sep}}/R_{\text{maj}}$  where  $P_{\text{sep}}$  is the power flowing through the separatrix. Here  $P_{\text{sep}} = (1 - f_{\text{rad}})P_{\text{heat}}$  where  $f_{\text{rad}}$  is the fractional power radiated away. The assumed  $P_{\text{sep}}/R_{\text{maj}}$  for different reactor relevant designs are shown in Table 4.1. ITER allows for  $P_{\text{sep}}/R = 16.1\text{MW m}^{-1}$  with a single null divertor. With a double null divertor it could be possible to handle up to twice that, depending on the level of plasma control.

$P_{\text{fus}} = 1\text{GW}$  corresponds to  $P_\alpha = 200\text{MW}$  and assuming a heating power of  $P_{\text{aux}} = 50\text{MW}$  a total  $P_{\text{heat}} = 250\text{MW}$ . If we assume  $f_{\text{rad}} = 80\%$ , as is done for the ST-FNSF device [136] and allow for a  $P_{\text{sep}}/R = 20\text{MW m}^{-1}$  we arrive at a major radius of  $R_{\text{maj}} = 2.5\text{m}$ . This will be used as the major radius of the device examined here.

This  $P_{\text{sep}}/R$  is above the equivalent value in ITER but that will be mitigated by a double null divertor configuration. This is a more conservative estimate compared to CTF, allowing for potential increases in  $P_{\text{aux}}$ . If  $P_{\text{aux}}$  were increased to  $100\text{MW}$  then  $P_{\text{sep}}/R$  would increase to  $24\text{MW m}^{-1}$ , still below the CTF assumption. Furthermore, it is significantly lower than the requirements for STPP. Even if the radiation fraction is lowered to  $50\%$  with  $P_{\text{aux}} = 100\text{MW}$  such that  $P_{\text{sep}}/R = 70\text{MW m}^{-1}$ , it is still lower than STPP. This is still a steep requirement of the divertor and will likely depend on advanced divertor configurations such as the Snowflake

or Super-X designs [138]. Furthermore, handling the exhaust on the inboard leg is more difficult in STs given that there is less space.

	ITER [139]	CTF [33]	ST-FNSF [136]	STPP [140]	BurST
$P_{\text{heat}}$ (MW)	150	51	112	710	250
$f_{\text{rad}}$ (%)	33	50	80	50	80
$P_{\text{sep}}$ (MW)	100	25.5	22.4	355	50
$R_{\text{maj}}$ (m)	6.2	0.85	1.7	3.42	2.5
Divertor type	SND	DND	DND	DND	DND
$P_{\text{sep}}/R$ (MW m <sup>-1</sup> )	16.1	30.0	13.2	104	20.0

Table 4.1: Comparison of different exhaust relevant parameters for future tokamak designs. SND corresponds to single null divertor and DND to double null divertor.

#### 4.1.4 Aspect ratio

Selecting the optimal aspect ratio,  $A$  is a balancing act. Reducing  $A$  allows for higher elongation,  $\beta_N$  and bootstrap current [35]. However, the space available for the centre column reduces. This leads to the toroidal field at the magnetic axis decreasing due to current density and force limits on the centre column and the  $1/R$  nature of the field. Furthermore, reducing  $A$  at fixed  $R_{\text{maj}}$  increases the radial build of the device. For a normal conducting coil it was found that to minimise the cost of electricity the aspect ratio should be set between  $1.5 < A < 2.0$  at fixed  $P_{\text{net}}$  [141]. Below this range the radial build of the device increased significantly and above it  $I_{\text{rod}}$  increased so much so that the recirculating power increased. The STPP design had a centre column with radius 1m and  $I_{\text{rod}} = 30\text{MA}$ . Using this centre column for BurST, results in an aspect ratio  $A = 1.67$ , which is in the optimal range.

#### 4.1.5 Plasma shaping

As illustrated by Equation 4.1, to maximise the bootstrap fraction it is desirable to maximise elongation and in turn minimise the internal inductance as shown in Equation 4.2. This equation however was generated using NSTX data which has an aspect ratio of  $A = 1.45$ . The aspect ratio dependence also affects the maximum elongation and can be accounted for using the following equation [136]

$$\kappa_{\text{max}} = 1.9 + 1.9\epsilon^{1.4} \quad (4.4)$$

Using this, the elongation limit of BurST is  $\kappa = 2.8$ . Neither Equation 4.2 or 4.4 fully capture the maximum elongation, but they do show the dependencies on  $l_i$  and  $\varepsilon$ . To ensure the maximum elongation is achievable it is still necessary to minimise the inductance via a hollow current profile.

Equations 2.8 and 2.28 illustrate how modifying the pressure profile and auxiliary current profile can impact the total current profile. Reducing  $p'$  in the core will lead to a hollow current profile. This can be achieved with a flattened core temperature or a higher pedestal temperature as that allows for a lower  $p'$  in the core at fixed  $P_{\text{fus}}$ . This is doubly beneficial as the increased gradient at the edge will drive more neoclassical current off axis. Otherwise, auxiliary current needs to be driven away from the axis. This can be demonstrated using SCENE.

Four scenarios are examined and are shown in Figure 4.1: Firstly, a “baseline” scenario (blue) where the pressure and auxiliary current profiles are set to be parabolic. Secondly, a scenario where the pedestal height was tripled (orange), thirdly where the core pressure flattened (green) and finally a case with an off axis current drive (red). Only the pressure profile or auxiliary current drive were changed in these simulations.

Figure 4.1a shows the  $p'$  profile and Figure 4.1b illustrates the different  $J_{\text{aux}}$ . Increasing the pedestal height drops the  $l_i$  from 0.60 to 0.38. Core pressure flattening has a weaker impact where  $l_i = 0.52$ .

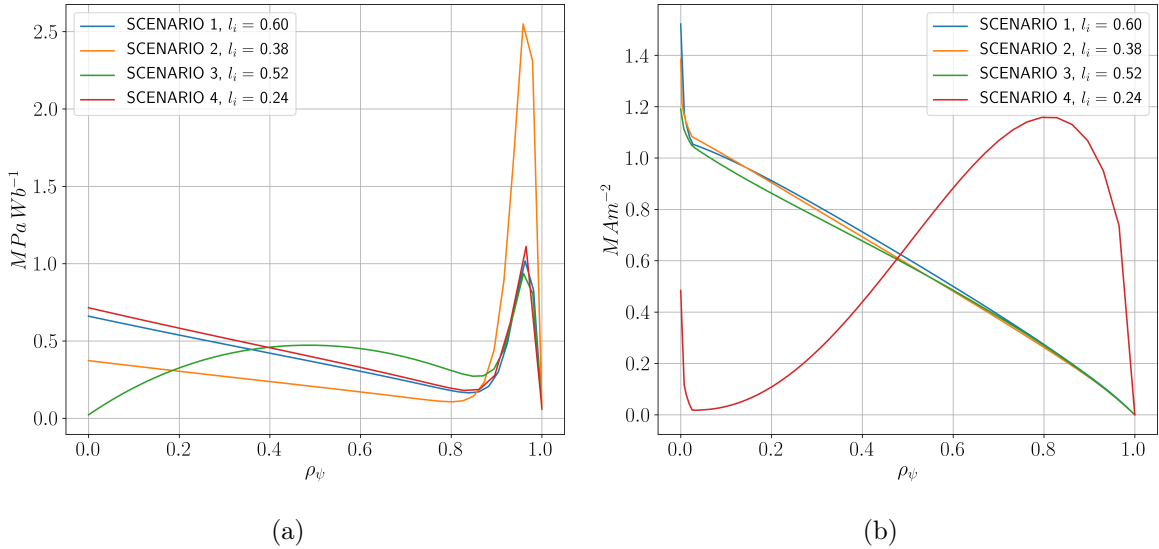


Figure 4.1: 4 different scenarios (outlined in the text) showing the impact on  $l_i$ , showing a)  $p'$  and b)  $J_{\text{aux}}$ .

In practice what we have direct control over is the auxiliary current profile. Figure 4.1b

illustrates a case where the current is driven primarily off axis, which has the largest impact on the inductance where  $l_i = 0.24$ . From Equation 4.2 these profiles suggest  $\kappa = 3.16$  would be feasible, but a more conservative  $\kappa = 2.8$  was set to match with Equation 4.4.  $\delta = 0.55$  was set to match STPP.

To gain an idea about the size of BurST, it compared to JET, ITER and DEMO in Figure 4.2. It can be seen that it has a similar radial build to JET and can fit inside the ITER and DEMO boundary. The vertical build is comparable to ITER and DEMO, highlighting the high elongation of achievable by STs.

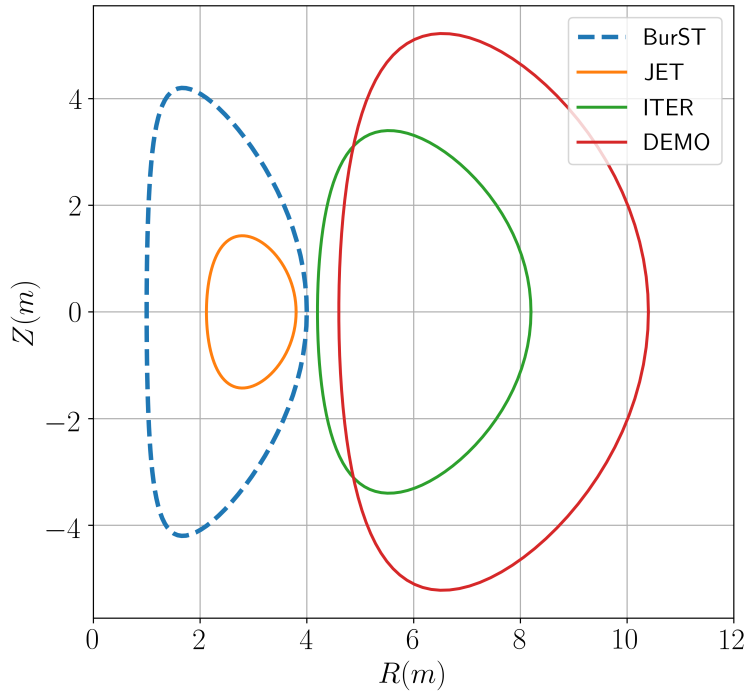


Figure 4.2: Comparison of the BurST plasma boundary to the JET, ITER and DEMO boundaries.

#### 4.1.6 Kinetic profiles

In SCENE the absolute temperature profile of the thermal species are specified, as in Equation 3.1. It has just been shown that the pedestal height can have a large impact on the plasma properties. The pedestal height and width are thought to be determined by the peeling-ballooning stability boundary [142], which would require analysis via a code such as Europed [143]. Using the Europed model, a temperature pedestal height of 5.3keV at  $\rho_\psi = 0.92$  was found for a BurST plasma with  $\beta_N = 5.1$ , utilising the assumption that the width of the pedestal,  $\Delta$ , scales like  $\Delta = 0.1(\beta_\theta^{\text{ped}})^{1/2}$ , consistent with MAST data [144]. This work set

the pedestal height to 5keV located at  $\rho_\psi = 0.9$ . To achieve this pedestal width in SCENE using Equation 3.1,  $T_{\text{grad}} = 20$  was found to be sufficient.  $\tau_0 = 2.0$  was set for a quadratic temperature profile and  $\alpha_T = 2.0$  and  $\tau_1 = 2.2$  were set to slightly flatten the core temperature as this ensured  $q$  was monotonic.

In Wesson’s *Tokamaks* [26] it is shown that the ideal temperature for fusion ignition lies between 10 – 20keV so this device was designed such that the volume average temperature,  $\langle T \rangle$ , is close to this. Initially  $T_i = T_e$  has been set and a starting core temperature of 28keV such that  $\langle T \rangle = 14.8\text{keV}$ , though this will be examined in Section 4.2.2.

The density profile is defined as in Equation 3.3. Using ITER assumptions as a baseline, the density pedestal height as a fraction of the central density was set to  $n_{e,\text{ped}}/n_{e0} = 0.9$  [104]. As with the temperature gradient, setting  $n_{\text{grad}} = 20$  in Equation 3.3 ensured the pedestal top occurred at  $\rho_\psi = 0.9$ . Density peaking is difficult due to fuelling generally occurring at the plasma edge via gas puffing; also it can cause impurity accumulation as predicted by neoclassical theory. Core fuelling is possible via the injection of fuel pellets, but is difficult given the high density of the reactor relevant conditions.  $\eta_0 = 1.5$  was set to allow for a slightly peaked profile [145]. The absolute density was set such that  $P_{\text{fus}} = 1.1\text{GW}$ , which results in a core electron density  $n_{e0} = 1.72 \times 10^{20}\text{m}^{-3}$  and a volume averaged density  $\langle n_e \rangle = 1.54 \times 10^{20}\text{m}^{-3}$ .

STPP was designed with a  $Z_{\text{eff}} \sim 1.6$ , so this was emulated here. Two thermal impurity species were modelled; a helium ash and heavy tungsten impurity. The helium ash density was set such that the ratio of the helium confinement time to the energy confinement time  $\tau_{\text{He}}/\tau_E \sim 4$  as in STPP. The tungsten impurity was then set such that the  $Z_{\text{eff}} \approx 1.6$ .

In reactor relevant conditions, it can be expected that the fast ion pressure from fusion  $\alpha$ s and NBI ions will form a significant fraction of the total pressure compared to the thermal pressure, which would have an impact on the equilibrium. The NBI would introduce an anisotropy in the pressure which would not be captured in ideal MHD and has previously shown to significantly impact the safety factor profile in JET [146]. There is further evidence that finite orbit width effects can modify both the Shafranov shift and safety factor profile [147].

SCENE is not able to include the impact of the fast ions in the equilibrium calculation, though other equilibrium solvers such as FLOW [148] are able to, and future work should compare the predictions between the two to determine the extent of the fast ion’s impact. SCENE is able to account for the bootstrap current driven by the  $\alpha$ ’s, though this tends to be relatively small compared to the thermally driven bootstrap current.

To determine realistic profiles requires a detailed examination with the use of a transport code that accounts for the different sources and sinks of heat and particles. Without this the confinement assumptions will need to be based off of empirical models such as the  $H_{98}$  scaling. Profile tailoring will be difficult due to the dominant  $\alpha$  heating necessary in a reactor and it will be shown in Chapter 5 that most of the auxiliary power will be deposited at the edge. This will further limit control of the profiles, especially in the core.

#### 4.1.7 Auxiliary current profile

As shown previously, an off axis auxiliary current profile is beneficial for lowering the inductance. It also impacts the  $q$  profile and needs to be tailored such that  $q > 2$  is maintained everywhere to avoid instabilities such as sawteeth and NTMs. In SCENE  $J_{\text{aux}}$  is specified by Equation 3.7.

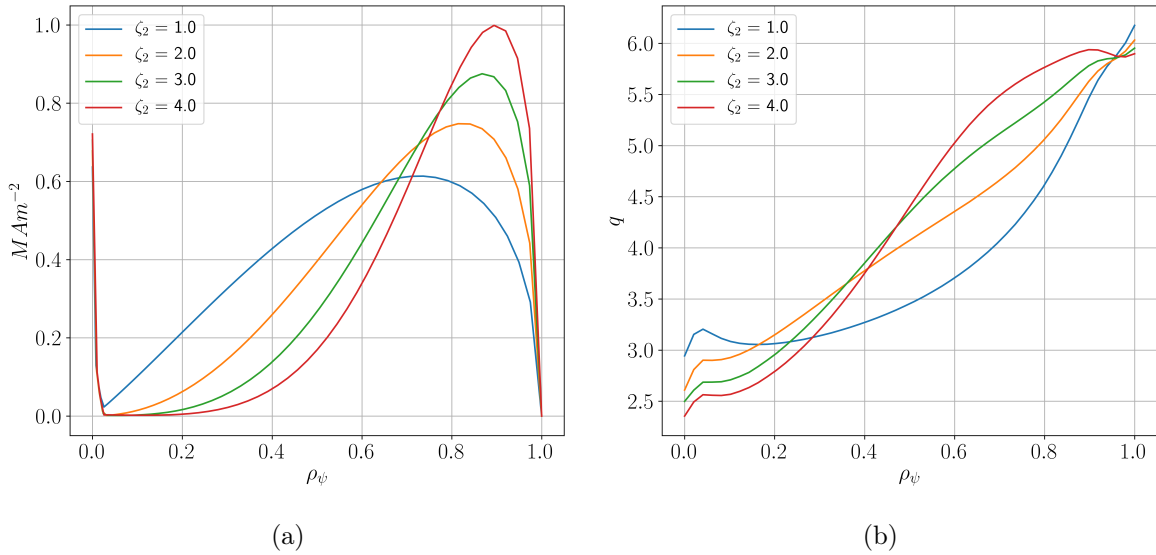


Figure 4.3: Impact of increasing  $\zeta_2$  on a)  $J_{\text{aux}}$  (thus the extent of off axis current drive) and on b)  $q$ .

The impact on the  $q$  profile of changing  $J_{\text{aux}}$  is illustrated in Figure 4.3. The following values were used here,  $\alpha_0 = 0.0, \zeta_0 = 1.0, \alpha_1 = 1.0, \zeta_1 = 0.5$ . The scan was done at fixed  $I_p = 21\text{MA}$  and  $P_{\text{fus}} = 1.1\text{GW}$ . This means all the current will be driven off axis<sup>†</sup>. The  $J_{\text{aux}}$  profile was moved more off-axis by increasing  $\zeta_2$  from 1 to 4.

These cases all satisfy  $q > 2$ , but allowing for a broad current profile results in a reverse shear  $q$  profile in the core. Moving the current towards the edge reduces the shear nearer the edge,

<sup>†</sup>Except for the current driven inside `psic`, where SCENE is set up to fill a current hole in the bootstrap current.

allowing for a monotonic  $q$  in the core. However, pushing the current too far towards the edge results in a reverse shear profile near the edge. An  $\zeta_2 = 2.5$  was settled on for this design as it ensured a completely monotonic  $q$  profile. The feasibility of generating this current profile will be examined in Chapter 5.

#### 4.1.8 Plasma current

Setting  $I_p$  is a balancing act. Increasing  $I_p$  will improve confinement and reduce  $\beta_N$ , however it will also increase the demands on externally driven current  $I_{\text{aux}}$ . This will require a larger auxiliary power increasing the operating costs of the reactor. At fixed  $P_{\text{fus}} = 1.1\text{GW}$  and  $J_{\text{aux}}$  as specified above, a scan in the total plasma current was done from 17MA to 23MA. This corresponds to a fixed  $p'$  whilst changing the  $ff'$ . Figure 4.4a illustrates how the different sources of current change when scaling up  $I_p$ . As the current is increasing,  $\beta_\theta$  is reducing, explaining the slight drop in  $I_{\text{bs}}$ . However, it is clear that the pressure driven currents don't change significantly in this scenario, so the difference in the total current must be made up by the auxiliary current, which corresponds to a larger  $P_{\text{aux}}$ .

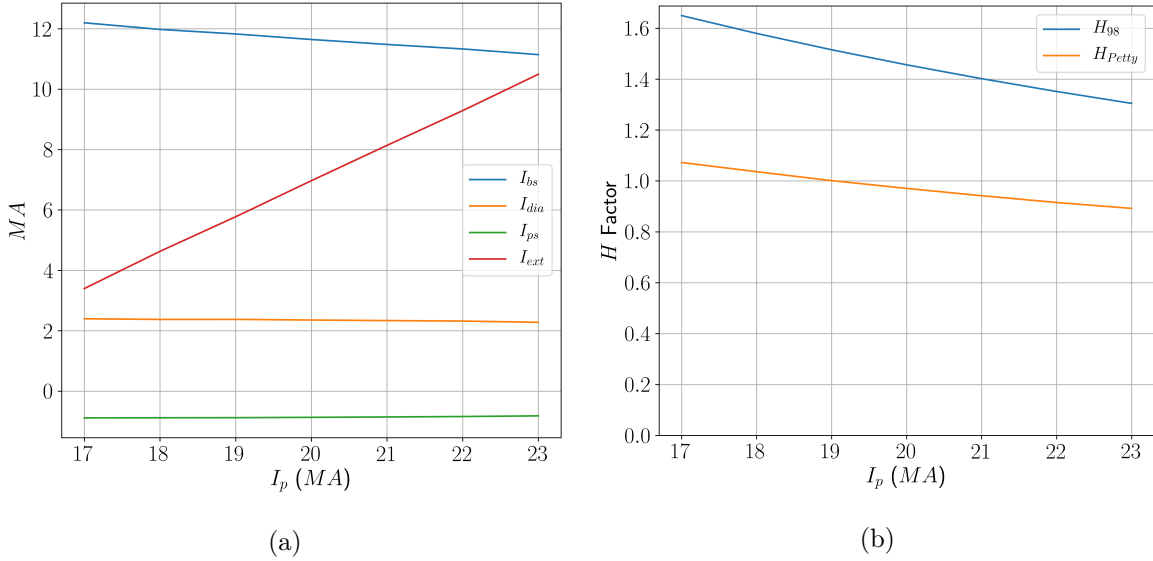


Figure 4.4: A scan in total  $I_p$  showing a) a breakdown of the contributions of the different pressure driven currents and the external current and b)  $H_{98}$  and  $H_{\text{Petty}}$ . Note this was done at fixed  $P_{\text{aux}} = 50\text{MW}$  and  $P_{\text{fus}} = 1.1\text{GW}$ .

This scan was done assuming fixed  $P_{\text{aux}} = 50\text{MW}$ , and thus the required  $H_{98}$  and  $H_{\text{Petty}}$  are shown in Figure 4.4b. The weaker Petty scaling with  $I_p$  can be seen here. This range was chosen as it changed  $H_{98}$  from 1.6 to 1.3, the confinement assumption made in STPP and CTF respectively.  $H_{98} \sim 1.3 - 1.4$  has been seen on NSTX [149], so assuming  $H_{98} = 1.4$  for

BurST indicates that  $I_p = 21\text{MA}$  is required. The specific choice of confinement assumption is relatively arbitrary as BurST operates in a regime so far away from the data used to generate these scaling laws, but is useful in putting reasonable bounds on what is feasible. It is interesting to note that this device seems much more reasonable when using the  $H_{\text{Petty}}$  scaling law, indicating the large impact the choice of scaling law can have. If  $H_{98} = 1$  was the condition used then a significantly higher  $I_p$  would be necessary,

#### 4.1.9 Auxiliary power

Current drive requires the deposition of auxiliary power, and here we estimate only the auxiliary power needed to drive the  $J_{\text{aux}}$  profile that we have prescribed. A rough estimation of power needed  $P_{\text{aux}}$  to drive  $I_{\text{aux}}$  is obtained using the current drive efficiency of different systems by re-arranging Equation 2.25 to get

$$P_{\text{aux}} = \frac{I_{\text{aux}} \langle n_{e20} \rangle R_{\text{maj}}}{\eta_{\text{CD}}} \quad (4.5)$$

Using Equation 4.5, gives the  $P_{\text{aux}}$  required to drive  $I_{\text{aux}}$ . Given that we have now prescribed the stored energy and the total plasma heating for this equilibrium, we have also in effect set the confinement time and  $H_{98}$ . Using ITER's predictions for  $\eta_{\text{NBI}} = 0.4\text{A m}^{-2}\text{W}^{-1}$  for the  $I_p = 21\text{MA}$  case in Figure 4.4, implies  $P_{\text{aux}} = 79\text{MW}$  is necessary. The impact of  $P_{\text{aux}}$  on  $H_{98}$  is relatively modest, reducing to 1.35, due to the dominant heating coming from the fusion  $\alpha$ 's. This also assumes that no additional power, above that necessary for current drive, is required for heating.

## 4.2 Different operating scenarios

### 4.2.1 Baseline scenario

Combining all of the assumptions made leads to a plasma equilibrium shown in Figure 4.5. The major plasma parameters for this equilibrium are shown in Table 4.2. This will be the baseline equilibrium from which different operational scenarios are examined.

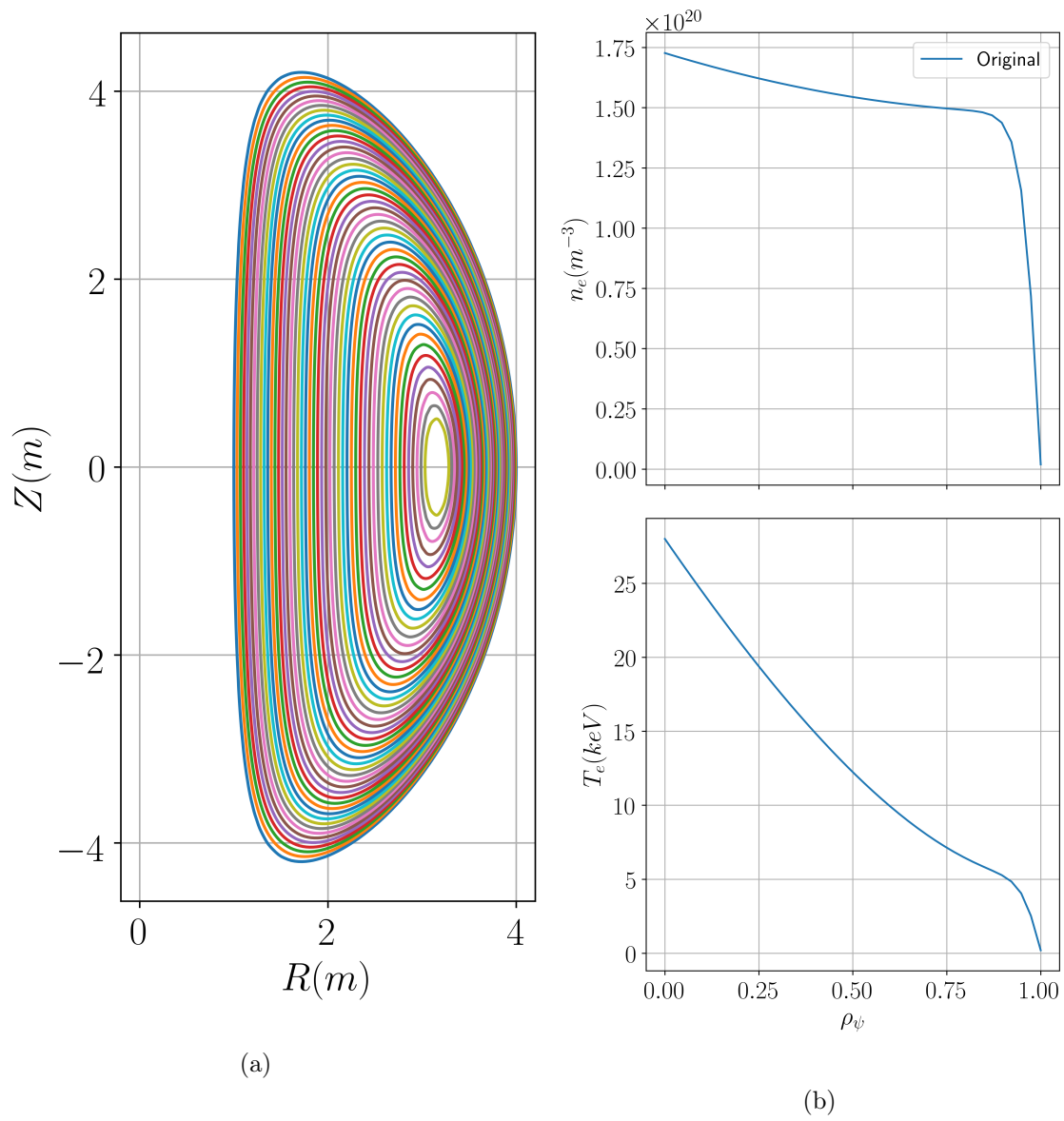


Figure 4.5: a) Flux surfaces and b) electron density and temperature profiles of the baseline equilibrium.

Parameter	Value	Reasoning
$R_{\text{maj}}$ (m)	2.5	Exhaust arguments using $P_{\text{sep}}/R_{\text{maj}}$
$a$ (m)	1.5	Allow space for STPP Centre column
$R_0$ (m)	3.15	Output from SCENE
$I_{\text{rod}}$ (MA)	30.0	Same current as STPP Centre column
$I_p$ (MA)	21.0	“Reasonable” $H_{98}$
$I_{\text{aux}}$ (MA)	8.2	Calculated using SCENE
$P_{\text{fus}}$ (MW)	1100	$P_{\text{net}} > 0$
$P_{\text{aux}}$ (MW)	79	Aux. current drive with $\eta_{\text{NBI}} = 0.4 \text{ A m}^{-2} \text{ W}^{-1}$
$\kappa$	2.8	Limits based off of NSTX data
$\delta$	0.55	Same as STPP
$H_{98}, H_{\text{Petty}}$	1.35, 0.94	Similar confinement assumption to CTF & STPP
$T_{e0}, \langle T_e \rangle$ keV	28.0, 14.8	Initial assumption
$n_{e0}, \langle n_e \rangle (\times 10^{20} \text{ m}^{-3})$	1.72, 1.54	Ensure $P_{\text{fus}} = 1.1 \text{ GW}$ given $T_e$ assumption
$l_i$	0.27	Maximise elongation
$\beta_N$	5.5	Output from SCENE
$q_0$	2.51	Avoid Sawteeth/NTM

Table 4.2: Basic plasma parameters for this baseline scenario and the reasoning behind them.

## 4.2.2 Operating temperature

From Equation 4.5, it can be seen that driving current becomes more efficient at lower densities, but confinement, according to the IPB98y2 scaling law, improves at higher densities. To consolidate this, a scan was performed at fixed  $P_{\text{fus}} = 1.1\text{GW}$  where the core temperature was changed from 10keV to 40keV. The pedestal widths were kept the same and heights as follows  $T_{e,\text{ped}} = 5\text{keV}$  and  $n_{e,\text{ped}}/n_{e0} = 0.9$ . The density and temperature profiles are shown in Figure 4.6a and Figure 4.6b respectively. This does mean that the total pedestal pressure is increasing as the density is increased. This is a questionable assumption to make so future work should calculate a feasible pedestal pressure in each scenario.  $P_{\text{aux}}$  has been appropriately set using Equation 4.5 assuming  $\eta_{\text{NBI}} = 0.4\text{A m}^{-2}\text{W}^{-1}$ .

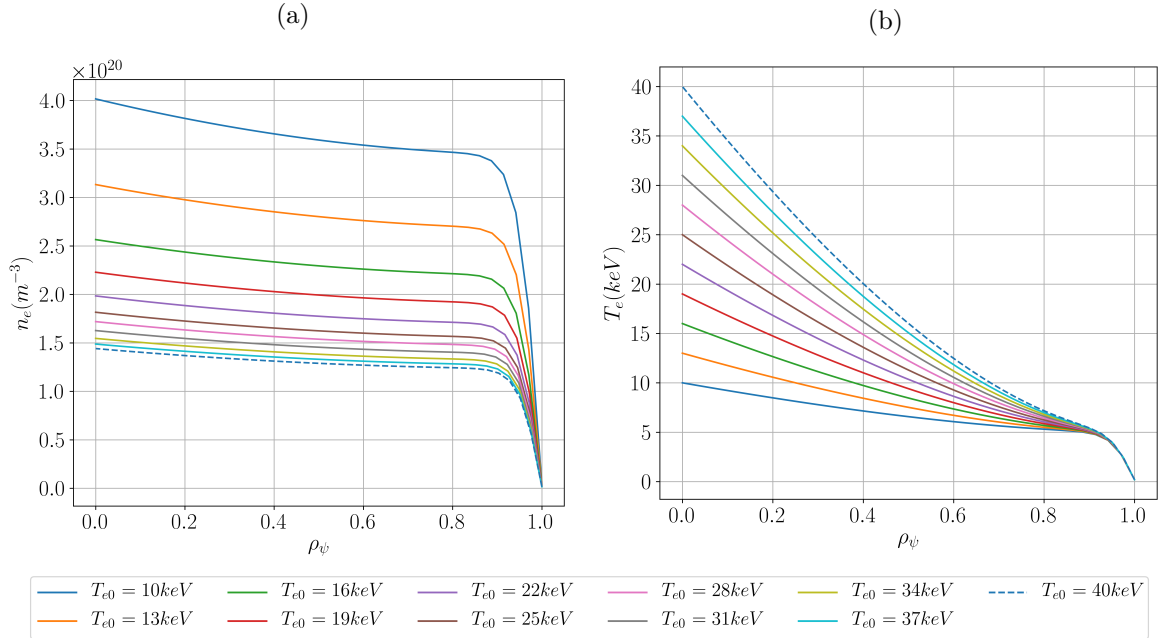


Figure 4.6: a) Density and b) temperature profiles examined at fixed  $P_{\text{fus}} = 1.1\text{GW}$ .

Figure 4.7a demonstrates how at the highest temperatures the current drive efficiency increases sufficiently such that the amount of power needed drops significantly. When  $T_{e0} = 40\text{keV}$  only 60MW of power would be needed. The low  $P_{\text{aux}}$  combined with the low density results in a very large  $H_{98}$  and  $H_{\text{Petty}}$ , shown by Figure 4.7b. The converse is true at lower core temperatures.

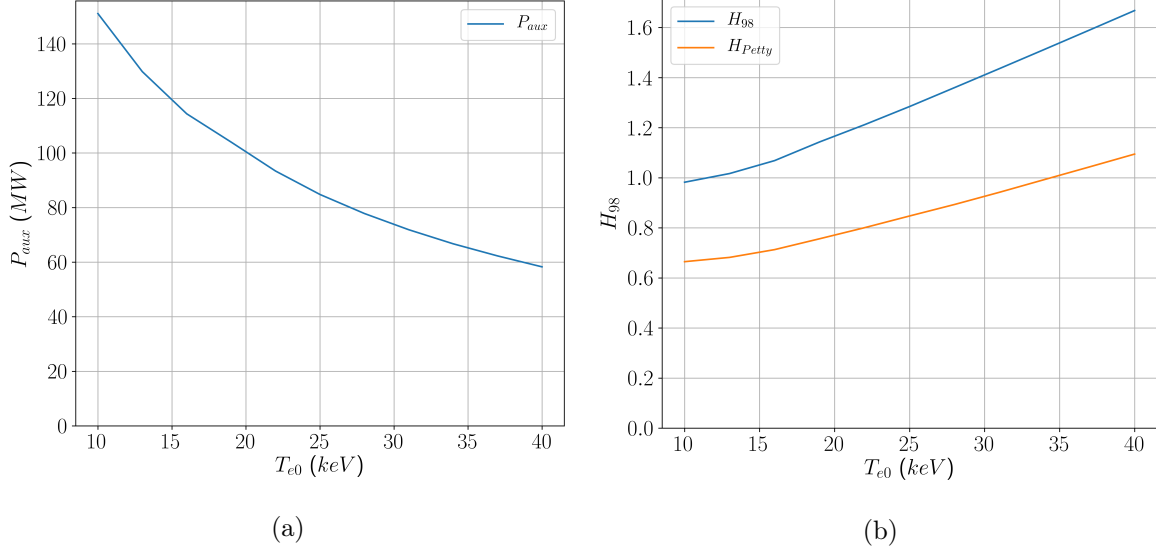


Figure 4.7: Impact of changing  $T_{e0}$  at fixed  $P_{\text{fus}} = 1.1 \text{ GW}$ , showing how a)  $P_{\text{aux}}$ , b)  $H_{98}$  and  $H_{\text{Petty}}$  change when  $\eta_{\text{NBI}} = 0.4 \text{ A m}^{-2} \text{ W}^{-1}$  is assumed.

### Impact of $T_{e0}$ and $I_p$

The total plasma current could be increased at the highest temperatures to bring  $H_{98}$  down to a more reasonable level. This is doubly beneficial as the confinement will improve given the larger  $I_p$  and the larger  $P_{\text{aux}}$  needed to drive  $I_{\text{aux}}$ .

To consolidate this, a 2D scan in  $I_p$  and  $T_{e0}$  was conducted. The plasma current was varied from 17MA  $\rightarrow$  23MA and the core temperature from 10 keV to 40 keV. Figure 4.8 illustrates contours of several plasma parameters. Figures 4.8a, 4.8b and 4.8c show  $P_{\text{aux}}$ ,  $H_{98}$  and  $H_{\text{Petty}}$  respectively. The two confinement scalings are qualitatively similar, but  $H_{\text{Petty}}$  requires a less optimistic assumption about the confinement. As before at low  $I_p$ , there is a larger  $\beta_\theta$ , resulting in a large  $I_{\text{bs}}$ . Furthermore, at the lowest  $T_{e0}$ , due to the large density pedestal, both  $I_{\text{bs}}$  and  $I_{\text{dia}}$  have a very large contribution in the pedestal. At the highest temperatures, the temperature gradient is much larger, increasing the contribution of  $I_{\text{bs}}$  and  $I_{\text{dia}}$ . In these regimes,  $I_{\text{aux}}$  is reduced, lowering the requirements on  $P_{\text{aux}}$ , explaining the minima in the Figure 4.8a. The high  $T_{e0}$ , low  $I_p$  regime is ruled out by the very high requirements of confinement.

In tokamak experiments, however, it has been found that the maximum achievable density is limited to the so-called Greenwald density,  $n_{\text{GW}}$  defined as [150]

$$n_{\text{GW}} = \frac{I_p}{\pi a_{\text{min}}^2} \quad (4.6)$$

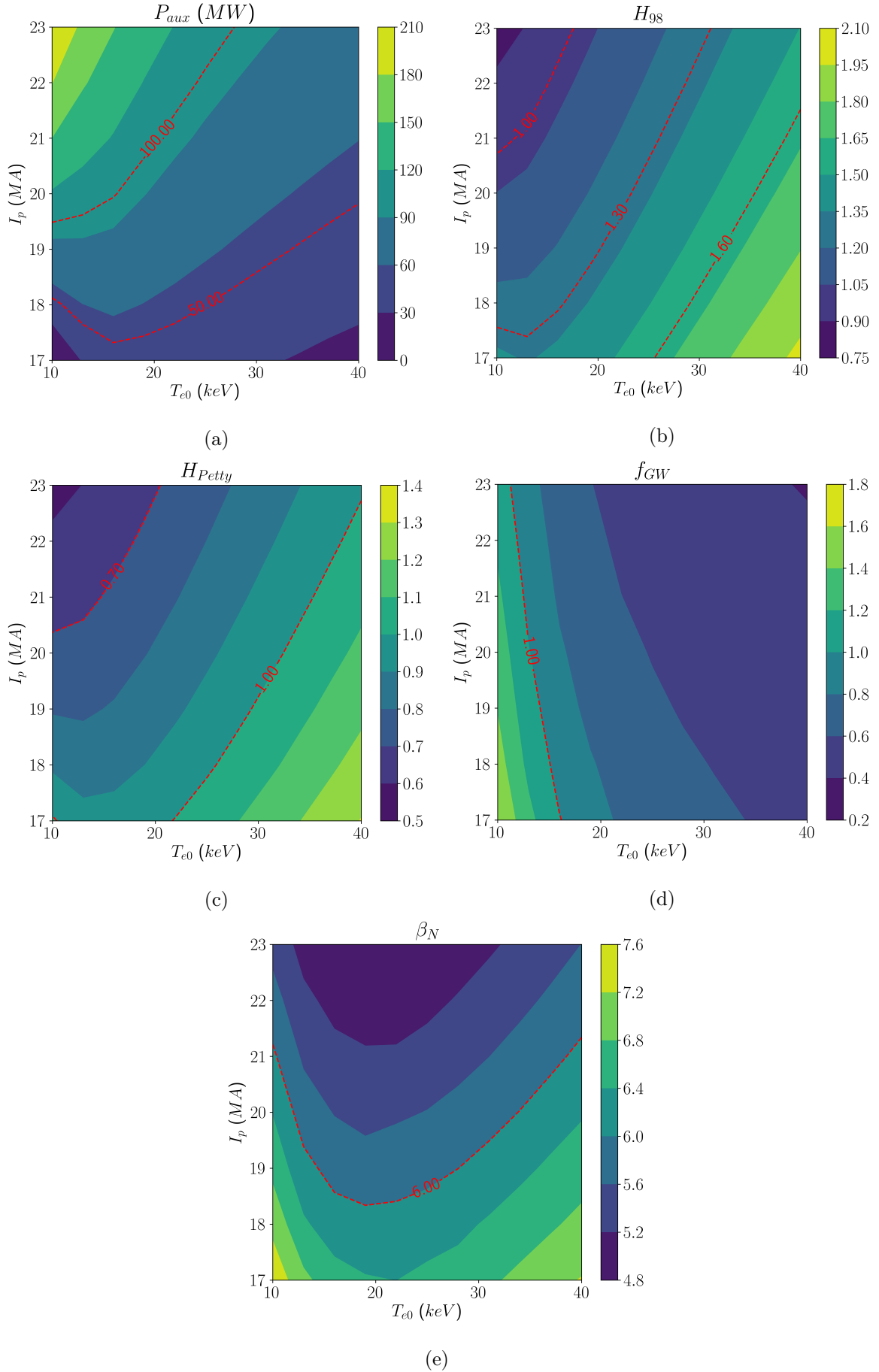


Figure 4.8: Contour plots for a 2D scan changing  $I_p$  and  $T_{e0}$  at fixed  $P_{fus} = 1.1\text{GW}$ , showing the variation of a)  $P_{aux}$ , b)  $H_{98}$  c)  $H_{Petty}$ , d)  $f_{GW}$  and e)  $\beta_N$ .

meaning the Greenwald fraction must satisfy  $f_{\text{GW}} = \frac{\langle n_e \rangle}{n_{\text{GW}}} \leq 1$ . Note, that this limit reduces as  $I_p$  is reduced. Figure 4.8d shows how the bottom left region exceeds the Greenwald density, preventing access to that area of parameter space. Moreover, the current drive systems need accessibility to the core and both RF and NBI systems have density limits that must be accounted for, which will be examined in Section 5.1.2.

Furthermore, at low  $I_p$  the plasma approaches MHD stability limits as  $\beta_N$  gets large. Figure 4.8e shows the  $\beta_N$  with a contour line at  $\beta_N = 6.0$ . Assuming  $\beta_N < 6.0$  sets our limit, this restricts  $I_p > 18.5\text{MA}$  for the full temperature range. There is a minimum in  $\beta_N$  at  $T_{e0} \sim 20\text{keV}$  which corresponds to the peak of the D-T fusion cross section, so the same fusion power can be achieved with slightly less pressure.

It is possible to place restrictions on the accessible parameter space using operational limits. The following restrictions are imposed in Figure 4.9a:  $P_{\text{aux}} < 100\text{MW}$ ,  $H_{98} < 1.6$ ,  $f_{\text{GW}} < 1.0$  and  $\beta_N < 6.0$ . The arrows indicate the direction left available by the imposed limit. This figure illustrates the area of available parameter space given the assumptions made, and it can be seen there is a reasonably large area available. The different restrictions are plotted making it clear what is preventing access to that region of parameter space. As more rigorous limits are defined, this graph can be further refined. This gives a clear operating space for the steady state regime. Of course, whether or not it is possible to access this regime is a completely different question, but one that must be addressed. However, that is outside the scope of this work.

We have assumed that  $H_{98} = 1.6$  is possible but that already illustrates the limitations of scaling laws. If  $H_{98} \leq 1$  was enforced then there would be no available operating space. Furthermore, the choice of scaling law has a large impact as if  $H_{\text{Petty}} < 1$  is used then there is still a significant area of operating space as shown in Figure 4.9b

We note that in this argument we have assumed  $\eta_{\text{NBI}} = 0.4\text{A m}^{-2}\text{W}^{-1}$  over the full range of plasma parameters explored in the scan. This has ignored all variations in current drive efficiency with many different plasma parameters, and limitations in the range of conditions where current drive systems can even couple to the plasma. Some of these issues will be revisited in Chapter 5.

If  $\eta_{\text{NBI}} = 0.4\text{A m}^{-2}\text{W}^{-1}$  is not possible and a lower efficiency is achieved then  $P_{\text{aux}}$  must be increased to drive the current. Figure 4.10 illustrates the impact on  $P_{\text{aux}}$  and  $H_{98}$  when  $\eta_{\text{NBI}} = 0.2\text{A m}^{-2}\text{W}^{-1}$ . Changing  $P_{\text{aux}}$  will have no impact on the  $\beta_N$  or  $f_{\text{GW}}$  limit. Figure 4.10a shows that at very low  $I_p$  it is in principle possible to drive the small auxiliary current needed with  $P_{\text{aux}} = 50\text{MW}$  for the parameter space at very low or very high  $T_{e0}$ . Unfortunately, both

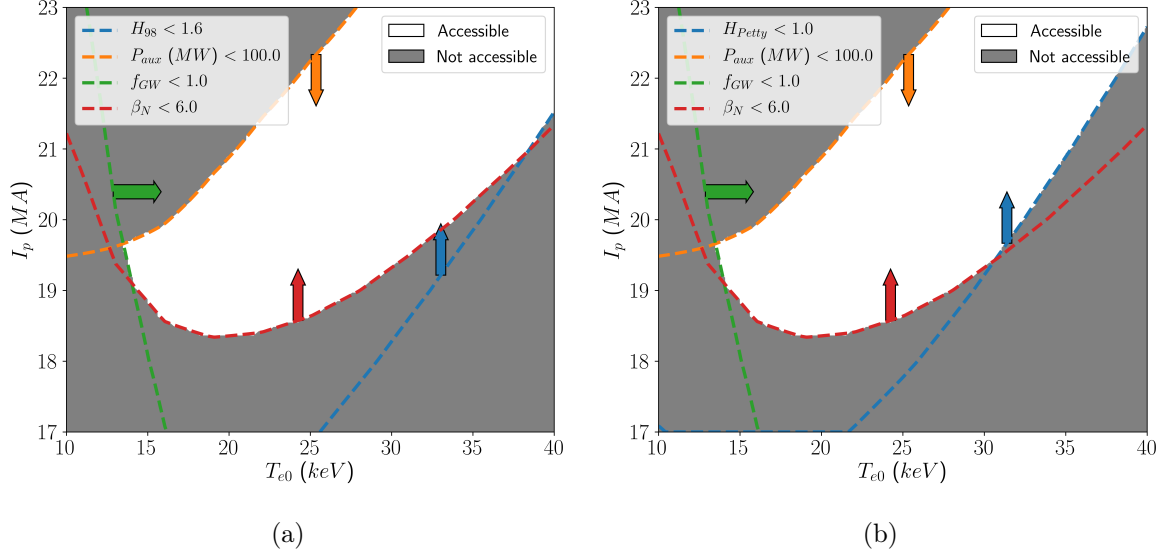


Figure 4.9: Available parameter space if the following restrictions are imposed:  $P_{aux} < 100\text{MW}$ ,  $f_{GW} < 1.0$ , and a)  $H_{98} < 1.6$  and b)  $H_{Petty} < 1.0$  assuming  $\eta_{NBI} = 0.4\text{A m}^{-2}\text{W}^{-1}$ . The arrows indicate the direction which is within the imposed limit.

of these regions at low  $T_{e0}$  and high  $T_{e0}$  are closed regions of operating space because they exceed the Greenwald density limit, or require  $H_{98} > 1.6$ , respectively. Though, due to the additional power required, there is a drop in the  $H_{98}$ .

Figures 4.11a and 4.11b show the available parameter space when applying the same restrictions as before, with  $\eta_{NBI} = 0.3\text{A m}^{-2}\text{W}^{-1}$  and  $0.2\text{A m}^{-2}\text{W}^{-1}$  respectively. With  $\eta_{NBI} = 0.3\text{A m}^{-2}\text{W}^{-1}$  and requiring  $P_{aux} < 100\text{MW}$  brings down the restriction to lower  $I_p$  operation. With  $\eta_{NBI} = 0.2\text{A m}^{-2}\text{W}^{-1}$ , this drops even further such that there no available parameter space. This suggests that  $\eta_{NBI} > 0.2\text{A m}^{-2}\text{W}^{-1}$  must be achieved for this reactor to work, or the limits must be relaxed.

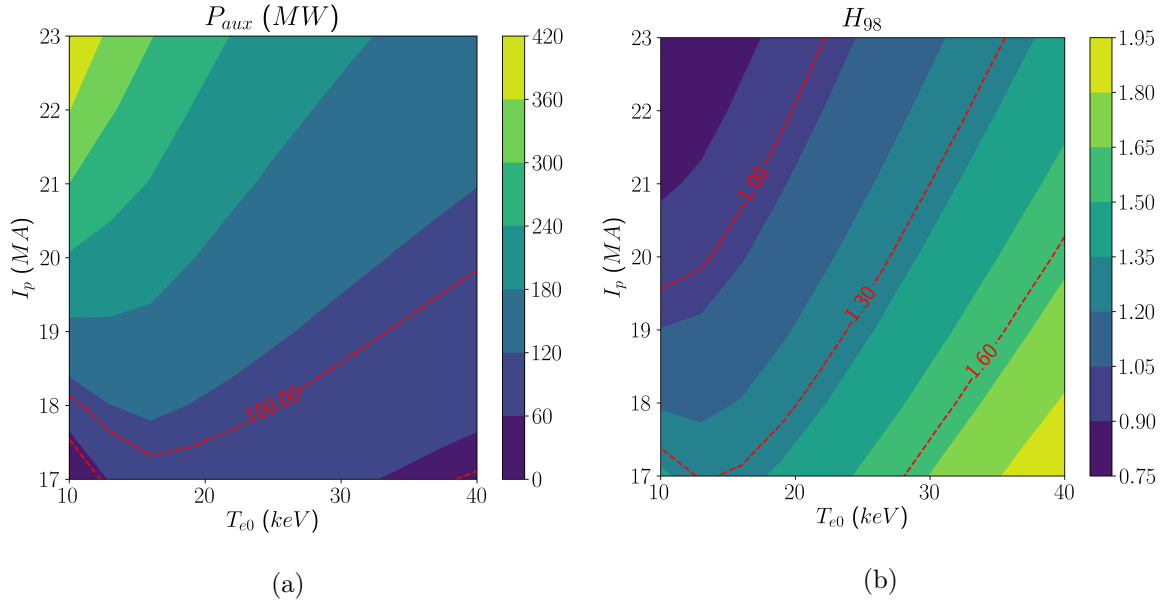


Figure 4.10: Contour plots for a 2D scan changing  $I_p$  and  $T_{e0}$  at fixed  $P_{\text{fus}} = 1.1\text{GW}$ , showing the necessary a)  $P_{\text{aux}}$  and b)  $H_{98}$  when  $\eta_{\text{NBI}} = 0.2\text{A m}^{-2}\text{W}^{-1}$  is assumed.

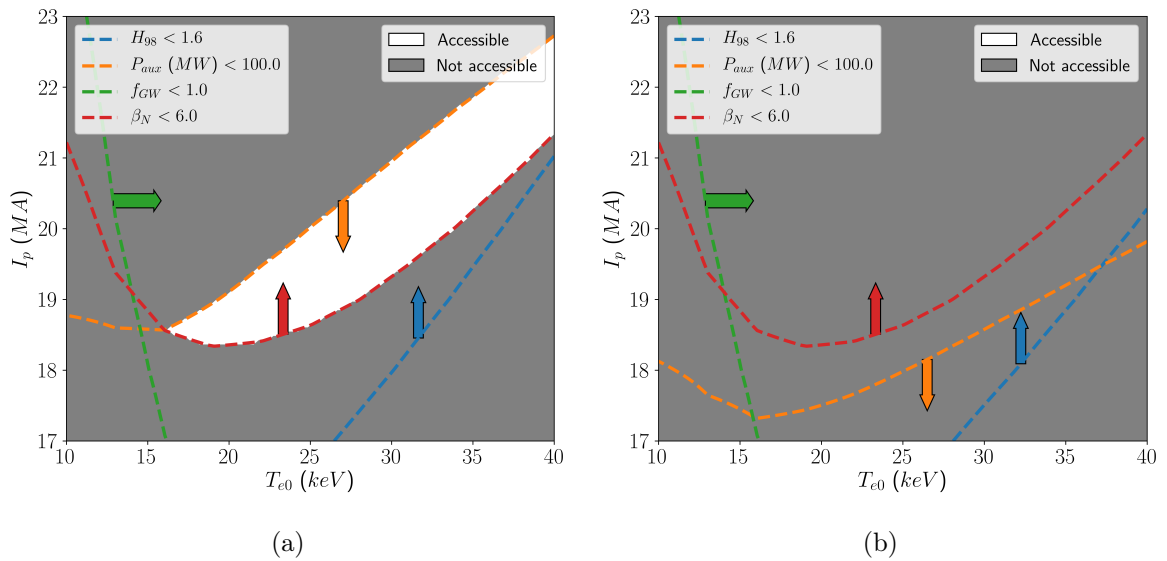


Figure 4.11: Available parameter space if the following restrictions are imposed:  $P_{\text{aux}} < 100\text{MW}$ ,  $H_{98} < 1.6$  and  $f_{\text{GW}} < 1.0$  assuming  $\eta_{\text{NBI}} =$  a) 0.3 and b)  $0.2\text{A m}^{-2}\text{W}^{-1}$ . The arrows indicate the direction which is within the imposed limit.

### 4.3 Higher toroidal field - superconducting centre column

In the work carried out above, the centre column was designed with regular conductors. Superconducting magnets are an attractive technology for a fusion power plant. They significantly reduce the need for recirculating power because they minimise resistive power losses. They

would provide access to a higher field which would slightly ease the requirements on the  $H_{98}$  confinement assumption as  $\tau_{98} \propto B_T^{0.15}$ , but have a much larger reduction in  $\beta_N \propto 1/B$  at fixed fusion power (pressure). The design in the previous section were  $\beta_N$  limited at low  $I_p$ , so a SC centre column would open up a large area of parameter space. Additional shielding would be needed to protect the coils from bombardment by fusion neutrons. The amount of shielding is set by the stopping distance of a fusion neutron and estimates vary from 0.3m to 0.5m to ensure the superconductors are sufficiently protected from neutron damage and heating [151, 152].

STPP had two designs for the centre column, one made of water cooled copper and the other of cryo-cooled aluminium. The power requirements are shown in Table 4.3, reproduced from [134]. The copper design only required 4MW of cooling but the power requirements were dominated by the 250MW of resistive power losses. For the aluminium design, due to the low resistance of cryo-cooled aluminium there was only  $\sim 8$ MW of resistive losses. But the cooling requirements were more significant as the cryo-plant had a coefficient of performance of 0.055, meaning for every 1MW of heat removed, an additional 18MW is required. An equivalent superconducting column would only be subjected to nuclear heating as there is no resistive heating.

	Water cooled copper	Cryo-cooled aluminium
Operational temperature (K)	298	30
Centre column shield (m)	0.10	0.37
Resistive power loss (MW)	250	7.9
Nuclear heating (MW)	100	0.47
Cooling power (MW)	4	159
Total power required (MW)	254	167

Table 4.3: Outline for STPP centre column designs, reproduced from [134].

A high field device has been the subject of many studies [32, 38] as it proposes another route to improving confinement. To see the impact of a higher toroidal field on the available parameter space, a scenario was examined using a high temperature superconductor (HTS) for a centre column with 0.5m of shielding. To justify the increased cost and engineering associated with HTS, the benefits of a higher field device need to be clearly outlined.

At a given temperature, superconductors have a critical current density and critical field below which it will remain superconducting. Rare earth barium copper oxides (REBCO) display

HTS behaviour [153] and have been examined extensively in the context of fusion [154–156]. CORC REBCO superconducting cable designs were found to operate at a maximum engineering current density of  $200\text{MA m}^{-2}$  at 20T [157]. To achieve such high current densities it is necessary to operate the cable at 4K, indicating the potential challenge with the cryostat. Using this design, the maximum field at the edge of the centre column was set to 20T. The current needed to generate this field can be calculated from Equation 4.7.

$$I_{\text{rod}} = \frac{2\pi R_{\text{edge}} B_{\text{edge}}}{\mu_0} \quad (4.7)$$

where the subscript ‘edge’ denotes that parameters value at the edge of the conductor. Table 4.4 compares the values in Equation 4.7 for the STPP aluminium centre column and CORC REBCO design. To generate 20T at the edge of the centre column requires 50MA. This would have an engineering current density of  $64\text{MA m}^{-2}$ . This is well below the engineering current density limit, indicating the limiting factor is the field at the edge of the coil. Another limiting factor is whether the electromagnetic stresses that such a current would generate can be handled by the structural material. It has been reported that a tokamak with a stainless steel structure could support a  $B_{\text{edge}} = 19\text{T}$  when  $R_{\text{edge}} = 0.5\text{m}$ , so this configuration is at the limit of what is feasible [158].

	Aluminium conductor	Superconductor
Operational temperature (K)	30	4
$R_{\text{edge}}$ (m)	0.63	0.5
$B_{\text{edge}}$ (T)	9.5	20
$I_{\text{rod}}$ (MA)	30	50
$B_{\text{geo}}$ (T)	2.4	4
Effective current density ( $\text{MA m}^{-2}$ )	24	64

Table 4.4: Comparison of the BurST centre column design when using an aluminium conductor and a CORC REBCO superconductor.

A similar 2D scan in  $I_p$  and  $T_{e0}$  was performed using the higher  $I_{\text{rod}}$  that can be provided by this CORC REBCO centre column. Figure 4.12a shows  $P_{\text{aux}}$  and this doesn’t change significantly as the toroidal field has little impact on the plasma currents.  $H_{98}$  is shown in Figure 4.12b and due to the higher field it drops enough such that the contour of  $H_{98} = 1.6$  gets pushed towards the bottom right. The largest impact, however, is on  $\beta_N$ , shown in Figure 4.12d, where it has been reduced sufficiently that  $\beta_N = 6.0$  is no longer a limiting factor. The

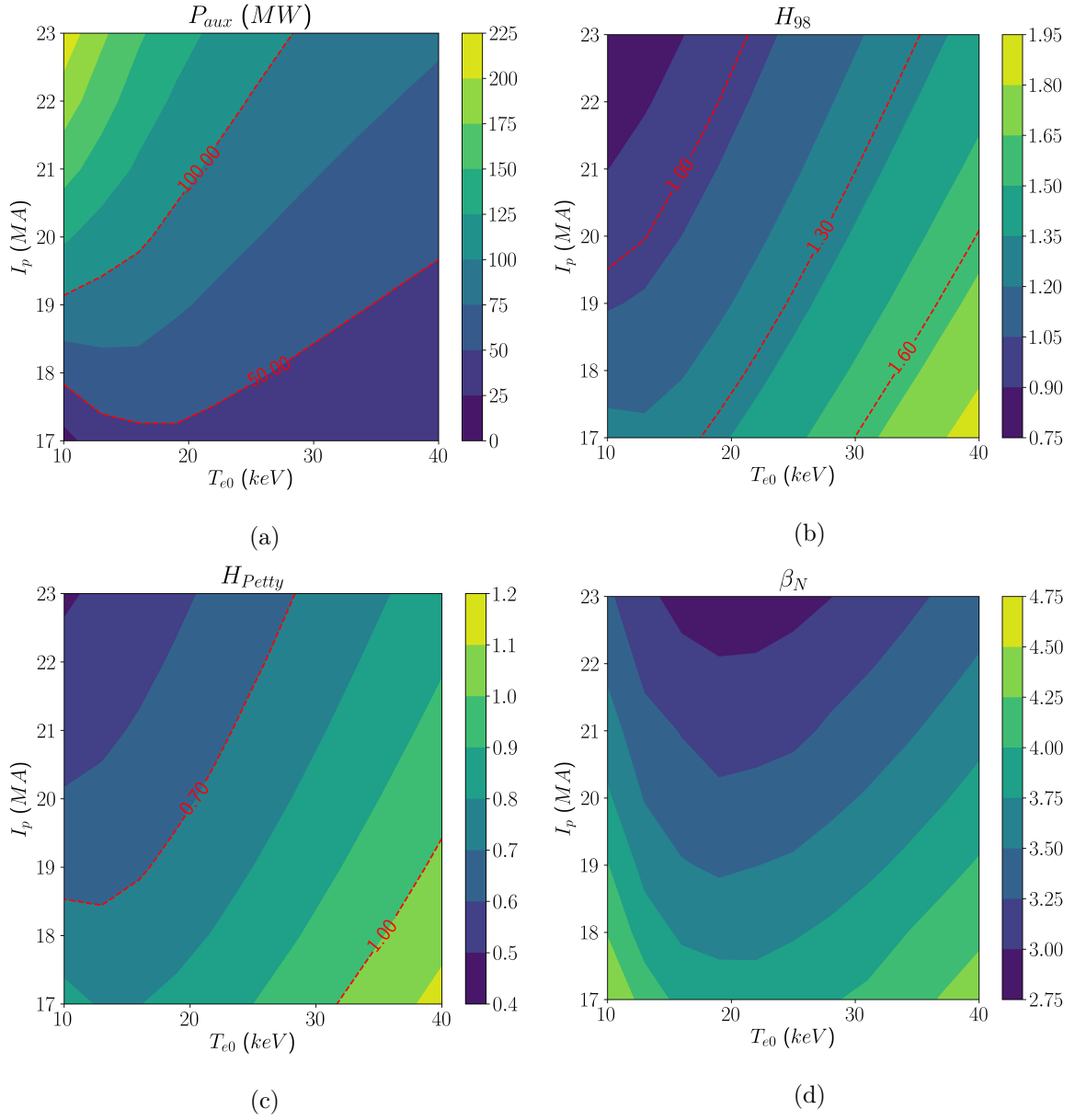


Figure 4.12: Contour plots for a 2D scan changing  $I_p$  and  $T_{e0}$  at fixed  $P_{\text{fus}} = 1.1 \text{ GW}$  with  $I_{\text{rod}} = 50 \text{ MA}$  showing the variation of a)  $P_{\text{aux}}$ , b)  $H_{98}$  c)  $H_{\text{Petty}}$  and d)  $\beta_N$  when  $\eta_{\text{NBI}} = 0.4 \text{ A m}^{-2} \text{ W}^{-1}$  is assumed.

overall effect is that the low  $I_p$  region is now limited by  $H_{98}$  rather than  $\beta_N$ , opening up a significant area of operation. Figure 4.13a shows the available operating space when imposing  $P_{\text{aux}} < 100\text{MW}$ ,  $H_{98} < 1.6$ ,  $\beta_N < 6.0$  and  $f_{\text{GW}} < 1.0$  assuming  $\eta_{\text{NBI}} = 0.4\text{A m}^{-2}\text{W}^{-1}$ . It appears that it would be possible to operate at  $I_p < 17\text{MA}$  given the right temperature profile.

Furthermore, as  $I_p$  is now limited by  $H_{98}$  rather than  $\beta_N$ , if  $\eta_{\text{CD}}$  is dropped,  $P_{\text{aux}}$  will increase which in turn will reduce  $H_{98}$  and give more operating space against the confinement limit. This is illustrated in Figure 4.13b, where at a higher  $B_\phi$ ,  $\eta_{\text{NBI}} = 0.2\text{A m}^{-2}\text{W}^{-1}$  has a large area of available operating space. Figure 4.13c shows that even  $\eta_{\text{NBI}} = 0.15\text{A m}^{-2}\text{W}^{-1}$  has some available operating space. This illustrates one of the benefits of operating at high field. Furthermore, as less re-circulating power is required, more power can be allocated to the auxiliary heating systems which could relax the  $P_{\text{aux}}$  assumption. This also applies to the lower field device examined in the previous section. If the limiting factor for a copper/aluminium centre column device is  $\beta_N$  or the re-circulating power is too high then turning to a superconducting device may be justifiable.

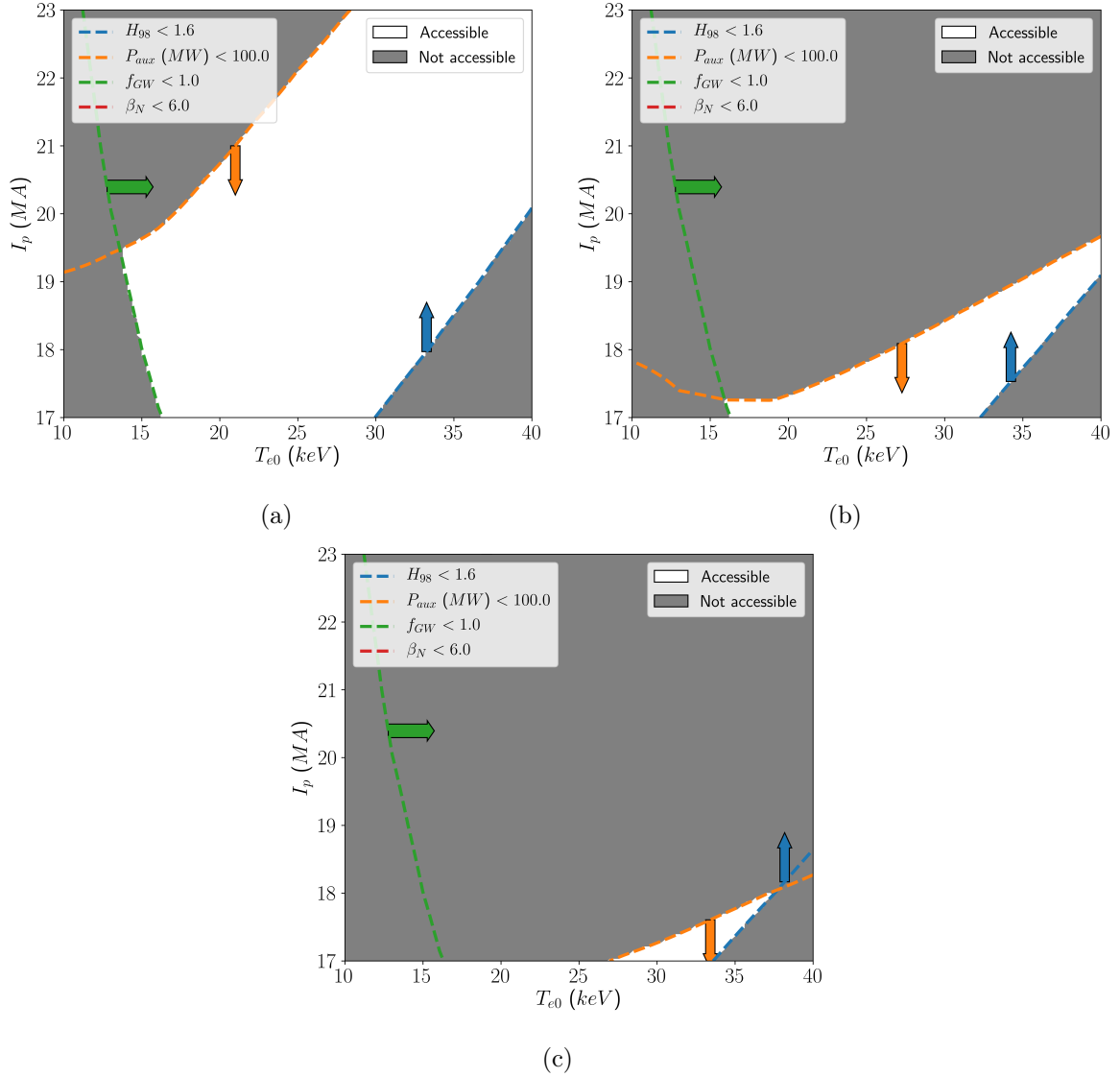


Figure 4.13: Available parameter space for the superconducting design if the following restrictions are imposed:  $P_{aux} < 100\text{MW}$ ,  $H_{98} < 1.6$  and  $f_{GW} < 1.0$  assuming  $\eta_{NBI} =$  a) 0.4 b) 0.2 and c)  $0.15\text{A m}^{-2}\text{W}^{-1}$ . The arrows indicate the direction which is within the imposed limit.

## 4.4 Summary

This chapter has examined different plasma scenarios that could lead to a  $P_{net} > 0$  device. A basic argument was made for the necessary fusion power to generate net electricity. From this, other plasma parameters were determined such as  $R_{maj}$  which was derived by looking at the exhaust issue. Using the STPP centre column, the aspect ratio was set and the elongation was set from limits on NSTX data. Supposing an ITER-like pedestal, kinetic profiles were assumed and an off axis current profile was set that resulted in a low  $l_i$ , monotonic  $q$  equilibrium. The auxiliary power was set by assuming a certain  $\eta_{CD}$  and from this a baseline equilibrium was

determined, with details in Table 4.2.

Once a baseline was determined, the impact of different kinetic profiles and plasma current were examined. By setting the following restrictions:  $P_{\text{aux}} < 100\text{MW}$ ,  $H_{98} < 1.6$ ,  $f_{\text{GW}} < 1.0$  and  $\beta_N < 6.0$ , it was possible to see what operational space is available. The baseline scenario fitted within these restrictions. It was shown that if  $\eta_{\text{CD}} > 0.2\text{A m}^{-2}\text{W}^{-1}$  is not achieved (with a regular conducting centre column) then there is no operational space available given the limits. It is crucial to design current drive systems that can achieve at least this efficiency to allow for some operating space. If  $\beta_N > 6.0$  could be achieved then operation at lower  $I_p$  and  $P_{\text{aux}}$  would be possible.

The impact of a superconducting centre column was also examined and it was found that it reduced  $\beta_N$  sufficiently that it was no longer a limiting factor when assuming  $\beta_N < 6.0$ . This opened up a significant area of operating space and allowed for a lower  $\eta_{\text{CD}}$ . Furthermore, the lower re-circulating power means more power can be used for the auxiliary current drive systems.

Future work should examine the limits used here in more detail. If access to high  $\beta_N$  regimes is possible then the available operating space is much larger. A detailed MHD stability study is required as that will have a significant impact on the reactor. A full power cycle study should be done to more accurately determine the minimum fusion power needed to achieve net power. If this could be relaxed then it would ease the requirements of other systems, especially the exhaust.

## Chapter 5

# Identifying neutral beam injection configurations

The previous section outlined different operating scenarios for BurST and illustrated the importance of achieving a good current drive efficiency. Neutral beam injection has been shown to have large current drive efficiencies and this chapter uses modelling to explore NBI configurations that can drive the necessary current for steady state flat-top operation. We will examine the equilibrium outlined in Table 4.2.

Given the profile of  $J_{\text{aux}}$  shown in Figure 4.3a, it will likely be necessary to have 2 NBI systems in place. One for the on axis current and the second for the off axis component. In this work, on axis current drive corresponds to the current needed to fill the hole left by the neoclassical currents. This is only required within  $\rho_\psi < 0.05$  where 0.12MA is necessary, with the remaining 8.08MA being required off axis. To easier illustrate the requirements in the core, the figures in this chapter will be shown as a function of  $\sqrt{\rho_\psi}$ .

Each “beam” in this chapter will corresponds to a single beamlet with a rectangular shape with a Gaussian half width and height of  $\sigma_R = 0.1\text{m}$  and  $\sigma_Z = 0.2\text{m}$  respectively. Additionally, this work will limit the energy of the beams to 1MeV, in line with the ITER design. The main focus of each section in this chapter is as follows

- Section 5.1: On axis beam
- Section 5.2: Off axis beam
- Section 5.3: Validity of  $\eta_{\text{CD}}$
- Section 5.4: Complete beam configuration
- Section 5.5: Summary

In more detail, Section 5.1 generates an NBI configuration suitable for driving the core current in the baseline scenario using NBeams. This prediction is then compared to the predictions made by NUBEAM and RABBIT to test the validity of the reduced models. The penetration depth of a 1MeV beam is explored when changing the density and temperature profiles. Next in Section 5.2, the requirements for the off axis current will be examined and the validity of the reduced models is determined. As most of the current needs to be driven off axis understanding the current drive efficiency here is vital. In Section 5.3, the validity of using  $\eta_{\text{NBI}}$  as a metric for the efficiency will be tested by examining different plasma temperatures and densities. A final beam configuration will then be generated and the heating profiles will be briefly examined in Section 5.4.

## 5.1 On axis beam

At the core of BurST, the flux surfaces are similar to that of a conventional tokamak, so it should be expected that NBeams and RABBIT would be able to match NUBEAM reasonably well.

The tangency radius  $R_t$ , which is the point at which the beam is tangential to the plasma (i.e orthogonal to the major radius vector), was set to  $R_t = 3.1\text{m}$ , aligned with the magnetic axis at  $R_0 = 3.15\text{m}$ . NBeams found that an 8MW 1MeV beam was sufficient to drive the current on axis. Figure 5.1 shows the toroidal current density profile defined as

$$J_\varphi = \frac{\langle \vec{J} \cdot \vec{B} \rangle}{\langle B^2 \rangle} \frac{f(\psi) \langle R^{-2} \rangle}{\langle R^{-1} \rangle} \quad (5.1)$$

The term with  $f$  on the right acts as a measure of the average toroidal field as is used by NUBEAM.

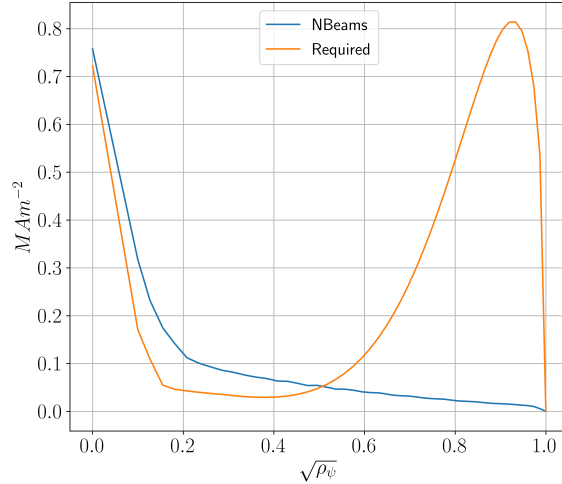


Figure 5.1: NBeams prediction for the current density for an 8MW 1MeV beam with  $R_t = 3.1\text{m}$  to drive the on axis current. The magnetic axis was at  $R_0 = 3.15\text{m}$  Shown as a function of  $\sqrt{\rho_\psi}$ .

### 5.1.1 Benchmark of NBeams and RABBIT

This NBI configuration was recreated in NUBEAM and RABBIT. For NUBEAM, simulations were done with up to 512,000 markers and it was found that using 32,000 markers was sufficient to obtain resolved results. Figure 5.2a and Figure 5.2b shows the beam deposition as seen from above and as a poloidal cross section.

The first outputs to compare between codes are the initial and the orbit averaged deposition,  $S_0$  and  $S_{av}$ . Figures 5.3a and 5.3b illustrates the  $S_0$  and  $S_{av}$  predictions made by each code (NBeams doesn't perform any orbit averaging so  $S_{av} = S_0$ ).

The agreement between the  $S_0$  for  $\sqrt{\rho_\psi} > 0.1$  predicted by NUBEAM, NBeams and RABBIT is quite reasonable, given that NBeams and RABBIT can be run in real time and NUBEAM requires  $\sim 100\text{CPUh}$ . There are however discrepancies, as at the very core NBeams over-predicts  $S_0$ . For RABBIT there appears to be a sharp drop in  $S_0$  at the very core, which is likely not physical.

Comparing  $S_{av}$  for the different codes it can be seen that RABBIT and NUBEAM agree reasonably well above  $\sqrt{\rho_\psi} > 0.1$ . But again in the very core, RABBIT under-predicts the deposition. Even though NBeams doesn't perform the orbit average the overall deposition is rather similar.

The fast ion density, un-shielded current and driven current are compared in Figure 5.4. Similar to what was seen above, RABBIT and NUBEAM agree well for  $\sqrt{\rho_\psi} > 0.1$  with the differences in the core being due to the drop in the deposition seen earlier in RABBIT.

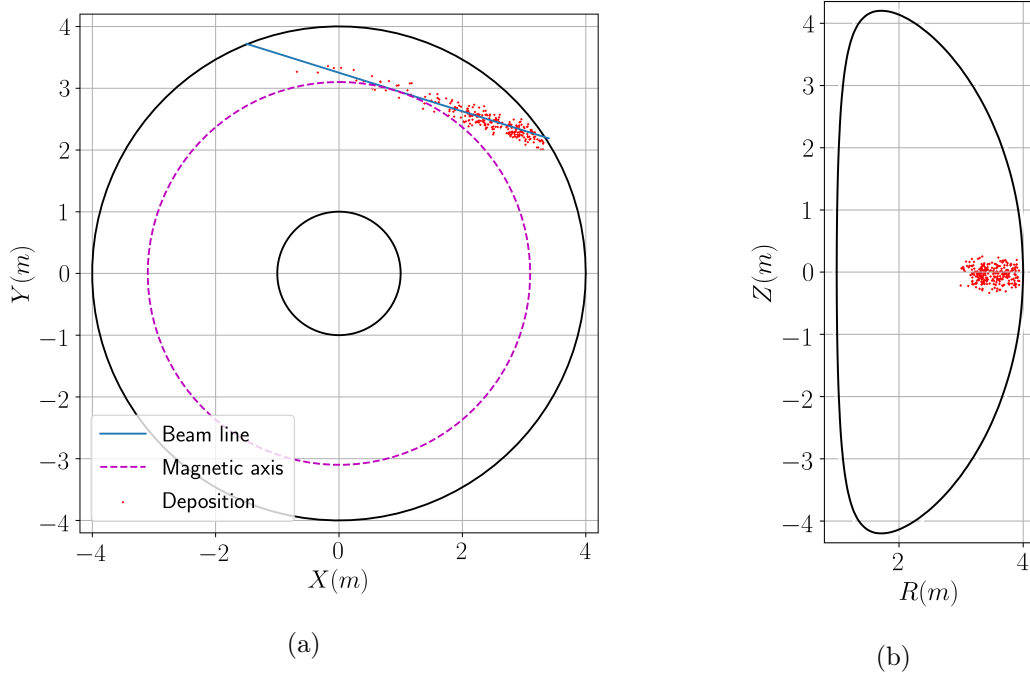


Figure 5.2: NUBEAM prediction for the marker deposition as seen from a) above and b) as a poloidal cross section for an 8MW 1MeV beam with  $R_t = 3.1\text{m}$  oriented in the horizontal plane.

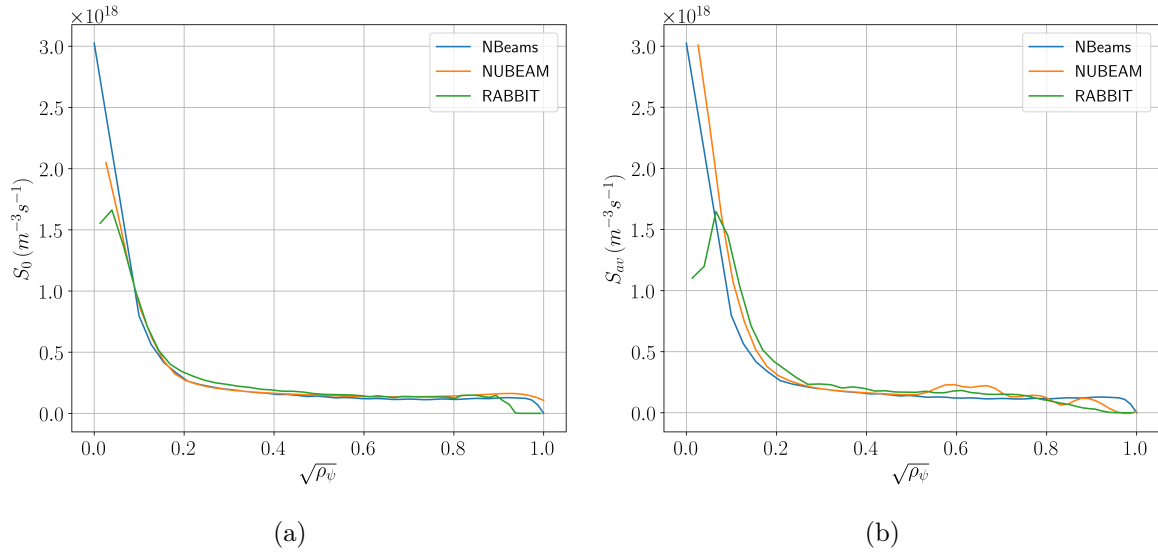


Figure 5.3: Comparison of NBeams, NUBEAM and RABBIT's prediction for the a) initial deposition, b) orbit average deposition of a 8MW, 1MeV beam with  $R_t = 3.1\text{m}$ . Note that NBeams doesn't perform an orbit average so  $S_0 = S_{av}$ .

NBeams matches NUBEAM reasonably well, but does over-predict the fast ion density and un-shielded current at the very core. Table 5.1 shows the integrated current predictions from

each code. RABBIT and NUBEAM agree to within 20%, and NBeams overestimates the total current by 40%. Looking at the current within  $\sqrt{\rho_\psi} = 0.2$ , all 3 codes agree within 10%. Even though RABBIT underestimates the current density at  $\sqrt{\rho_\psi} = 0$ , given the small surface area the impact on the total current is negligible. This indicates that the discrepancies mostly are due to the outer flux surfaces which will cause substantial differences in the total driven current because there is a larger surface area at the edge. NBeams largely over-predicts the current density above  $\sqrt{\rho_\psi} = 0.2$ . The shielding model of RABBIT and NUBEAM agree well, with NBeams overestimating the impact of the correction factor.

Parameter	NBeams	RABBIT	NUBEAM
$I_{\text{unshielded}}(\text{MA})$	1.18	0.97	0.82
$I_{\text{driven}}(\text{MA})$	0.88	0.64	0.55
$I_{\text{driven}}(\text{MA})$ for $\sqrt{\rho_\psi} < 0.2$	0.17	0.21	0.19
$\eta_{\text{shield}}$	0.74	0.66	0.68

Table 5.1: Comparison of NBeams, NUBEAM and RABBIT's prediction for the integrated currents and  $\eta_{\text{shield}}$  with an 8MW, 1MeV beam with  $R_t = 3.1\text{m}$

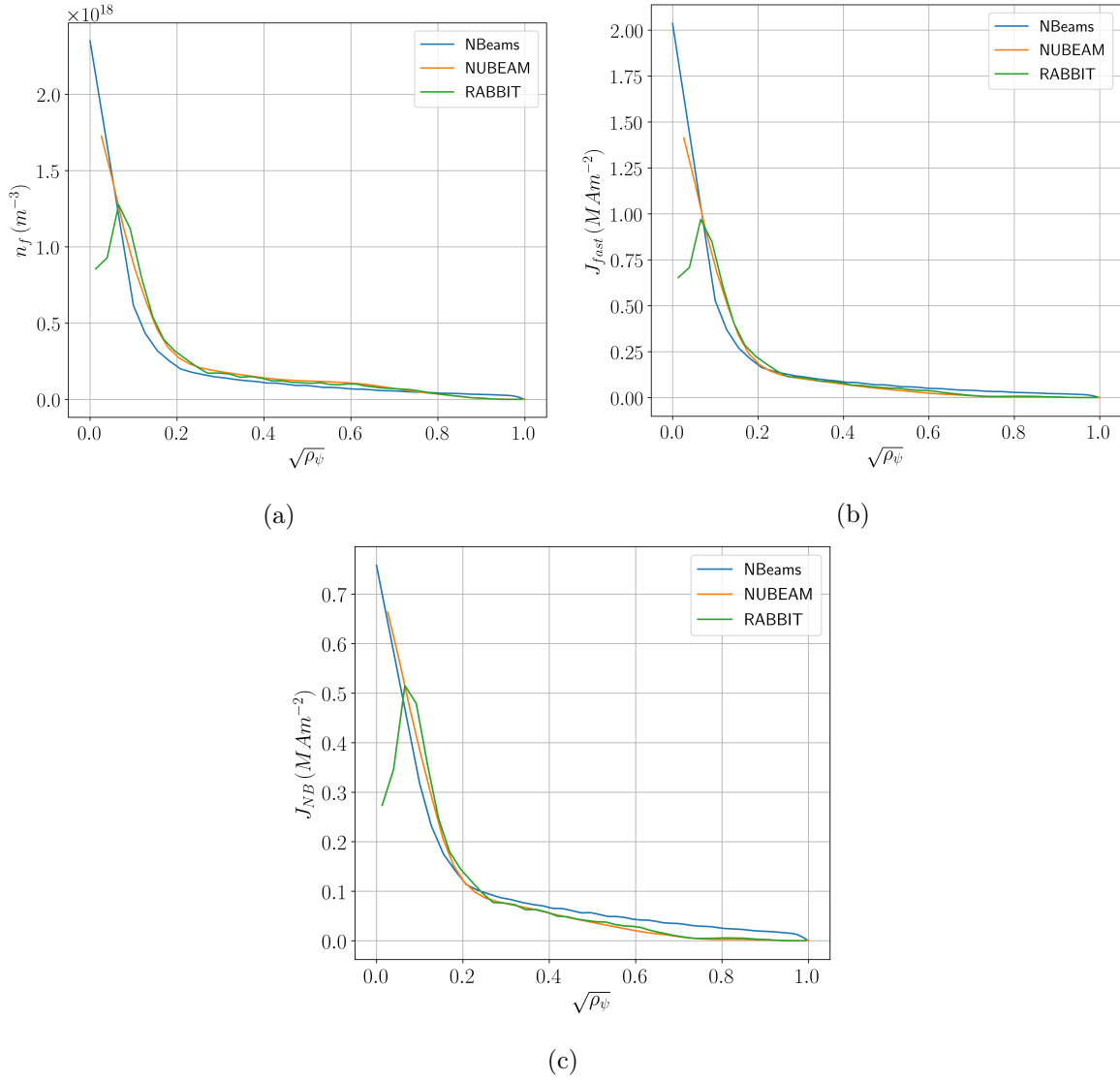


Figure 5.4: Comparison of NBeams, NUBEAM and RABBIT's prediction for the a) fast ion density, b) unshielded current and c) shielded current profile with a 8MW, 1MeV beam with  $R_t = 3.1\text{m}$ .

Overall, NBeams does reasonably well to predict the current density in the core and can be used to narrow down the parameter space when looking for suitable configurations. However, towards the edge it over-predicts the driven current. This indicates it may not perform well for the off axis current. RABBIT on the other hand does well when  $\sqrt{\rho_\psi} > 0.2$ , but at the very core there is a sharp drop in the deposition prediction which has a knock on impact on other predictions made.

### 5.1.2 Core beam penetration

The penetration depth of a 1MeV beam was examined for the different  $T_{e0}$ ,  $P_{\text{fus}} = 1.1\text{GW}$  scenarios examined in Chapter 4. The same 8MW beam was simulated for each  $T_{e0}$  scenario with  $I_p = 21\text{MA}$ . It was decided to use NBeams for this as it agreed well with NUBEAM for very small values of  $\sqrt{\rho_\psi}$ .

Figure 5.5a shows how the predicted current profile changes with temperature and as  $T_{e0}$  increases (and  $n_{e0}$  decreases) the driven current increases as expected. Given that the driven current will scale linearly with the power, it is possible to estimate the power needed in each scenario to achieve the required current density on axis. This is shown in Figure 5.5c and at the highest  $\langle n_{e20} \rangle$ , over 1GW would be necessary. To understand why the power increases exponentially, Figure 5.5b shows where the beam power is being deposited and at the highest densities the beam attenuation is so large that all the power is deposited at the edge. Thus the required power to achieve the necessary core current density becomes prohibitively large. Moreover, a majority of the current needs to be driven off axis so if  $P_{\text{aux}} < 100\text{MW}$  is required, then the power for the core current needs to be significantly lower than this. If a limit of 10MW is set for the core beam then the reactor must have  $\langle n_{e20} \rangle < 1.65\text{m}^{-3}$ , assuming  $E_b = 1\text{MeV}$ . Note the equilibrium defined in Table 4.2 has  $\langle n_{e20} \rangle = 1.54\text{m}^{-3}$ . Higher density operation would be possible if the beam energy were increased. At lower densities, it would be possible to use a lower energy beam, which may have a better current drive efficiency.

Figure 5.6 updates the plasma operation space of Figure 4.11a to exclude high density plasmas where NBeams calculations (at  $I_p = 21\text{MA}$ ) suggest that the required core auxiliary current needs  $> 10\text{MW}$  of NBI heating. This limit would of course change with different shaped density and temperature profiles. For example, a more peaked density profile would reduce the beam attenuation along its path, allowing for a higher  $\langle n_{e20} \rangle$ . Other technologies such as EBW, which does not have a density limit, may allow this limit to be entirely avoided.

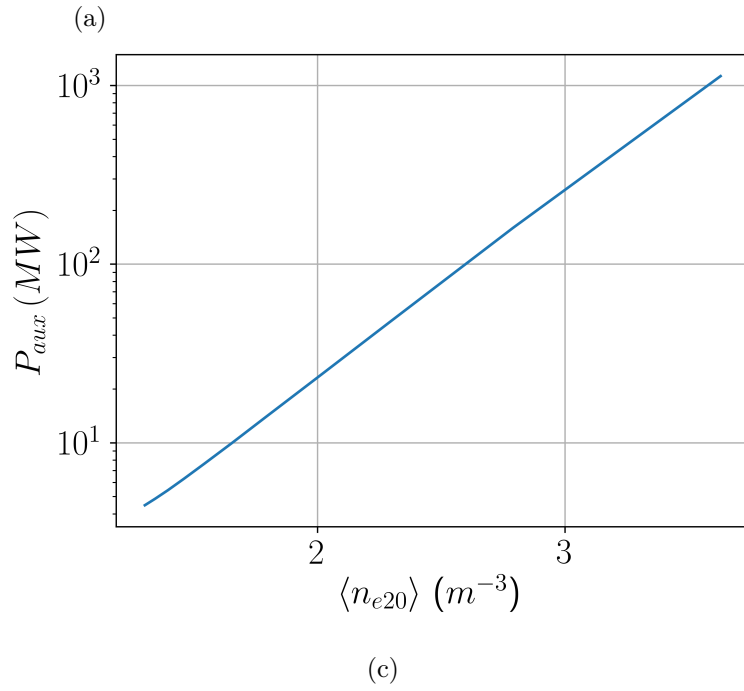
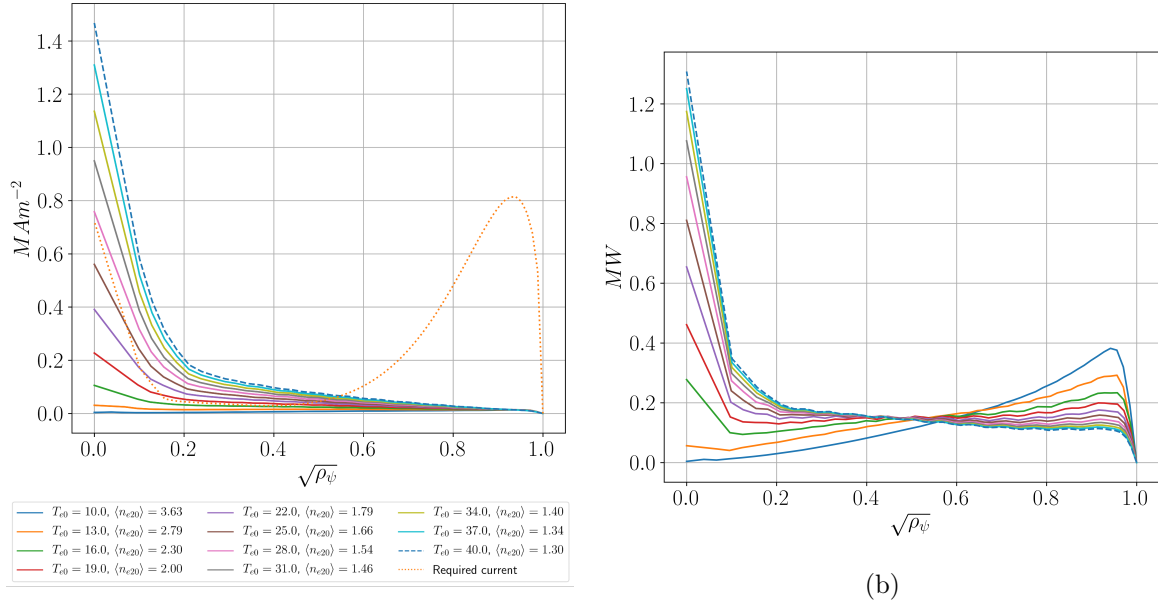


Figure 5.5: a)  $J_{\text{NBI}}$  b) power deposition with an 8MW 1MeV beam for a range of different core temperatures. The auxiliary power required to reach the necessary current density in the core is shown in c)

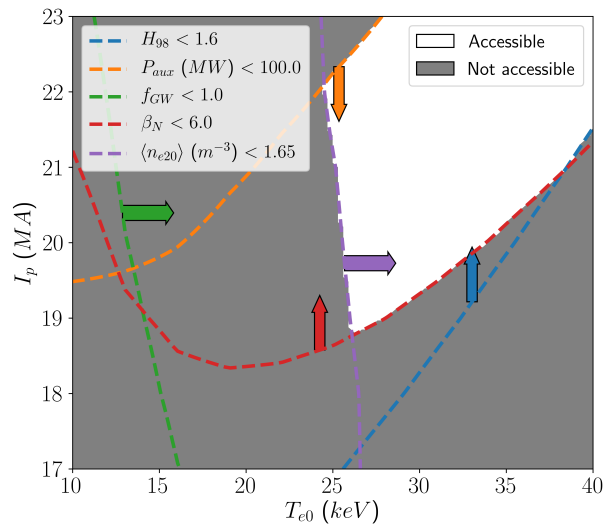


Figure 5.6: Available parameter space if the following restrictions are imposed:  $P_{aux} < 100\text{MW}$ ,  $H_{98} < 1.6$ ,  $f_{GW} < 1.0$  and  $\langle n_{e20} \rangle < 1.65$  and  $P_{fus} = 1.1\text{GW}$ . Here  $\eta_{CD} = 0.4\text{A m}^{-2}\text{W}^{-1}$  has been assumed and the arrows indicate the direction within the limit.

## 5.2 Off axis beam

A majority of the current needs to be driven away from the magnetic axis so it is crucial that the current drive efficiency is maximised here. Here it can be expected that orbit effects will play an important role due to the larger fraction of trapped particles. Once again the NBI configuration was set up with NBeams and a 90MW 500keV beam was found to be sufficient to drive 8.2MA off axis. The beam had a tangency radius  $R_t = 3.8\text{m}$  and an  $\eta_{NBeams} = 0.35\text{A m}^{-2}\text{W}^{-1}$  was achieved with the beam injected parallel to the horizontal plane. Figure 5.7 shows the current drive prediction. The exact profile of the current was not a perfect agreement, with NBeams predicting a broader profile than initially specified. Using an accurate NBI code, a more realistic  $J_{aux}$  can be specified to re-calculate the equilibrium. This can be iterated on until a converged self consistent equilibrium is defined.

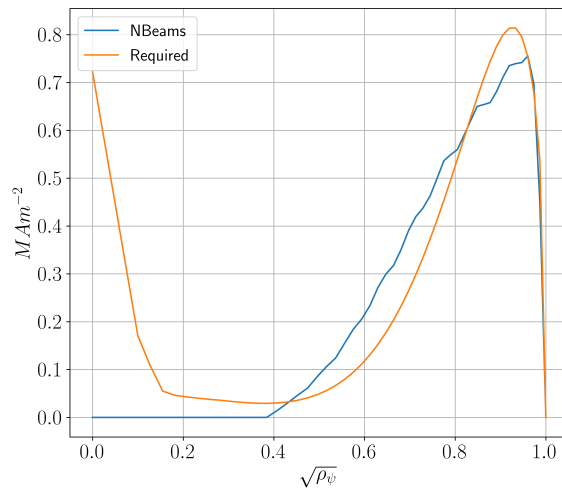


Figure 5.7: NBeams current drive prediction for an 90MW 500keV beam to drive the off axis current along with the required current as specified in SCENE.

Once again, NUBEAM and RABBIT were run with this configuration. The NUBEAM marker deposition is again shown from above and as a poloidal cross section in Figure 5.8.

It can be seen from Figure 5.9 that the overall agreement is much poorer. The initial deposition between NUBEAM and NBeams was found to be in good agreement. RABBIT however did not perform as well, with the beam being significantly shifted inwards. Figure 5.9b shows the orbit-averaged deposition and NUBEAM predicts a large inwards shift\*. This highlights the limitations of NBeams as this radial shift will have a significant impact on the final profiles. RABBIT does see an inwards shift but as  $S_0$  does not agree well it cannot be expected that

---

\*The profiles shift inwards due to the beam in co-injection. For a counter-injected beam the profile would shift radially outwards.

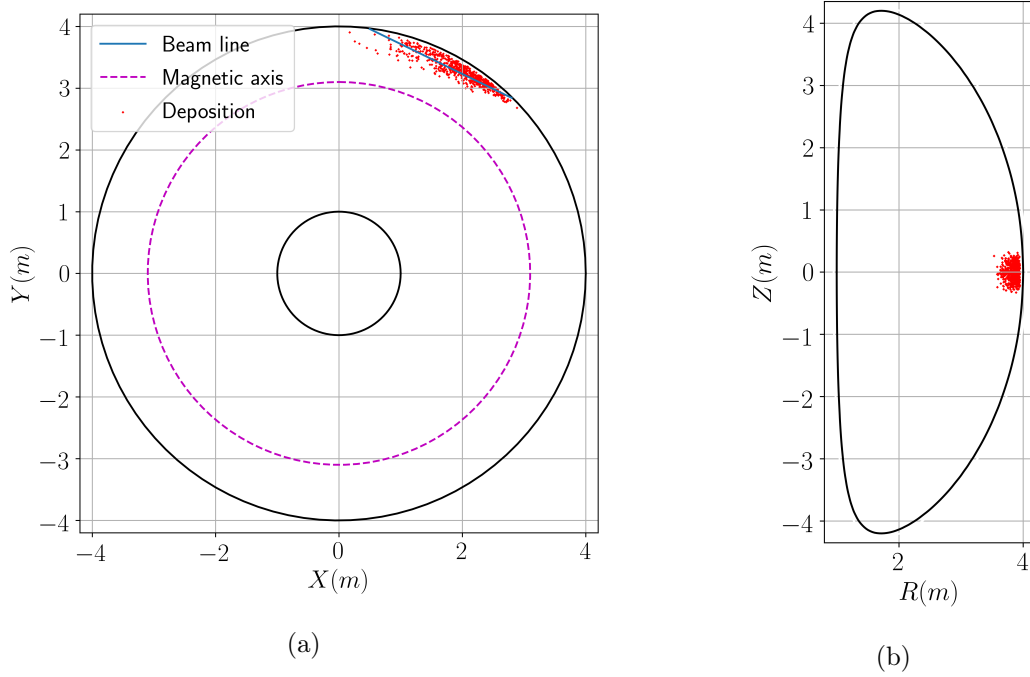


Figure 5.8: NUBEAM prediction for the marker deposition as seen from a) above and b) as a poloidal cross section for an 90MW 500keV beam with  $R_t = 3.8\text{m}$  oriented in the horizontal plane.

the  $S_{av}$  would match NUBEAM.

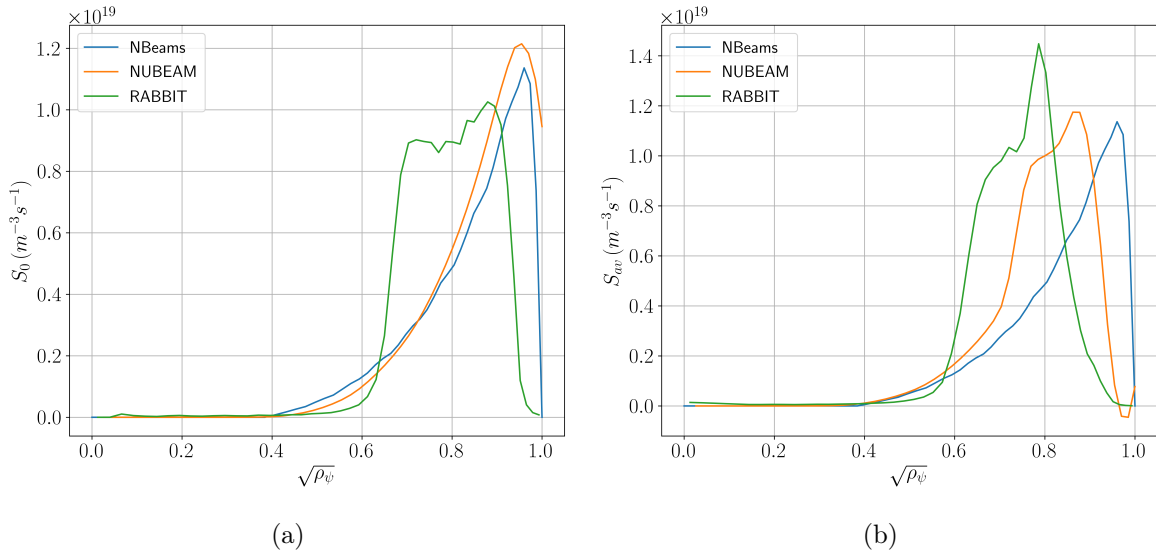


Figure 5.9: Comparison of NBeams, NUBEAM and RABBIT's prediction for the beam's a) initial deposition, b) orbit average deposition with a 90MW, 500keV beam with  $R_t = 3.8\text{m}$ . Note for NBeams doesn't perform an orbit average so  $S_0 = S_{av}$ .

The radial shift becomes very clear when examining  $n_f$ , shown in Figure 5.10a. There is

a large difference between NUBEAM and NBeams. RABBIT performs slightly better, but agreement is not as good as the on axis beam. The largest difference is in the current as NBeams significantly over-predicts the un-shielded and driven current. Table 5.2 outlines the current drive predictions for this beam configuration. NBeams overestimates the current by a factor of 3. RABBIT only does slightly better with a factor of 1.6.

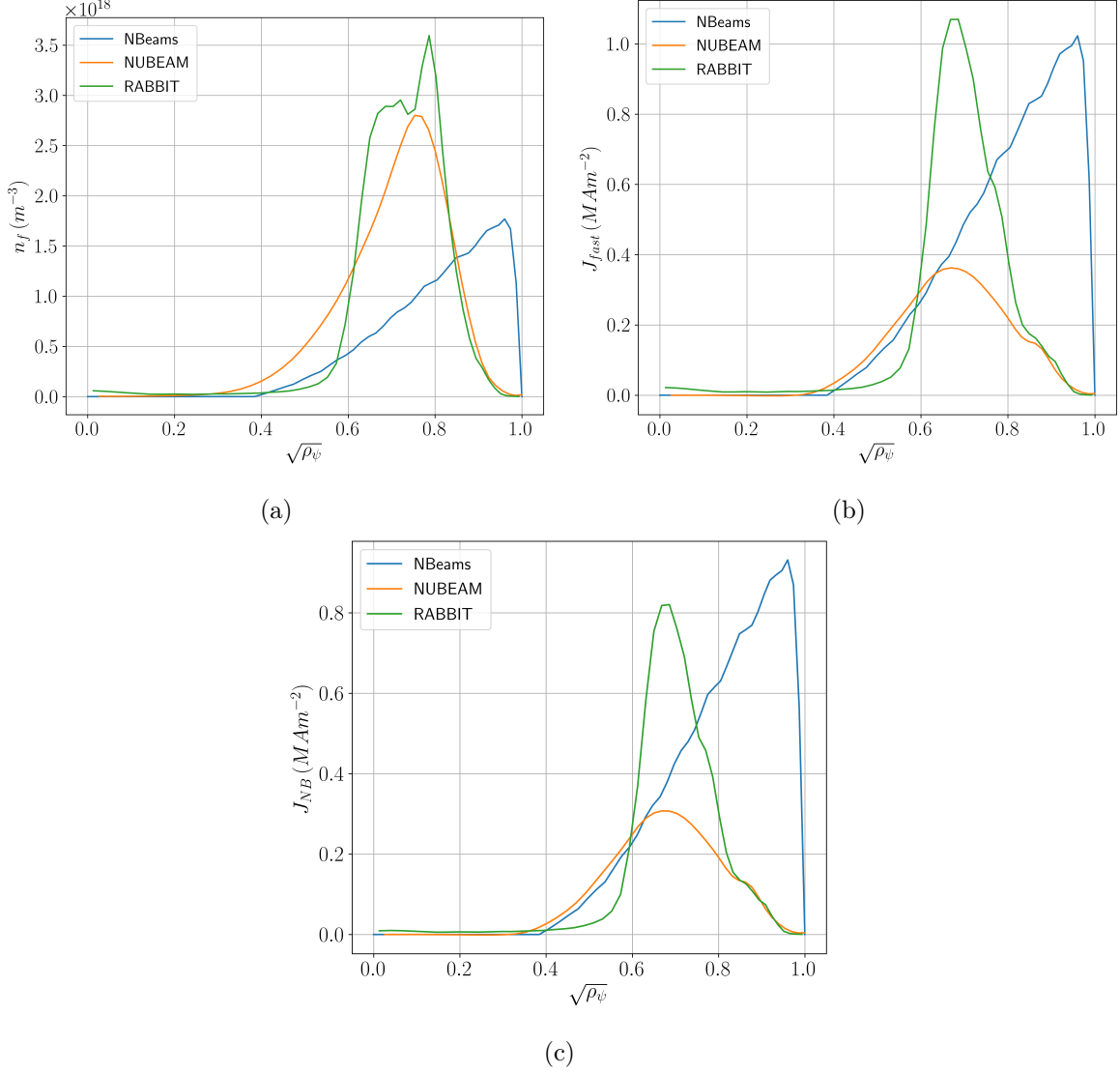


Figure 5.10: Comparison of NBeams, NUBEAM and RABBIT's prediction for the a) fast ion density, b) unshielded current and c) shielded current with a 90MW, 500keV beam with  $R_t = 3.8m$ .

By examining the steady state fast ion distribution it becomes clearer to why this is the case. Figure 5.11 shows the distribution function predicted by each code at  $\sqrt{\rho_\psi} = 0.74$ , note the different scales on the colour bars. NUBEAM is able to capture the trapped particle behaviour and there is a significant distribution of particles with negative pitch. Even at the

Parameter	NBeams	RABBIT	NUBEAM
$I_{\text{unshielded}}(\text{MA})$	9.39	5.47	2.99
$I_{\text{driven}}(\text{MA})$	8.21	4.19	2.58
$\eta_{\text{shield}}$	0.87	0.77	0.86
$\eta_{\text{NBI}}(\text{A m}^{-2} \text{W}^{-1})$	0.35	0.11	0.18

Table 5.2: Comparison of NBeams, NUBEAM and RABBIT’s prediction for the integrated currents,  $\eta_{\text{shield}}$  and  $\eta_{\text{NBI}}$  with a 90MW, 500keV beam with  $R_t = 3.8\text{m}$  parallel to the horizontal plane.

birth energy of 500keV, there are particles with negative pitch. As these particle spend part of their orbit going in the opposite direction to the current and field, they will reduce the overall driven current. NBeams does not perform any orbit tracking and assumes all particles are born passing meaning it is not possible to account for this effect. Moreover, it assumes a purely toroidal field which leads to an over-estimation of the birth pitch  $\xi_b$ . RABBIT will track the particle for a single orbit so should be able to account for particles born trapped, but would not be able to account for passing particles that become trapped as they slow down or vice versa. RABBIT does display some of the trapped particle behaviour. A peak at the birth energy with negative pitch can be seen as well as a peak at  $\xi = 0.5$ . But does not seem to fully capture the extent of the trapped particle as the number of particles at negative pitch seem to be under-estimated, which explains the over-estimation in the current.

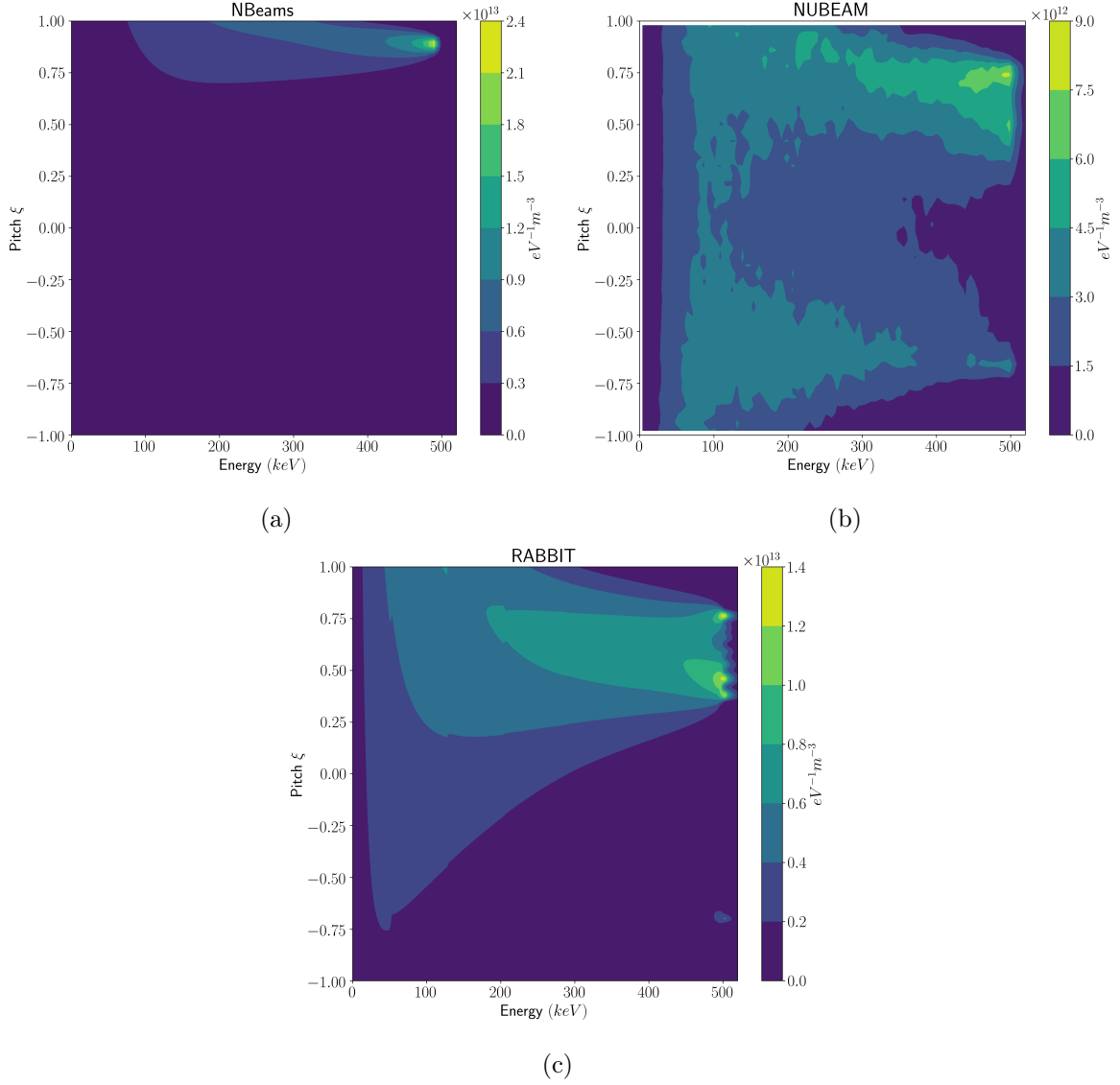


Figure 5.11: Fast ion distribution function for a) NBeams b) NUBEAM and c) RABBIT at  $\sqrt{\rho_\psi} = 0.74$  for the off axis beam aligned with the horizontal plane.

### 5.2.1 Field-aligned beam

This beam configuration previously outlined is not suitable for reactor relevant scenarios as an  $\eta_{\text{NBI}} = 0.11 \text{Am}^{-2} \text{W}^{-1}$  is predicted by NUBEAM. As discussed in Chapter 4, this is too low. Figure 4.11b would indicate that no scenario would be possible given the limitations imposed. For this configuration, NUBEAM finds  $\xi_b = 0.7$ , which is equivalent to the  $B$ -field pitch. If the beam were angled to be aligned with the field such that  $\xi_b \sim 1.0$  then fewer particles would be trapped. A simulation was performed where the beam was angled such that it crossed the mid-plane at an angle of  $\cos^{-1}(\xi_b) = 45^\circ$ . Figure 5.12a shows the NUBEAM deposition from above, which looks similar to the flat beam. Figure 5.12b shows the side on

view and the vertical spread of the beam can be seen much more clearly here. The resulting deposition profiles predicted by RABBIT and NUBEAM are shown in Figure 5.13. The flat beam simulated by NBeams is also shown. As fewer particles are born trapped, the inward shift is less extreme. The deposition predicted by RABBIT and NUBEAM are in much better agreement here, though RABBIT has a slightly stronger inwards shift. This in turn impacts the fast ion density and currents, shown in Figure 5.14, where the profiles are less peaked and shifted inwards. NBeams is not capable of modelling angled beams, but predicts a similar result to RABBIT and NUBEAM. This suggests that the NBeams prediction is a reasonable proxy for result when the beam is aligned with the field.

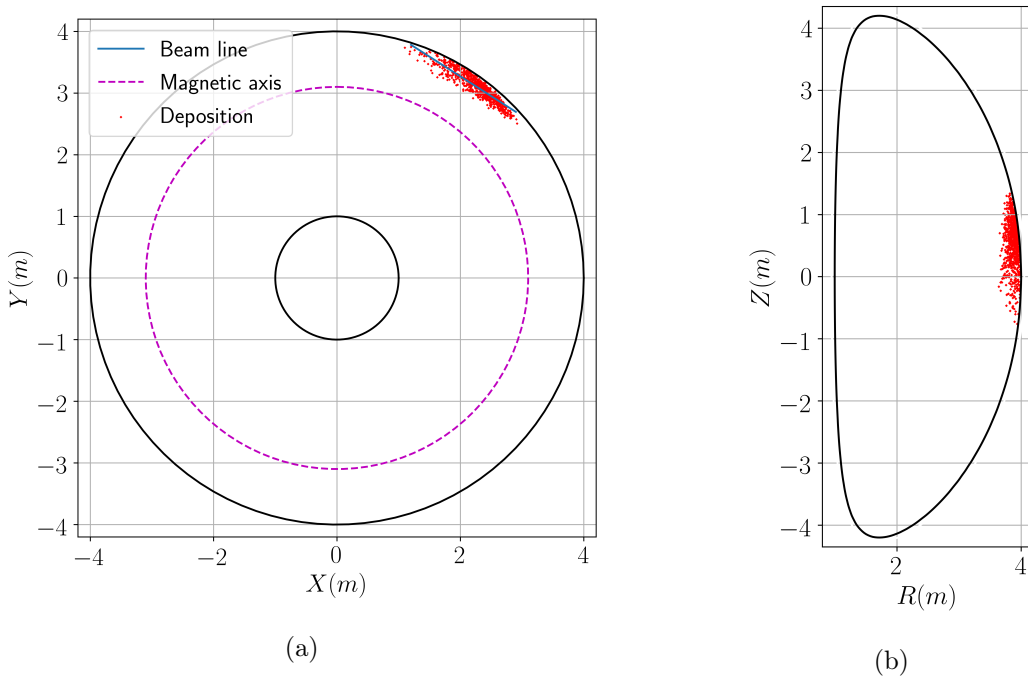


Figure 5.12: NUBEAM prediction for the marker deposition as seen from a) above and b) as a poloidal cross section for a 90MW 500keV beam with  $R_t = 3.8\text{m}$  angled at  $45^\circ$  to the horizontal plane.

The fast ion distribution function is shown in Figure 5.15 and illustrates that the birth pitch is very close to 1 for both NUBEAM and RABBIT, resulting in no significant trapping and allowing for a large current to be driven, shown in Table 5.3. The resulting current drive efficiency was found to be  $\eta_{NUBEAM} = 0.34\text{A m}^{-2}\text{W}^{-1}$  and  $\eta_{RABBIT} = 0.35\text{A m}^{-2}\text{W}^{-1}$  which is very similar to the predictions made for ITER. NBeams (which can't model angled beams) has a similar result, which further indicates it's potential uses as a proxy for when the beam is aligned with the field. Importantly, these predictions are in the acceptable range of current drive efficiencies necessary to fulfil the requirements outlined in Chapter 4. This tells

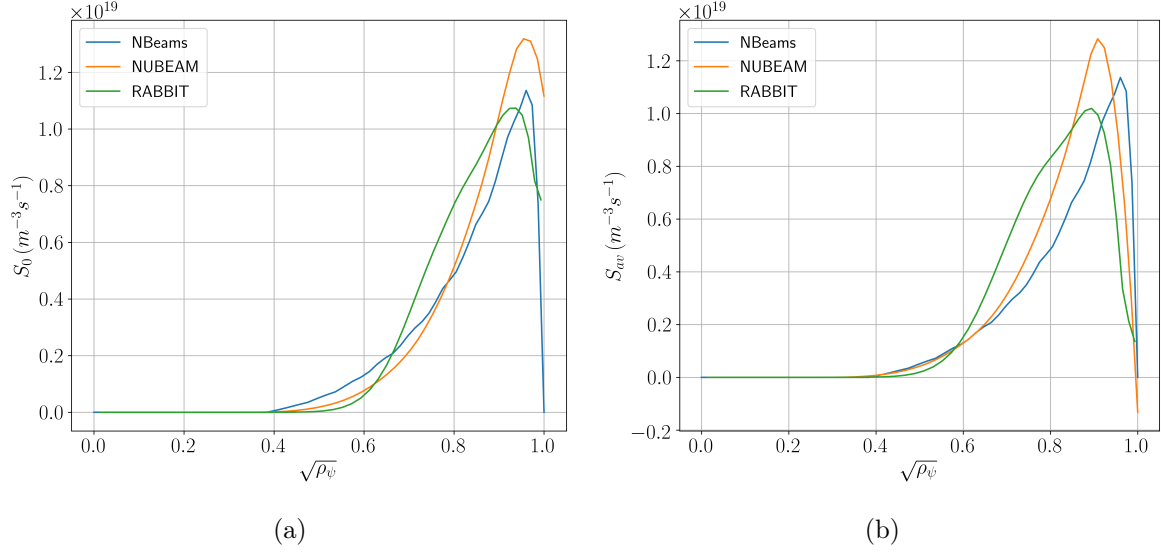


Figure 5.13: NUBEAM and RABBIT prediction for a) initial and b) orbit averaged deposition with a 90MW 500keV beam angled at  $45^\circ$  such that it is aligned with the magnetic field. Note NBeams is included but cannot model angled beams.

us that the off axis beam must be aligned with the field to ensure a reasonable current drive efficiency is achieved.

Parameter	NBeams	RABBIT	NUBEAM
$I_{\text{unshielded}}(\text{MA})$	9.39	9.05	10.65
$I_{\text{driven}}(\text{MA})$	8.21	7.91	8.21
$\eta_{\text{shield}}$	0.87	0.87	0.77
$\eta_{\text{NBI}}(\text{A m}^{-2} \text{W}^{-1})$	0.35	0.34	0.35

Table 5.3: Comparison of NBeams, NUBEAM and RABBIT's prediction for the integrated currents,  $\eta_{\text{shield}}$  and  $\eta_{\text{NBI}}$  with a 90MW, 500keV field-aligned beam with  $R_t = 3.8\text{m}$

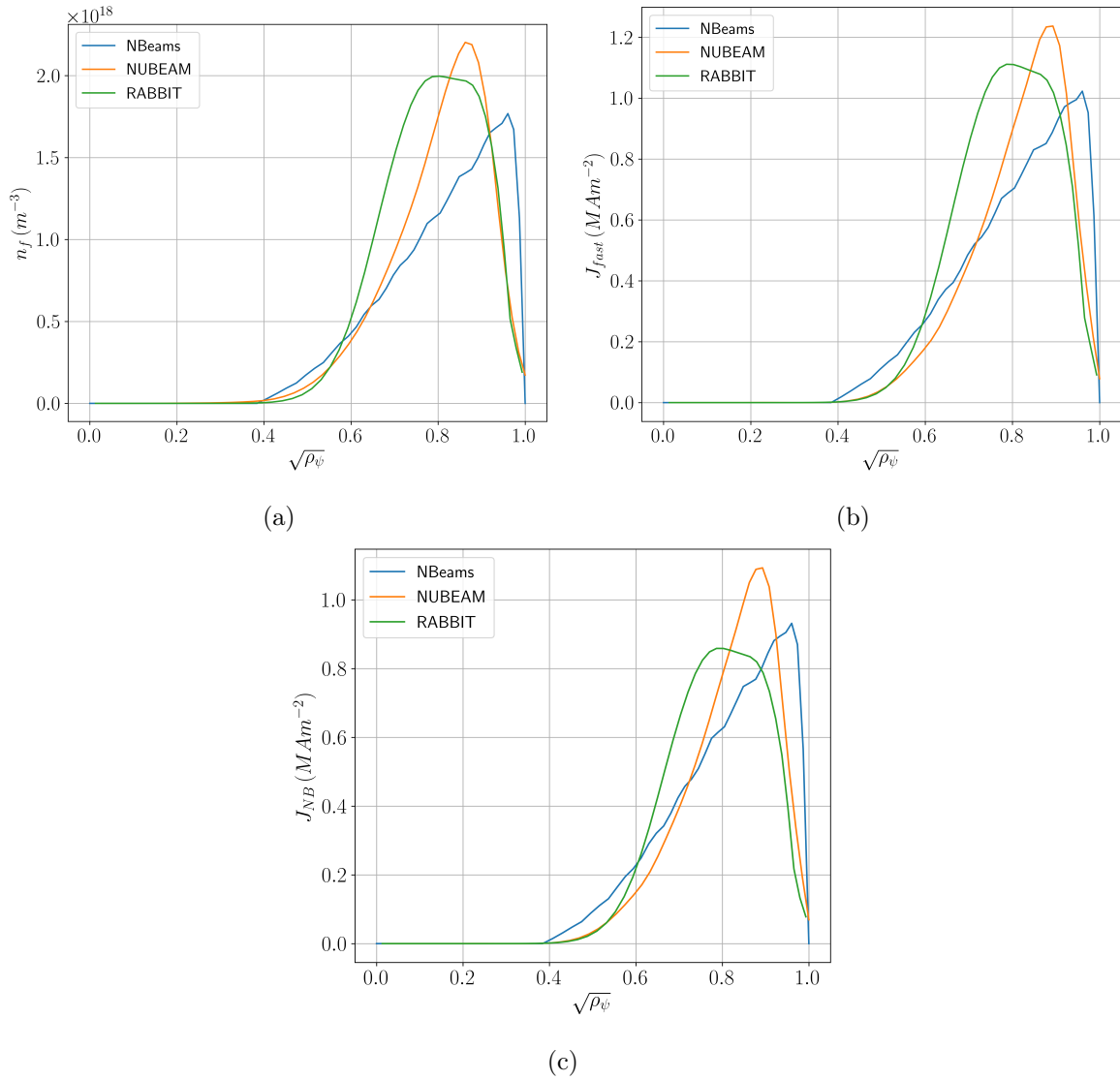


Figure 5.14: NUBEAM and RABBIT prediction for the a) fast ion density, b) unshielded current and c) shielded current with a 90MW 500keV beam angled at  $45^\circ$  such that it is aligned with the magnetic field. Note NBeams is included but cannot model angled beams.

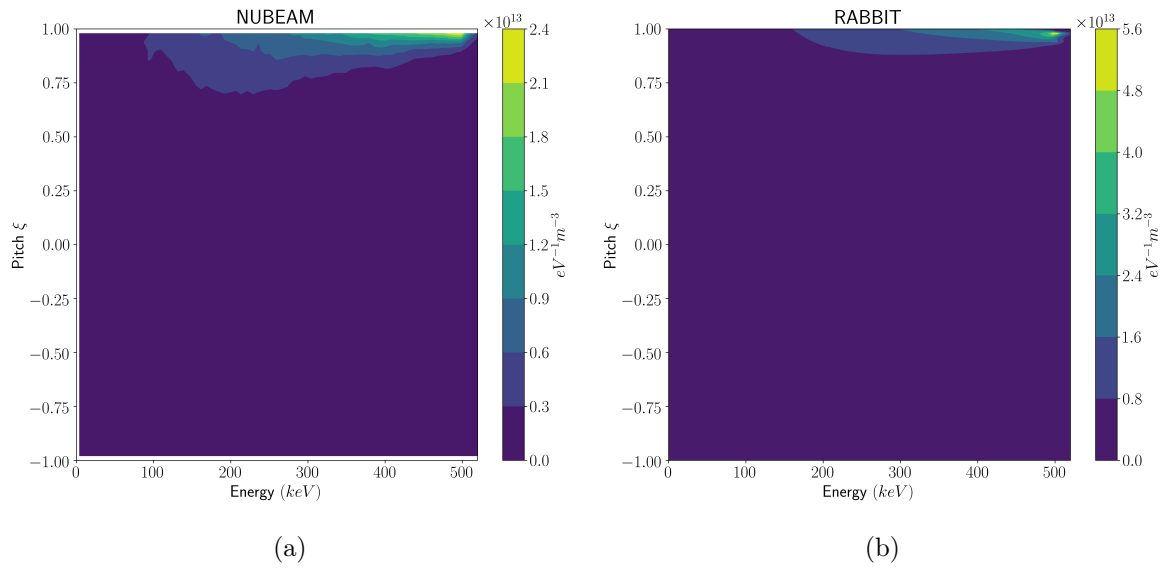


Figure 5.15: Fast ion distribution function for a) NUBEAM and b) RABBIT at  $\sqrt{\rho_\psi} = 0.74$  with a beam aligned to the magnetic field.

### 5.3 Temperature/Density dependence on $\eta_{\text{NBI}}$

Using the angled off axis beam configuration, the impact of the density and temperature on  $\eta_{\text{NBI}}$  was examined using NUBEAM. With the same magnetic equilibrium, the temperature and density profiles were inconsistently changed to isolate their impact on the current drive efficiency. This ensured that the trapping effects were identical for each simulation.

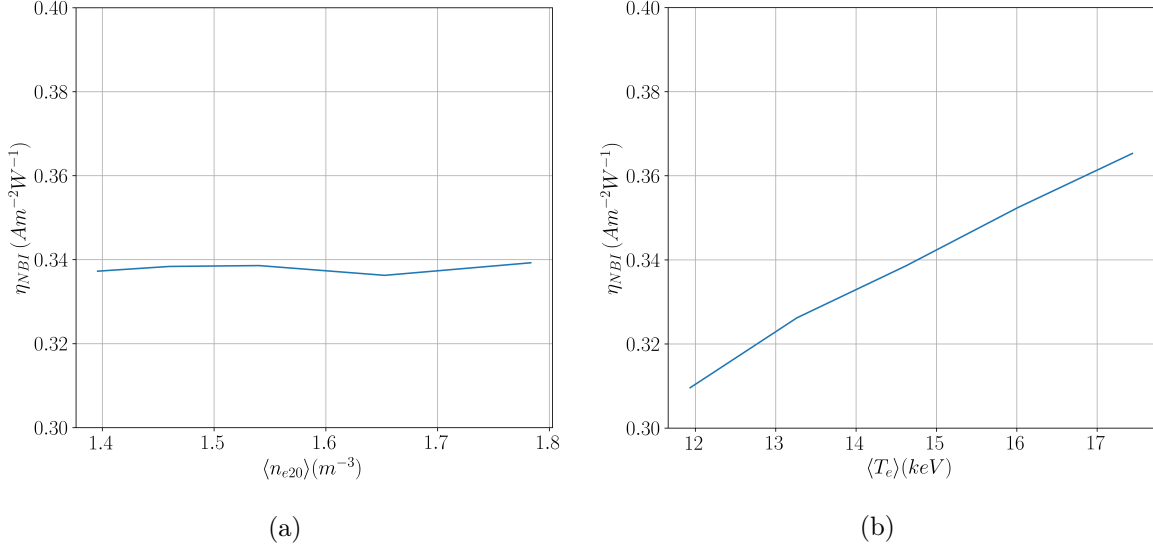


Figure 5.16:  $\eta_{\text{NBI}}$  for an angled 90MW, 500keV beam for a) a scan in  $\langle n_{e20} \rangle$  at fixed  $\langle T_e \rangle = 14.8\text{keV}$  and b) a scan in  $\langle T_e \rangle$  at fixed  $\langle n_{e20} \rangle = 1.54\text{m}^{-3}$  predicted by NUBEAM.

First, using the  $T_{e0} = 28\text{keV}$  profile (which has  $\langle T_e \rangle = 14.8\text{keV}$ ), the density was varied. The density profiles from  $T_{e0} = 21\text{keV}$  to  $34\text{keV}$  cases were used and the resulting current drive efficiency is shown in Figure 5.16a. It appears that  $\eta_{\text{NBI}}$  captures the density variation well. A similar scan was done using the different temperatures profiles with a fixed density profile from the baseline case. Figure 5.16b shows that there is a weak temperature dependence on temperature. It has been previously found that current drive efficiency was proportional to  $1/\langle T_e \rangle$  dependence [159]. But here that is found to over-compensate the impact of the temperature shown in Figure 5.17a.  $\eta_{\text{NBI}} \propto 1/\sqrt{\langle T_e \rangle}$  was found to better account for the temperature dependence. Defining a modified current drive efficiency as

$$\eta_{\text{CD}}^* = \frac{I_{\text{aux}} \langle n_{e20} \rangle R_{\text{maj}}}{P_{\text{aux}}} \sqrt{\frac{T_{\text{ref}}}{\langle T_e \rangle}} \quad (5.2)$$

where  $T_{\text{ref}}$  is a reference temperature taken to be  $T_{\text{ref}} = 15\text{keV}^\dagger$ . Figure 5.17b illustrates  $\eta_{\text{CD}}^*$  and it can be seen that  $\eta_{\text{NBI}}^* = 0.34\text{Am}^{-2}\text{W}^{-1}$  fits these NUBEAM simulations well.

<sup>†</sup>  $\sqrt{T_{\text{ref}}/\langle T_e \rangle}$  was used to preserve the units of  $\eta_{\text{CD}}$

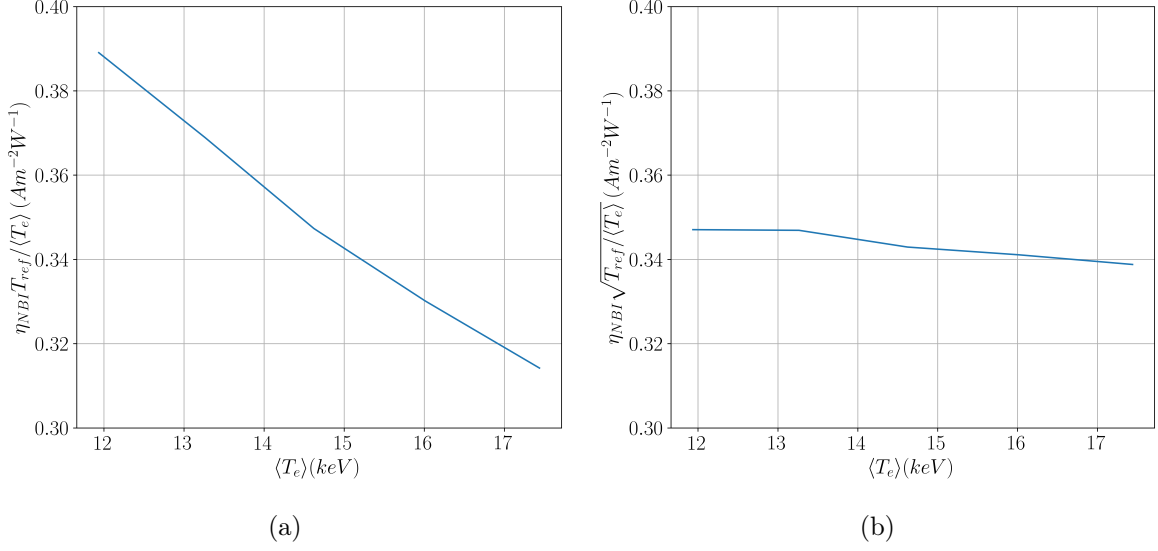


Figure 5.17: a)  $\eta_{\text{NBI}} \frac{T_{\text{ref}}}{\langle T_e \rangle}$  and b)  $\eta_{\text{NBI}} \sqrt{\frac{T_{\text{ref}}}{\langle T_e \rangle}}$  for an angled 90MW, 500keV beam for a scan in  $\langle T_e \rangle$  at fixed  $\langle n_{e20} \rangle = 1.54 \text{m}^{-3}$  predicted by NUBEAM. Here  $T_{\text{ref}} = 15 \text{keV}$ .

The overall impact would be to close off the low temperature regime and open up the higher temperature regime. Using this redefined current drive efficiency it is possible to examine the available space as has been done previously. Figure 5.18 illustrates how the baseline scenario lies within the accessible range.

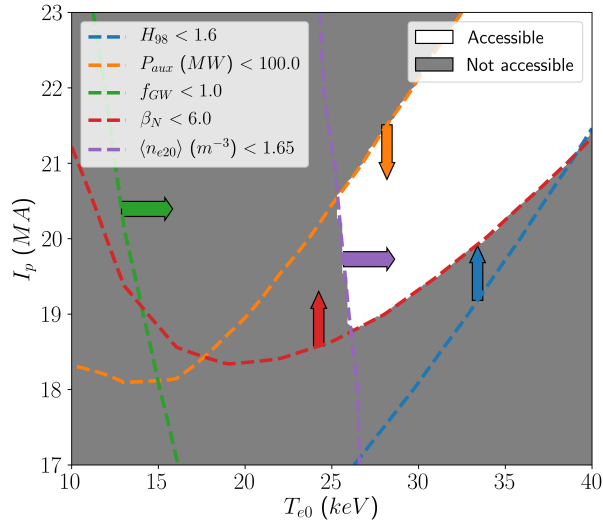


Figure 5.18: Available parameter space if the following restrictions are imposed:  $P_{\text{aux}} < 100 \text{MW}$ ,  $H_{98} < 1.6$ ,  $f_{\text{GW}} < 1.0$  and  $\langle n_{e20} \rangle < 1.65$  and  $P_{\text{fus}} = 1.1 \text{GW}$ . Here  $\eta_{\text{CD}}^* = 0.34 \text{A m}^{-2} \text{W}^{-1}$  has been assumed and the arrows indicates the direction that lies within the limit imposed.

## 5.4 Final beam configuration

Combining the two beam scenarios outlined, a complete NBI configuration can be created. In total 94MW of NBI power is simulated which drives 8.2MA of current. The on axis 1MeV beam needed 8MW and the off-axis 0.5MeV beam power was reduced to 86MW to match the required current. Now that an accurate  $J_{\text{aux}}$  has been specified, it can be compared to the specified profile in SCENE, shown in Figure 5.19a. The NUBEAM profile is shifted inwards compared to the specified profile. It is possible to use the profile predicted by NUBEAM in SCENE to re-calculate the full equilibrium. It would be difficult to shift the beam further outwards as it is already very close to the edge of the plasma. The energy of the beam could be reduced, which would generate more momentum, but would increase the power needed. Fitting the  $J_{\text{aux}}$  shown in Figure 5.14c to Equation 3.7 results in a  $\chi_1 = 1.20$  and  $\chi_2 = 3.85$ . Doing the same for the core current drive results in  $\chi_0 = 67^\ddagger$ . A new  $J_{\text{aux}}$  was specified and the equilibrium was re-calculated. With the updated equilibrium the NUBEAM calculation was repeated and is shown in Figure 5.19b. The agreement is much better here and this can be defined as our final beam configuration.

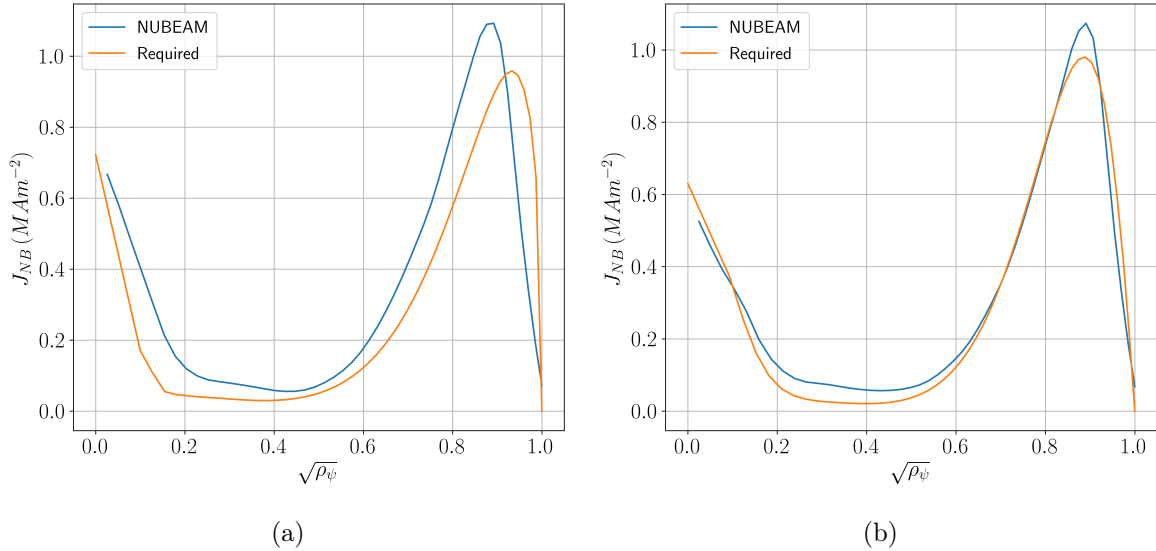


Figure 5.19: Comparing the a) initial specified  $J_{\text{aux}}$  profile and the b) NUBEAM matched  $J_{\text{aux}}$  to the NUBEAM predictions of the final beam configuration.

<sup>‡</sup>Modifying  $J_{\text{aux}}$  predominantly changes  $\hat{s}$  and  $q$ , which is still monotonic, but as the change is not large, it has little impact on the other global plasma parameters, meaning the accessible parameter space is largely unchanged.

### 5.4.1 Heating profiles

The total heating profile can also be examined for this case. NUBEAM is also able to track the fusion  $\alpha$ 's so their heating contribution to the different plasma species is shown in Figure 5.20. As most of the NBI is needed for off axis current drive, its heating will be focused at the edge. This leaves little flexibility for core heating, which is dominated by the fusion  $\alpha$ 's. These heating profiles can be used in a 1.5D transport simulation which is the eventual goal of this research. Table 5.4 outlines where the power is going in the reactor and the ions are being heated by 102MW and the electrons by 198MW. The dominant electron heating is due to the beam and  $\alpha$  energy being well above the critical energy  $E_c$ .

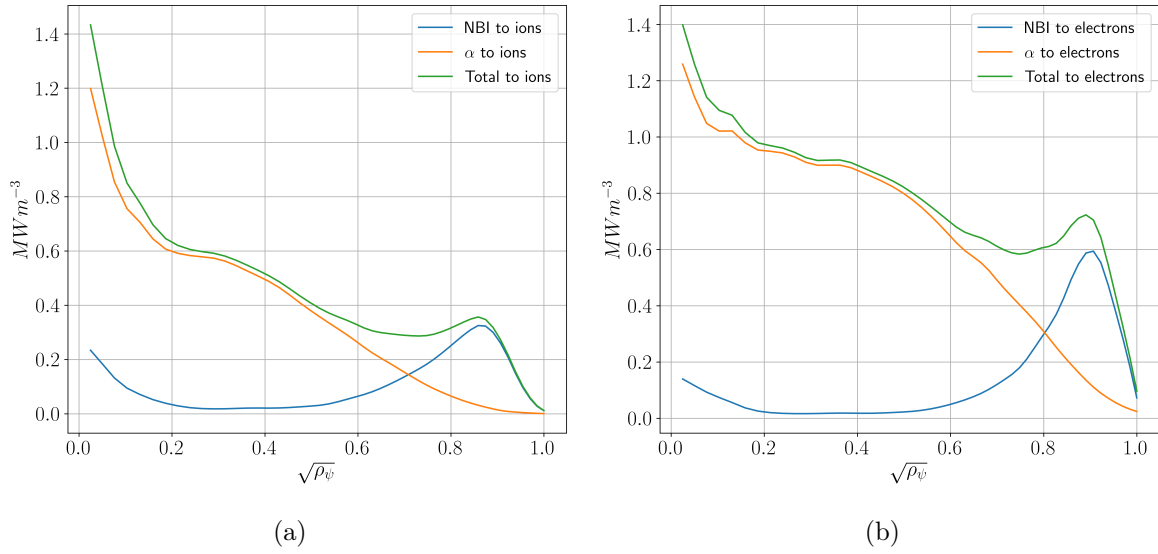


Figure 5.20: Heating profiles for the a) ions and b) electrons from the NBI and Fusion  $\alpha$ 's in the BurST scenario.

It is also possible to examine the ratio of the volume averaged fast ion pressure to the thermal species and it was found that  $\langle p_{\text{fast}} \rangle / \langle p_{\text{thermal}} \rangle = 0.18$ . As mentioned in Chapter 4, the fast ions were not included in the equilibrium calculation, so future work should look to include their impact.

Parameter	NBI	Fusion $\alpha$
Power to ions (MW)	33.6	68.7
Power to electrons (MW)	49.4	148.6
Thermalised (MW)	2.3	1.7
Prompt losses (MW)	0.1	5.4
Shine-through (MW)	4.4	N/A
Charge-exchange losses (MW)	4.3	1.6
Total Power (MW)	94.0	226.0

Table 5.4: Break down of the power deposition from the NBI and  $\alpha$  heating to the different species in BurST

## 5.5 Summary

This chapter has examined the feasibility of using NBI to drive the auxiliary current in BurST. Using NUBEAM a beam configuration was identified that was able to drive the current whilst keeping  $P_{\text{aux}} < 100\text{MW}$ . A current drive efficiency of  $\eta_{\text{NBI}} = 0.34\text{A m}^{-2}\text{W}^{-1}$  was achieved. It was necessary to angle the off axis beam such that it is aligned with the magnetic field. Furthermore, requiring core access imposes the limit  $\langle n_{e20} \rangle < 1.65\text{m}^{-3}$  if a maximum beam energy of 1MeV is assumed.

NUBEAM was also used to benchmark real-time capable codes NBeams and RABBIT. The deposition model in NBeams is quite accurate and its predictions are reasonably valid in the regime where trapped particle effects are not significant, like in the core. But as most of the current is driven off-axis suggesting it may be of limited use in a BurST regime. However, it gives a reasonable prediction of the driven current if it is compared to a beam aligned with the field such that orbit effects are less significant. RABBIT is able to capture some of the orbit effects but under-estimates the trapping. However it also performs significantly better when the beam is aligned. The deposition model of RABBIT does not agree as well with NUBEAM in the core which is where development may be necessary. Both NBeams and RABBIT can be used to create a reasonable NBI configuration, which can then be further refined using NUBEAM.

When varying the density profile,  $\eta_{\text{CD}}$  captured the behaviour of NUBEAM well. However, when varying the temperature profile,  $\eta_{\text{CD}}$  was insufficient in modelling the current drive efficiency, but a modification of  $\eta_{\text{CD}} \rightarrow \eta_{\text{CD}}^* = \eta_{\text{CD}} \sqrt{\frac{T_{\text{ref}}}{\langle T_e \rangle}}$  was found to capture the variation better. This was then used to update the available operating space of BurST, with the baseline

scenario still being within the specified restrictions.

Once built, the beams will have flexibility in the injection energy and power, but there is limited flexibility in the beam tangency radius and angling. DIII-D has an NBI system that was able to change the vertical angle by  $16^\circ$  [160]. Furthermore, any level of flexibility will require a larger beam port, taking up valuable tritium breeding space. This may limit the scenarios that could be explored in such a device.

Future work would need to examine the current drive efficiency of RF methods as they can help to ease some of the limits obtained here. If EBW can be utilised for the core current drive then the core penetration limit can be ignored entirely, but this may come at the cost of more auxiliary power depending on its current drive efficiency. The next chapter will examine the impact of flow shear on the turbulence and neutral beams are a source of momentum so will impact the rotation profile. Most of the power will be focused off axis and previous experiments at DIII-D have found that off axis NBI has minimal impact on the core rotation profile [161], suggesting that the momentum driven by the off axis beam will not get transported inwards. Therefore any rotation within  $\rho_\psi < 0.8$  will be driven by the on axis beam, though the off-axis beam may drive significant rotation in the pedestal.

The momentum confinement time in steady state would be given by the ratio of the plasma momentum content and the applied torque which can be approximated by

$$\tau_\varphi \approx \frac{m_i n_i v_\varphi R_0}{S_{av} m_b v_b R_t} \quad (5.3)$$

where  $v_\varphi$  is the toroidal rotation. Assuming that  $\tau_\varphi \sim \tau_E$  [162], then an approximation for  $v_\varphi$  can be made. For this scenario, a Mach number of  $v_\varphi/c_s = 0.13$  was found on axis, corresponding to a toroidal angular frequency of  $\omega_\varphi = 0.06c_s/a$ . Assuming a linear rotation profile, at  $\rho_\psi = 0.5$  the  $E \times B$  shearing rate will be  $0.009c_s/a$ , which is an order of magnitude lower diamagnetic flow shear  $\gamma_{\text{dia}} = 0.08c_s/a$ , described in Chapter 6. This suggests that the rotation driven by the NBI can be largely ignored as the plasma rotation will be dominated by the diamagnetically driven component. However, to accurately determine the rotation profile will require momentum transport modelling which is notoriously difficult [163].

## Chapter 6

# Optimisation of equilibrium parameters using linear gyrokinetics

This chapter will explore the linear micro-instabilities that arise in a high  $\beta$  ST. These instabilities are the drivers of turbulence so it is crucial to understand what impacts them in order to design a high performance machine. Gyrokinetics has been widely used to examine the turbulent transport in tokamaks and has predicted fluxes that have reasonably matched experimental data [84, 164]. There are still improvements to be made with these models, such as a better representation of fast ion physics and non-local effects [165], but it is currently the best tool available to inform predictive transport modelling which is fundamental for reactor design.

The aim of this chapter is to understand how the choices made in the previous chapters relating to magnetic field and the density, temperature and current profiles impact the linear micro-stability. This will inform us of directions to take the equilibrium to minimise the turbulent transport. To reiterate, this work will not focus on whether it is possible to reach the prescribed profiles, but purely on whether a transport steady state solution with the required fusion performance is possible.

This chapter will utilise GS2 as the initial value solver unless stated otherwise, though to be consistent with the results presented in Chapter 7, the CGYRO normalisations are used and are shown in Table 6.1.

The radial and bi-normal wavenumbers,  $k_x$  and  $k_y$  are normalised by the Larmor radius  $\rho_s$ . With this convention  $\rho_s$  is defined as

$$\rho_s = \frac{c_s}{eB_{\text{unit}}/m_D c} \quad (6.1)$$

Quantity	Unit	Description
length	$a_{min}$	minor radius
mass	$m_D$	deuterium mass
density	$n_e$	electron density
temperature	$T_e$	electron temperature
velocity	$c_s = \sqrt{T_e/m_D}$	deuterium sound speed
time	$a/c_s$	minor radius over sound speed

Table 6.1: Normalising quantities used in CGYRO and this thesis

where the normalising field  $B_{\text{unit}}$  is defined as

$$B_{\text{unit}} = \frac{q}{r} \frac{\partial \psi}{\partial r} \quad (6.2)$$

which is a flux surface quantity. This does lead to a slightly different definition of  $\beta_e$  compared to Chapter 2 where

$$\beta_{e,\text{unit}} = \frac{8\pi n_e T_e}{B_{\text{unit}}^2} \quad (6.3)$$

This work will examine the  $T_{e0} = 28\text{keV}$ ,  $I_p = 21\text{MA}$  design discussed in Chapter 4, with the major plasma parameters shown in Table 4.2. Three surfaces from this equilibrium will be explored;  $\rho_\psi = 0.3, 0.5 \& 0.85$ . The major plasma parameters along with Miller fits [103] are shown in Table 6.2 for each surface\*. The quality of the Miller fit for the  $\rho_\psi = 0.5$  surface is examined, with the flux surface and poloidal field shown in Figure 6.3a and 6.3b respectively. The fit is reasonably good illustrating the validity of using Miller parameters for this flux surface.

Convergence tests found that simulations required 128  $\theta$  grid points for each  $2\pi$  segment, 8 energy grid points and 16 un-trapped grid points<sup>†</sup>. Two species were simulated, an electron and deuterium ion species. To ensure quasi-neutrality,  $n_i = n_e$  and  $a/L_{n_i} = a/L_{n_e}$  was enforced. The layout of this chapter is as follows

- Section 6.1: Identifying the relevant instabilities on the  $\rho_\psi = 0.5$  surface
- Section 6.2: Examining the drives of the low  $k_y$  modes on the  $\rho_\psi = 0.5$  surface

---

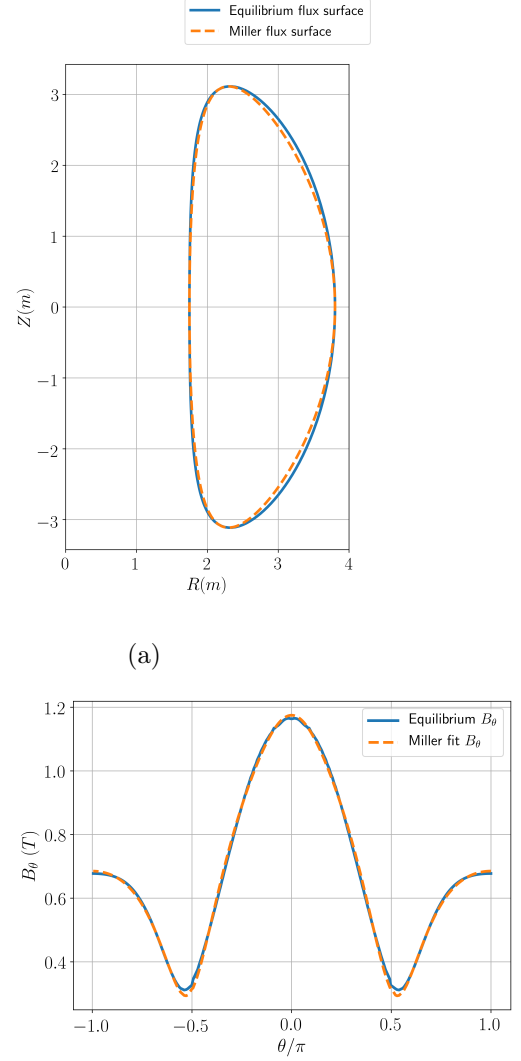
\*The Miller surface parameterisation is more easily ported to different gyrokinetic codes to allow for an easier direct comparison. Using a numerical equilibrium in GS2 generated the same result.

<sup>†</sup>Corresponding to  $n_{\text{gauss}} = 8$  in GS2. The number of trapped grid points is given by  $(N_\theta - 1)/2$

- Section 6.3: Examining the drives of the intermediate  $k_y$  modes on the  $\rho_\psi = 0.5$  surface
- Section 6.4: Determining the cause of stability of the high  $k_y$  modes on the  $\rho_\psi = 0.5$  surface
- Section 6.5: Micro-stability of the  $\rho_\psi = 0.3$  surface
- Section 6.6: Micro-stability of the  $\rho_\psi = 0.85$  surface
- Section 6.7: Micro-stability of an optimised equilibrium
- Section 6.8: Summary

Parameter	$\rho_\psi = 0.3$	$\rho_\psi = 0.5$	$\rho_\psi = 0.85$
$r/a$	0.50	0.66	0.89
$R_{\text{maj}}/a$	1.88	1.79	1.66
$n_{e20} \text{ (m}^{-3}\text{)}$	1.60	1.51	1.44
$T_e \text{ (keV)}$	17.8	12.2	5.8
$a/L_n$	0.26	0.43	0.56
$a/L_T$	1.86	2.77	3.50
$\Delta$	-0.52	-0.57	-0.47
$q$	3.42	4.30	5.53
$\hat{s}$	0.69	0.78	1.22
$\kappa$	3.23	3.03	2.84
$s_\kappa$	-0.17	-0.14	-0.06
$\delta$	0.40	0.45	0.47
$s_\delta$	0.16	0.19	0.26
$\beta_e$	0.27	0.15	0.06
$\beta_{e,\text{unit}}$	0.023	0.012	0.0035
$\rho^*$	0.0019	0.0014	0.00075
$\nu_{ei}(c_s/a)$	0.0085	0.017	0.068
$\gamma_{\text{dia}}(c_s/a)$	0.04	0.08	0.12

Table 6.2: Plasma and Miller parameters for 3 flux surfaces,  $\rho_\psi = 0.3, 0.5$  &  $0.85$  for the equilibrium in Table 4.2.



(b)

Figure 6.1: Miller fit shown for  $\rho_\psi = 0.5$  surface showing the a) flux surface contour and b) the poloidal field

## 6.1 Identifying the relevant micro-instabilities in BurST

### 6.1.1 Inclusion of different fields

Gyrokinetic simulations should, in principle, include all 3 components of the electromagnetic potential. Often, the  $A_{\parallel}$  and  $B_{\parallel}$  fields are left out in cases where they have little impact (low  $\beta$ ) to save computational time. In GS2 it is possible to solve the gyrokinetic equation with any combination of the fields ( $\phi, A_{\parallel}, B_{\parallel}$ ), so the importance of the electromagnetic terms was investigated. To begin with the  $\rho_\psi = 0.5$  surface is investigated. Four different scenarios were

explored with the following fields turned on:  $(\phi)$ ,  $(\phi + A_{\parallel})$ ,  $(\phi + B_{\parallel})$  and  $(\phi + A_{\parallel} + B_{\parallel})$ . Figure 6.2 shows the inclusion of different fields has a large impact on the predicted micro-stability of the modes, highlighting the highly electromagnetic nature of the fluctuations in this plasma. The growth rate,  $\gamma$ , is shown in the top figure and the mode frequency,  $\omega$  is shown below. Both graphs here are shown as log plots.

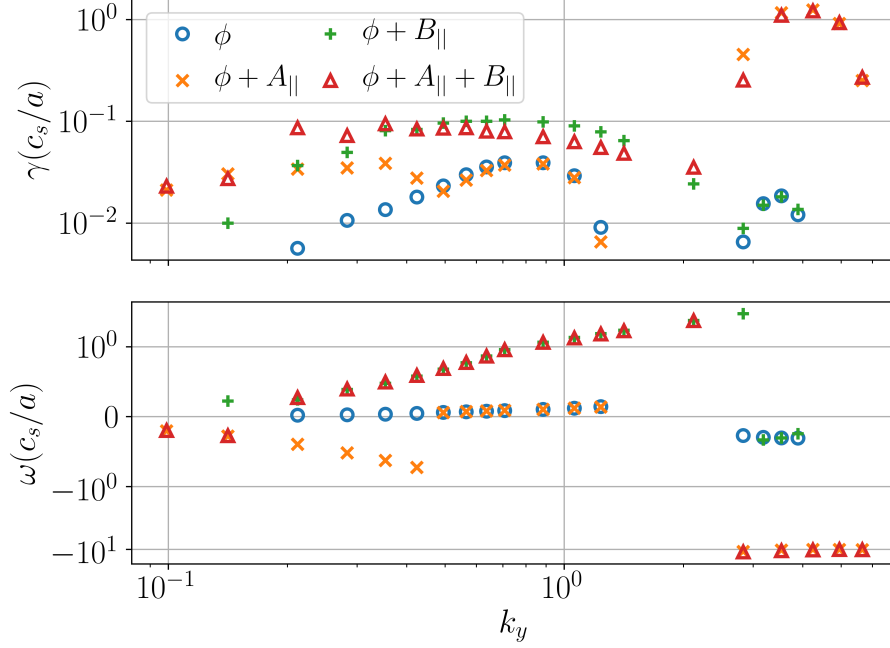


Figure 6.2: Impact of including different fields on the linear micro-instability predictions by GS2 for the  $\rho_{\psi} = 0.5$  surface of the baseline equilibrium. Note the log scale.

### Fields: $\phi$

The purely electrostatic case (blue circles) is stable when  $k_y < 0.2$ , with an ion temperature gradient (ITG) like mode appearing from  $k_y = 0.2 \rightarrow 1.5$ . The peak in the growth rate is  $\sim 0.04c_s/a$  which is lower than the diamagnetic flow shear,  $\gamma_{\text{dia}} = 0.08c_s/a$  so this will likely be very close to stable. Around  $k_y = 4$ , a trapped electron mode (TEM) is seen but has a very low growth rate. Above this  $k_y$ , all modes were found to be stable indicating that the ETG may not play a significant role electrostatically in this plasma scenario. This is similar to what was found for the STPP design which was also completely stable at high  $k_y$  [37].

### Fields: $\phi + A_{\parallel}$

With the inclusion of  $\phi + A_{\parallel}$  (orange crosses) different modes emerge when  $k_y < 0.5$ , and  $k_y > 3.0$ , both propagating in the electron direction. These will be shown to be micro-tearing

modes (MTM) which inherently are electromagnetic and the two MTMs seen here will be shown to be quite different in nature. In between these two modes the same ITG seen before appears to be the dominant mode. These MTMs will be examined in detail in Section 6.2.

**Fields:**  $\phi + B_{\parallel}$

Including only the  $B_{\parallel}$  (green plus symbol) terms appears to be strongly destabilising in the low  $k_y$  region, similar to what was found in high  $\beta$  NSTX-like equilibria [166]. This is a result of the  $B_{\parallel}$  fluctuation counteracting the stabilisation from the diamagnetic well from the  $\nabla B$  drift [167]. These modes rotate in the ion diamagnetic direction and will be shown to be kinetic ballooning modes (KBMs), which are electromagnetic pressure gradient driven modes which typically lead to stiff profiles that clamp the gradient to a critical value.

Unsurprisingly including  $B_{\parallel}$  without  $A_{\parallel}$  doesn't find the MTMs at low or intermediate  $k_y$ . Furthermore, it has little impact on the TEM modes or the high  $k_y$  modes.

**Fields:**  $\phi + A_{\parallel} + B_{\parallel}$

Looking at the fully electromagnetic (physically correct) dominant eigenvalue spectrum in Figure 6.2 there are several regions of interest. Firstly for  $k_y < 0.15$ , the MTM seen earlier emerges. In this chapter an MTM will refer to any electron direction mode that has field line tearing. This has a similar mode frequency and growth rate to the case without  $B_{\parallel}$ , indicating its lack of importance for these MTMs. Its eigenfunction shown in Figure 6.3a. The eigenfunctions have been normalised to the maximum value of  $|\phi|$ , indicating that the  $A_{\parallel}$  fluctuation is significantly larger than the electrostatic fluctuations at  $\theta = 0$ .

There appears to be two scales at work here, a broad oscillation in  $\theta$ , and a much narrower oscillation in  $\theta$  which corresponds to a single poloidal revolution due to the equilibrium variation. With such extended modes, the parallel electron dynamics will be playing an important role as the ions would not be able to travel that far down the field line due to their lower velocity. The extended nature of the mode in ballooning space required a parallel domain from  $-71\pi \rightarrow 71\pi$ , corresponding to  $k_x = k_y \hat{s}\theta = 26.1$ . Even linearly resolving such modes becomes computationally expensive. This suggests that nonlinear simulations may require going out to electron scales in  $k_x$ , indicating the potential challenge of fully resolved nonlinear simulations. Similar extended MTM eigenfunctions have been seen in simulations of MAST and NSTX discharges [93, 168].

There are several mechanisms that can drive a MTM. The first is from a parallel thermal force arising from the different frictional forces experienced by electrons travelling in opposite

directions along a temperature gradient. This generates a parallel current which in turn generates a perturbation in  $A_{\parallel}$  [169]. It was found that this mechanism could be examined in different limits and in the collisionless regime ( $\nu_{ee} < \omega$ ) this thermal force vanishes [170]. For this equilibrium,  $\nu_{ee} = 0.017c_s/a$ , which is well below the mode frequency where  $\omega \sim 0.5c_s/a$ , suggesting this mechanism is not expected to be relevant.

Another proposed mechanism is where electrons close to the trapped-passing boundary can easily scatter across it, which increases the effective collisionality allowing for a destabilising current driving the tearing instability. This is valid when  $\nu_{ee} < \varepsilon\omega$  [171], which is satisfied in this collisionality regime.

Both of these descriptions require a finite collisionality. However, this is not a complete description of MTMs as there are cases where the MTMs don't follow these two descriptions [172]. For example, collisionless MTMs have been found [173, 174], though the mechanisms here are not completely understood.

MTMs are generally identified with an even parity  $A_{\parallel}$  eigenfunction which is symmetric about  $\theta = 0$  (with  $\phi$  being odd) and they rotate in the electron diamagnetic direction. However this does not guarantee tearing and a more precise definition can be used that quantifies this. A mode is tearing if the perturbation results in a field line that does not return to the equilibrium flux surface. This can be characterised using the following equation [28, 175, 176]

$$C_{\text{tear}} = \frac{|\int A_{\parallel} dl|}{\int |A_{\parallel}| dl} \quad (6.4)$$

where  $C_{\text{tear}} = 1$  corresponds to a purely tearing mode and  $C_{\text{tear}} = 0$  has purely twisting parity. This MTM has a  $C_{\text{tear}} = 0.7$  indicating that this is indeed a predominantly tearing mode.

The perturbations in  $A_{\parallel}$  allow for a magnetic island to form across which particles can move freely. When several islands begin to overlap, the electrons are free to move along the perturbed fields lines off of their equilibrium flux surface. This can result in significant electron heat transport and is given as a potential reason for the high ratio of  $T_i/T_e$  often seen in STs [177, 178].

Between  $0.15 < k_y < 2.0$  kinetic ballooning modes (KBMs) were found to be the dominant instability. These modes have the same mode frequency as the case with just  $(\phi + B_{\parallel})$  but the growth rates are slightly modified. The eigenfunction at  $k_y = 0.35$  is shown in Figure 6.3b. These modes are much narrower in ballooning space and are purely twisting as they have  $C_{\text{tear}} = 0$ .

It can be seen that in these KBMs, the amplitude of  $B_{\parallel} > 40\%$ , when normalised to  $\phi$ . When

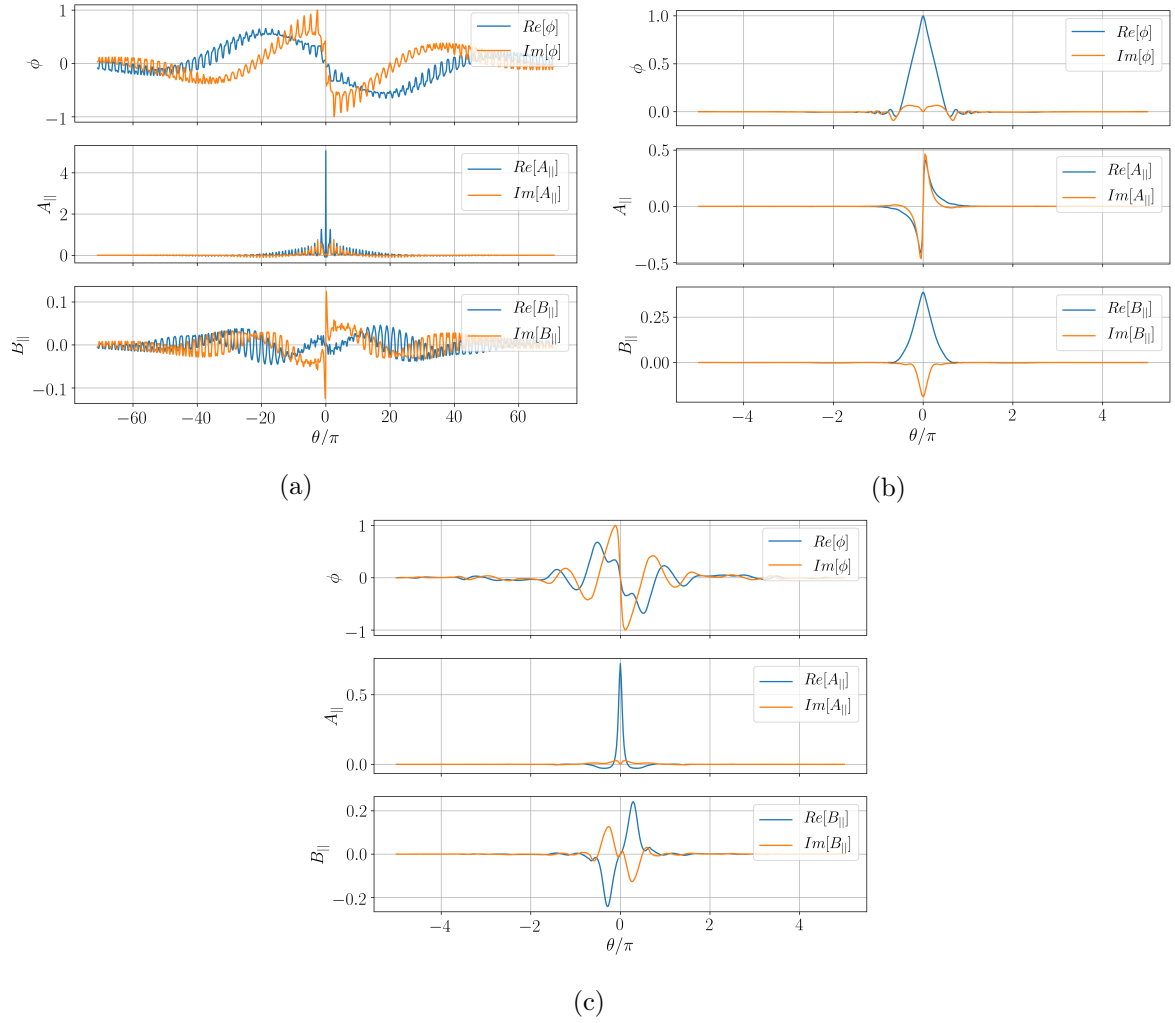


Figure 6.3: Eigenfunction for the dominant fully electromagnetic mode at  $k_y =$  a) 0.1, b) 0.35, and c) 4.2 in the baseline equilibrium at  $\rho_{\psi} = 0.5$ .

the compressional  $B$  is ignored the KBM is completely stabilised. This has been seen before in several high  $\beta$  ST equilibria [166, 179]. Interestingly, the inclusion of  $A_{\parallel}$  has little impact on this mode even though it has a large amplitude.

From  $3.0 < k_y < 7.0$ , the same high  $k_y$  MTMs seen in the  $(\phi + A_{\parallel})$  simulations were found and the eigenfunction at  $k_y = 4.2$  is shown in Figure 6.3c which are also tearing as  $C_{\text{tear}} = 0.5$ . These are much less extended than the MTMs seen at lower  $k_y$  but further indicate that multi-scale nonlinear simulations may be necessary.  $B_{\parallel}$  has little effect on these modes. Above  $k_y = 7.0$  all the modes were found to be stable.

Three different regions of interest can be defined: the low  $k_y$  region where  $k_y < 2.0$ , the intermediate region where  $2.0 < k_y < 10.0$  and the high  $k_y$  region where  $k_y > 10.0$ . These three regions will be focused on in more detail in Sections 6.2, 6.3 and 6.4 aiming to understand what drives these modes and potential ways to stabilise or avoid them.

It is clear that both magnetic terms are important in this equilibrium, so all results from here shall include all three fields.

### 6.1.2 Co-existing KBM and MTM

It is possible that if low  $k_y$  MTMs are subdominant, they could potentially significantly impact the nonlinear fluxes [179]. Co-existing MTMs and KBMs have been seen before in simulations of JET, DIII-D and NSTX plasmas [179–182]. To fully quantify their effects would require an eigensolver. However, in GS2 it is possible to force either an even or odd  $\phi$  eigenfunction, allowing for usage as a pseudo-eigensolver<sup>‡</sup>. By forcing an odd solution it is possible to examine the MTM, even if it is subdominant. It should be noted that this won't allow for all eigenvalues to be calculated, just the most unstable odd or even solution.

For this chapter, hollow data points will correspond to a even parity eigenfunction (w.r.t  $\phi$ ) and filled data points correspond an odd parity eigenfunction, though not necessarily tearing modes. To maintain consistency each type of mode will be represented with a particular colour and shape where possible. The KBMs will be represented by hollow blue circles.

Figure 6.4a shows the dominant odd and even instability growth rates for  $k_y = 0.1 \rightarrow 0.7$ , illustrating that the MTMs (filled orange triangles) are indeed subdominant here. The eigenfunction for  $k_y = 0.35$  is shown in Figure 6.4b and it is significantly less extended compared to the  $k_y = 0.1$  mode shown in Figure 6.3a, given that  $k_{\parallel} \propto k_y$ . Interestingly, these MTMs were unstable with only  $A_{\parallel}$  (both  $\phi$  and  $B_{\parallel}$  turned off), adiabatic ions, and without contributions from the trapped particles. This indicates that the important physics lies within the passing

<sup>‡</sup>GS2 can also be run as an actual eigensolver, but this eigensolver was not used in this work.

electrons. Furthermore, if the  $\nabla B$  and curvature drifts were turned off the mode went stable, indicating it wouldn't exist in a slab geometry.

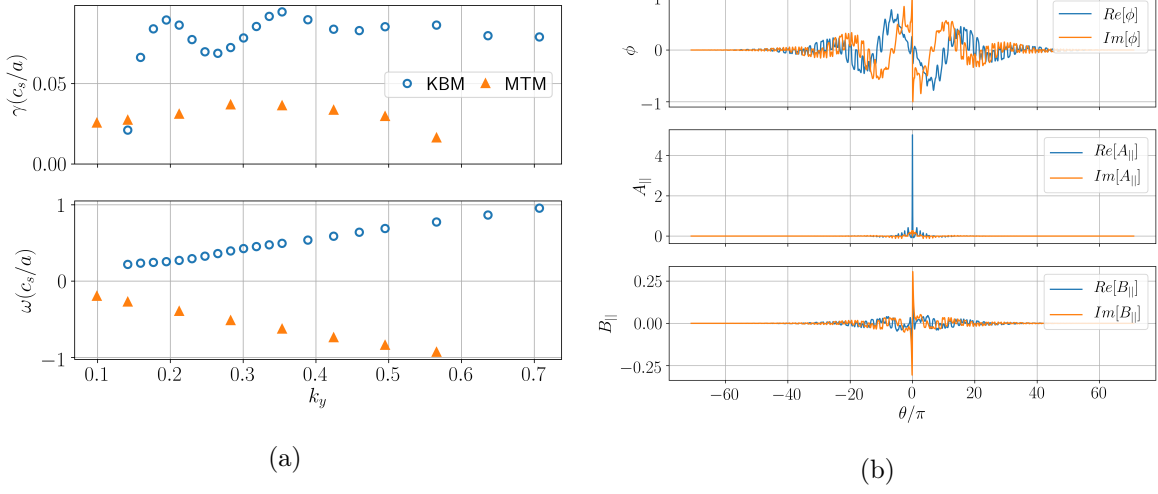


Figure 6.4: a) Linear spectra of the dominant odd and even modes for  $k_y = 0.1 \rightarrow 1.0$ . The hollow marker denotes an even parity eigenfunctions and a filled marker an odd eigenfunction. b) Dominant odd eigenfunction at  $k_y = 0.35$ .

The KBMs seen here have a two peaks, one at  $k_y = 0.2$  and one at  $k_y = 0.35$ . There does not appear to be a mode transition between the two peaks and their eigenfunctions looked similar, indicating the sensitivity of these KBMs to the bi-normal wavenumber, especially at such low growth rates.

## 6.2 Routes to stabilise long wavelength turbulence in the core

This section explore what terms drive or stabilise these low  $k_y$ , long wavelength modes and possible directions to modify the equilibrium that may be beneficial for confinement. These simulations will consider  $k_y = 0.35$ , which has the peak KBM growth rate. It will be shown that the KBMs are suppressed by a small amount of flow shear prioritising the need to stabilise the MTMs.

### 6.2.1 Impact of flow shear

As mentioned in Chapter 2, flow shear acts to advect the mode through  $\theta_0$  space. By examining how the mode stability is impacted by  $\theta_0$ , a qualitative assessment can be made about the effectiveness of the flow shear stabilisation. It is not possible to force an odd or even solution when  $\theta_0 \neq 0$  as the system is no longer up down symmetric, so only the dominant (i.e fastest growing) mode can be examined here.

Figure 6.5a illustrates how the KBM growth rate is very sensitive to  $\theta_0$  and is quickly stabilised as  $\theta_0$  moves away from zero. This suggests that flow shear will help to stabilise the KBMs and will act to increase their critical gradient.

However, Figure 6.5a shows the MTM (filled triangles) growth rate is largely unaffected by variations in  $\theta_0$  implying that flow shear would have little impact on the mode. The eigenfunction for  $\theta_0 = \pi$  is shown in Figure 6.5b and the same MTM structure is seen. Even when the mode is on the inboard side where the curvature is good, the mode is unstable. This indicates that the drifts reversal, which can occur at the outboard side, may not impact these modes.

These results demonstrate that there is a balance between KBMs and MTMs in this region. A small amount of flow shear will reduce the impact the KBM has on the transport as the mode will spend very little time in the region that is KBM unstable. However, the MTM which persists across  $\theta_0$ , will likely contribute significantly to the fluxes regardless of flow shear. This is illustrated in Figure 6.5c, where  $\gamma_{E \times B}$  is included for this simulation. The vertical dashed black line shows diamagnetic flow shear level  $\gamma_{\text{dia}}$ . With no flow shear the effective growth rate (black circles) is that of the KBM's growth rate  $\gamma = 0.093c_s/a$ . This is stabilised by a small amount of flow shear, but the effective growth rate remains at the MTM's level of  $\gamma \approx 0.04c_s/a$ .

This motivates the equilibrium being modified such that the MTM are stabilised given that these KBMs will likely be wiped out by flow shear.

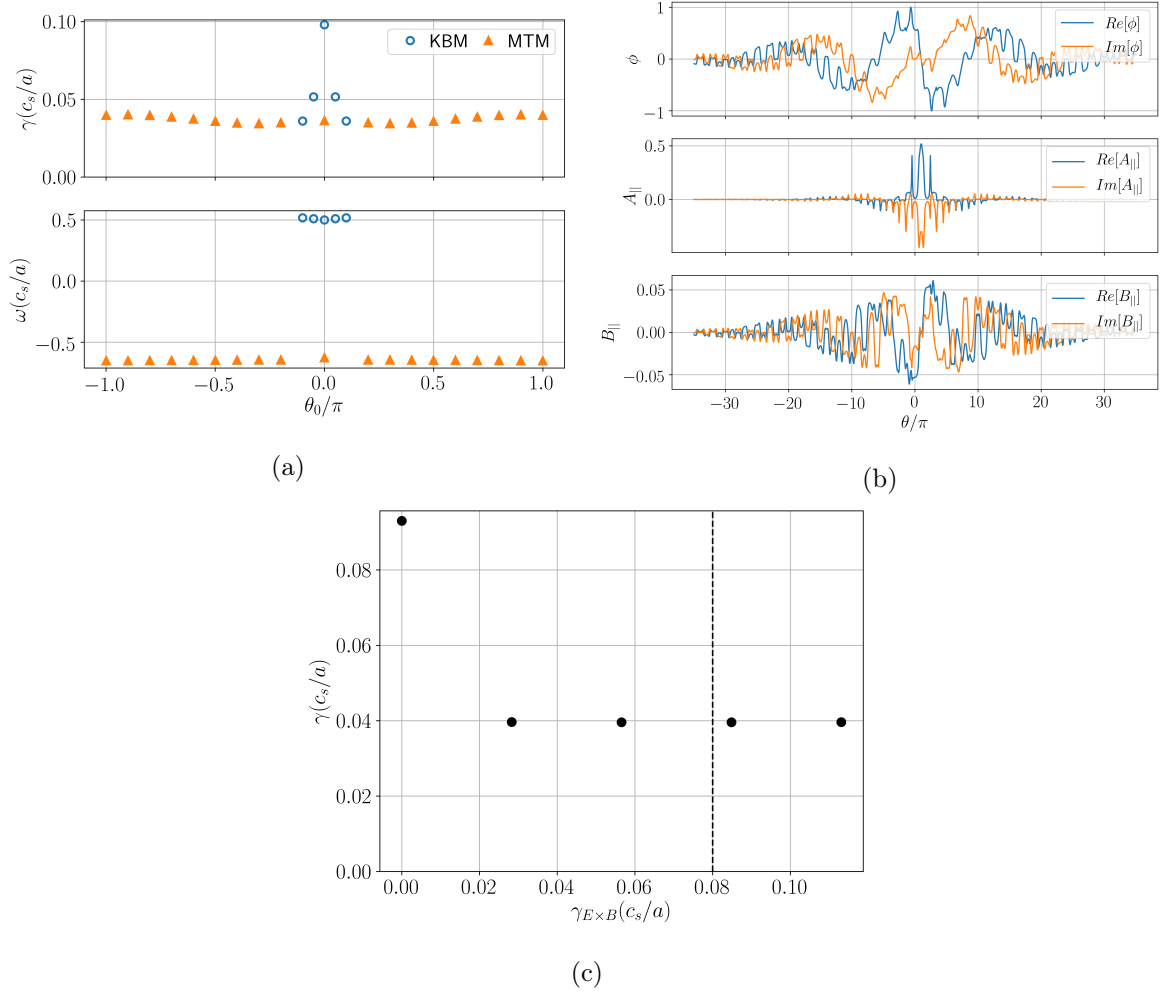


Figure 6.5: a)  $\theta_0$  scan for  $k_y = 0.35$  showing the narrow nature of the KBM and the unaffected MTMs. b) The MTM eigenfunction when  $\theta_0 = \pi$ . c) Effective growth rate when including flow shear where the vertical black line represents the diamagnetic flow shear  $\gamma_{\text{dia}}$ .

An important open question, beyond the scope of this work, is how the plasma transitions from a state where the KBM is dominant to one where the MTM is dominant, and the impact of this on the transport.

## 6.2.2 Impact of kinetic profiles

This section will investigate the impact the kinetic profiles will have on the low  $k_y$  KBMs and MTMs. Changing the kinetic profiles will change the kinetic gradients  $a/L_n$  and  $a/L_T$ , so the impact of these needs to be quantified to identify desirable operating scenarios. In this section the electron and ion temperature gradient will be independently changed to explore their impact on the KBMs and MTMs. Next the density gradient of the electrons and ions will be scanned together such that quasi-neutrality is maintained.

In gyrokinetic codes, the equilibrium is defined using the pressure profile, and in GS2 the pressure gradient is defined by  $\beta'_{e,\text{unit}} = -\beta_{e,\text{unit}}a/L_p$ . In this section the equilibrium was maintained by keeping  $\beta'_{e,\text{unit}}$  fixed, whilst inconsistently changing the kinetic gradients, allowing for the impact of the kinetic gradients to be isolated.

Changing the density and temperature profiles will also impact the collisionality as  $\nu_* \propto n_s/T_s^2$ , so the high density, low temperature scenarios will have a much higher collisionality. Furthermore, the impact of impurities and fast ions will need to be determined. This work won't include an impurity species, but will investigate the impact  $Z_{\text{eff}}$  has on these modes. No fast ion species have been included in this work, but as Chapter 5 has shown they can have a significant contribution to the total pressure. Previous studies have found that energetic NBI ions had a stabilising influence on the KBMs seen on JET [183, 184]. There is some evidence that MTMs are unaffected by fast ions [185], so if MTMs are expected to be the dominant source of transport in BurST then the effectiveness of fast ion stabilisation will need to be examined, but this is left as future work.

### Electron Temperature gradient

The impact of the electron temperature gradient was examined by scanning from  $a/L_{Te} = 0 \rightarrow 7.0$ . This corresponds to  $a/L_p = 3.63 \rightarrow 10.63$ . It is expected that this will have a significant impact on both modes, as MTMs are traditionally driven unstable by the electron temperature gradient and KBMs are driven unstable by the total pressure gradient. The eigenvalues are shown in Figure 6.6a, with the equilibrium value shown with the vertical black dashed line.

There appears to be a critical gradient where the KBM is completely stable at  $(a/L_{Te})_{\text{crit}}^{\text{KBM}} = 2.0$ , corresponding to  $a/L_p = 5.63$ . Its growth rate increases exponentially with  $a/L_{Te}$  which may lead to stiff transport, though with flow shear this may not be a big concern. The mode frequency is dropping as the temperature gradient increases. But it seems a small drop in the  $a/L_{Te}$  would allow for the MTM to become the dominant instability.

Looking at the dominant odd eigenmode, it can be seen that there's a critical gradient  $(a/L_{Te})_{\text{crit}}^{\text{MTM}} = 1.0$ . This critical gradient may be the limiting factor on the electron temperature profile as MTMs can drive significant electron heat flux. The mode frequency scales with the temperature gradient and this follows predictions made by Catto and Rosenbluth [171], which predicted that the mode frequency of an MTM is given by  $\omega_{\text{MTM}}^{\text{CR}} \sim \omega_e^*[1 + \eta_e/2]$  where  $\omega_e^*$  is the electron diamagnetic frequency defined as  $\omega_e^* = k_y(a/L_{ne})$  and  $\eta_e = (L_{ne}/L_{Te})$ . The orange dashed line shows  $\omega_{\text{MTM}}^{\text{CR}}$ , indicating that this scaling fits well.

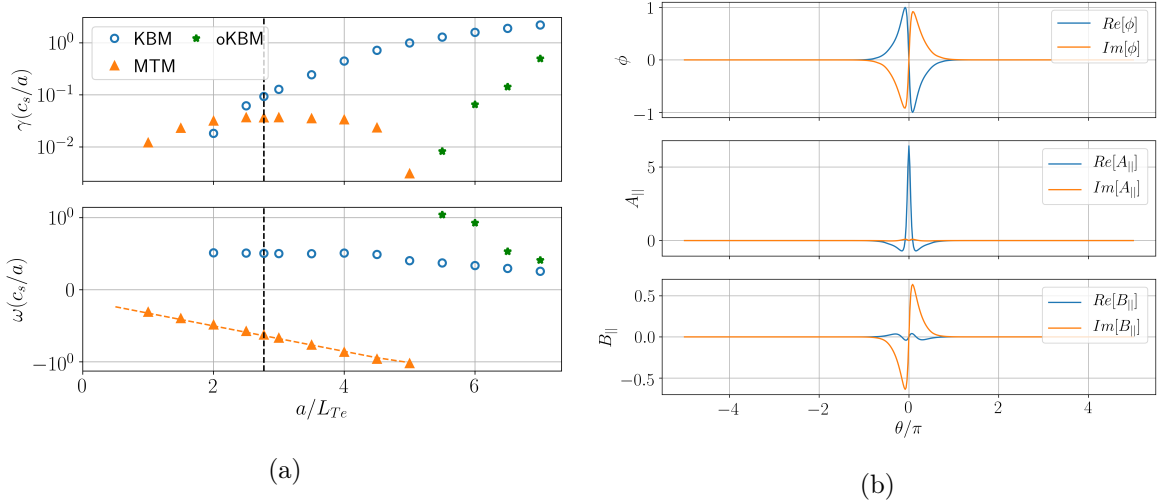


Figure 6.6: a) Examining the impact of plasma  $a/L_{Te}$  when  $k_y = 0.35$ . The dominant even (KBM) and odd (MTM) instabilities are shown, with the KBM demonstrating much stiffer behaviour. Note the log scale in  $\gamma$ . The dashed line shows the analytic prediction  $\omega_{MTM}^{CR}$  defined in the text. b) Eigenfunction of for the ion direction mode (filled green stars) for  $a/L_{Te} = 7.0$ ; despite being odd parity, the mode is not tearing as  $C_{tear} = 0.0$ .

The MTM growth rate has a much weaker dependence on the  $a/L_{Te}$  compared to the KBM and actually appears to level out, suggesting that small changes made to the electron temperature gradient may not have an impact on the transport. At sufficiently high gradient the MTM gets stabilised, this has been seen before in MAST simulations [172] where MTMs also followed  $\omega_{MTM}^{CR}$ . This was thought to be related to a resonance with a drift frequency. If  $|\omega|$  is increased sufficiently then this resonance is disturbed and the mode becomes damped. This bifurcation could lead to a scenario where the high temperature gradient is actually stabilising if it is possible to push through the lower gradient regime.

However, when  $a/L_{Te} > 5.0$ , an ion direction mode emerges that has an odd  $\phi$  eigenfunction, shown in Figure 6.6b. Its frequency is tending towards the KBM frequency. This however, is not a tearing mode as it has  $C_{tear} = 0.0$ . This rather appears to be an odd parity KBM, which will be labelled as an oKBM and will be represented with the filled green stars as seen in Figure 6.6a. This oKBM is a higher order eigenstate of the KBM and has been seen before in steep-gradient simulations [186]. Any quasi-linear model may need to account for this extra source of transport. Access to these temperature gradients may be possible if these oKBMs are also stabilised by flow shear, but the level of transport driven by the MTM must first be quantified. If this is an oKBM, it should be seen when scanning through  $a/L_{Ti}$ .

### Ion temperature gradient

A similar scan was performed for the ion temperature gradient by scanning from  $a/L_{Ti} = 0 \rightarrow 7$  whilst keeping the other kinetic gradients fixed. Again, this corresponds to  $a/L_p = 3.63 \rightarrow 10.63$ . The KBM and MTM are shown in Figure 6.7. The KBM has a similar critical gradient to the previous scan with  $(a/L_{Ti})_{\text{crit}}^{\text{KBM}} = 2.0$ , as expected if the relevant parameter is  $a/L_p$ . Once again the KBM is strongly destabilised by  $a/L_{Ti}$  and the mode frequency in this case actually increases with  $a/L_{Ti}$ , which suggests that the KBM frequency scale like  $\eta_i/\eta_e$ .

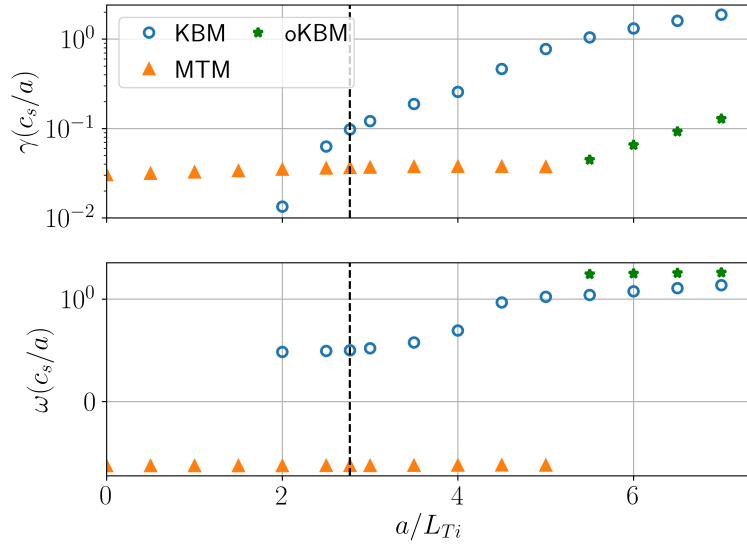


Figure 6.7: Examining the impact of plasma  $a/L_{Ti}$  when  $k_y = 0.35$ . The dominant even (KBM) and odd (MTM) instabilities are shown, with the KBM demonstrating much stiffer behaviour. The oKBM is again found at high  $a/L_{Ti}$ .

Examining the MTM, its growth rate and mode frequency are largely unaffected by  $a/L_{Ti}$  as expected. Once again if the ion temperature gradient is pushed high enough then when  $a/L_{Ti} > 5.5$  an oKBM appears, which is the same threshold as the  $a/L_{Te}$  scan.

It has been found in MTM driven transport, that 98% of the heat transport can occur in the electron channel [179]. This suggests that  $a/L_{Ti}$  will predominantly be limited by the the electron-ion exchange power assuming the KBMs can be ignored due to flow shear.

### Density gradient

A density gradient scan was performed from  $a/L_n = -1 \rightarrow 1$ , corresponding to  $a/L_p = 3.54 \rightarrow 7.54$ , and it can be seen from Figure 6.8 that when increased the KBM is destabilised, which further supports that fact that this is a pressure gradient driven mode. The KBM is stable when  $a/L_n < 0$  corresponding to  $a/L_p = 5.54$  which is similar to the critical value in

the temperature gradient scan. The mode frequency is unaffected which supports the idea that  $\omega_{\text{KBM}}$  scales with  $\eta_i/\eta_e$  which remains unchanged in this scan. When the density gradient is negative the KBM is stabilised and a TEM (hollow red diamonds) appears.

The MTM seems to be stabilised by a large  $|a/L_n|$ , which has been seen before on NSTX [168] and on MAST [187]. This again was thought to be due to the mode frequency changing and disrupting a resonance, though the peak growth rate here occurs as  $\omega = 0.4c_s/a$  and in the  $a/L_{Te}$  scan it occurred at  $\omega = 0.6c_s/a$ .

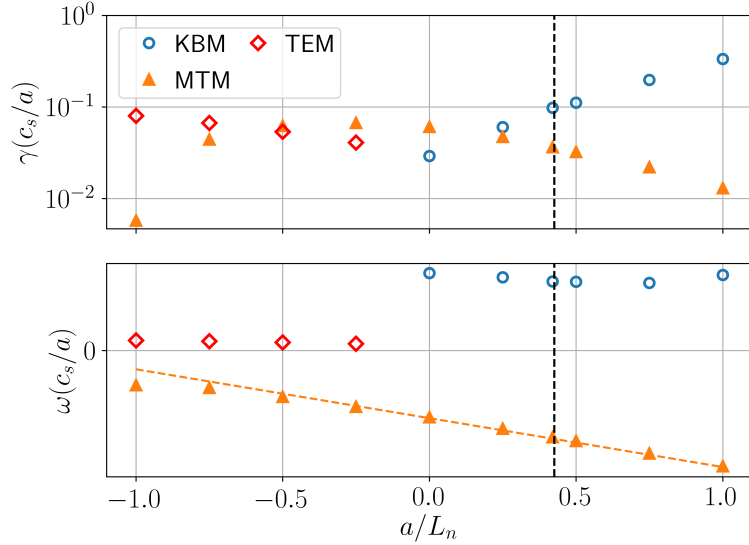


Figure 6.8: Examining the impact of  $a/L_n$  when  $k_y = 0.35$ . The dominant even (KBMs and TEMs) and odd (MTM) instabilities are shown, with the KBM demonstrating much stiffer behaviour.

### Total pressure gradient

It has been shown that increasing any of the kinetic gradients drives the KBM unstable. Assuming the KBM is driven by the total pressure gradient, if the total pressure gradient is kept fixed a similar growth rate should be seen. However, if the temperature gradient is exchanged for density gradient then it should be expected that the MTM will be stabilised. This should be doubly beneficial for the stability as the drive from  $a/L_{Te}$  is reduced and the stabilisation from  $a/L_n$  is being increased. A scan was performed at fixed  $a/L_p$  where the density gradient was changed from  $a/L_n = 0 \rightarrow 1.5$  and  $a/L_{Te} = a/L_{Ti}$  was set. The eigenvalues are shown in Figure 6.9. It can be seen that the MTM is indeed stabilised, and when  $a/L_n > 1.0$ , the MTM is completely stable.

This critical gradient occurs at the same values as the pure density gradient scan, indicating

that the electron temperature gradient is not having an impact on the MTM growth. This is explained by the “levelling” out of the MTM growth rate seen in Figure 6.6a during the  $a/L_{Te}$  scan, indicating that small changes in  $a/L_{Te}$  will not impact these MTMs significantly.

Overall, this implies that a peaked density profile could be beneficial in reducing MTM-based transport. The KBM is also stabilised slightly indicating it has a stronger dependence on the temperature gradient. Moreover, this scan maintains a consistent equilibrium as the Grad-Shafranov equation doesn’t differentiate between density and temperature when accounting for the pressure.

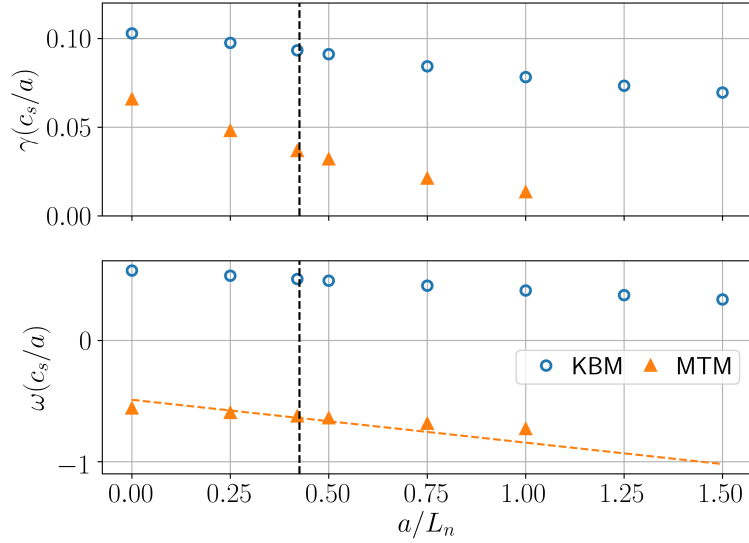


Figure 6.9: a) A scan was performed at fixed  $a/L_p$  where the contribution of  $a/L_n$  was varied for  $k_y = 0.35$ .  $a/L_{Te} = a/L_{Ti}$  was enforced.

## Collision Frequency

In Chapter 4 different temperature/density scenarios were examined at a fixed  $P_{fus} = 1.1\text{GW}$  which would directly impact the collisionality of the plasma given that  $\nu_* = \nu_{ee}/\varepsilon\omega_b$  and  $\nu_{ee} \propto n_e/T_e^{3/2}$ .

MTMs are generally reported to be highly sensitive to the electron collision frequency, so a scan was conducted from  $\nu_{ee} = 0 \rightarrow 0.14c_s/a$  and  $\nu_{ei}$  was consistently changed assuming  $T_e = T_i$ . A electron collision frequency of  $0.14c_s/a$  (which corresponds to  $\nu_* = 0.05$ ) is rather high for reactor relevant conditions and the highest density case investigated in Chapter 4 had  $\nu_{ee} = 0.16c_s/a$  at  $\rho_\psi = 0.5$  and likely would not be feasible due to density limits.

When examining the MTM, as shown in Figure 6.10a, it appears that collisions are destabilising for this mode. Note the linear scale here. Additionally, the collisions reduce the extent

of the mode in ballooning space as shown in Figure 6.10b where  $\nu_{ee} = 0.14c_s/a$ . This is due to the passing electrons undergoing a collision before they can propagate further along the field line. As the collision frequency is dropped towards 0, the MTM growth rate tends to 0. This suggests that the confinement will scale favourably as collisionality is reduced, aligned with previous confinement scaling laws in STs where  $B\tau_E \propto \nu_{*e}^{-0.82}$  [188]. One conclusion is that to reduce the electron transport a low collisionality regime is favourable.

However, Figure 6.10a also shows that as the collision frequency is increased the KBM is stabilised and a similar feature has been seen in a hybrid TEM/KBM mode in simulations of NSTX [179]. There is a critical collision frequency at which the dominant mode switches from a KBM to a MTM and the KBM becomes stable for  $\nu_{ee} > 0.12c_s/a$ .

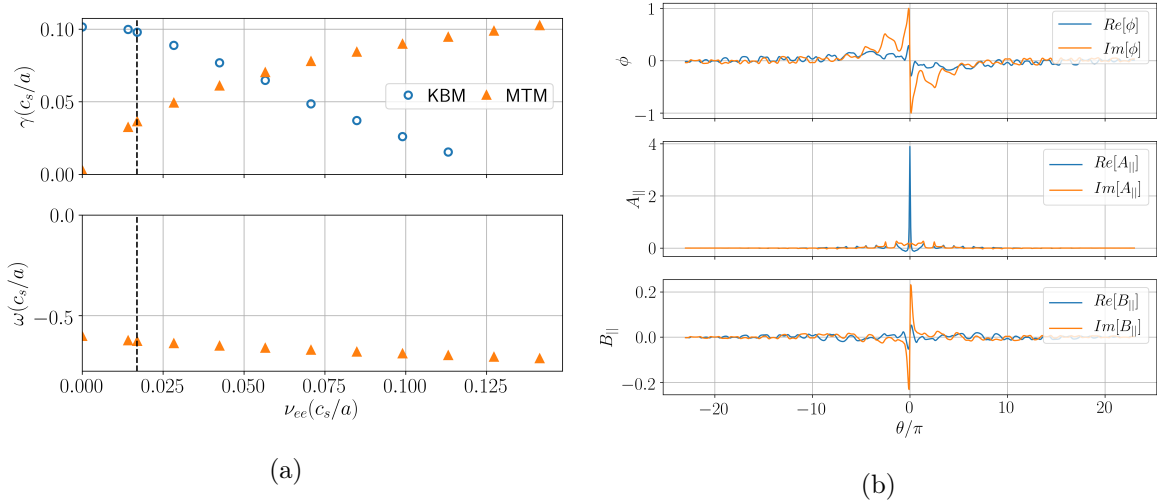


Figure 6.10: a) Impact of collision frequency showing the dominant odd and even parity mode for different values of  $\nu_{ee}$  when  $k_y = 0.35$ . Note the linear scale here. b) the eigenfunction when  $\nu_{ee} = 0.14c_s/a$ .

A scenario can be imagined where due to the large electron transport, the temperature gradient will drop, stabilising the MTM. However, the lower electron gradient will also lower the temperature and increase the collisionality which could drive the MTM even more unstable. This bootstrapping process could result in very low plasma temperatures. Conversely, if electron heating is sufficient to get over the peak growth rate for the MTM such that increasing  $a/L_{Te}$  is stabilising for these MTM, then this feedback loop is positive. This could lead to a bifurcation where a high  $a/L_{Te}$  regime may be possible.

Finding an equilibrium point between the lowered  $a/L_{Te}$  and higher  $\nu_{ee}$  will be critical in determining the electron temperature. This can then in turn impact the ion temperature through the collisional exchange power.

## $Z_{\text{eff}}$

Previous work has also found  $Z_{\text{eff}}$  to be destabilising for MTMs, via its impact on the collision frequency as  $\nu_{ei} \rightarrow Z_{\text{eff}}\nu_{ei}$  in the Lorentz collision operator [168, 179]. The simulations conducted thus far had  $Z_{\text{eff}} = 1.0$ , but in reality there will be impurities and helium in the plasma, raising the  $Z_{\text{eff}}$ . STPP was designed with an assumed  $Z_{\text{eff}} \approx 1.6$ , so it is crucial to quantify the impact it may have. A scan was performed from  $Z_{\text{eff}} = 1.0 \rightarrow 2.0$ . It should be noted that impurities were not included in the simulation such that  $Z_{\text{eff}}$  is being inconsistently set. This only has an impact on the collision operator. Figure 6.11 illustrates the dependency on  $Z_{\text{eff}}$ , with a doubling of  $Z_{\text{eff}}$  causing the MTM growth rate to increase from  $0.36 \rightarrow 0.51c_s/a$ . A similar growth is seen when the collision frequency is doubled instead where  $\gamma = 0.54c_s/a$ , which further confirms how  $Z_{\text{eff}}$  acts to increase the effective collision frequency between the ions and electrons, which drives the MTM. Moreover, when removing electron-electron collisions the mode was unaffected, further highlighting that electron-ion collisions are the relevant drive for this MTM. Figure 6.11 indicates the KBM growth rate is weakly stabilised, similar to the  $\nu_{ee}$  scan. In summary, any impurities in the plasma would cause a slight downshift in the MTM critical gradient.

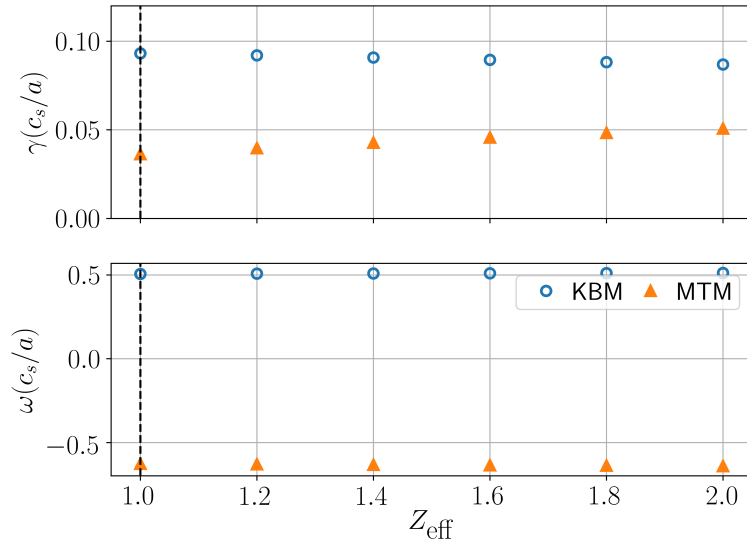


Figure 6.11: Examining the impact of  $Z_{\text{eff}}$  on the KBMs and MTMs for  $k_y = 0.35$  and  $\nu_{ee} = 0.14c_s/a$ .

### 6.2.3 Impact of magnetic equilibrium

Both MTMs and KBMs are inherently electromagnetic modes, so the total magnetic field will have a significant impact on the modes via  $\beta_e$ . Furthermore, there is evidence that both of

these modes are impacted by both  $q$  and  $\hat{s}$ , which are set by the field and current profile. Both of these were also inputs to SCENE, so it is possible to vary the assumptions about the magnetic equilibrium to see how to further stabilise these modes.

### Impact of $\beta_{e,\text{unit}}$ and $\beta'_{e,\text{unit}}$

A scan was conducted in  $\beta_{e,\text{unit}} = 0.0 \rightarrow 0.024$ , where  $\beta_{e,\text{unit}} = 0.024$  at  $\rho_\psi = 0.5$  approximately corresponds to a 40% drop in the field compared to the reference case in Table 6.2. The superconducting design examined in Chapter 4 would have  $\beta_{e,\text{unit}} = 0.004$  at  $\rho_\psi = 0.5$ . This must be explored carefully as changing  $\beta_{e,\text{unit}}$  would in turn change  $\beta'_{e,\text{unit}}$  and in GS2 it is possible to inconsistently change  $\beta_{e,\text{unit}}$  and  $\beta'_{e,\text{unit}}$ . Firstly  $\beta'_{e,\text{unit}}$  is kept fixed at the equilibrium value and this is shown in Figure 6.12a.

Looking at the even modes, when  $\beta_{e,\text{unit}} = 0$ , a weakly unstable TEM appears. Above a critical value of  $\beta_{e,\text{unit}} = 0.01$ , the KBM mode becomes unstable, before it begins to saturate around  $\beta_{e,\text{unit}} = 0.02$ . Looking at the MTMs, again there is a critical  $\beta = 0.006$ , below which the MTM is stable. This is driven unstable by  $\beta_{e,\text{unit}}$ , but when  $\beta_{e,\text{unit}}$  increases sufficiently then the oKBM is seen, which is very sensitive to  $\beta_{e,\text{unit}}$  and quickly begins to approach the KBM growth rate.

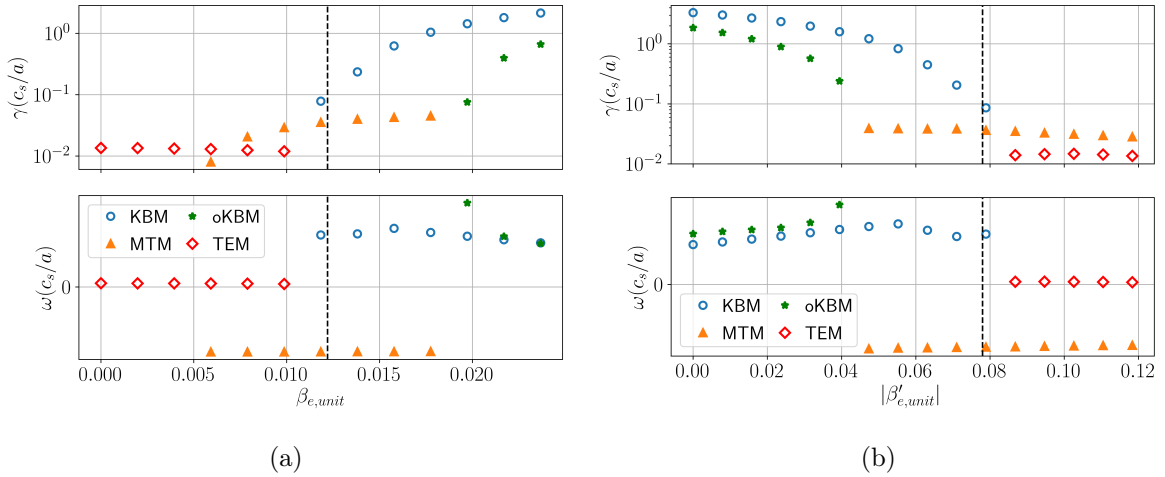


Figure 6.12: Examining the impact of a)  $\beta_{e,\text{unit}}$  at fixed  $\beta'_{e,\text{unit}}$  and b)  $\beta'_{e,\text{unit}}$  at fixed  $\beta_{e,\text{unit}}$  on the linear micro-instabilities at  $k_y = 0.35$ .

$\beta'_{e,\text{unit}}$  is used to calculate the equilibrium and has large impacts on the magnetic drifts and local current, meaning that only changing  $\beta_{e,\text{unit}}$  results in an inconsistent equilibrium. Nevertheless, scan was performed in  $\beta'_{e,\text{unit}}$  at the fixed equilibrium  $\beta_{e,\text{unit}}$  to isolate its impact. This is shown in Figure 6.12b where it can be seen that at low  $\beta'_{e,\text{unit}}$ , the KBM/oKBM are

the dominant instability. These are quickly stabilised and the dominant odd mode switches from an oKBM into the MTM and the dominant even mode switches from a KBM to a weakly unstable TEM. The MTM is not significantly affected by  $\beta'_{e,\text{unit}}$  and the reason can be determined by examining the drifts.

Figure 6.13 illustrates how  $\omega_{\nabla B}$  and  $\omega_{\text{curv}}$  are modified by changing  $\beta'_{e,\text{unit}}$ . The total curvature is approximately the sum of  $\omega_{\nabla B}$  and  $\omega_{\text{curv}}$ . Here a negative drift frequency corresponds to “good curvature” and positive is “bad curvature”. Increasing  $\beta'_{e,\text{unit}}$  makes  $\omega_{\nabla B}$  negative such that the combination of the two drifts becomes stabilising on the outboard side, resulting in “good curvature”. However, this is only significant when  $|\theta| < \pi$ , i.e. the first poloidal revolution. For ballooning modes like KBMs, this will be stabilising. For very extended modes, like the MTM,  $\omega_{\nabla B}$  is positive on the outboard side after a single poloidal revolution meaning the stabilising effect won’t occur. Although the MTMs are weakly stabilised by increasing  $\beta'_{e,\text{unit}}$ , this suggests that the drift reversal won’t have a significant impact.

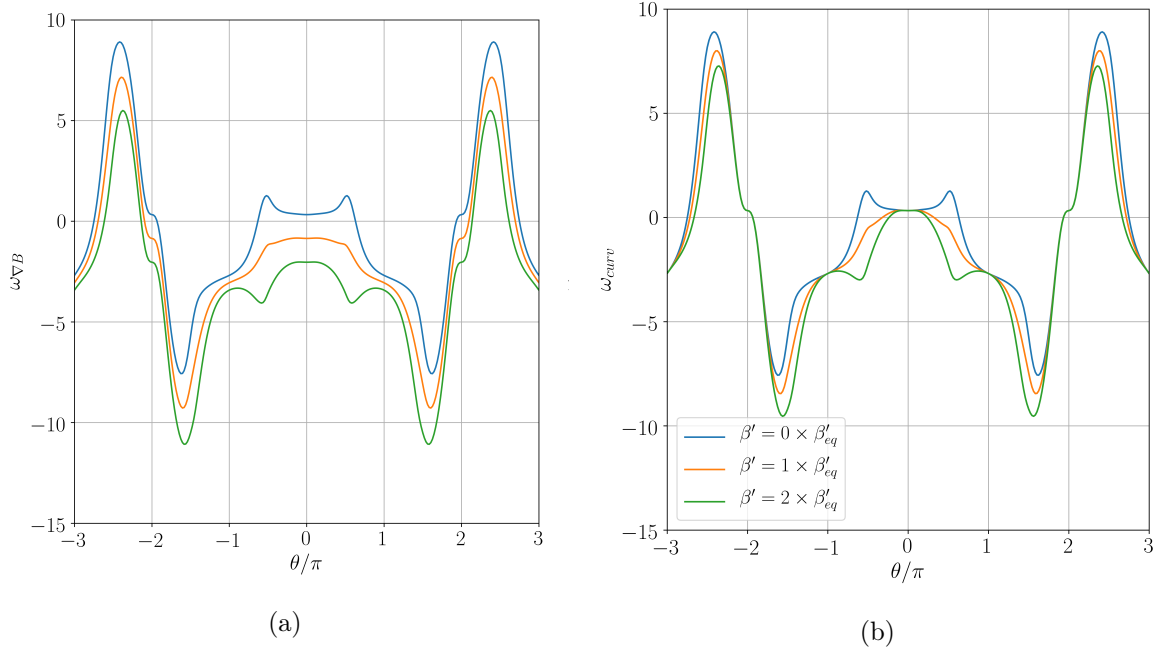


Figure 6.13: The impact  $\beta'_{e,\text{unit}}$  has on  $\omega_{\nabla B}$  and  $\omega_{\text{curv}}$ . The  $\nabla B$  drift is negative for the high  $\beta'$  cases when  $|\theta| < \pi$ , which is stabilising for ballooning modes.

A scan was also performed to consistently change both  $\beta_{e,\text{unit}}$  and  $\beta'_{\text{unit}}$  together to see how these MTMs and KBMs are impacted<sup>§</sup>. This corresponds to ensuring that  $\beta_{e,\text{unit}} = \beta_{e,\text{unit}} a/L_p$  was maintained throughout this scan. Operating at lower  $\beta_{e,\text{unit}}$  will help to stabilise the

<sup>§</sup>This scan alone does not show the impact of a higher field as other local parameters like  $q$  are impacted by the field.

MTMs. However, as  $\beta_{e,\text{unit}}$  is lowered, there is a smooth transition from a KBM to an ITG. Similar results have been found before in NSTX, where the modes were labelled as hybrid ITG/KBM [166]. At high  $\beta_e$  the stabilisation from the higher  $\beta'_{e,\text{unit}}$  seems to win out over the higher drive from  $\beta_{e,\text{unit}}$ . At lower  $\beta_{e,\text{unit}}$  the hybrid ITG/KBM has a larger growth rate compared to the equilibrium case. There is a critical  $\beta_{e,\text{unit}} = 0.004$ , below which this MTM is stable, and at sufficiently high  $\beta_{e,\text{unit}}$ , the mode begins to stabilise due to the higher  $\beta'_{e,\text{unit}}$ . A higher field device will be investigated in Section 6.2.4.

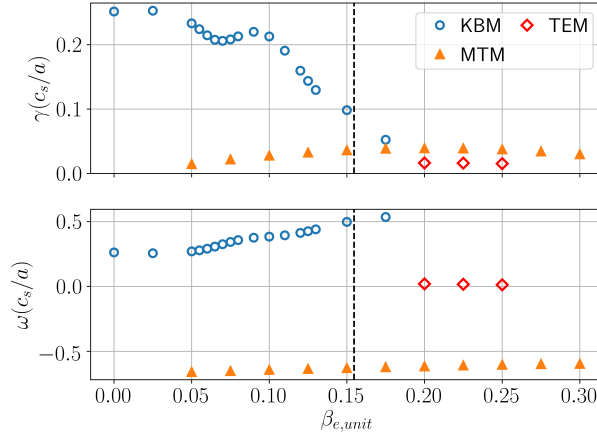


Figure 6.14: Changing  $\beta_{e,\text{unit}}$  and  $\beta'_{\text{unit}}$  consistently. It can be seen that there is a smooth transition between the ITG at  $\beta_{e,\text{unit}} = 0$  to the equilibrium  $\beta'_{e,\text{unit}} = 0.012$ .

### Safety factor and Magnetic shear

The  $n = \infty$  ballooning stability boundary is often used as an initial indicator for the onset of KBMs [189] and in GS2 there is a module that can calculate this boundary [88]. Figure 6.15 shows how this ideal stability boundary changes with  $q$ , illustrating a somewhat complicated relation between the ideal ballooning mode and  $q$ . As  $q$  increases the stability boundary moves to high  $\hat{s}$  and lower  $|\beta'|$ . Therefore pushing to a higher  $q$  will make access to the second stability region easier. At sufficiently low  $q$ , the stability boundary gets pushed to higher  $|\beta'|$  enabling the equilibrium to lie in the first stability region.

Evidently, the ideal ballooning mode is not sufficient in predicting the KBM threshold as it predicts this equilibrium to be stable, but it can give an idea of how the KBM will behave. Figure 6.16a shows a scan in  $q$ . For  $q < 3.0$  an ITG (hollow cyan pentagons) mode is dominant but after this the KBM becomes the dominant instability. As  $q$  is increased the KBM peaks and then becomes stabilised as the ideal boundary gets pushed further away from the equilibrium value. Eventually at sufficiently high  $q$  the KBM becomes stable and a TEM

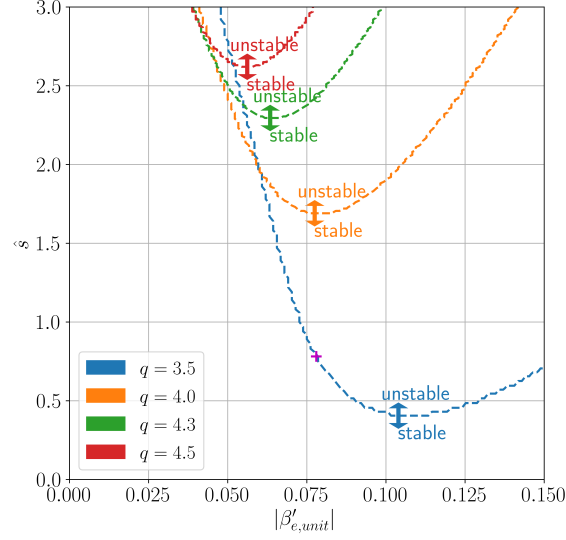


Figure 6.15:  $\hat{s} - |\beta'|$  diagram showing how the the ideal ballooning stability boundary moves with  $q$ . The reference equilibrium value of  $\hat{s}$  and  $|\beta'_{e,unit}|$  is shown by the magenta cross and has  $q = 4.3$  (green curve).

appears, indicating that operating at high  $q$  may help to increase the KBM critical gradient. A scan was also conducted with  $\hat{s}$  and Figure 6.16b shows how the KBM is destabilised by  $\hat{s}$ , consistent with the ideal ballooning mode.

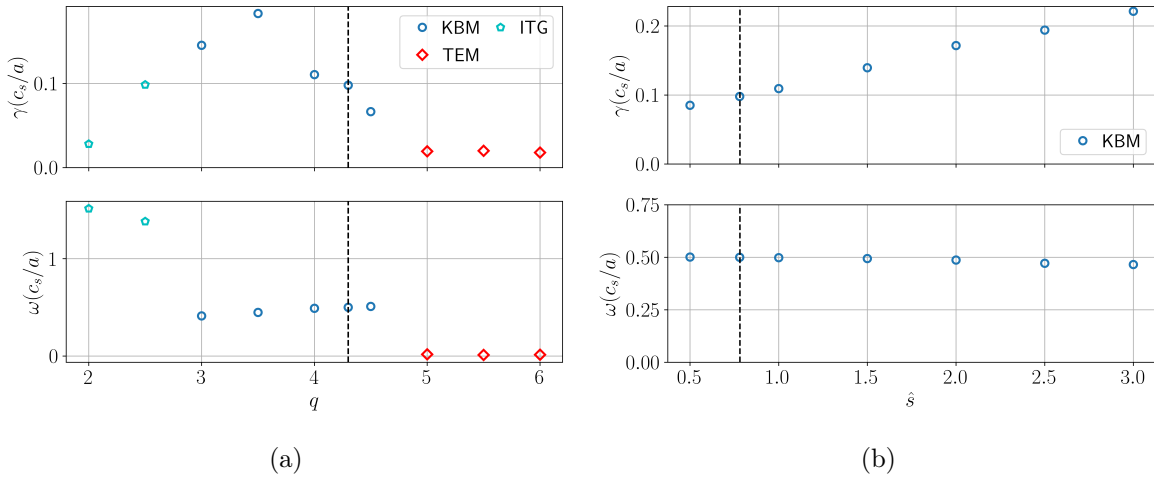


Figure 6.16: Dominant even eigenvalues when changing a)  $q$  and b)  $\hat{s}$  for  $k_y = 0.35$ .

Next, the impact  $\hat{s}$  and  $q$  have on the MTMs is explored, and it can be expected that increasing  $q$  will be destabilising for this MTM given that  $\nu_* \propto q$ . To isolate the impact on the MTM and avoid the oKBM being driven unstable, the  $q$  scan was run with  $\nu_{ee} = 0.14c_s/a$ . Figure 6.17a illustrates how there appears to be a linear relationship between  $q$  and the MTM growth rate, consistent with a  $\nu_*$  scaling. The magnetic shear dependency displays non-monotonic

behaviour as shown in Figure 6.17b.

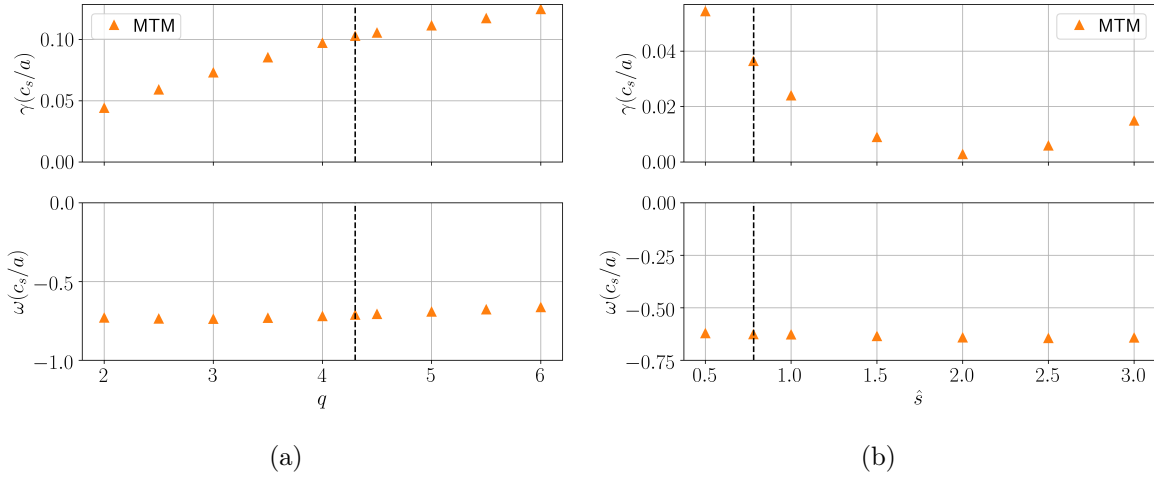


Figure 6.17: Dominant odd eigenvalues when changing a)  $q$  (at  $\nu_{ee} = 0.14c_s/a$ ) and b)  $\hat{s}$  for  $k_y = 0.35$ .

The impact of  $\hat{s}/q$  is often examined as it is related to Landau damping and field line bending. For the MTM seen here it appears that  $\hat{s}/q$  has a non-monotonic behaviour, so the impact on the turbulent transport will be difficult to predict. This has been seen before on MAST [187]. But there are examples where  $\hat{s}/q$  is stabilising for MTMs like in DIII-D [181] and counter-examples where  $\hat{s}/q$  to be destabilising, such as on NSTX [168] attributed to higher field line bending. This further highlights the complicated behaviour of MTMs so further work is needed to understand the dependence on  $q$ -profile.

## 6.2.4 Impact of higher toroidal field

It is clear that increasing  $q$  destabilises the MTM seen here. This has some consequences on a higher  $I_{\text{rod}}$  design which will predominantly change  $B_\varphi$ . At fixed  $I_p$ ,  $\beta_{e,\text{unit}} \propto 1/B_\varphi^2$  and  $q \propto B_\varphi$ , so a high field design may have a lower  $\beta_{e,\text{unit}}$ , stabilising the MTM, but the higher  $q$  may act to destabilise it.

To investigate the impact of higher field, SCENE was used to consistently generate equilibria with a higher toroidal field. The value of  $I_{\text{rod}}$  was increased from 30 MA to 50 MA<sup>¶</sup>, whilst all the other inputs were kept the same. When doing this, most of the equilibrium parameters stayed within 1% of the baseline value. The main parameters that did change for  $\rho_\psi$  were

- $\beta_{e,\text{unit}} : 0.012 \rightarrow 0.004$

<sup>¶</sup>The 50GW case corresponds to the superconducting case examined in Chapter 4

- $\beta'_{e,\text{unit}} : -0.08 \rightarrow -0.03$
- $q : 4.3 \rightarrow 7.3$
- $\hat{s} : 0.78 \rightarrow 0.70$

Figure 6.18 illustrates this scan in  $I_{\text{rod}}$ , with  $\beta_{e,\text{unit}}$  shown by the dashed red line. The KBM is weakly stabilised by the higher rod current. It seems that the stabilisation from the lower  $\beta_{e,\text{unit}}$  and higher  $q$  is counteracted by the lower  $\beta'_{e,\text{unit}}$ . For the MTM there is a very weak stabilisation as the increased  $q$  counteracts the lower  $\beta_{e,\text{unit}}$ . If  $I_{\text{rod}}$  is sufficiently increased, as  $\beta_{e,\text{unit}} \rightarrow 0$ , these modes should become stable, but  $I_{\text{rod}} = 50\text{MA}$  is approaching the limits of engineering.  $q$  could be dropped by increasing  $I_p$  to help stabilise the MTM, but this comes at a cost in  $P_{\text{aux}}$  to drive the additional current. Another option would be change the  $J_{\text{aux}}$  profile, which would change both  $q$  and  $\hat{s}$  as shown in Chapter 4.

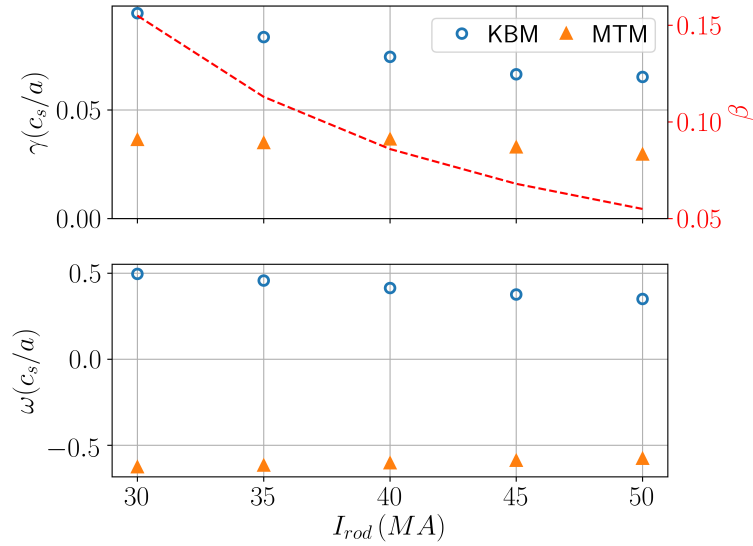


Figure 6.18: Examining the impact of a higher field device by increasing  $I_{\text{rod}}$  for  $k_y = 0.35$  at  $\rho_\psi = 0.5$ .

## 6.2.5 Summary

This section examined the main drivers of the micro-stability for the low  $k_y$  region at  $\rho_\psi = 0.5$ . The main instabilities seen were KBMs and MTMs. It was found that the KBMs were narrow in  $\theta_0$ , indicating their susceptibility to flow shear stabilisation, but the MTM seemed to be independent of  $\theta_0$ . This motivates designing an equilibrium that will stabilise these MTMs anticipating that, perhaps, the KBM can be suppressed by flow shear.

The impact of the kinetic profiles on the dominant instabilities in BurST was investigated. It was found that a peaked density profile will help to stabilise the MTMs, so examining core fuelling and particle transport will be crucial in designing an optimised scenario. It was also found that, at a fixed pressure gradient, density peaking was stabilising to the KBMs. Furthermore, the MTM is sensitive to collisions, so operating at low density/high temperature will further help to reduce the the impact of MTMs. Increasing  $Z_{\text{eff}}$  also was found to be destabilising via its impact on  $v_{ei}$ . Future work should explore the necessary fuelling requirements to maximise density peaking and to assess the consequences of this for impurity accumulation in STs.

The initial linear calculations indicates that operating at high field is not as beneficial as intuition would suggest. A higher field results in a lower  $\beta_{e,\text{unit}}$  and higher  $q$ . These two counter act each other for the MTM such that the mode is very weakly stabilised by a higher field. The KBM is also rather weakly stabilised as the lower  $\beta'_{e,\text{unit}}$  counteracts the stabilisation from lower  $\beta_{e,\text{unit}}$  and higher  $q$ . To further complicate matters, the KBM benefits from a lower  $\hat{s}/q$ , but the impact on the MTMs is more complicated. Further nonlinear transport analysis will be necessary to determine which regime would drive more transport and thus needs to be optimised for.

## 6.3 Routes to stabilise intermediate wavelength MTMs in the core

A different type of MTM appears from  $k_y = 3.0 \rightarrow 6.0$ , so this section will examine these modes at  $k_y = 4.2$ . These will be represented by filled magenta squares. Performing a similar analysis to the work described above, the impact different parameters will have on these MTMs is examined. Its impact on the total transport may not be as large if the KBM/MTM modes are significant, so it would be worth prioritising the stabilisation of the low  $k_y$  modes.

### 6.3.1 Impact of flow shear

A  $\theta_0$  scan was performed to determine the sensitivity to flow shear. Figure 6.19a illustrates this MTM has a narrow peak in  $\gamma$  around  $\theta_0 = 0$ , indicating that it will be stabilised by a small amount of flow shear.

However, a different tearing parity mode appears at  $\theta_0 = \pm\pi$  that rotates in the ion diamagnetic direction but has an odd parity  $\phi$  about  $\theta_0 = \pi$ . The eigenfunction is shown in Figure 6.19b and it has  $C_{\text{tear}} = 0.9$ , making it more tearing than the MTM situated around  $\theta_0 = 0$ . This is labelled as an iMTM (grey filled hexagons) and a tearing ion direction mode has not been reported in the literature before (to the best of the author's knowledge), especially one that has a maximum growth rate on the inboard side. This highlights the exotic nature of this equilibrium.

Between  $0.1\pi < |\theta_0| < 0.7\pi$ , both modes are stable. Including flow shear will move the modes through the stable region, resulting in a lower overall growth rate. Simulations were performed with varying levels of  $E \times B$  shear and were run for several Floquet periods to ensure the full behaviour was being captured. Figure 6.19c shows that the inclusion of flow shear reduces the effective growth, even for very low values of  $\gamma_{E \times B}$ , such that at diamagnetic levels of flow shear the mode is close to stable. This suggests that the impact of these MTMs on the total transport may not be significant

The impact of the kinetic profiles and magnetic equilibrium, as examined in the previously, will be focus of the following subsections, noting that this may not be hugely significant because of the impact of flow shear.

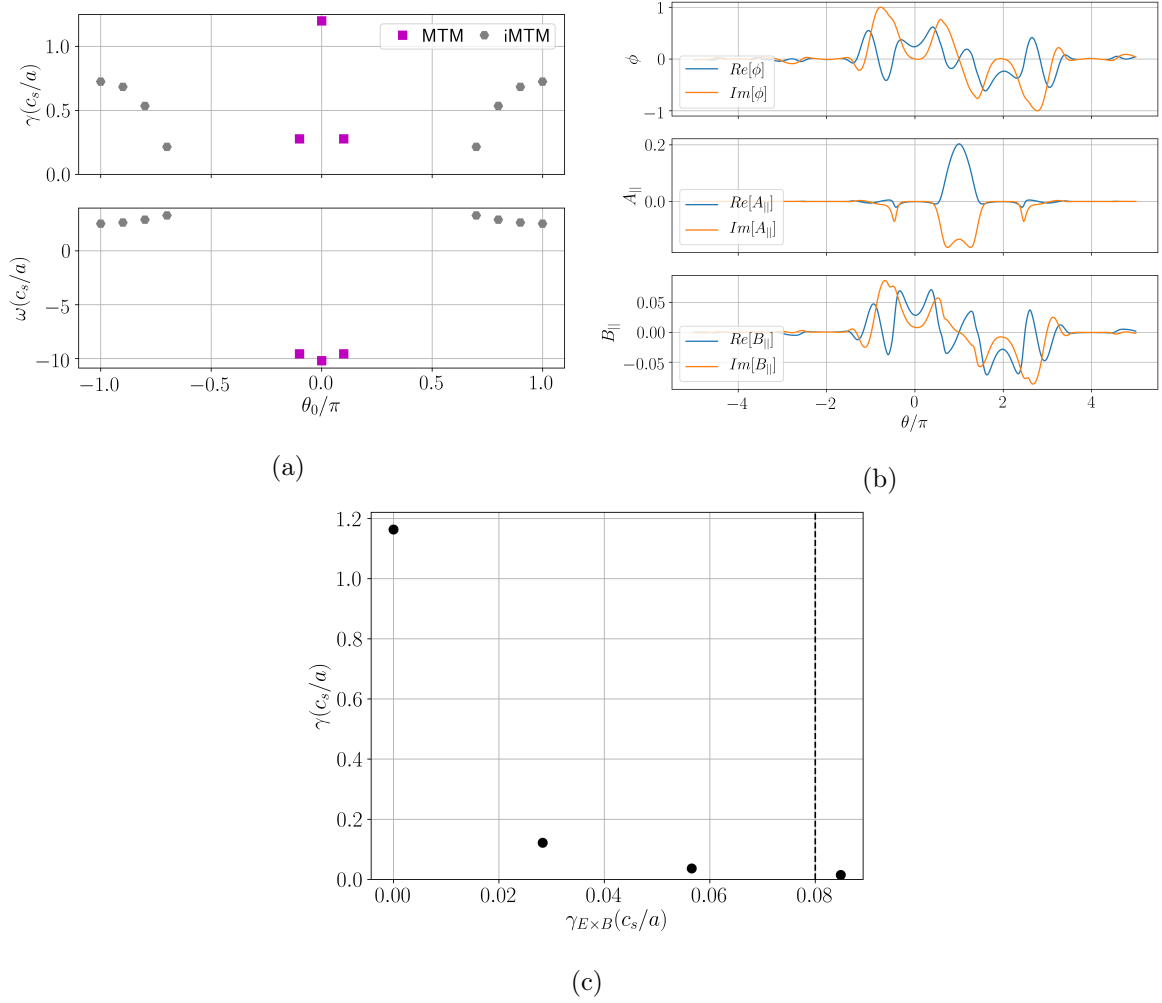


Figure 6.19: a)  $\theta_0$  scan of the dominant mode at  $k_y = 4.2$ , b) eigenfunction for the inboard iMTM and c) effective growth rate with  $E \times B$  shear. The vertical black line shows  $\gamma_{\text{dia}}$ .

### 6.3.2 Impact of kinetic profiles

#### Kinetic gradients

It is expected that these MTMs will be impacted by the kinetic gradients so scans in  $a/L_{Te}$  and  $a/L_n$  are shown in Figures 6.20a and 6.20b respectively. Once again a peak is seen in both gradients. The critical electron temperature gradient occurs at  $a/L_{Te} = 1.0$ , similar to the lower  $k_y$  MTM seen earlier. It peaks at  $a/L_{Te} = 3.5$  and then begins to drop off.

For the density gradient, the equilibrium happens to lie at the peak of the growth rate spectrum so increasing the density gradient would help to stabilise the mode, but the effect is not as large compared to the impact on the low  $k_y$  MTMs. Given the similar behaviour as the low  $k_y$  modes, similar measures can be taken to stabilise these modes, noting that their impact on transport will not be as significant given the flow shear stabilisation.

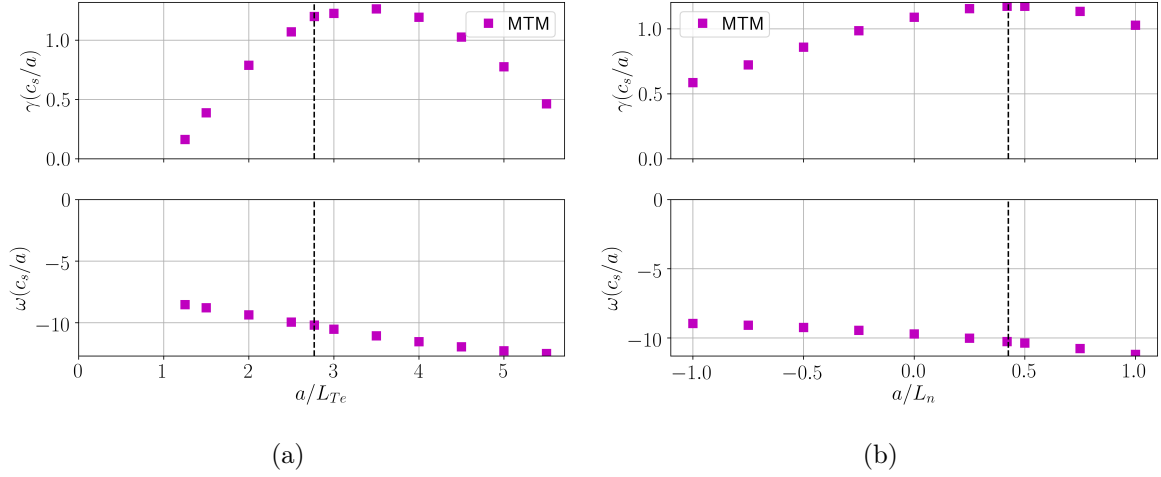


Figure 6.20: Examining the impact of a)  $a/L_{Te}$  and b)  $a/L_n$  on the MTMs at  $k_y = 4.2$ .

### Collision Frequency

Examining the impact of collisions, it can be seen from Figure 6.21 that these are collisionless MTMs, highlighting the completely different nature of these modes compared to the longer wavelength MTMs discussed in the previous section. Collisionless MTMs have been seen before [173, 174, 190], but their mechanism is not fully understood.

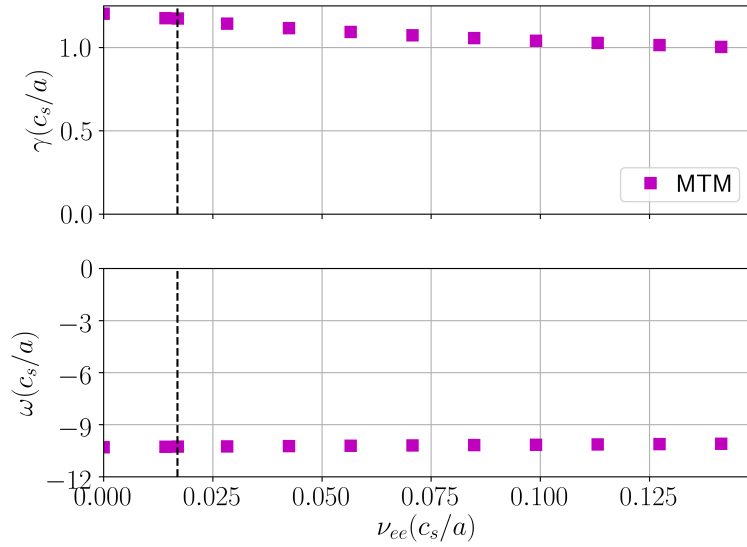


Figure 6.21: Examining the impact of  $\nu_{ee}$  on the MTMs at  $k_y = 4.2$ .

It can be seen that the dependence on  $\nu_{ee}$  is quite weak, as a factor 10 increase in collision frequency from  $\nu_{ee} = 0.014 \rightarrow 0.14c_s/a$  only caused a 15% drop in the growth rate, suggesting the choices made here will have little impact on these modes. Collision frequencies much higher than this are likely not achievable by reactors.

### 6.3.3 Impact of magnetic equilibrium

#### Impact of $\beta_{e,\text{unit}}$ and $\beta'_{e,\text{unit}}$

Figure 6.22a shows a scan of changing  $\beta_{e,\text{unit}}$  at fixed  $\beta'_{e,\text{unit}}$ . A critical  $\beta_{e,\text{unit}} = 0.003$  was found for this mode, corresponding to a 70% increase in the field. Below this a weakly unstable TEM is seen, which was also seen in the electrostatic case in Figure 6.2. Figure 6.22b shows how changing  $\beta'_{e,\text{unit}}$  impacts the MTM. This is very different to the low  $k_y$  MTMs which were largely unaffected by  $\beta'_{e,\text{unit}}$ . At lower  $\beta'_{e,\text{unit}}$  this MTM is stabilised, but another MTM appears at  $\beta'_{e,\text{unit}} = 0$ , likely also driven unstable by  $\beta_{e,\text{unit}}$ . At  $\beta'_{e,\text{unit}} = 0.0$ , this MTM has  $C_{\text{tear}} = 0.3$  which is lower than that for the equilibrium  $\beta'_{e,\text{unit}}$  at  $\theta_0 = 0$  which had  $C_{\text{tear}} = 0.5$ .

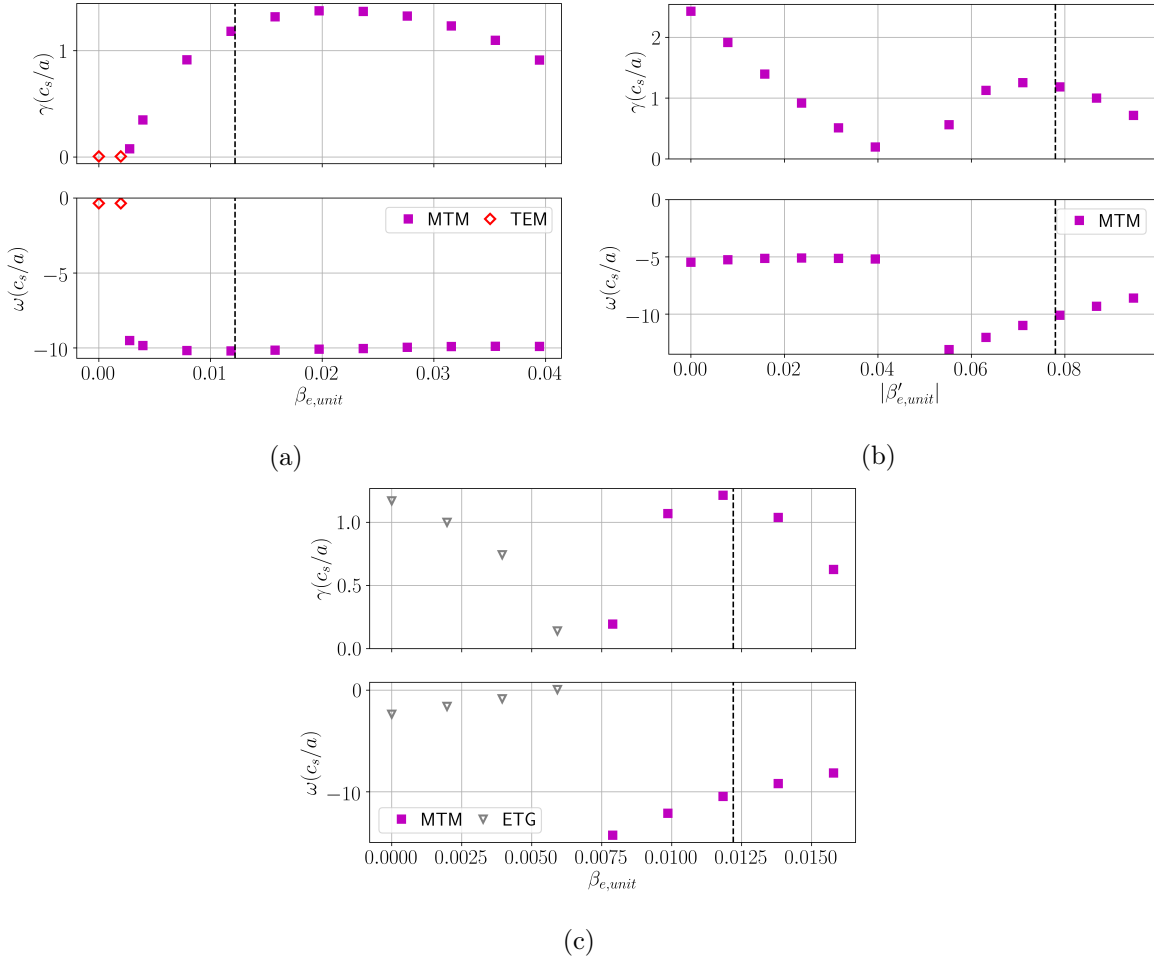


Figure 6.22: Examining the impact of changing a)  $\beta_{e,\text{unit}}$  at fixed  $\beta'_{e,\text{unit}}$  and b)  $\beta'_{e,\text{unit}}$  at fixed  $\beta_{e,\text{unit}}$  and c)  $\beta_{e,\text{unit}}$  and  $\beta'_{e,\text{unit}}$  together on the MTMs at  $k_y = 4.2$ .

To examine the relevance of this low  $\beta'_{e,\text{unit}}$  MTM, a scan was done where  $\beta'_{e,\text{unit}}$  and  $\beta_{e,\text{unit}}$  were changed together i.e.  $\beta_{e,\text{unit}} = \beta_{e,\text{unit}} a/L_p$  was maintained throughout this scan. Figure 6.22c shows that at sufficiently low  $\beta_{e,\text{unit}}$ , the original MTM is stabilised and the new MTM

does not appear. However, an ETG mode (hollow grey upside-down triangle) appears when operating at lower  $\beta_{e,\text{unit}}$  and  $\beta'_{e,\text{unit}}$ . This ETG will be explored in more detail in the Section 6.4. But this suggests that this low  $\beta'_{e,\text{unit}}$  MTM will not be relevant.

### Safety factor profile

Figure 6.23a shows a scan in  $q$  and it can be seen that there is a peak in the growth rate at  $q = 4.0$ , so an increased  $q$  will help to stabilise this mode. As mentioned earlier a higher field device will likely have a higher  $q$ , so the combination of lower  $\beta_{e,\text{unit}}$  and higher  $q$  indicates that this mode will be stabilised by a higher  $B_\varphi$ . At very high  $q$  an iMTM mode with  $C_{\text{tear}} = 0.7$  was found, though it exists for a very narrow window. Looking at  $\hat{s}$  in Figure 6.23b, there is a non-monotonic dependence similar to the lower  $k_y$  MTM. Though it seems to be a weak dependence so will likely not to be significant for this MTM.

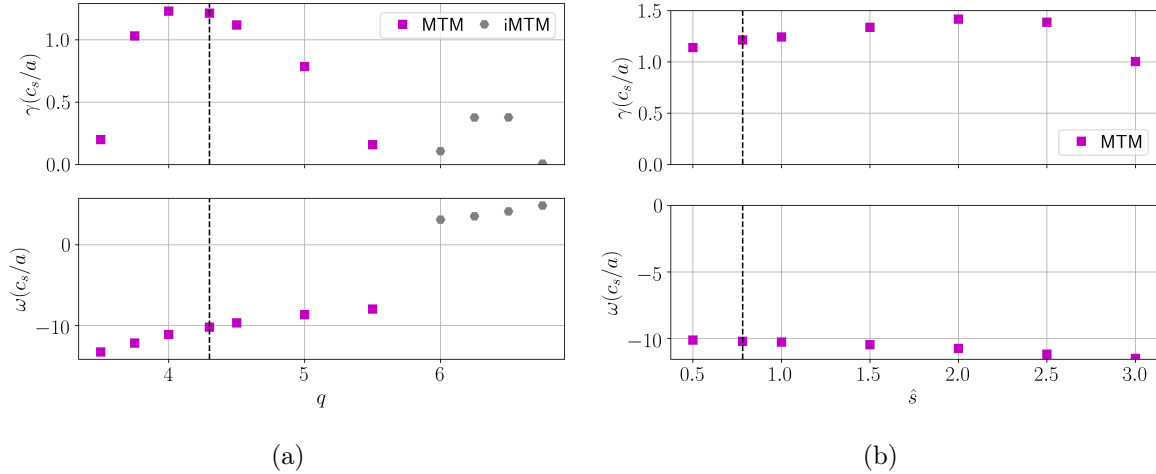


Figure 6.23: Impact of a)  $q$  and b)  $\hat{s}$  on the MTMs at  $k_y = 4.2$ .

### 6.3.4 Impact of higher toroidal field

Examining the impact of a higher  $B_\varphi$ , the MTM was examined under the  $I_{\text{rod}}$  scan. Figure 6.24 shows that operating at higher field stabilises the mode and when  $I_{\text{rod}} > 40\text{MA}$  this MTM goes stable. The ETG mode seen in Figure 6.22c does not get de-stabilised and in the next section it will be shown that this is a consequence of the higher  $q$  at higher field.

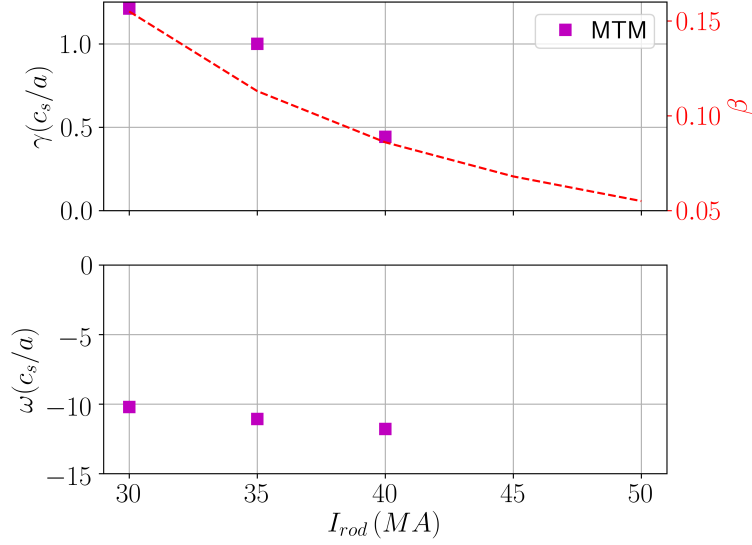


Figure 6.24: Examining the impact of a higher field device by increasing  $I_{rod}$  on the MTMs for  $k_y = 4.2$ .

### 6.3.5 Summary

At intermediate scales a collisionless MTM was found, which alone demonstrates the difference compared to the low  $k_y$  MTM which required collisions. A key result found was that these MTMs are susceptible to flow shear stabilisation. At diamagnetic levels of flow shear this mode is close to stable suggesting it may not contribute significantly to transport. When optimising an equilibrium it is therefore not so important to consider this mode as long as its drives are not significantly increased.

When examining the impact of the kinetic gradients, this MTM was found to follow similar trends to the lower  $k_y$  MTM, although the stabilisation by the density gradient was not found to be as strong. This MTM was weakly stabilised by collisions but overall it would appear that the collisionality will not have a significant effect.

As  $\beta_{e,unit}$  and  $\beta'_{e,unit}$  were scaled down together the MTM was stabilised, but an ETG mode was destabilised. However, it was found that employing a higher rod current to bring down  $\beta_{e,unit}$  did not destabilise the ETG, likely due to the associated higher  $q$ . When  $I_{rod} > 40MA$ , the MTM was completely stable.

Overall, its impact on the transport is likely minimal as a consequence of the flow shear stabilisation, but can be reduced further with a higher toroidal field.

## 6.4 Cause of short wavelength mode stability

This equilibrium was found to be stable when  $k_y \rho_e \sim \mathcal{O}(1)$ . STPP was also found to be stable in the electron scale [37]. ETG-like instabilities are generally found at the electron scale in other tokamaks. To understand why they are stable here, different plasma parameters were scanned as done in previous sections.

### 6.4.1 Impact of kinetic profiles

Given that ETG is expected, the impact of  $a/L_{Te}$  was examined. Scans were for  $a/L_{Te} = 5.0, 6.0 \& 7.0$ . The equilibrium value of  $a/L_{Te} = 2.77$  is well below this temperature gradient range, illustrating the large increase in drive necessary to find any ETG. Figure 6.25a shows how ETG modes can be found if the drive is sufficiently high. It can be seen that increasing  $a/L_{Te}$  does drive the mode seen here unstable, consistent with ETG. This shows that a significant increase in temperature gradient would be necessary for this region of  $k_y$ -space to be unstable. The eigenfunction for  $k_y = 35$  at  $a/L_{Te} = 7.0$  is shown in Figure 6.25b. The  $A_{||}$  component is very small when normalised to  $\phi$  suggesting it is not significant for these ETG modes.

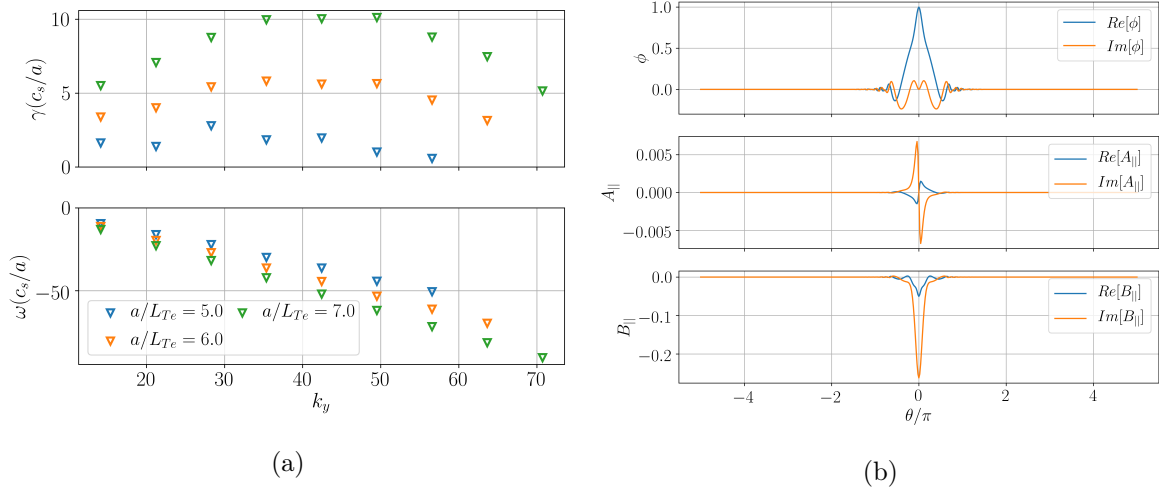


Figure 6.25: a) Growth rate spectrum for high values of  $k_y$  at different  $a/L_{Te}$ . The equilibrium value was  $a/L_{Te} = 2.77$ . b) Eigenfunctions for  $k_y = 35$  when  $a/L_{Te} = 7.0$ .

To examine why the critical  $a/L_{Te}$  is high for this equilibrium other parameters will be examined. The stability at  $k_y = 35$  will be investigated more carefully.

## 6.4.2 Impact of magnetic equilibrium

### Impact of $\beta_{e,\text{unit}}$ and $\beta'_{e,\text{unit}}$

Section 6.3.3 showed this ETG appeared when reducing  $\beta_{e,\text{unit}}$  and  $\beta'_{\text{unit}}$ . As they were both reduced, the MTM was stabilised and an ETG was destabilised, so it is expected that they will play an important role in the stabilisation here.

Figure 6.26a shows how the growth rate changes for the 3 different temperature gradients when changing  $\beta_{e,\text{unit}}$ .  $\beta_{e,\text{unit}}$  is found to be destabilising to these high gradient ETG modes, up to a critical value  $\beta_{e,\text{unit}} = 0.02$ , when there is a rollover and at sufficiently high  $\beta_{e,\text{unit}}$  these ETG are stabilised. However, at the equilibrium value of  $a/L_{Te}$ , the mode was completely stable regardless of the  $\beta_{e,\text{unit}}$ . A similar scan was conducted with  $\beta'_{e,\text{unit}}$  and this appears to be a cause of the stability. Increasing  $\beta'_{e,\text{unit}}$  strongly stabilises the ETG mode, such that when  $\beta'_{e,\text{unit}} = 0$  the ETG mode is unstable even at the equilibrium  $a/L_{Te}$ . This has been seen before by Roach *et al* [191] and is attributed to high  $\beta'$  reducing the bounce average drift frequency, further suggesting the drifts appear to be an important factor in stabilising these ETG modes. This all indicates a potential disadvantage with operating at higher field. The resulting lower  $\beta'_{e,\text{unit}}$  could destabilise the ETG modes and have a detrimental effect on electron thermal transport.

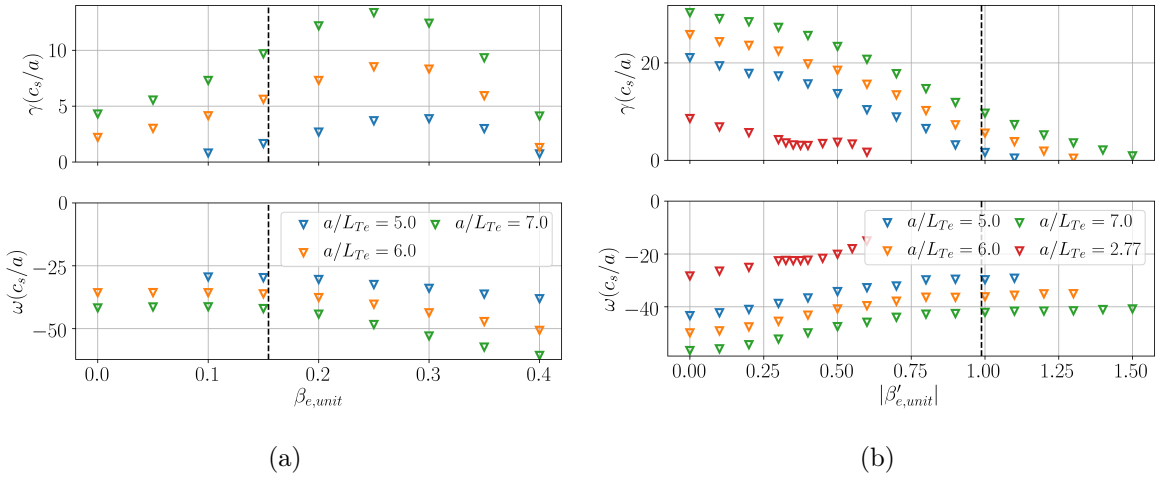


Figure 6.26: Impact of a)  $\beta_{e,\text{unit}}$  and b)  $\beta'_{e,\text{unit}}$  at different  $a/L_{Te}$  with  $k_y = 35$ .

### Safety factor profile

A critical gradient formula for ETG-like turbulence was found by Jenko *et al* [192] as follows

$$\left(\frac{a}{L_{Te}}\right)_{\text{crit}}^{ETG} \propto \left(1.3 + 1.9\frac{\hat{s}}{q}\right) \quad (6.5)$$

This was generated from simulations of a low  $\beta$ , conventional aspect ratio tokamak. To examine its validity for this ST equilibrium, scans were performed in  $a/L_{Te}$  at different values of  $q$  and  $\hat{s}$  to find the critical gradient. Equation 6.5 suggests that the critical gradient will increase with  $\hat{s}/q$  but Figures 6.27a and 6.27b indicate this is not the case here. Performing a linear fit to these growth rates, an estimate of the critical gradient can be made and this is shown in Figure 6.28. It is clear that the scaling of Equation 6.5 does not describe this regime. Rather, operating at low  $\hat{s}/q$  is actually beneficial to these modes.

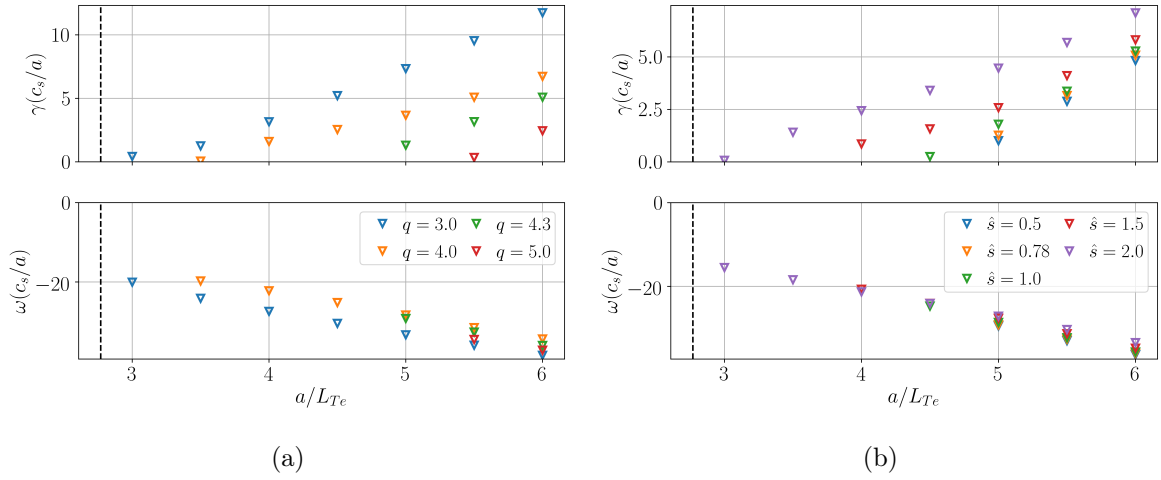


Figure 6.27: Impact of a)  $q$  and b)  $\hat{s}$  with different  $a/L_{Te}$  at  $k_y = 35$ .

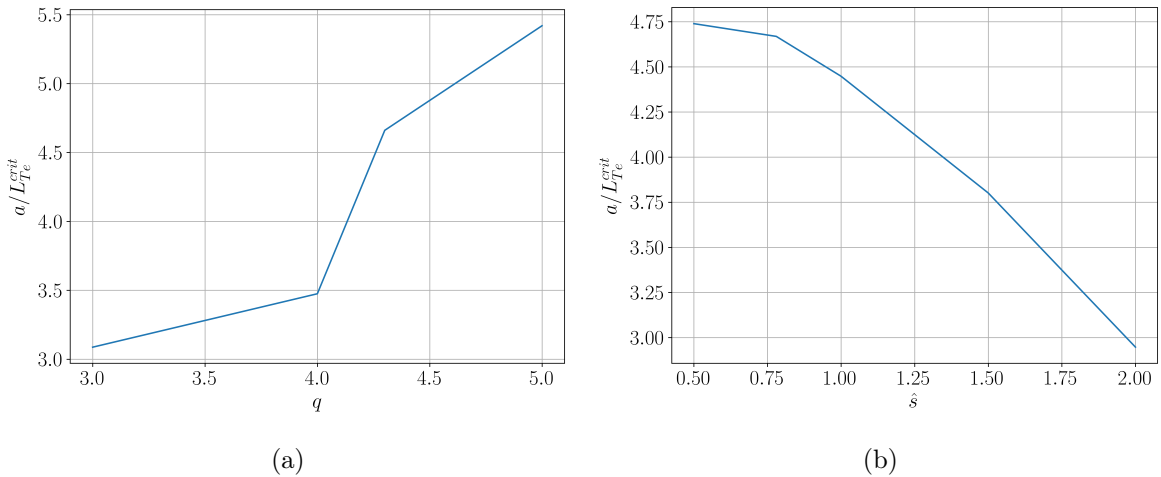


Figure 6.28: Critical  $a/L_{Te}$  threshold for various a)  $q$  and b)  $\hat{s}$  at  $k_y = 35$ .

### 6.4.3 Impact of higher field

Once again, the impact of a higher  $B_\varphi$  was explored. Here the equilibria were taken from SCENE runs with different values of  $I_{\text{rod}}$  outlined earlier and 3 different temperature gradients were examined. Figure 6.29 shows that operating at higher field destabilises these ETG modes, indicating the destabilisation from  $\beta'_{e,\text{unit}}$  is overcoming the stabilisation from lower  $\beta_{e,\text{unit}}$  and higher  $q$ . Nevertheless, for  $a/L_{Te} = 2.77$ , the modes are stable, so for the reference equilibrium it is not a concern.

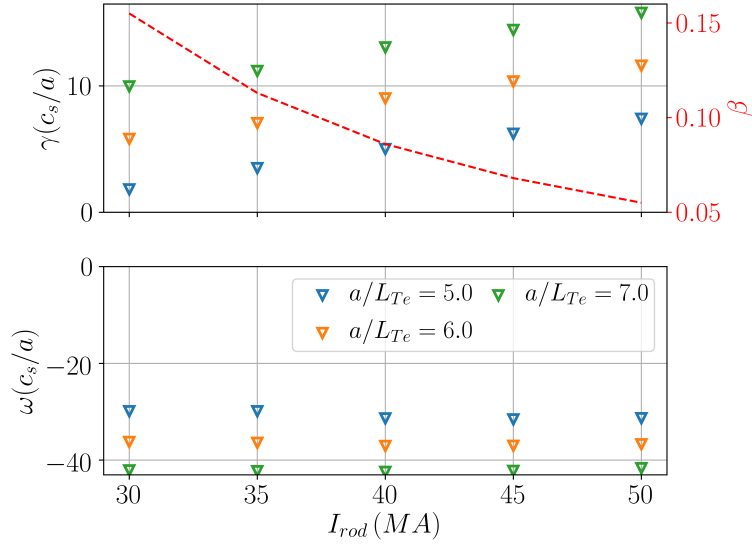


Figure 6.29: Examining the impact of  $I_{\text{rod}}$  on the ETG modes for 3 higher temperature gradients at  $k_y = 35$ .

### 6.4.4 Summary

It has been seen that the main reason for the stability of ETG modes is the high value of  $\beta'_{e,\text{unit}}$  in the reference equilibrium. This suggests that operating at higher field may have some detrimental effect on the high  $k_y$  transport, but for the equilibrium here, the  $I_{\text{rod}} = 50$ MA case was still found to be stable. Furthermore, the ETG critical gradient was found to favour a low  $\hat{s}/q$ , which contradicts previous estimates of the critical gradient found for conventional aspect ratios. This indicates that previous scaling laws are not valid in this high  $\beta$  ST regime, motivating the need for accurate nonlinear and quasi-linear models. Having said that, the high  $k_y$  modes will likely not have a significant impact on the transport, unless  $q$  drops sufficiently.

## 6.5 Stability of a deep core flux surface

So far this chapter has examined the  $\rho_\psi = 0.5$  surface. The  $\rho_\psi = 0.3$  surface will be briefly explored to see if similar modes arise. This surface has a much higher  $\beta_{e,\text{unit}}$  so it can be expected that the KBMs and MTMs seen thus far may be driven further unstable. The lower density gradient is expected to help stabilise the KBM, but the impact on the MTM will be less clear. Furthermore, the lower collision frequency may help to stabilise the MTM.

### 6.5.1 Stability at different scales

The dominant odd and even instabilities at  $\rho_\psi = 0.3$  are shown in Figure 6.30; a similar picture to the mid-flux surface is seen. At the low  $k_y$  both the KBMs and MTMs are seen. This further highlights the need for a transport model to account for both of these sources of transport. Around  $k_y = 4$ , the collisionless MTM seen earlier appears. From  $k_y = 1 \rightarrow 3$  and  $k_y > 6$ , it can be seen that the equilibrium is stable.

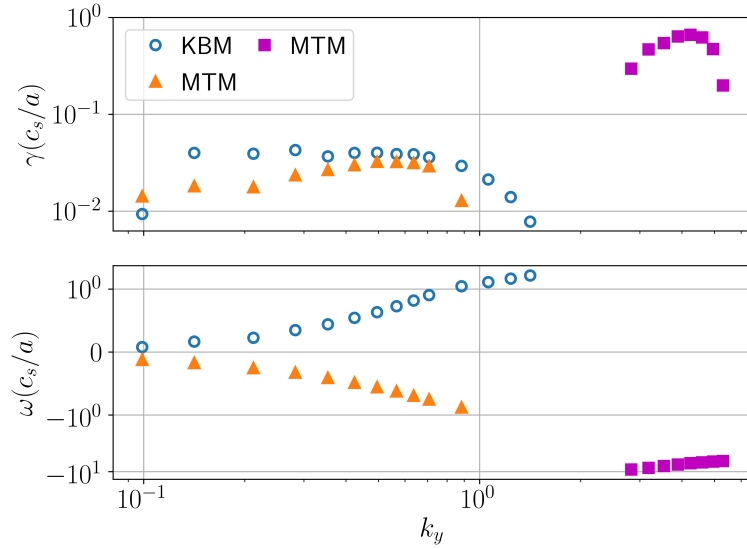


Figure 6.30: a) Dominant odd and even mode for the  $\rho_\psi = 0.3$  surface of the baseline equilibrium.

The eigenfunctions for the KBM and MTM at  $k_y = 0.35$  and the collisionless MTM at  $k_y = 4.2$  are shown in Figure 6.31. The nature of the instabilities seen here are similar to those found that  $\rho_\psi = 0.5$  and suggests that the methods found to stabilise those modes will be applicable here.

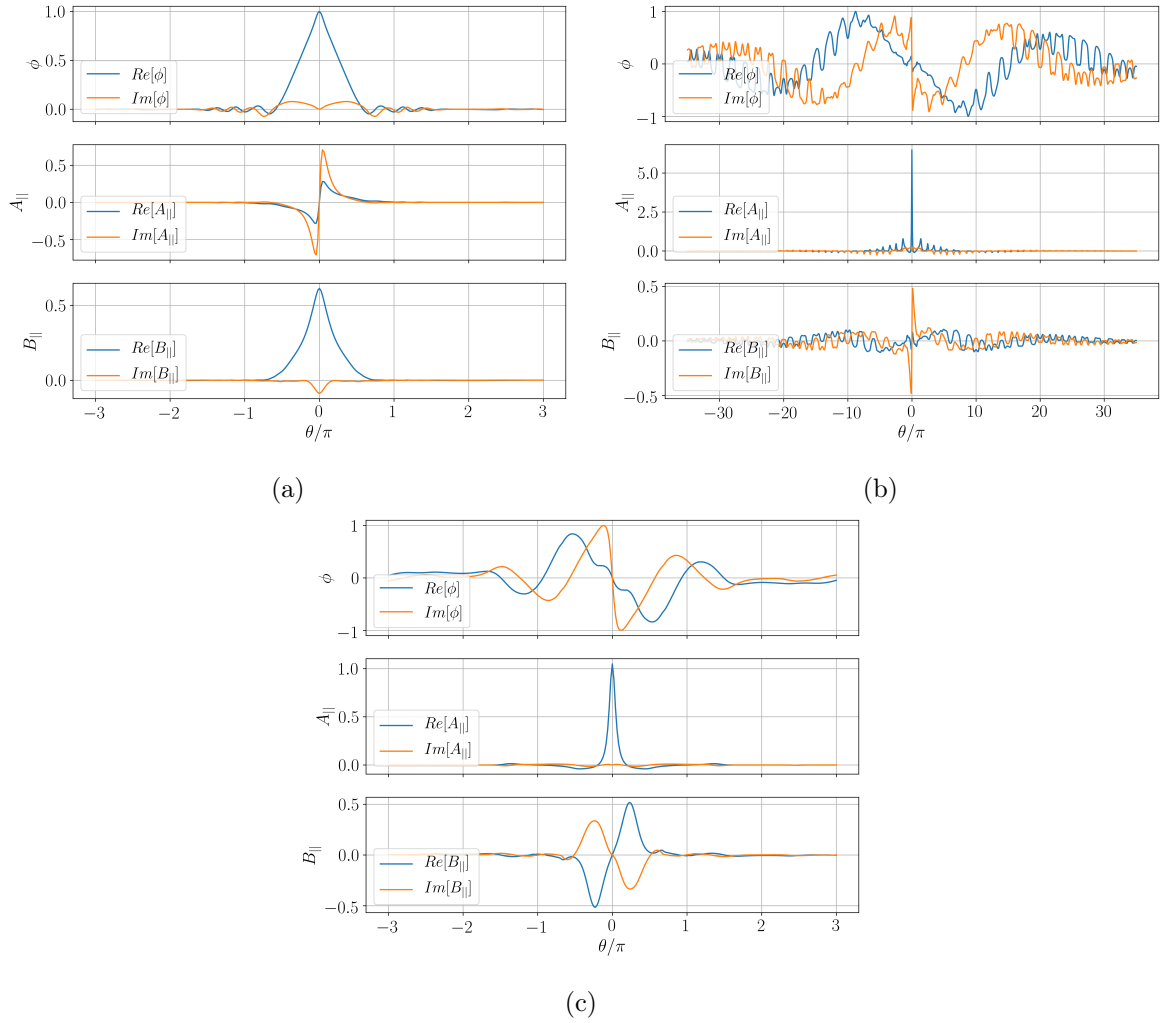


Figure 6.31: Eigenfunctions found for the a) KBM at  $k_y = 0.35$  b) MTM at  $k_y = 0.35$  c) MTM at  $k_y = 4.2$  for the  $\rho_\psi = 0.3$  surface of the baseline equilibrium.

## 6.6 Stability of an edge flux surface

The process was repeated for a surface much closer to the edge, where  $\rho_\psi = 0.85$ . The pedestal top in this simulation was set to  $\rho_\psi = 0.9$ . Here there is a larger population of trapped particles so the impact this has on the modes needs to be explored. This surface has a much lower  $\beta_{e,\text{unit}}$ , but the kinetic gradients are larger so the impact on the MTMs/KBMs seen thus far is not clear.  $\beta'_{e,\text{unit}}$  however has reduced which could destabilise the KBMs. Furthermore, it has a higher collisionality compared to the mid flux surface, which could drive the low  $k_y$  MTMs more unstable.

### 6.6.1 Stability at different $k_y$

With the Miller parameters outlined in Table 6.2, a scan in  $k_y$  was conducted examining the dominant odd and even eigenmodes, shown in Figure 6.32a. At low  $k_y$  a familiar scene is found where both KBM and MTMs co-exist together. However, a new MTM appears around  $k_y \sim 1$  with  $C_{\text{tear}} = 0.7$ . Its eigenfunction is shown in Figure 6.32b. These will be represented with filled brown thin diamonds. This looks similar to the tearing parity eigenfunction seen earlier, though it is significantly less extended, due to the higher  $k_y$ . Around  $k_y = 4$  the collisionless MTMs found previously appear. A narrow window of ETG is seen at  $k_y \sim 35$ , explained by the lower  $\beta'_{e,\text{unit}}$  of this surface.

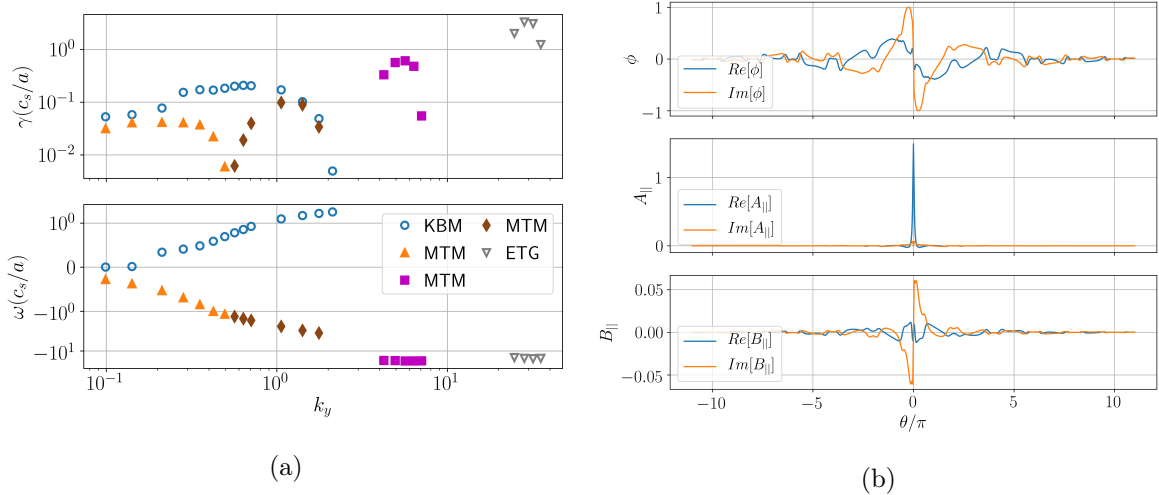


Figure 6.32: a) Dominant odd and even modes for  $\rho_\psi = 0.85$  and b) Eigenfunction of the MTM mode when  $k_y = 1.05$ .

### 6.6.2 Routes to stabilise short-intermediate wavelength MTMs in the edge

The “new” MTM will be further investigated here to see what drives them unstable and how to potentially stabilise them. This section will examine  $k_y = 1.05$ , which provides the peak MTM growth rate. These modes have a similar growth rate to lower  $k_y$  MTM so a mixing length argument like  $\gamma/k_{\perp}^2$  would suggest that these will have a smaller impact on the total transport. Thus they may not be as important for the transport but this can only be confirmed with a good understanding of the physics.

#### Flow shear

Looking at the  $\theta_0$  dependence, shown in Figure 6.33, this MTM is very narrow in  $\theta_0$ . As mentioned earlier, when  $\theta_0 \neq 0$ , GS2 is only able to find the dominant mode, and for  $\theta_0 > 0.1\pi$ , there are no unstable modes at  $k_y = 1.05$ . This suggests that this mode is very sensitive to  $\theta_0$  and was stabilised by a low flow shear of  $\gamma_{E \times B} = 0.02c_s/a$ ; this is below the diamagnetic levels. This provides further evidence that this MTM is unlikely to play a significant role in the transport for the profiles of the reference equilibrium. A question remains - how sensitive to the density and temperature profiles is it?

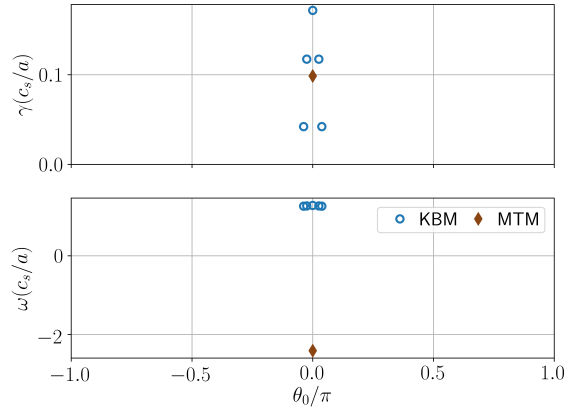


Figure 6.33: Impact of  $\theta_0$  on the MTM seen at  $k_y = 1.05$  when  $\rho_{\psi} = 0.85$ .

#### Kinetic gradients

Examining the impact of the kinetic gradients, Figure 6.34a shows that the equilibrium is close to marginal stability as the the critical electron temperature gradient occurs as  $a/L_{Te} = 2.5$ ; a slight drop from the reference case would stabilise this mode. Figure 6.34b illustrates that this MTM follows the behaviour of the previous MTM with regards to the density gradient with a peak in growth rate. This occurs at  $a/L_n = 1.0$  and to get it completely stable would

required  $a/L_n > 1.8$ . Such a peaked density profile is likely not feasible. It could be dropped further, though that would negatively affect the low  $k_y$  MTMs seen earlier. The peak of the growth rate here occurs at a value of  $a/L_n$  that is above the equilibrium value, which differs to the previous two MTMs. This means that modest density peaking will be unfavourable to these modes. Future work should explore what affects the position of this peak and whether the equilibrium can be designed in such a way that it lies below the equilibrium value of  $a/L_n$ . This would allow for access to peaked density regimes that aren't detrimental to the electron transport. The impact of peaked density profiles on impurity accumulation may then become an issue.

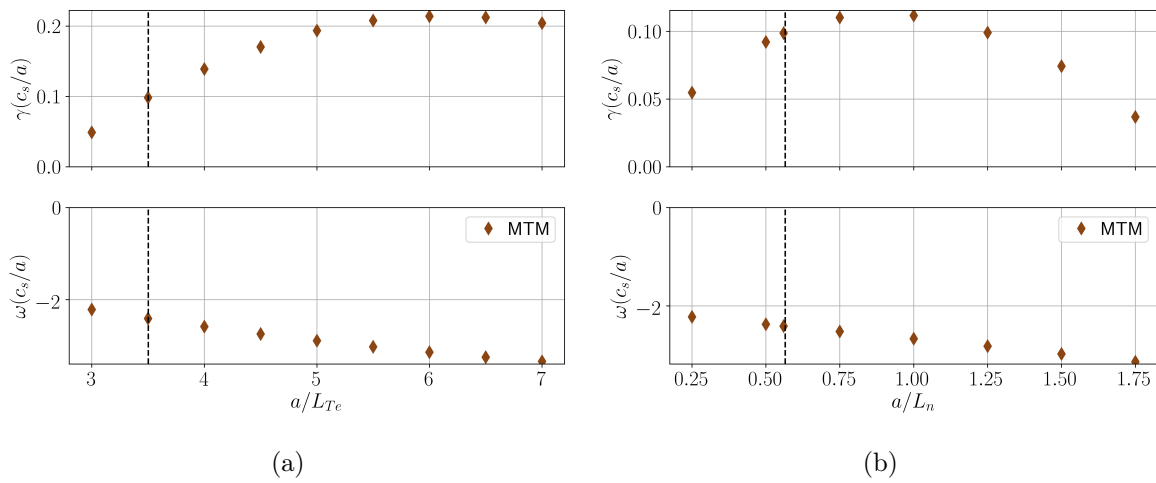


Figure 6.34: Impact of a)  $a/L_{Te}$  and b)  $a/L_n$  on MTM seen at  $k_y = 1.05$  when  $\rho_\psi = 0.85$ .

## Collision Frequency

Figure 6.35 shows the collision frequency dependence. Increasing the collision frequency is destabilising, but as the collision frequency is dropped, there appears to be a minimum in the growth rate. This MTM is unstable in the collisionless limit, further illustrating the difference in nature to the lower  $k_y$  MTM that was examined. A physical reactor would not operate at  $\nu_{ee} = 0.0$ , and this close to the pedestal it would be unlikely that the collisionality would be able to get low enough that this becomes a factor. Nevertheless, this indicates that operation at high temperature/low density will be beneficial.

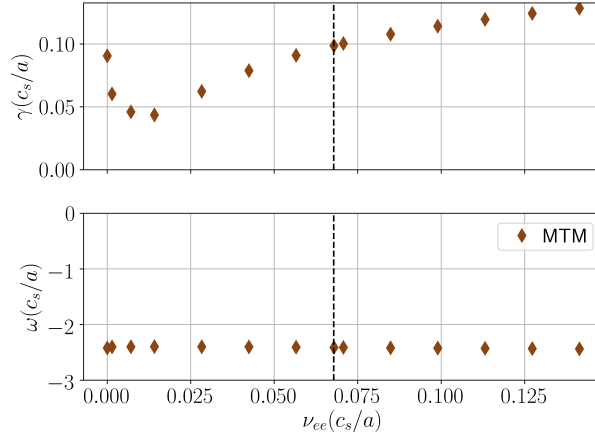


Figure 6.35: Impact of  $\nu_{ee}$  on MTM seen at  $k_y = 1.05$  when  $\rho_\psi = 0.85$ .

### $\beta$ and $\beta'$

This MTM also requires a finite  $\beta_{e,\text{unit}}$  and is stable when  $\beta_{e,\text{unit}} < 0.0025$ . The growth rate increases rapidly with  $\beta_{e,\text{unit}}$  above this value as shown in Figure 6.36a. From Figure 6.36b, it is visible that this MTM is stabilised by  $\beta'_{e,\text{unit}}$ , unlike the low  $k_y$  MTM. To consolidate this, a consistent  $\beta_{e,\text{unit}}, \beta'_{e,\text{unit}}$  scan was performed and it can be seen from Figure 6.36c, that the critical  $\beta_{e,\text{unit}}$  is down shifted, such that this mode is stable below  $\beta_{e,\text{unit}} < 0.002$ . This implies that if the field is sufficiently increased, this mode may be stabilised. Interestingly, a small drop in  $\beta_{e,\text{unit}}$  actually causes the growth rate to increase, implying that a small increase in the field may actually destabilise this mode.

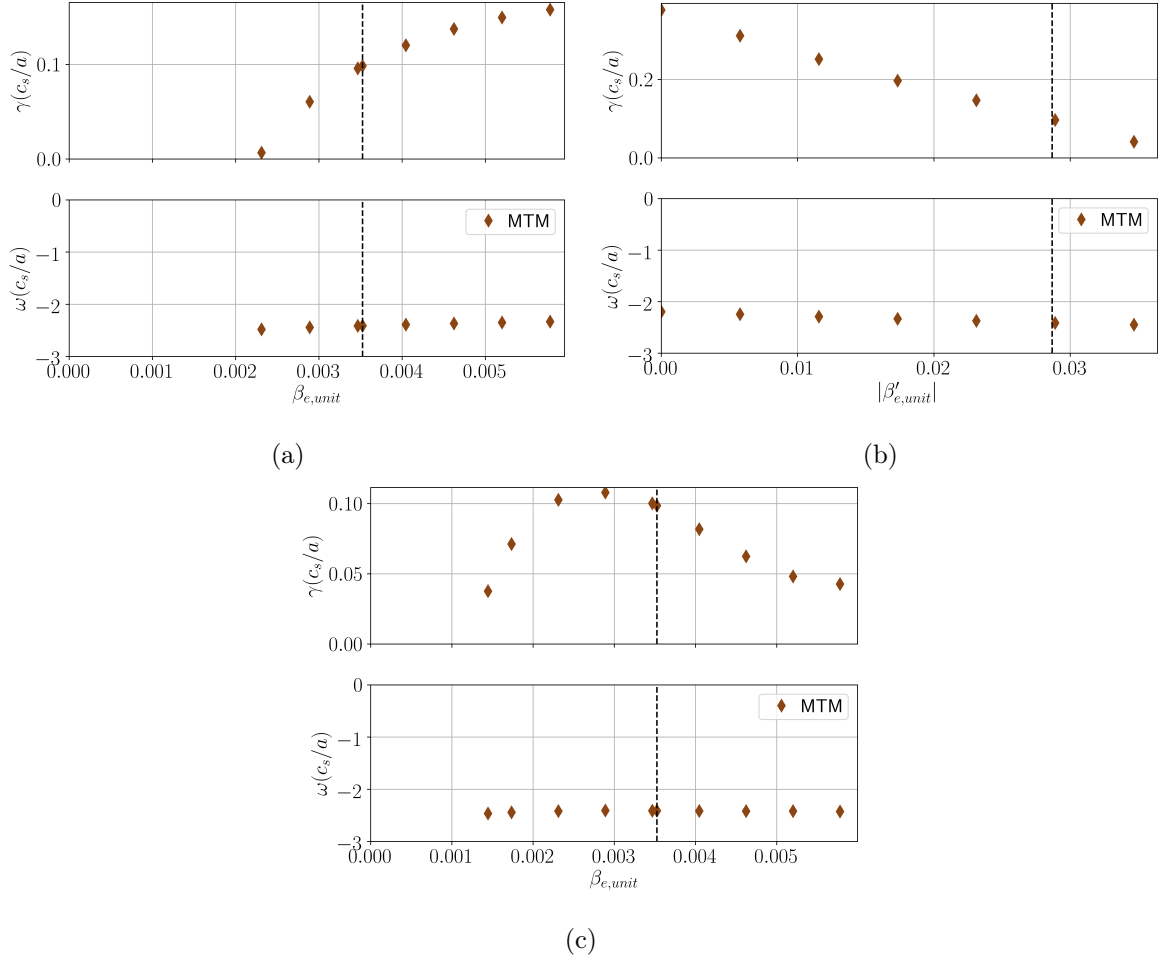


Figure 6.36: Impact of a)  $\beta_{e,unit}$  at fixed  $\beta'_{e,unit}$  and b)  $\beta'_{e,unit}$  at fixed  $\beta_{e,unit}$  and c) consistent  $\beta_{e,unit}$  and  $\beta'_{e,unit}$  for the MTM seen at  $k_y = 1.05$  when  $\rho_\psi = 0.85$ .

### Safety factor profile

The impact of the safety factor profile was considered. Figure 6.37a shows a peak growth rate at  $q = 5.0$ . Pushing to higher field would push to a higher  $q$ , helping to stabilise this mode further. The impact of  $\hat{s}$  is illustrated in Figure 6.37b and it can be seen that there is a minimum around  $\hat{s} = 1.0$ , but it is not possible to completely stabilise this mode by changing  $\hat{s}$ .

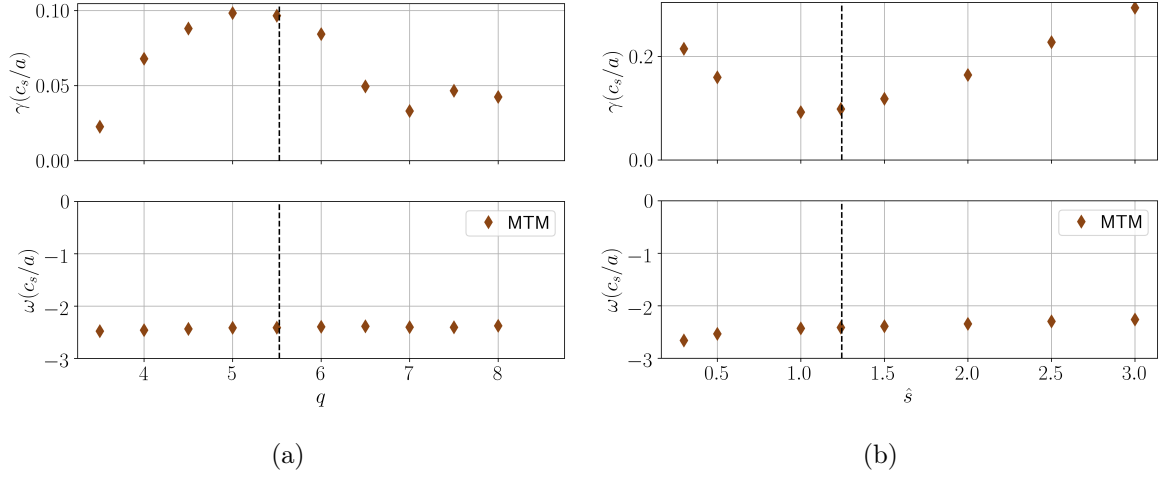


Figure 6.37: Impact of a)  $q$  and b)  $\hat{s}$  on MTM seen at  $k_y = 1.05$  when  $\rho_\psi = 0.85$

### 6.6.3 Impact of higher toroidal field

The impact of changing  $I_{\text{rod}}$  on these MTMs is investigated. From Figure 6.38, it can be seen that a small increase in  $I_{\text{rod}}$  actually destabilises this mode, consistent with the  $\beta_{e,\text{unit}}-\beta'_{e,\text{unit}}$  scan conducted earlier. Above  $I_{\text{rod}} = 35\text{MA}$  this MTM is then stabilised. This highlights again how a higher field device may actually destabilise a mode if there is a strong  $\beta'_{e,\text{unit}}$  dependence.

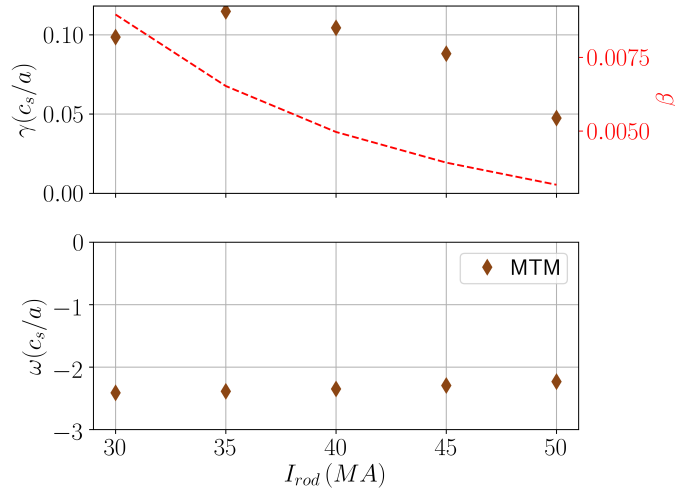


Figure 6.38: Impact of  $I_{\text{rod}}$  on MTM seen at  $k_y = 1.05$  when  $\rho_\psi = 0.85$ .

### Summary

A new collisionless MTM has been found at  $k_y = 1.05$  when  $\rho_\psi = 0.85$ . It was found to be very narrow in  $\theta_0$ , such that with  $\gamma_{E \times B} = 0.02c_s/a$ , the mode would be completely stabilised.

This is below the diamagnetic level meaning it will have minimal impact on the transport. It behaved similarly to the previous MTM in that it is destabilised by  $a/L_{Te}$  and is stable when  $a/L_{Te} < 3.0$ . It also displays the peaked behaviour when scanning through  $a/L_n$ , though the peak of the growth rate lies beyond the equilibrium gradient, meaning peaked densities will be destabilising. A small increase in  $I_{rod}$  was found to be destabilising, but when sufficiently increased the mode was stabilised, but did not go completely stable.

## 6.7 Equilibrium optimised for core turbulent transport

The results of the previous sections suggest that the flow shear will wipe out the KBMs and the high  $k_y$  MTMs found so far. It was also demonstrated that increasing the density gradient was beneficial in stabilising the low  $k_y$  MTMs. If the  $a/L_T$  is reduced whilst increasing  $a/L_n$  to keep  $a/L_p$  fixed, then it may be possible to design an equilibrium in which the majority of the linear instabilities are stable.

Using this information a new equilibrium was designed in SCENE with a more peaked density profile. Thus, the pedestal height was set to be 40% of the core, as opposed to 90% in the baseline, at fixed  $P_{fus} = 1.1\text{GW}$ . The pedestal width was kept the same. To reduce the temperature gradient drive for the KBMs, the core temperature for both species was dropped from 28keV to 20keV. Furthermore, the auxiliary current profile found using NUBEAM in Chapter 5 was used, though given the different temperature/density the deposition will likely not be a perfect match. It was possible to have a monotonic  $q$  profile with  $q_0 = 2.14$ . The equilibrium was then re-calculated and the amount of auxiliary current needed has dropped to 7.13MA, due to the higher density gradient generating more bootstrap and diamagnetic current. The auxiliary power was then set using  $\eta^*$  in Equation 5.2 given the updated  $\langle T_e \rangle$ ,  $\langle n_e \rangle$  and  $I_{ext}$ . The resulting equilibrium parameters are outlined in Table 6.3.

The parameters are broadly similar to the baseline case, with the exception of the density and temperature values. For example, this equilibrium had an  $n_{e0}/\langle n_e \rangle = 1.58$ , compared to  $n_{e0}/\langle n_e \rangle = 1.12$  in the baseline case. There is experimental evidence from AUG and JET of achieving  $n_{e0}/\langle n_e \rangle$  up to 2.0 with sufficient NBI fuelling [193, 194], which motivates the use of a core NBI for heating, current drive and particle deposition, though higher core densities will make penetration more difficult. If this is not sufficient then core pellet injection will be necessary.

The Miller and plasma parameters for the  $\rho_\psi = 0.5$  surface is detailed in Table 6.4. It can be seen that many of the parameters are very similar to the baseline parameters in Table 6.2,

with the notable exception of the higher  $a/L_n$  and lower  $a/L_T$  as expected. However,  $a/L_p$  has increased overall from 6.40 to 7.48, so it may be expected that the KBMs will be driven more unstable, though as seen in earlier sections, this is counteracted by the increased  $\beta'_{e,\text{unit}}$ .  $\hat{s}/q$  has increased, due to the differences in the auxiliary, bootstrap and diamagnetic current profiles. This is expected to destabilise the KBMs but its impact on the MTMs is less clear.

Parameter	Value
$R_{\text{maj}}$ (m)	2.5
$a$ (m)	1.5
$R_0$ (m)	3.05
$I_{\text{rod}}$ (MA)	30.0
$I_p$ (MA)	21.0
$I_{\text{aux}}$ (MA)	7.13
$P_{\text{fus}}$ (MW)	1100
$P_{\text{aux}}$ (MW)	83
$\kappa$	2.8
$\delta$	0.55
$H_{98}, H_{\text{Petty}}$	1.26, 0.83
$T_{e0}, \langle T_e \rangle$ (keV)	22.0, 14.1
$n_{e0}, \langle n_e \rangle$ ( $\times 10^{20} \text{m}^{-3}$ )	2.19, 1.38
$l_i$	0.38
$\beta_N$	5.13
$q_0$	2.07

Table 6.3: Basic plasma parameters for the optimised scenario

Parameter	$\rho_\psi = 0.5$
$r/a$	0.67
$R_{\text{maj}}/a$	1.83
$n_{e20}$ ( $\text{m}^{-3}$ )	1.36
$T_e$ (keV)	12.8
$a/L_n$	1.40
$a/L_T$	2.34
$\Delta$	-0.48
$q$	3.14
$\hat{s}$	0.97
$\kappa$	2.87
$s_\kappa$	-0.11
$\delta$	0.34
$s_\delta$	0.21
$\beta_e$	0.14
$\beta_{e,\text{unit}}$	0.013
$\rho^*$	0.0014
$\nu_{ei}(c_s/a)$	0.013
$\gamma_{\text{dia}}(c_s/a)$	0.055

Table 6.4: Plasma and Miller parameters for the  $\rho_\psi = 0.5$  surface of the optimised equilibrium.

The dominant instabilities are presented in Figure 6.39. Similar to the baseline scenario, in the low  $k_y$  region KBMs and extended MTMs are found. However, the peak MTM growth rate is  $\gamma_{\text{MTM}} = 0.0038c_s/a$ , significantly lower than the baseline scenario where it was  $\gamma_{\text{MTM}} = 0.035c_s/a$ . The KBM peak growth rate is has increased from  $\gamma_{\text{KBM}} = 0.09c_s/a$  to  $\gamma_{\text{KBM}} = 0.19c_s/a$ , but these modes are still narrow in  $\theta_0$  so it will be shown that these are wiped out

by flow shear. The higher  $k_y$  MTMs are also seen and have a lower growth rate reducing from  $1.2c_s/a$  to  $0.9c_s/a$ , and it is expected that the flow shear will help to stabilise these modes as well. Finally above  $k_y = 6$ , the equilibrium was found to be completely stable, similar to the baseline case. It should be noted that these modes peak at a lower  $k_y$  compared to the baseline case and this is expected as  $\rho^*$  has not significantly changed but the value of  $q$  is lower. Specifically, given that  $k_y = nq/r$ , to find a given toroidal mode number  $n$  at lower  $q$ , a lower  $k_y$  is needed.

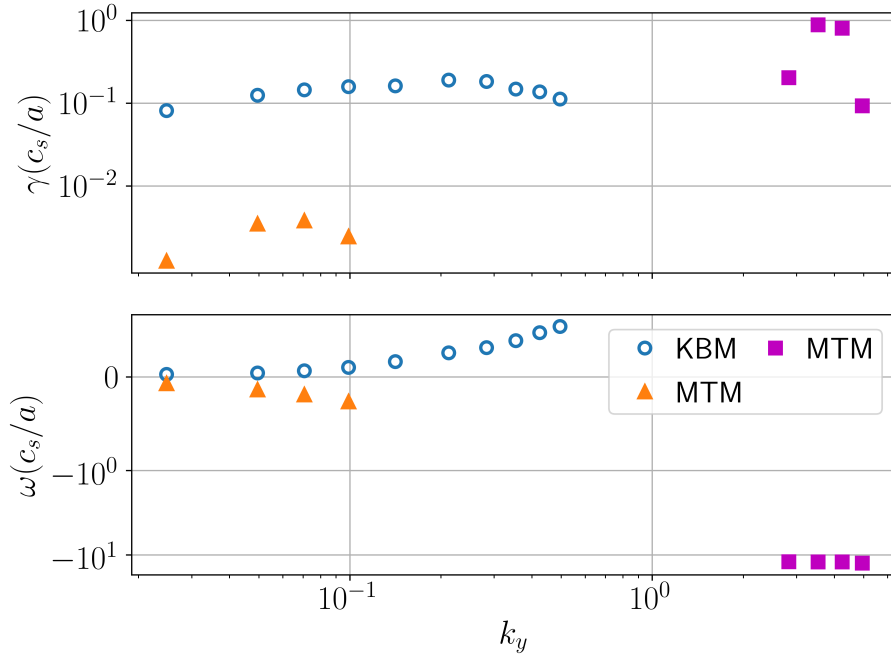


Figure 6.39: Dominant odd and even mode for the  $\rho_\psi = 0.5$  surface of the optimised equilibrium without flow shear outlined in Table 6.4.

A simulation was run for this case with  $E \times B$  flow shear at the diamagnetic level of  $\gamma_{\text{dia}} = 0.055c_s/a$ . The effective growth rate is shown in Figure 6.40 and it was found that above  $k_y = 0.2$  the equilibrium was completely stable. Below this value, the MTMs did cause a very slowly growing mode with a growth rate  $\mathcal{O}(10^{-3})c_s/a$ ; this is sufficiently low that this equilibrium is considered to be marginally stable. If such a peaked density is possible to obtain during the ramp up then this would be a very desirable property as the plasma may operate close to neoclassical levels of transport. The impact of impurities and fast ions needs to be examined as they may drive the MTM more unstable, increasing the effective growth rate. In particular, density peaking can lead to impurity accumulation in the core of conventional tokamaks, which would be detrimental to the performance of a reactor. While quantifying the level of impurity accumulation and impact on radiative losses is important, this equilibrium

suggests a high performance high  $\beta$  ST may be possible.

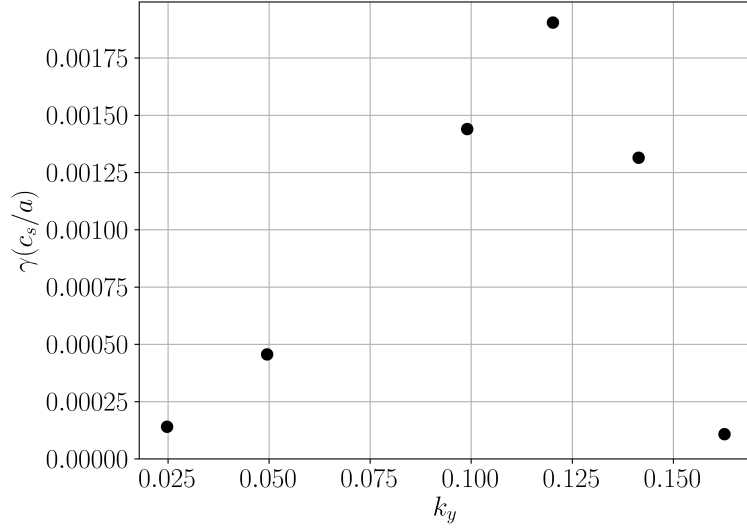


Figure 6.40: Effective growth rate for the  $\rho_\psi = 0.5$  surface of the optimised equilibrium with diamagnetic levels of flow shear.

## 6.8 Summary

Overall, it has been shown that MTMs are prevalent in our baseline high  $\beta$  ST equilibrium. They were found at both long and intermediate scales, though at long wavelength they appear to be subdominant compared to KBMs. The KBMs were very narrow in  $\theta_0$ , such that at diamagnetic levels of flow shear, they would be suppressed. These were driven by all of the different kinetic gradients and were destabilised by  $\beta_{e,\text{unit}}$ . However, they were stabilised by  $\beta'_{e,\text{unit}}$ , such that when increasing the toroidal field, the overall effect was a very weak stabilisation.

The low  $k_y$  MTMs growth rate was found to increase with increased  $\nu_*$ . The impact of  $\hat{s}/q$  was non-monotonic indicating that further understanding is required here. Furthermore, it was found that these modes are relatively insensitive to  $\beta'_{e,\text{unit}}$ , but were destabilised by  $\beta_{e,\text{unit}}$ . This, combined with the destabilising  $q$ , resulted in the MTM growth rate not changing significantly at higher toroidal field. Operating at low collisionality reduces the growth rates for these MTMs suggesting a high temperature/low density device is preferable. Furthermore, density peaking will further assist in stabilising these modes. Care should be taken, as a peaked density profile will likely impact  $q$  and  $\hat{s}$  via the change in the bootstrap current. Furthermore, previous devices have found that density peaking can lead to impurity accumulation in the core (a consequence of neoclassical transport) which will lead to a range of other issues with

radiative losses.

The intermediate  $k_y$  MTMs were found to be collisionless and were narrow in  $\theta_0$ , such that a small amount of flow shear was sufficient to stabilise the mode. They had a similar response to the lower  $k_y$  MTMs when changing the kinetic gradients, but were relatively insensitive to  $\hat{s}$ . However, it was found that operating at sufficiently high  $q$  helped to stabilise them. This resulted in a strong stabilisation of this intermediate  $k_y$  MTM when increasing  $I_{\text{rod}}$ .

This equilibrium was found to be stable in the electron scale range of  $k_y$  and the primary cause of that was found to be the large  $\beta'_{e,\text{unit}}$ . When increasing the ETG drive sufficiently, it was shown that a higher field makes the ETG more unstable as the stabilisation from the lower  $\beta_{e,\text{unit}}$  and higher  $q$ , was counteracted by the destabilising nature of lower  $\beta'_{e,\text{unit}}$ , similar to the KBMs seen earlier. Furthermore, operating at low  $\hat{s}/q$  was found to be stabilise the KBMs, but had a more complicated relationship with the MTMs.

An optimised equilibrium was generated with a more peaked density profile and flatter temperature profile. With flow shear the equilibrium was found to be close to marginally stable, indicating that operating close to neoclassical levels of transport may be feasible if such an equilibrium can be accessed. However, the level of impurity accumulation from the density peaking needs to be determined as it may lead to a radiative collapse.

To quantify the level of transport driven from each of these different modes requires nonlinear simulations or a reduced physics model capable of capturing the nonlinear properties of the different types of modes expected to play a role on the transport. This will inform on which modes contribute the most to the transport and thus should be prioritised in their stabilisation. The next chapter discusses the accuracy of existing quasi-linear models, highlights some of the challenges that will need to be addressed and the initial progress in this direction.

## Chapter 7

# Assessment of quasi-linear transport models for a high $\beta$ ST

The previous chapter illustrates the instabilities arising in a high  $\beta$  ST reactor, guiding the physics that any plasma turbulence model should capture. In particular, both KBM and MTM based transport could be prevalent in a BurST regime and this chapter will explore the validity of quasi-linear theory to describe these. The first step of testing a quasi-linear model is to ensure that the linear physics is being captured correctly. This can be done in part by comparing the eigenvalues predicted by different linear gyrokinetic solvers. Without accurate linear physics there can be no confidence in the quasi-linear predictions. Initially, in Section 7.1 the predictions made by GS2, CGYRO and TGLF for the linear eigenvalues in the BurST regime will be examined and it will be shown that the eigensolver in TGLF is not sufficient in modelling this reactor. This motivates developing a new model, QLGYRO, which combines the CGYRO linear initial value solver with the TGLF saturation rule. This allows for a direct test of the quasi-linear assumption and saturation rule in TGLF, without concern for the validity of the linear physics.

With an accurate linear solver, a high level strategy for testing quasi-linear models is to compare the flux predictions with those from full nonlinear simulations. This can be further probed by comparing the predictions for the quasi-linear weights and saturated potential. These can be tested independently and will help to highlight any shortcomings in the quasi-linear method. Thus a set of nonlinear simulations are needed. Electromagnetic nonlinear simulations are generally challenging near the ideal ballooning limit and with large scale MTMs. An attempt was made at nonlinear BurST simulations in Section 7.2, though it proved difficult to obtain converged results due to the extremely large computational cost.

This further motivates the use of accurate quasi-linear models as they provide a potential route to flux predictions with significantly less computing power.

It is still necessary to benchmark QLGYRO especially in high  $\beta$  ST regimes and that is the subject of this chapter, taking the following approach. Starting from a simple conventional aspect ratio tokamak plasma and building up towards a high  $\beta$  ST regime, the validity of QLGYRO will be explored in progressively challenging equilibria. Initially the GA-STD equilibrium, which was used to develop the original TGLF saturation rule, will be examined in Section 7.3. QLGYRO and TGLF are compared to nonlinear CGYRO simulations. Several parameter scans are performed around the GA-STD case to explore whether the quasi-linear codes are able to capture the trends correctly. This will be especially useful to validate the approach taken to compare the results. Next, a low  $\beta$  MAST equilibrium will be examined in Section 7.4 to see if the quasi-linear models perform well for a ST equilibrium, whilst ensuring the transport is still dominated by electrostatic fluctuations similar to the GA-STD case. Following this, a higher  $\beta$  NSTX equilibrium will be examined in Section 7.5 where MTMs are found to be the dominant linear mode. This is directly relevant for BurST as MTM-based transport is expected to be important. Again, for both the MAST and NSTX equilibria, QLGYRO and TGLF are compared to CGYRO to see how the quasi-linear approximation fares and where it begins to break down. In each case the predictions made for the quasi-linear weights and saturated potential, defined in Chapter 3, are examined. An overall breakdown of this chapter is as follows

- Section 7.1: Motivating the need for QLGYRO
- Section 7.2: Exploring the requirements for nonlinear BurST simulations
- Section 7.3: Validity of quasi-linear models for GA-STD equilibria
- Section 7.4: Validity of quasi-linear models for MAST equilibria
- Section 7.5: Validity of quasi-linear models for NSTX equilibria
- Section 7.6: Summary

## 7.1 Need for QLGYRO

For any quasi-linear model it is crucial that the linear physics is being accurately captured. One method to check this is to compare the linear eigenvalues predicted by each turbulent code. In this section we will make a comparison between TGLF, GS2 and CGYRO. The

dominant mode predicted by each code for  $\rho_\psi = 0.5$  surface of the baseline BurST equilibrium, outlined in Table 4.2, is compared in Figure 7.1. All three codes used the Miller formulation for the equilibrium. These predictions include all three fields and it can be seen that GS2 and CGYRO agree well. These CGYRO simulations were performed with 64  $\theta$  grid points, 8 energy grid points and 24 pitch angle grid points. At the lowest  $k_y$ , both CGYRO and GS2 find the extended MTMs. From  $k_y = 0.2 \rightarrow 2.0$ , they both find a KBM. Around  $k_y = 4$ , both find the collisionless MTM and above  $k_y > 6$ , they find the equilibrium to be completely stable. The agreement between the two codes demonstrates the linear gyrokinetic equation is being correctly solved by both codes.

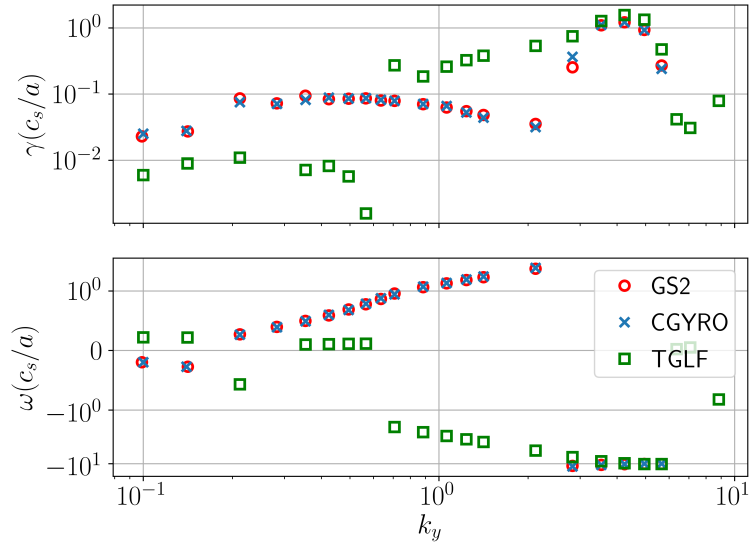


Figure 7.1: Linear spectra of the fully electromagnetic dominant mode predicted by GS2, CGYRO, and TGLF for the BurST baseline equilibrium.

However, the TGLF prediction is noticeably different to the GS2 and CGYRO result. These TGLF runs used 32 Hermite polynomials to fit the eigenfunction and integrals along the field line were approximated using Gauss-Hermite quadrature with 32 nodes, effectively resulting in a mesh of 32  $\theta$  points. The maximum range of  $\theta$  it can model is from  $-9\pi \rightarrow +9\pi$ . This is currently the highest resolution achievable by TGLF and is generally more than sufficient for the modes found in lower  $\beta$  conventional tokamaks. However, the extended MTM found in Chapter 6 extended from  $-71\pi \rightarrow 71\pi$ , demonstrating that the range in TGLF is not sufficient. In addition, for  $k_y < 2$  it does not find the clear spectrum of KBM. However, TGLF does find a MTM at  $k_y = 4.2$ , similar to the other two codes at  $k_y \sim 4$ , but it finds it to be unstable across a much wider range of  $k_y$ , down to  $k_y \sim 1$ . Nevertheless, it does illustrate that TGLF is able to capture MTMs, albeit not perfectly.

The above result suggests that TGLF will not be sufficient to model the transport in this BurST regime. The work presented here will not focus on improving the TGLF eigensolver, although the development of a fast eigensolver suitable in the high  $\beta$  ST regime will help accelerate the scenario development of BurST. Rather, this chapter will focus on testing the quasi-linear approximation and saturation rule via QLGYRO, which ensures the linear physics is correctly captured. If the quasi-linear approximation and saturation rule agree with nonlinear simulations, then use of QLGYRO in a transport solver can be justified.

Linear CGYRO is unable to force an odd or even eigenfunction like GS2, meaning that usage as a pseudo-eigensolver is not currently possible\*. It will only find the dominant mode such that any sub-dominant MTMs will not be accounted for in the quasi-linear transport calculations. Though this is a significant shortcoming in the current QLGYRO model/approach, if such a solver, such as GS2, is incorporated into QLGYRO then this issue could be overcome.

It is worth highlighting that it was possible to find the low  $k_y$  MTMs by turning off  $B_{\parallel}$  in QLGYRO, as this would ensure the MTMs are the dominant mode. When doing so both CGYRO and GS2 agreed well, but TGLF still was not able to find these MTMs.

In the next section we will examine an attempt at performing nonlinear turbulence simulations of the high  $\beta$  BurST equilibrium with CGYRO, and examine the problems encountered when doing so.

## 7.2 Nonlinear BurST simulations

An attempt was made to perform nonlinear simulations of the plasma turbulence in the BurST equilibrium outlined in Table 4.2 with the relevant gyrokinetic parameters in Table 6.2. All three fields were kept, as it was shown in Chapter 6 that all three are necessary to capture the relevant physics. These simulations used the same Miller parameters and numerical grid as the linear simulation outlined in the previous section. 24 bi-normal wavenumbers were simulated from  $k_y = 0.0 \rightarrow 1.61$ , resulting in a box size of  $L_y = 90\rho_s$ . This  $k_y$  range was originally chosen to encompass the low  $k_y$  KBMs and MTMs seen in Figure 7.1, without encroaching on the high  $k_y$  MTMs. 256 radial wavenumbers from  $k_x = -10.9 \rightarrow 10.9$  were simulated resulting in a radial box size of  $L_x = 80\rho_s$ .

Figure 7.2a shows a time trace of the fluxes for the different fields (line style) and species

---

\*It would be feasible to add this in as a feature in CGYRO. Otherwise it is also possible to use GYRO which has an eigensolver method. However, GYRO uses a finite differences scheme in the radial direction such that such high radial resolutions become prohibitively expensive rather quickly.

(colour). It can be seen that the flux is predominantly in the electron channel from  $A_{\parallel}$ , as expected from MT transport. This is not consistent with KBM transport which tend to have a more even ratio of electron to ion heat flux [195]. Figure 7.2b zooms in on the other fluxes and it is clear that these have not yet saturated and appear to be growing. This highlights the importance of capturing these MTMs in a BurST regime as they appear to be a dominating transport process, even though linearly they are sub-dominant. The fluxes are normalised to the gyro-Bohm flux defined as

$$Q_{\text{gB}} = n_e T_e c_s \left(\frac{\rho_s}{a}\right)^2 \quad (7.1)$$

For this equilibrium  $Q_{\text{gB}} = 0.6\text{MW m}^{-2}$  and the surface area of this flux surface is  $\sim 240\text{m}^{-2}$ . Given that the total  $P_{\text{heat}} = 310\text{MW}$ , a maximum heat flux of  $\sim 2Q_{\text{gB}}$  would be sustainable. The flux shown here is well over this, suggesting that this temperature profile would collapse with the level of transport predicted.

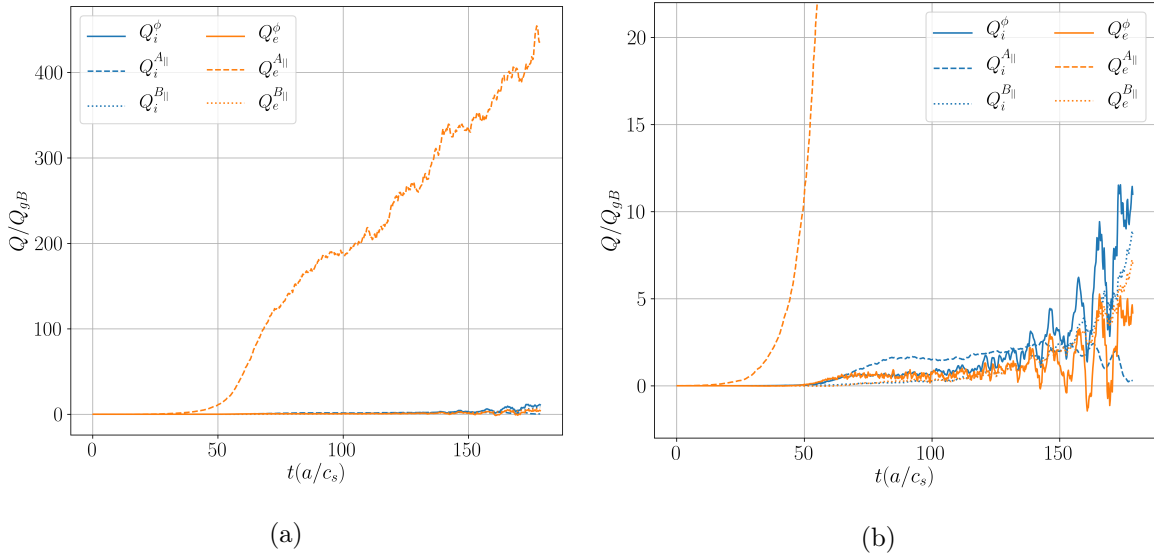


Figure 7.2: a) Time trace of the different flux components for the BurST equilibrium, with the electron flutter flux dominating the spectrum, indicative of MT transport. b) Zoomed in on the other fluxes. Note that this simulation has not saturated.

However, it is also clear that the flux is continuously building up and does not appear to have saturated. Running these simulations for longer becomes computationally expensive, largely due to the time-step dropping down to  $\mathcal{O}(10^{-4})a/c_s$  to satisfy integration stability limits. This simulation alone required over 200,000CPUh on the Marconi cluster.

An issue found by Guttenfelder *et al* [196] was that if a high enough  $k_x$  is not simulated then a build up of electrostatic potential occurs as the highest  $k_x$  as there is not enough dissipation.

This becomes especially important for modes with extended eigenfunctions where electrons are able to stream far along the field line. The MTMs found here extend out to  $k_x \approx 40$  which effectively requires a multi-scale simulation. Figure 7.3 shows the potential as a function of  $k_x$  summed over  $k_y$  at  $\theta = 0$ . It is clear from here that the build up of potential at high  $k_x$  is occurring, suggesting that a higher  $k_x$  is necessary.

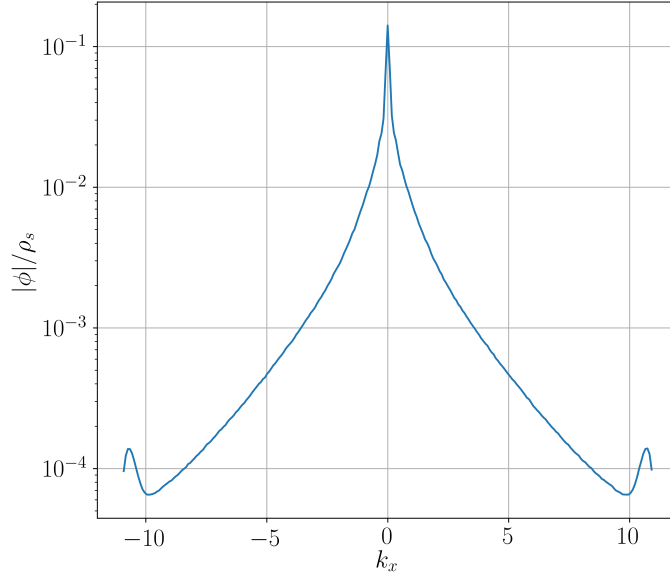


Figure 7.3:  $k_x$  spectrum of  $\phi$  summed over  $k_y$  at  $\theta = 0$ . A build up of potential is seen at the highest  $k_x$ , suggesting insufficient radial resolution to properly capture the dissipative damping mechanism.

Performing multi-scale simulations with reasonable box sizes was not affordable with the computational resources currently available to the author. Different methods were attempted in order to see if a converged result was possible without needing such a high resolution.

A simulation was performed with a smaller radial box and more radial modes in an attempt to see if this would improve convergence. 384 radial wavenumbers from  $k_x = -18.7 \rightarrow 18.7$  were simulated resulting in a radial box size of  $L_x = 65\rho_s$ . The number of bi-normal modes was also reduced to 16 going from  $k_y = 0 \rightarrow 1.5$  resulting in a box size of  $L_y = 63\rho_s$ . However, Figure 7.4a shows that this build up still occurs with  $\phi(k_x \approx 18)$  being at similar levels to the simulation with the larger box.

An option explored was to modify the equilibrium such that the MTM are less extended in ballooning space. It was seen in linear simulations that increasing the collisionality helped reduce the extent of the modes. However, this would also further destabilise the MTMs potentially increasing the transport. A simulation was conducted with the collisionality increased

by approximately a factor of 3 to  $\nu_{ee} = 0.05c_s/a$  using the original numerical set up. Figure 7.4b illustrates that the build up at high  $k_x$  still occurs. Future work can examine whether increasing  $\nu_{ee}$  further will prevent this build up.

Another method considered was to increase the magnetic shear. Chapter 6 showed this was stabilising for the MTMs and given that  $k_x = k_y \hat{s} \theta$ , for the same bi-normal box length and number of radial modes, a much higher  $k_x$  would be reached, making it doubly beneficial. A simulation was performed with  $\hat{s} = 1.5$  and the resulting  $k_x$  spectrum is shown in Figure 7.4c. Even when going out to such a high  $k_x$ , the build up is still seen.

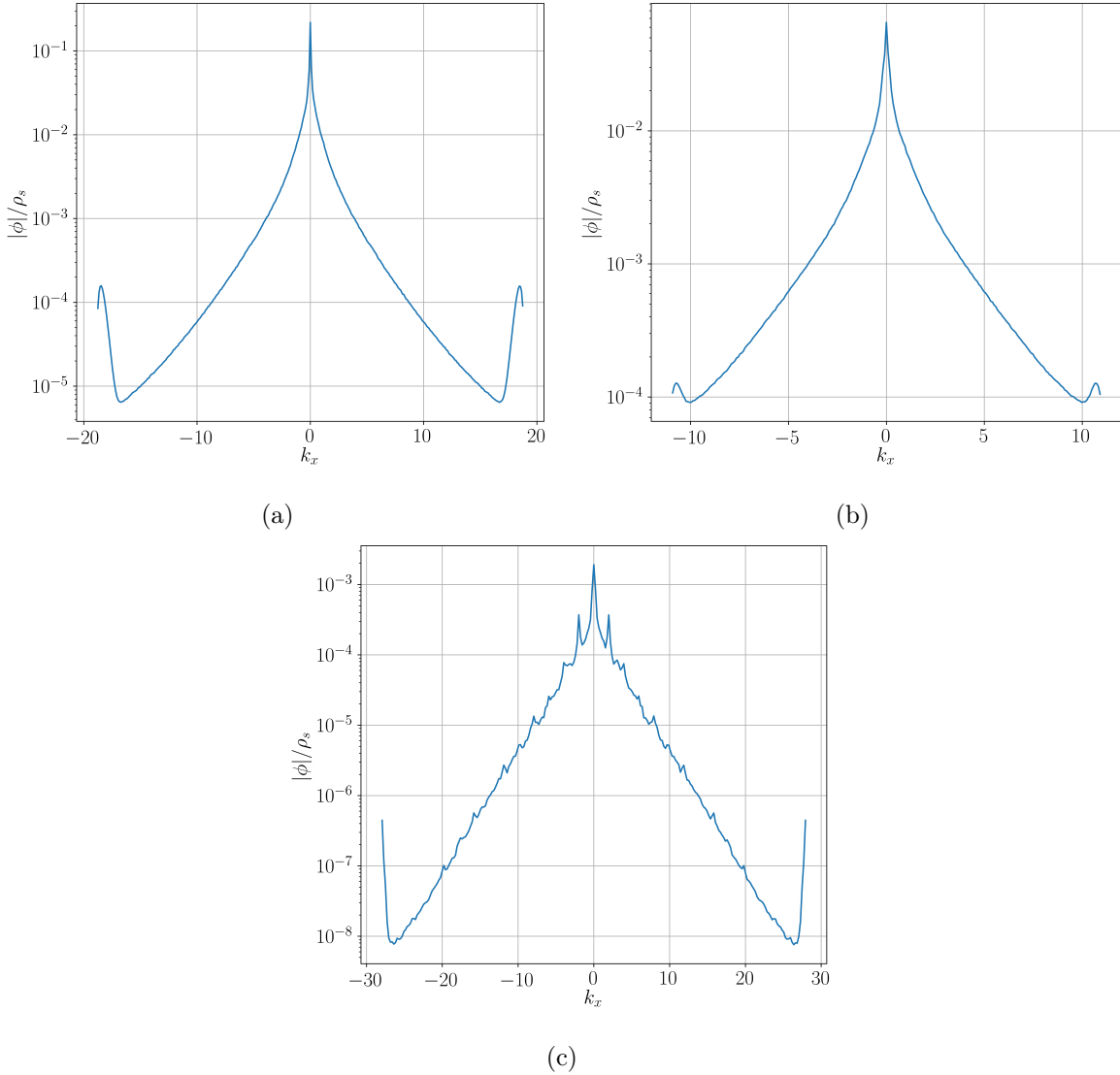


Figure 7.4:  $k_x$  spectrum of  $\phi$  with a) 384  $k_x$  modes and  $L_x = 65\rho_s$  b) increased collisionality of  $\nu_{ee} = 0.05c_s/a$  and c) increased  $\hat{s} = 1.5$ .

The numerical dissipation was artificially increased at the high  $k_x$  by a factor of 5 but this problem build up still persisted. Finally, reducing  $\beta$  or including flow shear also did not help

with the issue.

Due to constraints with computing time, it was not possible to further increase the resolution, but it appears that higher resolution simulations may be required to find saturated results.

To bench-mark QLGYRO and any other model for transport in this regime will require converged nonlinear simulations; while the results provided here provide some clues, this research is left as future work. If the quasi-linear weights and saturation rule are validated in a MTM dominated ST regime then it would be reasonable to use the quasi-linear models to explore the BurST regime in detail. The remainder of this chapter examines QLGYRO and TGLF in simpler equilibria that are easier to find converged results but nevertheless challenge quasi-linear theory in new ST relevant regimes. This entire chapter will utilise CGYRO as the linear initial-value solver for QLGYRO. Any results from here onward labelled as CGYRO will refer only to nonlinear CGYRO simulations.

### 7.3 GA-STD - ITG turbulence

To begin with, QLGYRO was bench-marked against nonlinear simulations of a simple conventional aspect ratio equilibrium. The GA-STD case is often used as a simple equilibrium and is based on a DIII-D like plasma. The equilibrium parameters used for these runs are shown in Table 7.1. These simulations were performed with 32  $\theta$  points, 8 energy grid points, 16 pitch angles. Two kinetic species were included; deuterium ions and electrons. 16 bi-normal wavenumbers from  $k_y = 0.0 \rightarrow 1.005$  with a box size of  $L_y = 94\rho_s$  and 128 radial wavenumbers from  $k_x = -4.42 \rightarrow 4.42$  with  $L_x = 90\rho_s$  were found to be sufficient to model this equilibrium. This case was run to  $t = 1500a/c_s$  to ensure convergence. Both  $\phi$  and  $A_{||}$  were included in this simulation, though the low  $\beta_{e,\text{unit}}$  means the impact of the electromagnetic term will be negligible. These simulations are have been explored thoroughly with many different codes and is useful to check our approach in a more familiar parameter space before STs are explored in subsequent sections.

$r/a$	$R/a$	$\kappa$	$s_\kappa$	$\delta$	$s_\delta$	$q$	$\hat{s}$	$\Delta$
0.5	3.0	1.0	0.0	0.0	0.0	2.0	1.0	0.0
$a/L_{Te}$	$a/L_{Ti}$	$a/L_n$	$\beta_{e,\text{unit}}$	$\beta'_{e,\text{unit}}$	$T_i/T_e$	$\nu_{ee}(c_s/a)$	$\gamma_{E \times B}(c_s/a)$	$Z_{\text{eff}}$
3.0	3.0	1.0	0.05%	0.0	1.0	0.1	0.0	1.0

Table 7.1: Miller and plasma parameters for GA-STD case

The time trace of the different components of the energy flux are shown in Figure 7.5, which looks converged albeit with large spikes in flux. The dashed line shows the component of flux arising from  $A_{\parallel}$  and it can be seen that for this case it is very close to 0; this is unsurprising given the low  $\beta_{e,\text{unit}}$ . Numerical values of the turbulent fluxes and their  $k_y$  spectrum are derived from averages of the final 50% of the time trace (Figure 7.5) and error bars are taken from its standard deviation.

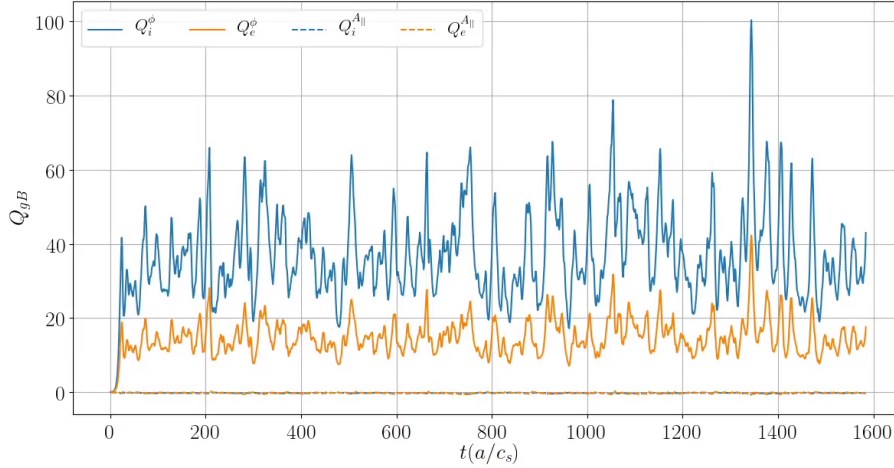


Figure 7.5: Time trace of the flux components of the GA-STD case.

TGLF/QLGYRO were then run for this case with the same  $k_y$  spectrum and resulting electrostatic heat flux spectrum,  $Q^{\phi}(k_y)$ , is shown in Figure 7.6. The spectra between the 3 codes agree very well. The total electrostatic energy flux predictions are shown in Table 7.2 with QLGYRO and TGLF both being within error. Currently neither QLGYRO nor TGLF generate an uncertainty, and the way to go about deriving it is not entirely clear. A solution sometimes taken is to use experimental uncertainties in profiles and run TGLF with a range of inputs from which an uncertainty can be derived. While this is possible in TGLF, the computational cost of QLGYRO makes it a less feasible option.

	$Q_i/Q_{gB}$	$Q_e/Q_{gB}$
CGYRO	$38 \pm 12$	$15 \pm 5$
QLGYRO	37	14
TGLF	36	12

Table 7.2: Electrostatic energy flux prediction made by nonlinear CGYRO, QLGYRO and TGLF for the GA-STD case.

From, Figure 7.6 it can be seen that the most important part of the spectrum to resolve is the

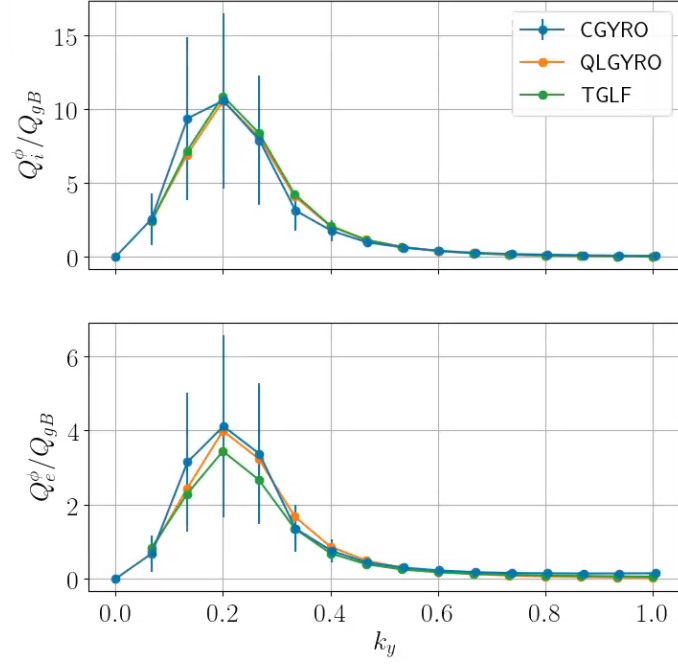


Figure 7.6: Electrostatic energy flux spectrum prediction by CGYRO, QLGYRO and TGLF as a function of  $k_y$  for the GA-STD case.

low  $k_y$  region, which dominates the total flux. As mentioned in Section 3.4.2, the quasi-linear flux estimate is given by  $Q_s^x(k_y) = w_s^x(k_y)|\Phi(k_y)|^2$ , where the quasi-linear weights,  $w_s^x$  and the saturated potential  $|\Phi|$  are defined in Equations 2.80 and 2.81 respectively. To test the models, the quasi-linear estimates for these terms can be compared against their nonlinear equivalent.

CGYRO provides the fluxes and saturated potential from which the weights can be derived, whereas TGLF/QLGYRO provide the weights (from the linear solver) and saturated potential (from a model) from which the fluxes are derived.

Figure 7.7a illustrates how the deuterium quasi-linear weight predictions,  $w_D^\phi$ , between QLGYRO and TGLF agree, illustrating that TGLF is able to capture the linear physics correctly in this regime. It is critical for a transport model that these weights are captured correctly as well as the linear eigenvalues.

Compared to the nonlinear simulation, both TGLF and QLGYRO underestimate the weights in the low  $k_y$  region and then overestimate them for the high  $k_y$  region. Furthermore, TGLF does not capture  $w_e^\phi$  as well as QLGYRO. It more strongly underestimates the low  $k_y$  region, explaining the slightly lower electron heat flux and over estimates the high  $k_y$ , though this has little impact on the total flux.

However, in both cases, it appears that the  $w_D^\phi$  spectrum appears to be shifted towards a higher

$k_y$  compared to the equivalent nonlinear CGYRO result. This would suggest that flux in the low  $k_y$  region should be underestimated. Given that  $Q_i(k_y)$  agrees very well indicates that the underestimation in the linear weights must be compensated in the saturated potential, which are calculated independently in TGLF/QLGYRO. This is confirmed in Figure 7.7b where  $|\Phi|$  is illustrated and is overestimated in TGLF and QLGYRO compared to CGYRO. This occurs because the TGLF saturation rule has been tuned such that the total flux profile is matched for such DIII-D like cases, not the saturated potential. Several scans were performed to see if the balance between  $w_s^\phi$  and  $|\Phi|$  is maintained, as we now describe. All of these runs had the same numerical resolution and were run to at least  $1000a/c_s$ .

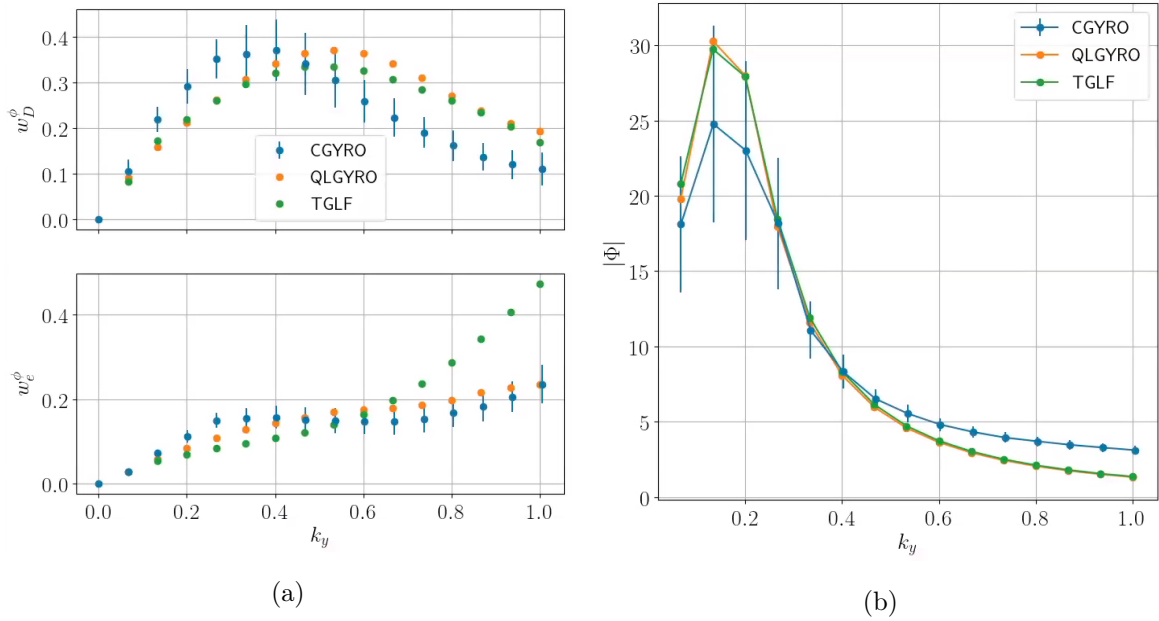


Figure 7.7: a) Quasi-linear weights  $w^\phi$  and b) saturated potential  $|\Phi|$  prediction by CGYRO, QLGYRO and TGLF for the GA-STD case.

### 7.3.1 Parameter scans around GA-STD

A number of parameters were selected to make scans around:  $a/L_T$ ,  $R_{\text{maj}}/a$  and  $\kappa$ .

Firstly, a scan in  $a/L_T$  was performed as this is often the parameter changed during 1.5D transport analysis to flux match experiments. Both  $a/L_{Te}$  and  $a/L_{Ti}$  were changed together from  $2 \rightarrow 5$ . From Figure 7.8a, it can be seen both QLGYRO and TGLF match the nonlinear flux estimation well, though at low temperature gradient both TGLF and QLGYRO begin to underestimate the fluxes. It should be noted that the term  $c_0$  defined in Equation 3.30 was set by matching TGLF to CGYRO GA-STD scans in  $a/L_T$ , so this result is as expected.

A scan in  $R_{\text{maj}}/a$  was performed from 3.0 down to 2.0. Figure 7.8b illustrates that both

TGLF and QLYRO tracks the trend of the CGYRO fluxes well. Both codes do appear to underestimate  $Q_e$  compared to CGYRO, but are currently within the uncertainty. Figure 7.8c shows a scan in  $\kappa$  from  $1 \rightarrow 2.5$  and it can be seen that TGLF appears to overestimate the  $Q_i$  at the higher elongations, but this is less of a problem in QLYRO. QLYRO remains within the uncertainty throughout all of these scans.

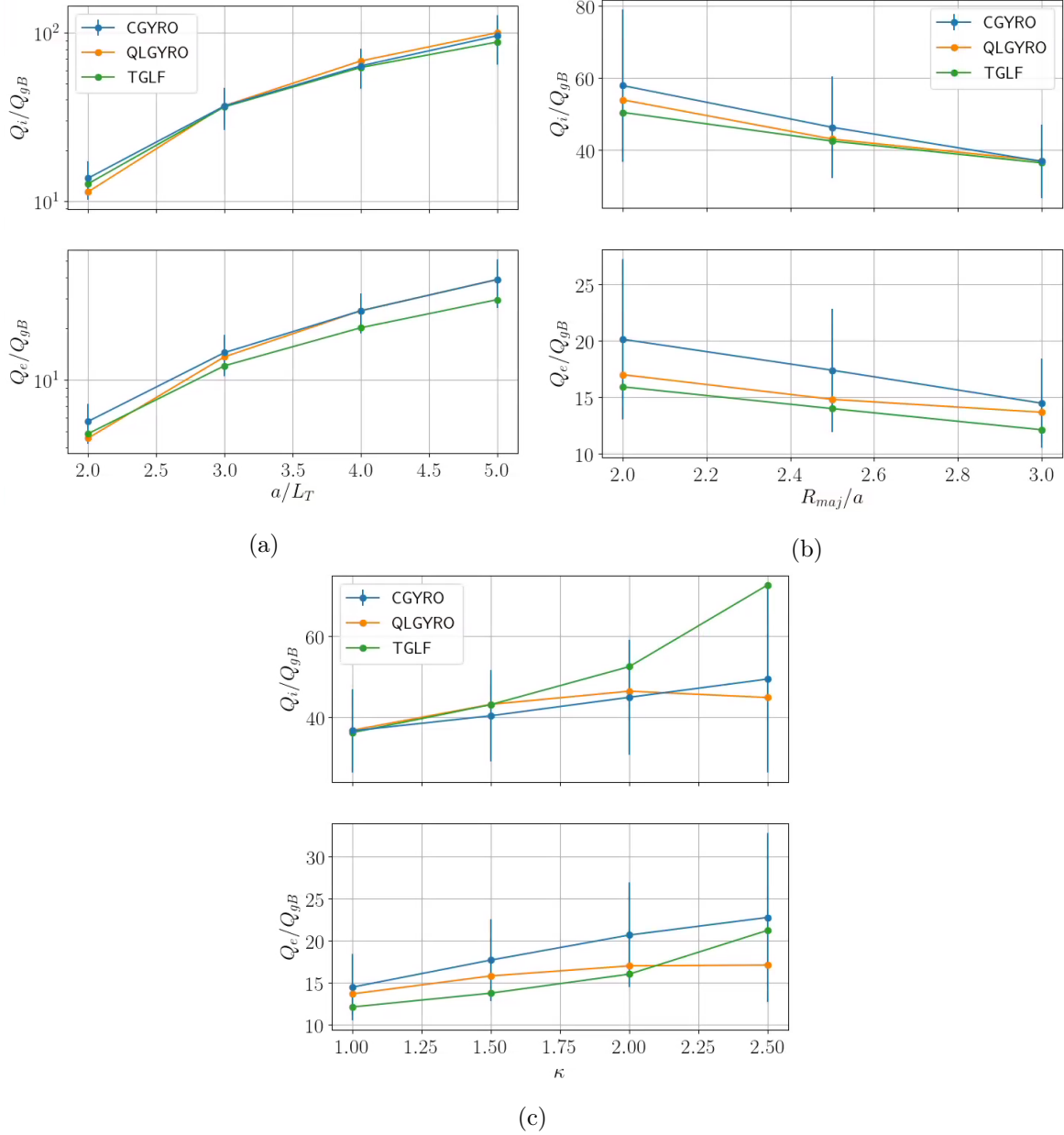


Figure 7.8: Total electrostatic energy flux prediction by CGYRO, QLYRO and TGLF when scanning through a)  $a/L_T$  b)  $R_{maj}/a$  and c)  $\kappa$  for the GA-STD case.

This illustrates how TGLF and QLYRO are successful in predicting the nonlinear fluxes for low  $\beta$  simple equilibria. Although there is good agreement between the fluxes for these

scans, the quasi-linear weights were still under-estimated in the low  $k_y$  region, which was then compensated for in the model for the saturated potential. Furthermore, as the elongation is increased, TGLF begins to deviate from the nonlinear runs, which illustrates that the linear solver is beginning to struggle. BurST will need to operate at high elongation so it is crucial that any linear solver is valid in such a regime. In all of these cases, the quasi-linear weights were under-estimated in the low  $k_y$ , which was then compensated for by the saturation model. When examining more complex equilibria, the balance between the saturation rule and weights may not always be maintained. If this shift in weight spectrum is accounted for then a more accurate model for the potential can be developed, giving more confidence in the flux predictions.

## 7.4 MAST - ITG turbulence

A low  $\beta_e$  MAST equilibrium was examined, where an ITG mode was the dominant instability. Thus we can extend the results of the GA-STD case towards tight aspect ratio, whilst the low  $\beta$  ensures the transport remains dominated by electrostatic fluctuations. Shot #27274 was analysed with the equilibrium Miller parameters taken from [84] and are shown in Table 7.3.

$r/a$	$R/a$	$\kappa$	$s_\kappa$	$\delta$	$s_\delta$	$q$	$\hat{s}$	$\Delta$
0.80	1.49	1.46	0.25	0.20	0.36	2.31	4.00	-0.31
$a/L_{Te}$	$a/L_{Ti}$	$a/L_n$	$\beta_{e,\text{unit}}$	$\beta'_{e,\text{unit}}$	$T_i/T_e$	$\nu_{ee}(c_s/a)$	$\gamma_{E \times B}(c_s/a)$	$Z_{\text{eff}}$
5.2	5.77	2.64	0.088%	0.021	0.92	0.83	0.27	1.59

Table 7.3: Experimental Miller and plasma parameters for MAST #27274 at  $r/a = 0.8$  [84]. Note simulations conducted here enforced  $a/L_{Te} = a/L_{Ti}$  and were performed without flow shear.

These simulations were run without flow shear, for simplicity. Similar to the previous section, a scan was performed in  $a/L_T$ , where  $a/L_{Te} = a/L_{Ti}$  was enforced and both were changed together. These simulations were run with 32  $\theta$  points, 8 energy grid points, 16 pitch angles. Two kinetic species were included; deuterium ions and electrons. 16 bi-normal wavenumbers from  $k_y = 0.0 \rightarrow 1.05$  with a box size of  $L_y = 90\rho_s$  and 192 radial wavenumbers from  $k_x = -6.96 \rightarrow 6.96$  with  $L_x = 86\rho_s$  were found to be sufficient to model this equilibrium. These were performed with  $\phi$  and  $A_{\parallel}$ , anticipating that  $B_{\parallel}$  will be less important at low  $\beta_e$ . When comparing the flux predictions made by the different codes, Figure 7.9 illustrates how

both TGLF and QLGYRO overestimate the heat flux at lower  $a/L_T$  by several orders of magnitude. One possibility is that the Dimits shift [130] is not being captured in the quasi-linear models. To test this TGLF and QLGYRO were run with a  $a/L_T = 1.0$ , closer to the linear threshold, but the fluxes did not drop significantly. To find the cause of the discrepancy, the quasi-linear weights and saturated potential from  $a/L_T = 2$  and  $a/L_T = 5.2$  were examined in more detail.

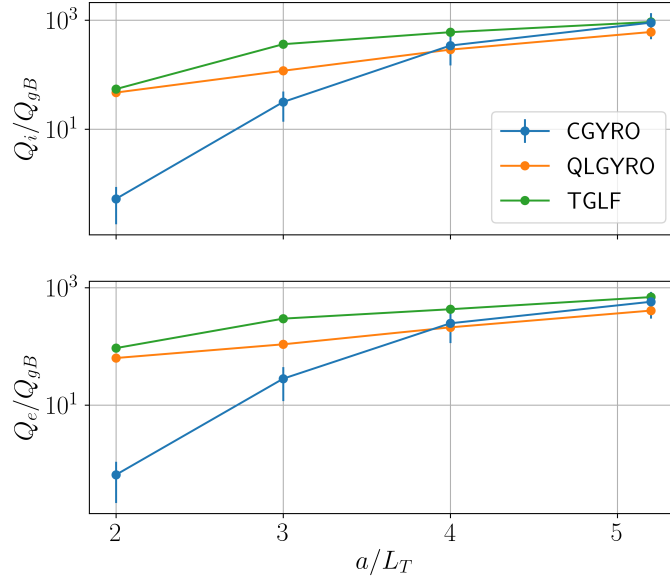


Figure 7.9: Total electrostatic energy flux prediction by CGYRO, QLGYRO and TGLF as a function of  $a/L_T$  for the MAST #27274 equilibrium.

### Quasi-linear weights

The discrepancy in the fluxes must arise from either the weights or the model for the saturated potential (or even both). Figures 7.10a and 7.10b shows how  $w^\phi$  compares when  $a/L_T = 2.0$  and  $a/L_T = 5.2$  respectively. It can be seen that for both cases in the low  $k_y$  region QLGYRO and TGLF slightly under-estimate the weights for both species. This would suggest that the fluxes should be under-estimated rather than over-estimated, especially not by orders of magnitude. In the  $a/L_T = 5.2$  simulation,  $w_D^\phi$  is over-estimated in the high  $k_y$  region, though the impact on the fluxes should be small. The reasonable agreement between TGLF and QLGYRO indicates that TGLF is able to capture the linear physics successfully in this regime.

This is reminiscent of the GA-STD simulation, where the weights were also under-estimated in the low  $k_y$  region. The lower gradient matching the nonlinear case more closely is under-

standable as the nonlinear drive is lowered such that the deviation from the linear physics is reduced. Overall, both QLGYRO and TGLF do reasonably well in calculating the weights, especially in the low  $k_y$  region.

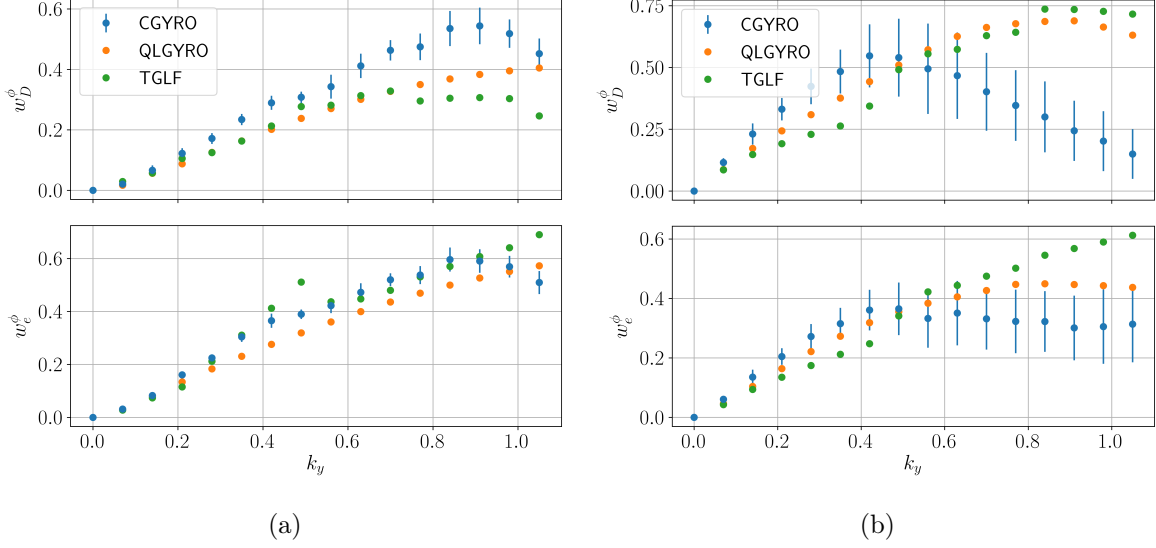


Figure 7.10: Quasi-linear weights  $w^\phi$  prediction by CGYRO, QLGYRO and TGLF for the MAST #27274 equilibrium when a)  $a/L_T = 2.0$  and b)  $a/L_T = 5.2$ .

### Saturated potential

Given the reasonable agreement in the weights, the deviation must originate from the saturation rule. Looking at  $|\Phi|$  in Figure 7.11 for each of these cases, it can be seen that the agreement here is significantly worse. Figure 7.11a shows how the saturation rule overestimates  $|\Phi|$  for the  $a/L_T = 2$  simulation, explaining the overestimation in the TGLF and QLGYRO flux predictions. In contrast to the quasi-linear weights, where the higher gradient case performed better than the lower gradient case. Figure 7.11b shows the saturated potential for the  $a/L_T = 5.2$  case and although the agreement is better, the spectrum of  $|\Phi|$  is not captured well by either quasi-linear model. The saturation rule in TGLF has been designed such that  $|\Phi|$  will be forced to 0 as  $k_y \rightarrow 0$ , so capturing the behaviour seen in Figure 7.11 would not be possible.

As mentioned in Section 3.4.2, in TGLF/QLGYRO the saturated potential at the outboard mid-plane is approximated by

$$|\Phi(k_x = 0, k_y, \theta = 0)| = \frac{\gamma^{\text{eff}}}{k_{x,\text{rms}} k_y}$$

Assuming this model is valid, the discrepancy must be arising from a term in this equation, so

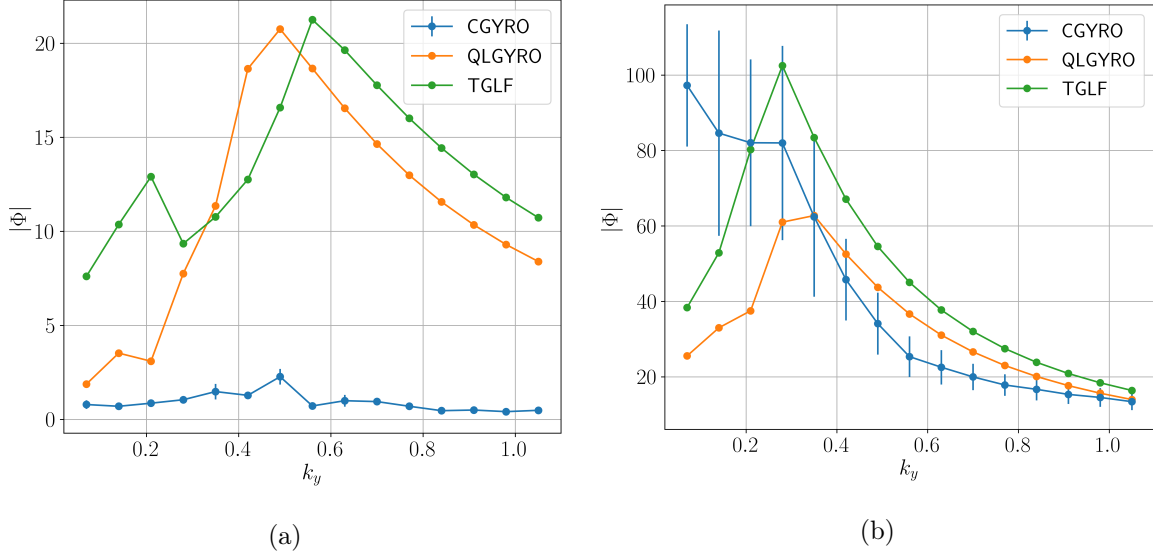


Figure 7.11: Saturated potential  $|\Phi|$  prediction by CGYRO, QLGYRO and TGLF for the MAST equilibrium when a)  $a/L_T = 2.0$  and b)  $a/L_T = 5.2$ .

by examining each of them it will be possible to find where the discrepancy lies. Given that  $\Phi(k_x, k_y, \theta)$  is calculated in the nonlinear CGYRO simulations,  $k_{x,\text{rms}}$  can also be calculated. Comparing the predictions made for  $k_{x,\text{rms}}$ , it can be seen from Figure 7.12a that QLGYRO and TGLF generally lie within error of CGYRO for the  $a/L_T = 2$  run. The higher gradient case shown in Figure 7.12b also agrees well, especially at the low  $k_y$ . It is clear that any differences seen here would not cause either QL code to overestimate the heat flux by two orders of magnitude, suggesting the prediction for  $k_{x,\text{rms}}$  is not the source of the disagreement. The term  $\gamma_{\text{eff}}$  must be the cause of the error. It is possible to calculate a nonlinear equivalent for  $\gamma_{\text{eff}} = k_{x,\text{rms}} k_y |\Phi(k_x = 0, k_y, \theta = 0)|$ . This is illustrated in Figure 7.13a. For the low gradient case, both QLGYRO and TGLF overestimate  $\gamma_{\text{eff}}$ . Figure 7.13b illustrates the  $a/L_T = 5.2$  case, which, although not perfect, is significantly better.

For QLGYRO and TGLF, the effective growth rate used is calculated from a model for the zonal flow velocity  $V_{\text{ZF}}$  as shown in Equation 3.31. The zonal flow is defined in Equation 3.27, and approximated by  $V_{\text{ZF}} \approx \text{MAX}(\gamma/k_y)$ . This model assumes that the zonal flow will continue to increase until it matches the largest linear drive, at which point the turbulence will saturate.

Comparing the TGLF/QLGYRO results to CGYRO, shown in Figure 7.14, it can be seen that when  $a/L_T \geq 3.0$ , QLGYRO predicts  $V_{\text{ZF}}$  well, indicating that Equation 3.29 is a good approximation. But at the lowest temperature gradient this zonal approximation does not fair well. However, as QLGYRO under-predicts  $V_{\text{ZF}}$  it would be expected that it would also

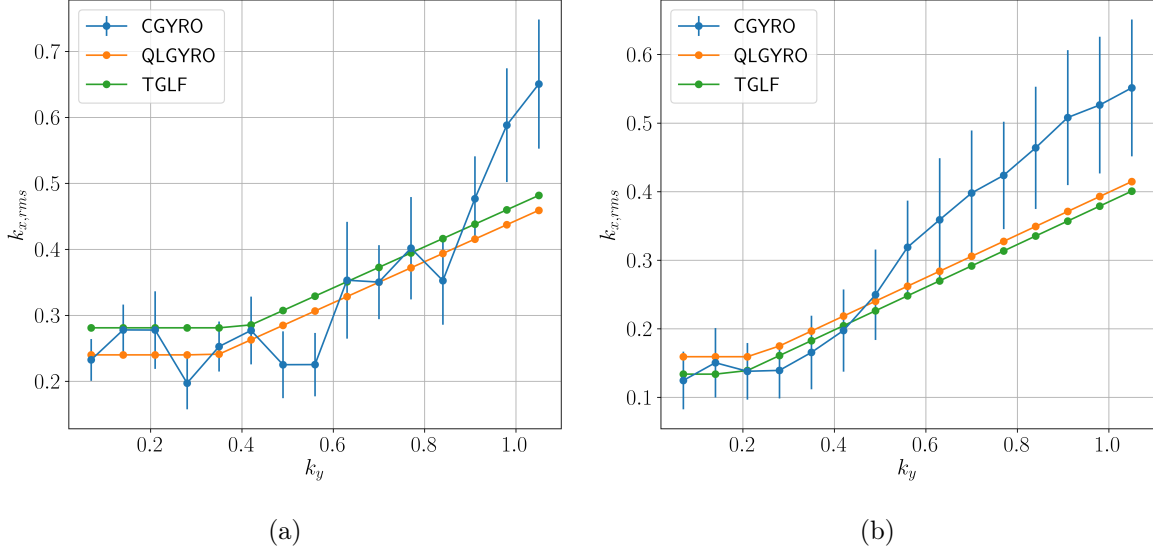


Figure 7.12:  $k_{x,rms}$  prediction by CGYRO, QLGYRO and TGLF for the MAST #27274 equilibrium when a)  $a/L_T = 2.0$  and b)  $a/L_T = 5.2$ .

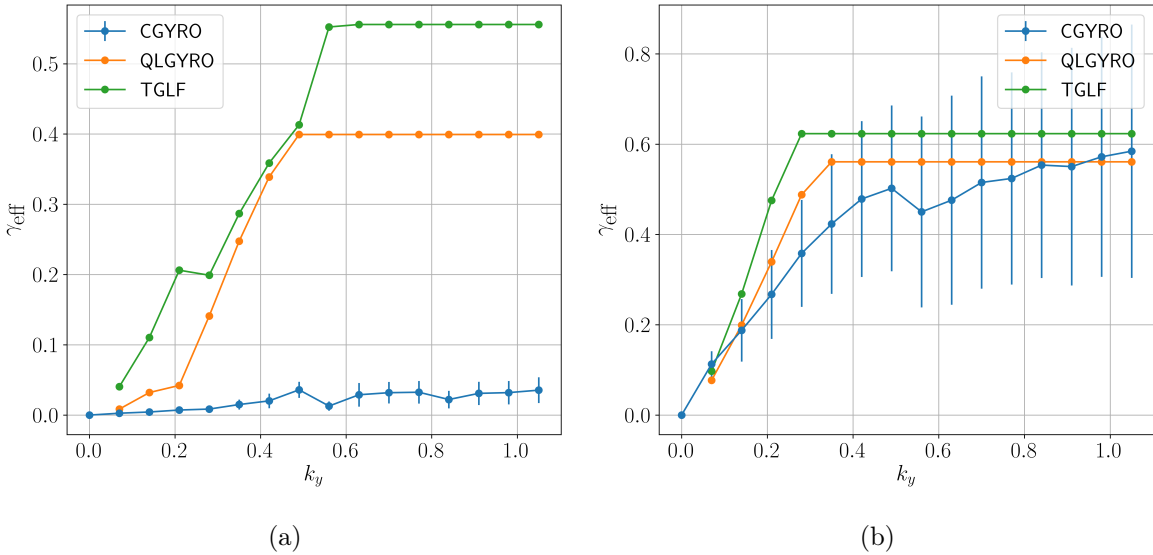


Figure 7.13: Effective growth rate  $\gamma_{\text{eff}}$  prediction by CGYRO, QLGYRO and TGLF for the MAST #27274 equilibrium when a)  $a/L_T = 2.0$  and b)  $a/L_T = 5.2$ .

under-predict the flux, but that is not seen here. Furthermore, for the  $a/L_T = 3.0$  simulation,  $V_{ZF}$  agrees well between CGYRO and QLGYRO, but QLGYRO still overestimates the flux. This suggests that the relation between  $\gamma_{\text{eff}}$  and  $V_{ZF}$  is not consistent. Another potential issue is the fitting of  $c_0$  from Equation 3.31 to a GA-STD like equilibrium. As this MAST equilibrium is far away from such a simple equilibrium, the fitting used here may not be valid. To understand what improvements need to be made for this saturation rule will require a range

of nonlinear simulations to benchmark against which is outside the scope of this work. It may be the case that the model itself needs to be re-examined. Regardless, further bench-marking in the ST regime will be pivotal for the development of BurST.

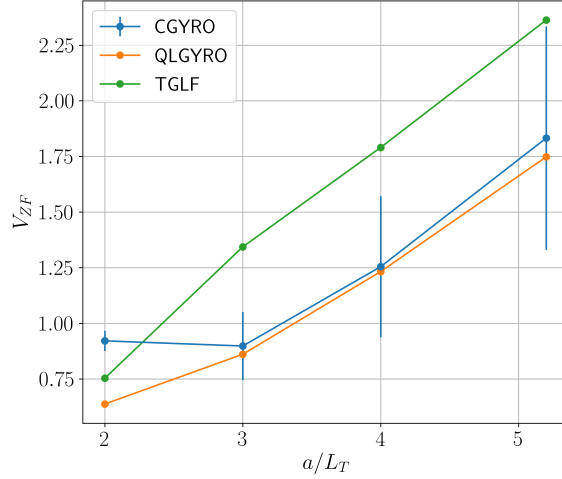


Figure 7.14: Saturated zonal flow  $V_{ZF}$  prediction by CGYRO, QLGYRO and TGLF for the MAST #27274 equilibrium as a function of  $a/L_T$ .

### 7.4.1 Summary

This section has shown that TGLF and QLGYRO are able to capture the quasi-linear weights in a MAST regime, especially with a lower drive. This validates the use of quasi-linear models in a ST regime where the dominant mode is an ITG. However, the current TGLF saturation rule is not able to model the saturated potential. The model is able to capture  $V_{ZF}$  and  $k_{x,rms}$  reasonably well in QLGYRO (except at low  $a/L_T$ ), suggesting that there is a piece of missing physics not captured in  $c_0$  or the model itself needs to be re-examined.

## 7.5 NSTX - MTM turbulence

As outlined in Chapter 6, capturing the behaviour of micro-tearing transport will be a crucial aspect of designing BurST. There has been some development of reduced transport models with MTMs in recent years which have had some success in modelling nonlinear simulations. In Rafiq *et al* 2016 [197], a MT dispersion relation was derived using a unified fluid/kinetic approach from which a saturation mechanism was identified in the high collisionality limit, similar to that in Drake *et al* [170]. When applied in a predictive simulation of a high collisionality NSTX shot, it matched the experimental data well [198]. However, when applied

to a lower collisionality shot, it over-predicted the transport and given that BurST will operate at low collisionality it is crucial that this regime is correctly modelled.

In [99], the quasi-linear weights were calculated linearly and compared to nonlinear simulation, though a different definition is used for the weights. The choice of normalisation used there was combination of the perturbed electron density and parallel flow moments, and is discussed further in Section 7.5.2. This model was successful in matching several nonlinear simulations of a simple conventional aspect ratio equilibria. Fundamentally, the stochastic magnetic field generated by micro-tearing turbulence is an irreversible process and cannot be directly captured by a quasi-linear model [98]. However, the success of the previously outlined models empirically suggest that quasi-linear models are a potentially viable route to modelling MT turbulence in an integrated modelling suite. In this section, by comparing the quasi-linear weights to their nonlinear equivalent, the validity of quasi-linear theory can be tested.

To examine the validity of quasi-linear models in this regime, an NSTX shot will be examined which has a higher  $\beta$  than the MAST discharge, and where MTMs are the dominant mode. This equilibrium was taken from [196], in which nonlinear GYRO simulations were conducted. The Miller parameters for this equilibrium are outlined in Table 7.4. Using CGYRO linearly, MTMs were found and it was seen that  $B_{\parallel}$  had little impact on the linear physics, so the nonlinear simulations were conducted with only  $\phi$  and  $A_{\parallel}$ .

$r/a$	$R/a$	$\kappa$	$s_{\kappa}$	$\delta$	$s_{\delta}$	$q$	$\hat{s}$	$\Delta$
0.6	1.53	1.71	0.12	0.13	0.17	1.71	1.70	-0.29
$a/L_{Te}$	$a/L_{Ti}$	$a/L_n$	$\beta_{e,\text{unit}}$	$\beta'_{e,\text{unit}}$	$T_i/T_e$	$\nu_{ee}(c_s/a)$	$\gamma_{E \times B}(c_s/a)$	$Z_{\text{eff}}$
2.73	2.36	-0.83	2.45%	8.19%	0.95	1.45	0.17	2.92

Table 7.4: Experimental Miller and plasma parameters for NSTX shot #120968 at  $r/a = 0.6$  [168].

An attempt was made to match the GYRO simulation result from [196]. Two simulations from that paper are discussed; a “low” and “high” resolution, that are outlined in Table 7.5. Two kinetic species were included; deuterium ions and electron. The CGYRO simulation domain used here is outlined in Table 7.5. A Sugama collision operator was used for this simulation, which does not allow for an inconsistent  $Z_{\text{eff}}$ , hence  $Z_{\text{eff}} = 1.0$  was adopted rather than the experimental value of 2.92 given in Table 7.4. This will impact the transport as it was found that when using a higher  $Z_{\text{eff}}$  with a Lorentz collision operator, these MTMs were driven more unstable linearly [168], similar to the MTMs in Chapter 6. To account for this

with a Sugama operator would require the inclusion of impurities, which was also found to drive the MTMs more unstable.

	GYRO “low”	GYRO “high”	CGYRO
$L_x(\rho_s)$	80	80	92
$L_y(\rho_s)$	60	100	90
$n_{k_y}$	8	16	12
$n_{k_x}$	400	540	256
$\Delta k_y$	0.105	0.063	0.070
$\Delta k_x$	0.079	0.079	0.068
$k_{y,\max}$	0.735	0.945	0.770
$k_{x,\max}$	15.6	21.1	8.65

Table 7.5: Comparison of simulation domains in [196] and the CGYRO domain used for the NSTX simulation.

### 7.5.1 Without flow shear

To begin with, a CGYRO simulation was run without flow shear in an attempt to match to previous nonlinear GYRO predictions by Guttenfelder *et al*[196]. Figure 7.15 illustrates the time-trace of the heat fluxes from the new CGYRO simulation and, similar to the previous GYRO results, CGYRO predicts predominantly electron heat flux via flutter transport, whilst the electrostatic heat transport is close to 0, indicative of MTM based transport. However, similar to the BurST simulations described above, the flux here does not appear to saturate. Moreover, Table 7.6 shows that the flux predictions made by CGYRO is significantly higher than GYRO.

	GYRO “low”	GYRO “high”	CGYRO
$Q_e/Q_{gB}$	3.28	4.10	> 200

Table 7.6: Electromagnetic flutter electron energy flux predictions for the NSTX case without flow shear. The GYRO results are taken directly from [196]

The cause of the discrepancy was initially thought to be due to insufficient dissipation at the highest  $k_x$ , similar to what was seen in the BurST simulation in Figure 7.3. Figure 7.16a, shows the potential spectrum as a function of  $k_x$ . There is no large build up at the highest

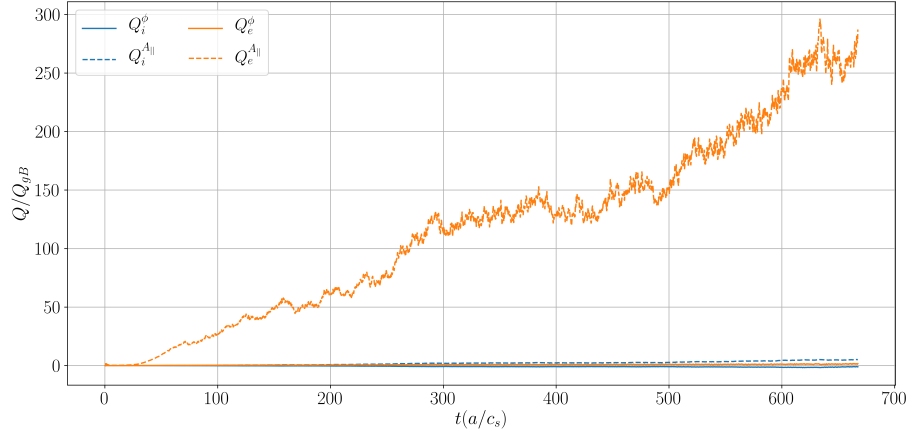


Figure 7.15: Time trace of the flux components prediction by CGYRO for the NSTX #120968 equilibrium without flow shear.

$k_x$  suggesting that the radial resolution is sufficient. Another simulation was conducted with 384  $k_x$  modes, going up to  $k_{x,\max} = 13.44$ , but the simulation did not converge.

To further diagnose this issue,  $A_{||}$  was examined spectrally in both  $k_x$  and  $k_y$ . Figure 7.16b illustrates the  $k_x$  spectrum of  $A_{||}$  summed over  $k_y$  at  $\theta = 0$ . No build up is seen at high  $k_x$ , but  $A_{||}$  has a strong peak at the  $k_x = 0$ , indicating that in real space  $A_{||}$  is radially extended across the box. Such large structures begin to stretch the limit of the local flux tube approximation. For instance, this flux surface has  $\rho_* \approx 1/134$ , meaning  $L_x = 92\rho_s$  corresponds to  $0.69a$ , which actually extends outside of the plasma. This potentially indicates that a global model may be necessary, though that is outside the scope of this work.

Examining the  $k_y$  spectrum of  $A_{||}$  in Figure 7.16c, it can be seen that the  $k_y = 0.07$  mode, the smallest non-zero  $k_y$ , does not appear to saturate. This gradual build up of potential has been seen before in KBM based transport and is generally classified as being in a “runaway” phase or having undergone a non-zonal transition [199, 200], though whether similar arguments even apply to MTM transport will require more detailed examination. This runaway behaviour was not seen in GYRO. It is not clear to the author why this did not occur in GYRO, but a potential reason is the finite difference scheme used in GYRO which introduces additional numerical diffusion compared to spectral methods, which may have been sufficient to suppress these modes.

This runaway is sometimes mitigated by reducing  $\beta_e$ , so a simulation was run with  $\beta_{e,\text{unit}}$  halved, but the same issue with the low  $k_y$  mode was seen. Reducing the minimum  $k_y$  to  $k_y = 0.035$  was also attempted, but again the build up occurred at the lowest  $k_y$ . Detailed convergence studies beyond this becomes computationally expensive as the case outlined in

Table 7.5 took 200,000CPUh.

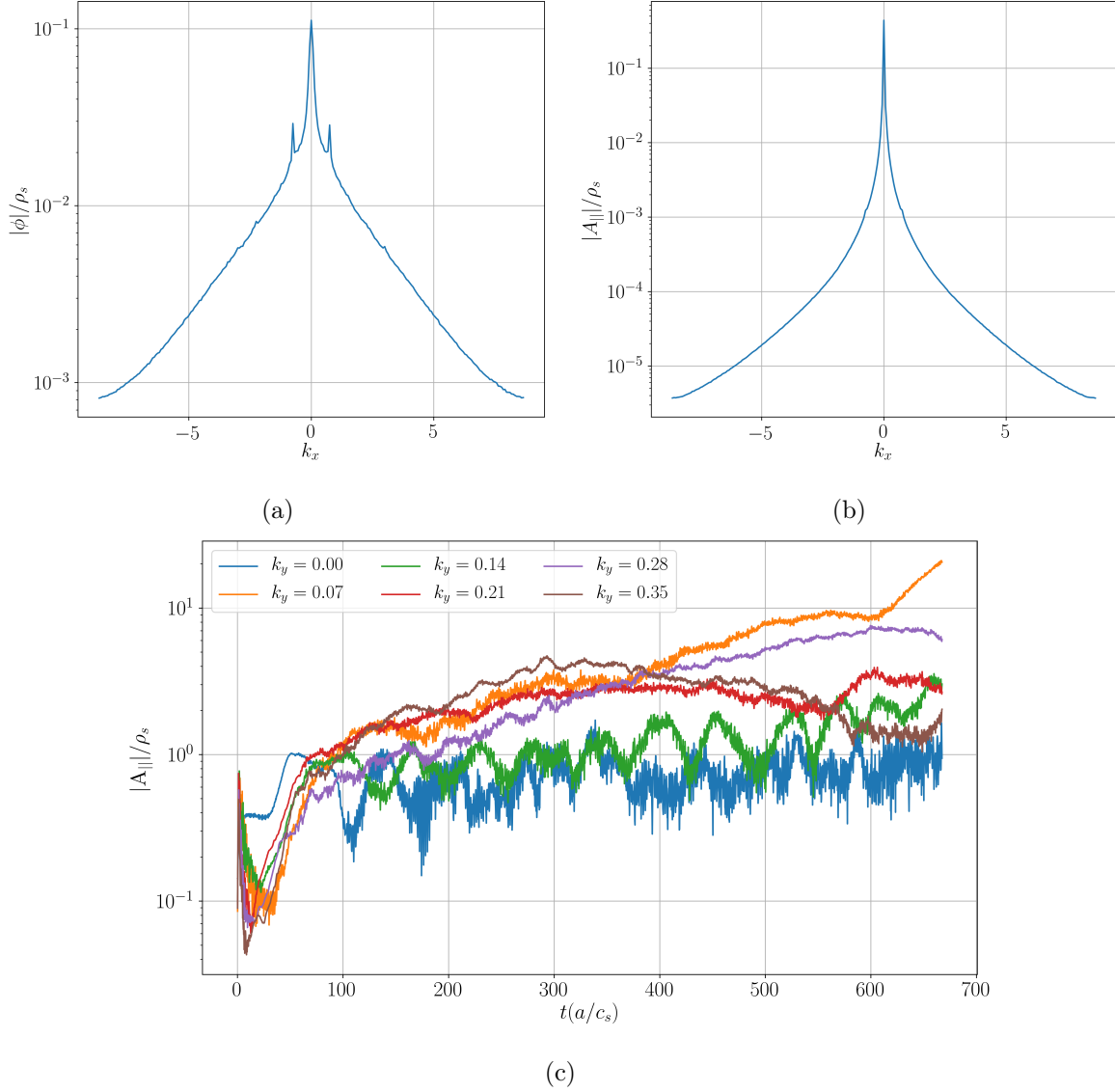


Figure 7.16: a)  $k_x$  spectrum of  $\phi$  where no build up at high  $k_x$  is seen. b)  $k_x$  spectrum of  $A_{\parallel}$  with no build up seen, but it is very peaked at  $k_x = 0$ . c) Time trace of  $A_{\parallel}$  for the lowest  $k_y$ , with the lowest  $k_y$  in the “runaway” phase, especially beyond  $t = 600a/c_s$ .

## 7.5.2 With flow shear

Previous work has shown that these MTMs were sensitive to flow shear [196]. A linear scan in  $\theta_0$  was conducted and it was found that the MTM was stable for  $\theta_0 > 0.15\pi$ . A simulation was conducted including the experimental levels of flow shear and it was found that the heat fluxes did saturate, shown in Figure 7.17a<sup>†</sup>. The flux is still predominantly in the electron

<sup>†</sup>This was not effective in the BurST simulation as those MTMs are independent of  $\theta_0$ .

channel demonstrating that MT transport is still prevalent. The time trace of  $A_{\parallel}$  is shown in Figure 7.17b and the lowest  $k_y$  mode is repeatedly building up and dropping down, caused by the flow shear advecting the mode into a stable region. Figure 7.17c illustrates the flux spectrum which looks well behaved.

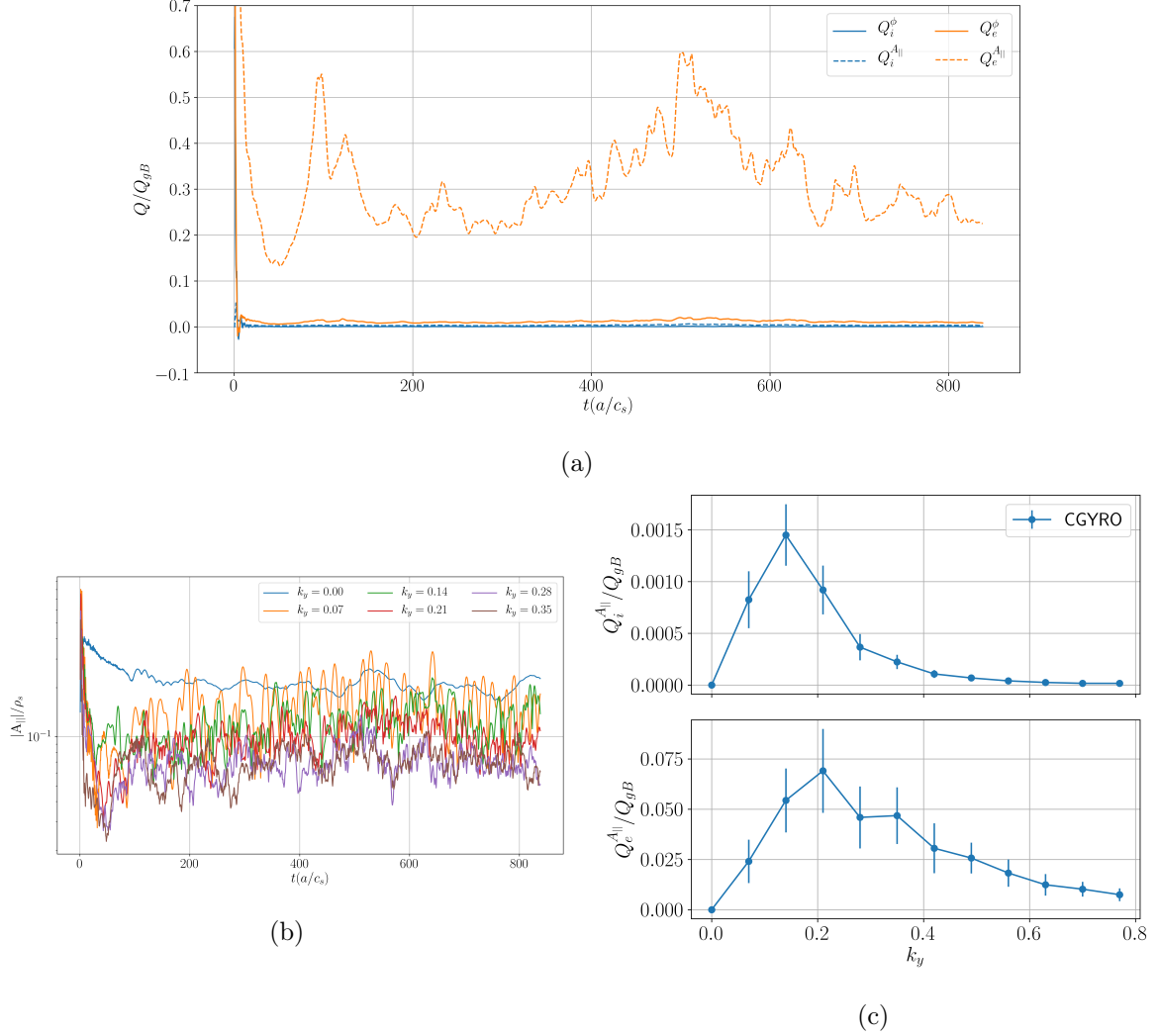


Figure 7.17: NSTX MTM simulation with flow shear showing the a) time trace for the heat flux, b)  $k_y$  spectrum of  $A_{\parallel}$  and c) the  $k_y$  magnetic flutter heat flux spectrum.

Table 7.7 shows that compared to GYRO, CGYRO does over predict the fluxes, though they are in the same ballpark now (it should be noted that no uncertainties were provided for these GYRO simulations). Different grid sizes, collision operators and spectral methods could all come into play here. Getting good agreement between nonlinear results from two different codes is notoriously difficult especially in a MT regime.

Given that this CGYRO simulation appears to be converged, the remainder of this section will examine the quasi-linear approximation for this case. This equilibrium was modelled in

	GYRO “low”	CGYRO	QLGYRO	TGLF
$Q_e/Q_{gB}$	0.1	$0.35 \pm 0.10$	11.9	149

Table 7.7: Electromagnetic flutter electron energy flux predictions for the NSTX case with flow shear. The GYRO result is taken directly from [196]

TGLF and QLGYRO. QLGYRO was run with the same version of CGYRO and used the same resolution. The maximum resolution in TGLF was used 32 Hermite basis functions with 32  $\theta$  points.

### Linear eigenvalues

Figure 7.18a shows the eigenvalues predicted by TGLF (with the default settings) and QLGYRO. The agreement between the two codes is quite poor; however, there are a few  $k_y$  modes where it looks as if TGLF is finding a reasonable value of  $\gamma$  and  $\omega$ , such as  $k_y = 0.42$ , for example. It was found that here TGLF was finding a different Gaussian width  $\theta_w = 0.41$  that maximised the growth rate compared to the other  $k_y$  where it found  $\theta_w > 1$ . As  $\theta_w$  sets the resonating/averaging boundary, this affects the fraction of passing electrons which are important for MTMs. By reducing the range of  $\theta_w$  when performing the initial guesses to  $\theta_w = 0.3 \rightarrow 0.5$ , TGLF was able to find MTMs for a larger range of  $k_y$ . However, it was not able to find the MTMs at the lowest  $k_y$ , which are arguably the most important area to get correct for transport, and the growth rate is much larger than QLGYRO at higher  $k_y$ . This  $\theta_w$  setting was used to determine the quasi-linear weights in the next section.

This raises a potential concern when using TGLF in a transport solver; as fitting parameters like this one may need to be tuned on a mode by mode basis. This is avoided entirely by QLGYRO which is one major advantage.

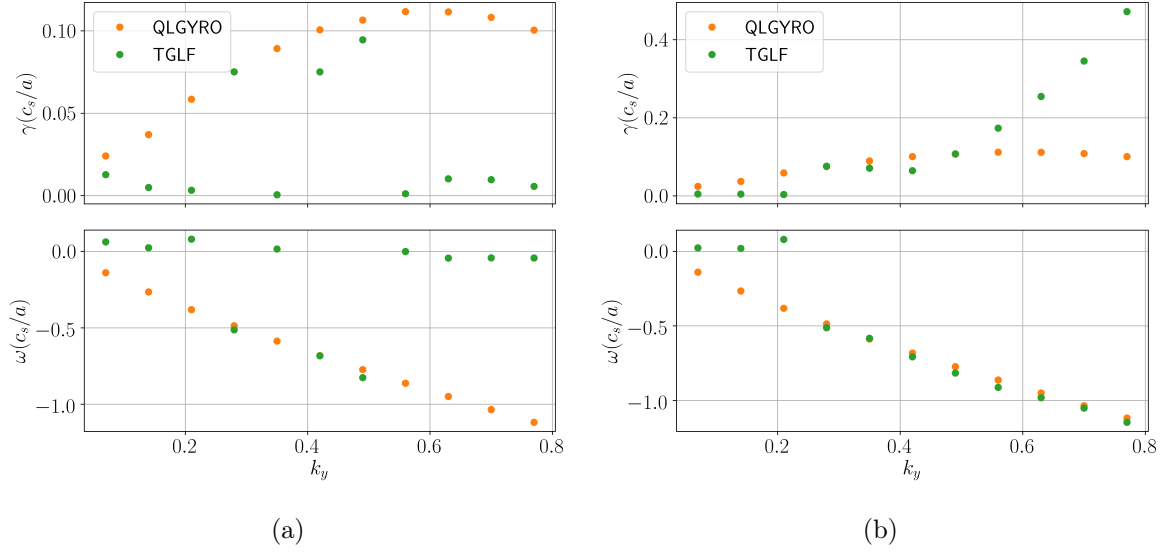


Figure 7.18: Eigenvalues comparing QLGYRO to TGLF when using a range of a)  $0.3 \rightarrow 1.65$  (default setting) and b)  $0.3 \rightarrow 0.5$  for the initial guesses of  $\theta_w$ .

### Quasi-linear weights

Neither QLGYRO nor TGLF match the nonlinear CGYRO flux prediction, as shown in Table 7.7. To see if the issue lies in the weights, Figure 7.19 illustrates the magnetic flutter quasi-linear weights,  $w^{A_{\parallel}}$ , predicted by each code, and it is clear that the agreement is significantly poorer compared to the MAST case. It can be seen that TGLF does not match QLGYRO well and significantly over-predicts the ion weights. For MTMs the electron transport is generally the dominant channel so it is more important that this channel is captured correctly. For the electrons TGLF does reasonably well for  $k_y \geq 0.28$ , which is where TGLF found MTMs, but it is not as good compared to the tests with the MAST equilibrium. For the  $k_y$  where MTMs were not found, the electron weights are close to 0, which will have a significant impact on the flux predictions. Overall, given the speed at which TGLF can be run, this may be an acceptable compromise in a transport solver if an accurate saturation model is developed.

QLGYRO doesn't match the nonlinear CGYRO weights either. The electron quasi-linear weights are under-predicted in the low  $k_y$  region and over-predicted in the high  $k_y$  region. A simulation was run to a higher  $k_y$  to see if the weights eventually roll over as they had for the MAST/GA-STD simulations, but they continued to increase at higher  $k_y$ .

The quasi-linear weights are designed to be independent of the value of the saturated fields, and therefore factor out the impact on the transport of the phase difference between the field and energy fluctuations. However the weights defined in Equation 2.80, which will be referred to as the conventional weights, only guarantees that the electrostatic flux is independent of

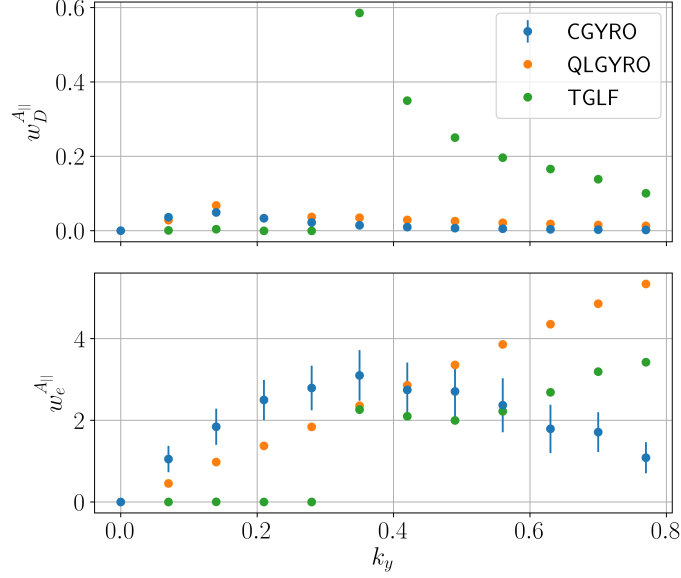


Figure 7.19: Quasi-linear weights prediction by CGYRO, QLGYRO and TGLF when using  $\phi$  as the normalising field for all 3 codes.

the field. The electromagnetic flutter transport is driven by  $A_{||}$ , so for Equation 2.80 to be valid, the linear result must be able to reproduce the ratio of  $\phi$  and  $A_{||}$  found in nonlinear simulations. To examine this,  $R_{A_{||}}^{\phi}$  is defined as the ratio of the squared normalised fields, given by

$$R_{A_{||}}^{\phi} = \frac{|\Phi|^2}{c_s^2 |\mathbf{A}_{||}|^2} \quad (7.2)$$

where

$$|\mathbf{A}_{||}|^2 = \left( \frac{ae}{\rho_s T_e} \right)^2 \sum_{k_x} \langle |A_{||}|^2 \rangle_F \quad (7.3)$$

This means the magnetic flutter quasi-linear weight is made independent of the field by considering  $w^{A_{||}} R_{A_{||}}^{\phi}$ . Figure 7.20a illustrates  $R_{A_{||}}^{\phi}$  for the different codes. For the very lowest  $k_y$ , the agreement between QLGYRO and CGYRO is good, but quickly begins to deviate for  $k_y > 0.3$ . TGLF largely overestimates the ratio in the low  $k_y$  region where the code failed to find MTMs. In the higher  $k_y$  region, both linear codes substantially under-estimate the ratio. As mentioned previously, in [99], the perturbed electron density and parallel flow are used to calculate the weights as opposed to the fields. However, they are affected by both  $\phi$  and  $A_{||}$ . Given that the ratio of fields is not correctly captured linearly then this discrepancy would be carried forward in the quasi-linear weight calculation.

The magnetic flutter quasi-linear weight can be made independent of the field amplitude by

considering  $w^{A_{\parallel}} R_{A_{\parallel}}^{\phi}$  (which will be referred to as the modified weights). This is examined in Figure 7.20b and it can be seen that the modified ion weights agree reasonably well between QLGYRO and CGYRO. For the electrons, the trend of the QLGYRO weights is similar to the nonlinear result, but across the board it under-estimates them. TGLF under-estimates the modified electron weights even more.

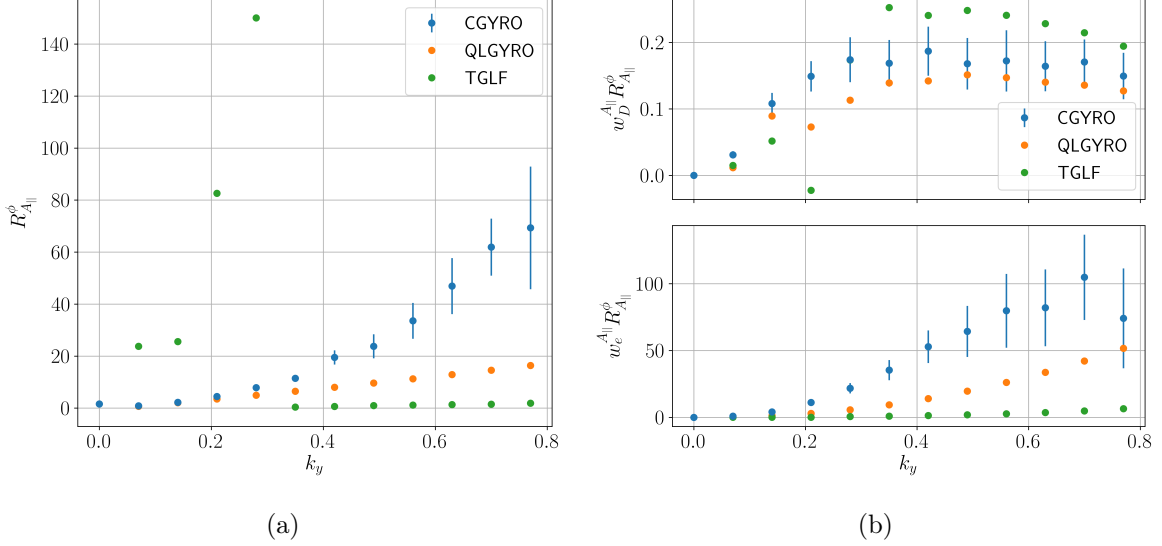


Figure 7.20: a)  $R_{A_{\parallel}}^{\phi}$  which shows the ratio of  $\phi$  and  $A_{\parallel}$ . b) Modified quasi-linear weight  $w^{A_{\parallel}} R_{A_{\parallel}}^{\phi}$  prediction by CGYRO, QLGYRO and TGLF.

Any discrepancies between the linear and nonlinear results can only lie in the nonlinear interaction term shown in Equation 2.72, which is dependent on the full electromagnetic potential. With this case both  $\phi$  and  $A_{\parallel}$  will play a significant role<sup>‡</sup>. A simulation was run where the nonlinear  $A_{\parallel}$  term was turned off such that only the  $E \times B$  convective nonlinearity is considered:

$$\frac{\vec{\nabla}g}{B} \cdot \vec{b} \times \vec{\nabla}_{\perp} \left[ \phi - v_{\parallel} A_{\parallel} \right] J_0(k_{\perp} \rho_s) \rightarrow \frac{\vec{\nabla}g}{B} \cdot \vec{b} \times \vec{\nabla}_{\perp} \left[ \phi \right] J_0(k_{\perp} \rho_s)$$

Recall that these nonlinear simulations also had  $B_{\parallel}$  turned off.  $A_{\parallel}$  is still involved via the linear terms describing the background gradients, drifts and closure via Maxwell's equations. The electron heat flux saturated, albeit at a higher value of  $Q_e/Q_{gB} = 2.6 \pm 0.4$  (*c.f.* Table 7.7), indicating that  $\phi$  alone provides a saturation mechanism. Figure 7.21a illustrates the ratio of field and here the agreement is actually much poorer compared to the case with the full nonlinear term. However, when examining the modified weights in Figure 7.21b, the agreement between QLGYRO and CGYRO is nearly perfect for the electrons. This indicates

<sup>‡</sup>For the previous MAST equilibria,  $\beta_{e,\text{unit}}$  was so low that the  $A_{\parallel}$  term would be negligible

that the shift in the electron weights is caused by the  $A_{\parallel}$  in the non-linearity term. The agreement between the ion weights is actually worse, suggesting the potential is relevant for these.

When running a case with just  $A_{\parallel}$  in the non-linearity, the electron flux becomes extremely large, at over  $500Q_{gB}$ , indicating that  $\phi$  is required for saturation.

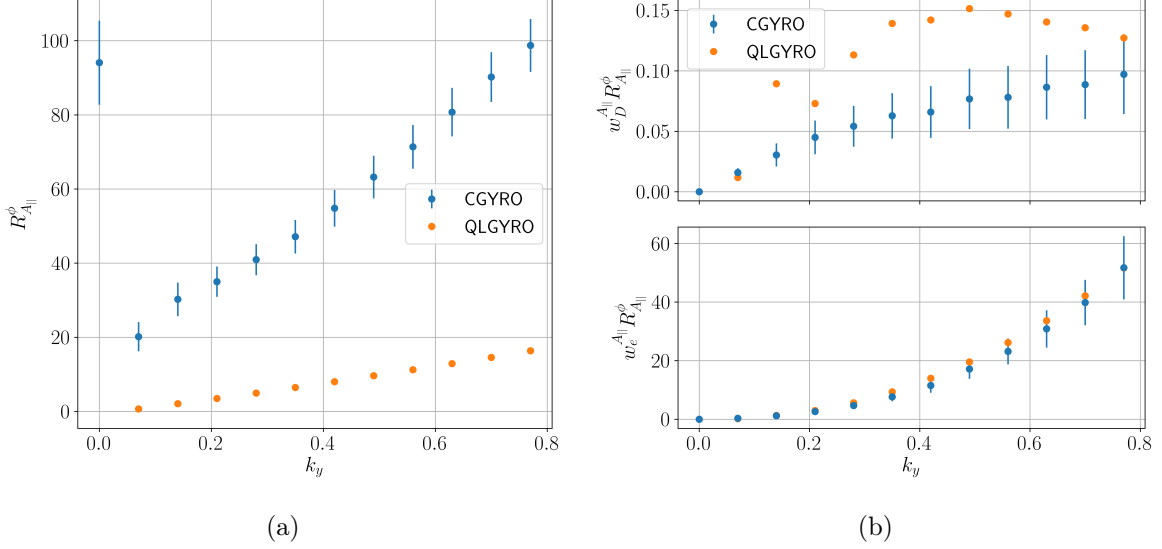


Figure 7.21: Simulation where  $A_{\parallel}$  is turned off in the non-linear term illustrating a)  $R_{A_{\parallel}}^{\phi}$  which shows the ratio of  $\phi$  and  $A_{\parallel}$ . b) Modified quasi-linear weight  $w^{A_{\parallel}} R_{A_{\parallel}}^{\phi}$  predictions by CGYRO, QLGYRO and TGLF.

### Saturated fields

Table 7.7 showed that QLGYRO overestimated the electron heat flux prediction compared to CGYRO. Given that the conventional weights were under-estimated in QLGYRO suggests that the saturated potential must be largely over-estimated in QLGYRO, which is confirmed in Figure 7.22a. This figure shows the prediction for  $|\Phi|$  made by QLGYRO and CGYRO - unsurprisingly they are not in agreement and QLGYRO largely over-estimates the potential, especially above  $k_y = 0.35$ . Note, the QLGYRO prediction goes to zero at low  $k_y$  due to the TGLF quench rule outlined in Chapter 3.

Overall, this suggests two potential methods for using quasi-linear theory. Firstly, would be to continue to use the conventional weights with a saturation model for  $\Phi$ . This would require an additional model for  $R_{A_{\parallel}}^{\phi}$  as the previous sub-section showed this ratio is not captured correctly in linear models. Though this requires the zonal flow mixing to be the saturating mechanism which is not evidently true given that  $A_{\parallel}$  is relevant in the nonlinear term.

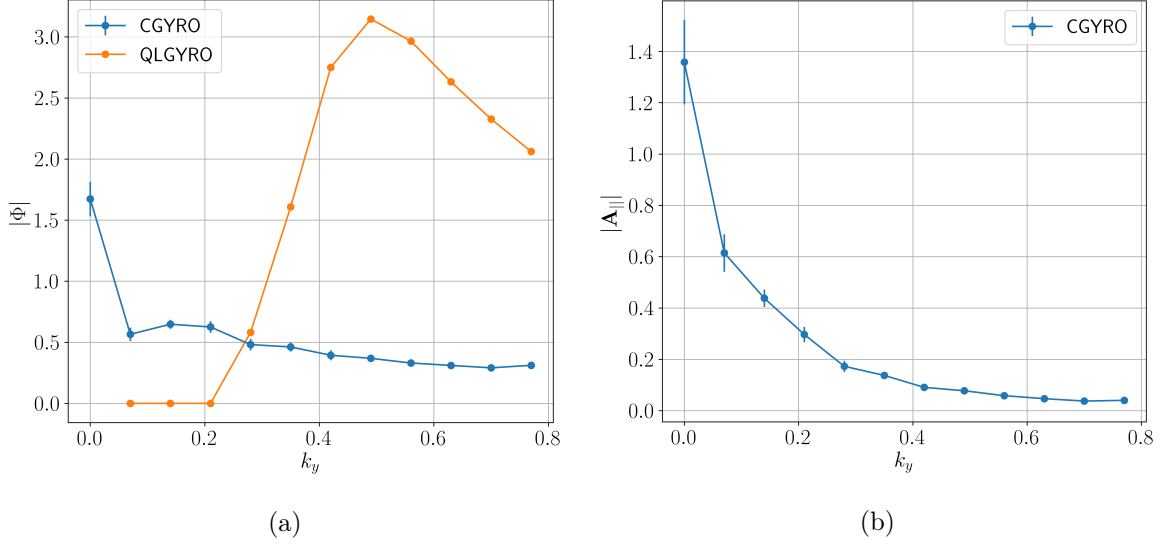


Figure 7.22: Saturated potential of the nonlinear CGYRO run showing a)  $|\Phi|$  and the QLGYRO prediction. b) shows the saturated  $|A_{||}|$  predicted by CGYRO.

The second method is to use the modified weights, which are naturally independent of the saturated fields. QLGYRO still under-estimated compared to nonlinear CGYRO, but it followed the trend better. Furthermore, when removing  $A_{||}$  from the nonlinear term, the quasi-linear weights between the linear and nonlinear result agreed very well. If the modified weights are to be used, then a new saturation model is required for  $A_{||}$ , where the nonlinear result from the NSTX simulation is shown in Figure 7.22b.

To derive a model for  $A_{||}$  will require an understanding of the saturation mechanism along with several nonlinear high  $\beta$  simulations to benchmark it. But to postulate, an equivalent expression for an effective growth rate can be defined in terms of  $A_{||}$ . Saturation may occur when the nonlinear interaction term  $(\delta v_{A_{||}} \cdot \nabla)$  matches the linear growth  $\gamma$ . The nonlinear interaction will approximately be of the form  $(\delta v_{A_{||}} \cdot \nabla) \propto k_y k_x A_{||}$ . This appears to be similar to TGLF's model for  $\phi$  in Equation 3.34. Defining an equivalent effective growth rate as

$$\gamma_{eff}^{A_{||}} \propto k_y k_{x,rms}^{A_{||}} c_s |A_{||}| \quad (7.4)$$

where  $k_{x,rms}^{A_{||}}$  is the root mean square of  $A_{||}$  when  $\theta = 0$ , given by

$$k_{x,rms}^{A_{||}} = \sqrt{\frac{\sum_{k_x} k_x^2 |A_{||}(k_x, k_y, \theta = 0)|^2}{\sum_{k_x} |A_{||}(k_x, k_y, \theta = 0)|^2}} \quad (7.5)$$

Examining this quantity for CGYRO in Figure 7.23 shows how it increases from  $k_y = 0$  up to  $k_y = 0.2$ , after which it saturates to a given level, hinting at a saturation mechanism. This has a similar functional form to the  $\gamma_{eff}$  used in the electrostatic case. Speculating the cause,

it may be due to the flow shear advecting the modes through  $\theta_0$  that causes the saturation of these modes. A model could be developed that examines the range of  $\theta_0$  over which the MTMs are unstable and the value of  $\gamma_{E \times B}$  to find the saturation level. This will require the development of a new saturation rule as this mechanism is not captured by the current TGLF saturation rule.

Interestingly, when running this case without flow shear and just  $\phi$  in the nonlinear term, the flux saturated at  $Q_e/Q_{gB} = 2.9 \pm 0.2$ , similar to the case with flow shear. Firstly, this indicates that  $\phi$  is able to provide a saturation mechanism which is independent of flow shear given the similar values of flux. Secondly, it indicates the “runaway” like behaviour seen earlier is caused by  $A_{||}$ , but this behaviour is dependent on flow shear. The first mechanism may be important in a BurST regime given that the MTMs found there were unaffected by flow shear. A saturation rule may need to account for both of these effects and its development is crucial in the design of BurST.

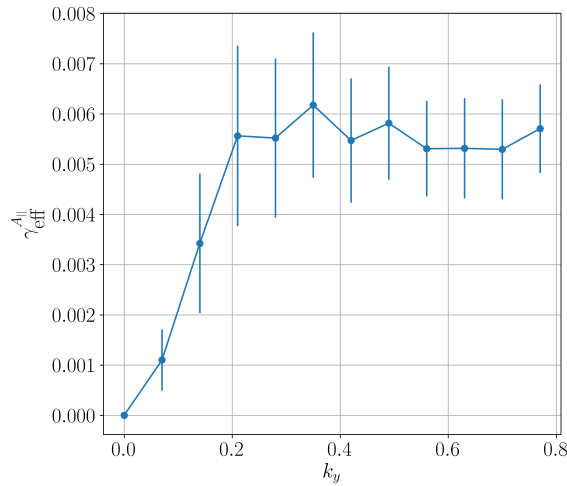


Figure 7.23: Effective growth rate using  $A_{||}$  predicted by CGYRO. It displays a similar functional form to the TGLF equivalent and suggests there is a saturation mechanism.

## 7.6 Summary

This chapter has examined the validity of quasi-linear transport modelling for several different regimes. Initially it was shown that GS2 and CGYRO agreed well linearly across the full  $k_y$  spectrum when simulating the BurST baseline equilibria. However, TGLF did not perform as well as it was not able to find the KBMs or low  $k_y$  MTMs. It had some success in finding the high  $k_y$  MTMs, but found them to be unstable across a much larger range of  $k_y$ . This suggests that the TGLF eigensolver is not currently suited for modelling the BurST regime.

Next an attempt was made at performing a nonlinear BurST simulation with CGYRO. However, it was not possible to obtain saturated results due to the very high radial resolution needed to model the low  $k_y$  MTMs. This is a major concern for designing BurST as nonlinear simulations are crucial to benchmark any quasi-linear transport model. Future work will be to attempt a multi-scale simulation that can capture this behaviour. A simulation can also be performed with the optimised equilibrium introduced in Section 6.7 where the MTMs were less unstable, but it will still be necessary to capture this MT transport for scenario development.

A new model was developed called QLGYRO that combines the linear solver in CGYRO with the TGLF saturation rule. This ensures the correct linear physics is captured, side-stepping any issues with the TGLF eigensolver. QLGYRO and TGLF were bench-marked against nonlinear CGYRO simulations in several different regimes. Initially, the low  $\beta$ , conventional aspect ratio GA-STD case was examined and it was found that both TGLF and QLGYRO performed well in this regime. Both codes were found to under-estimate the quasi-linear weights in the low  $k_y$  region, but this was compensated by the model for the saturated potential meaning the flux profile matched the nonlinear CGYRO result well.

When examining the low  $\beta$  MAST equilibria with ITG modes, it was found that TGLF and QLGYRO agreed with nonlinear CGYRO near to the experimental value of  $a/L_T$ , but over-predicted the fluxes by several orders of magnitude when  $a/L_T$  was reduced towards the linear threshold. The weights agreed reasonably well across the full range of  $a/L_T$ , which validates the use of quasi-linear models, but a more complete saturation model is required. When analysing the TGLF model for the saturated potential, it was seen that the issue arose from the model for the  $\gamma_{\text{eff}}$ . Several MAST nonlinear simulations will be required to understand the underlying cause of this discrepancy and develop an appropriate correction.

Finally a higher  $\beta$  NSTX equilibrium with MTMs was examined as this is crucial for BurST. Without flow shear the nonlinear simulation did not saturate, but this was a different issue to the BurST simulation mentioned above as it was found that the radial resolution was sufficient. Rather, this NSTX simulation displayed behaviour similar to a high  $\beta$  runaway effect seen previously in gyrokinetic simulations, suggesting a lack of saturation mechanism. It was found that these MTMs were susceptible to flow shear which allowed the simulation to saturate. The resulting flux was comparable to, but higher than GYRO fluxes presented previously, and appeared to be well converged.

Using this simulation, a benchmark of TGLF and QLGYRO was performed. When modifying TGLF inputs it was possible to find MTMs, but the growth rates found did not match the

QLGYRO (linear CGYRO) result, indicating that the TGLF eigensolver requires further development for high  $\beta$  STs. Using the standard definition of quasi-linear weights, it was found that QLGYRO under-estimates the electron weights in the low  $k_y$  region and largely over-estimated them in the high  $k_y$  region. When accounting for the ratio of fields such that the weight becomes field independent, the modified quasi-linear weights followed the nonlinear trend better, but consistently under-estimated the weights. Furthermore, when turning off  $A_{\parallel}$  in the nonlinear interaction term, the modified electron quasi-linear weights agreed nearly perfectly between QLGYRO and CGYRO. If the impact of the nonlinear  $A_{\parallel}$  term can be understood then it may be possible to improve the model for the modified weights to account for this - this is the subject of future work. Furthermore, the saturated fields were briefly examined and it was found that  $\gamma_{\text{eff}}^{A_{\parallel}}$  had a similar functional behaviour to the TGLF equivalent of  $\gamma_{\text{eff}}$ , hinting at an additional saturation mechanism, provided by the nonlinear parallel derivative. Significant work is required in the development of saturation rule and if the saturation mechanism is better understood then a new model can be derived. Regardless, the quasi-linear weights appear to provide a reasonable path to a reduced transport model, even in a MT dominant regime.

The results presented in this chapter suggest that there is potential for a quasi-linear model that is capable of capturing MTM turbulence and such a model is crucial for BurST scenario development. Directions for future work are provided, which will include the study of several more MT regimes to guide the development of new weight models and saturation mechanisms.

## Chapter 8

# Summary and Discussion

The aim of this thesis was to examine the plasma physics issues of a high  $\beta$  ST reactor (BurST) that could generate net electricity to speed up the timeline of fusion. In particular, this work attempts to find a viable steady state flat-top scenario where the total auxiliary power requirements were quantified. The modelling tools available and their validity in a BurST-like regime were examined as these are crucial for scenario development and design optimisation.

### Steady state scenarios

Chapter 4 examined the plasma requirements for a net electric power plant in terms of fusion power, and it was concluded that  $P_{\text{fus}} > 1\text{GW}$  would be sufficient. This is contingent on, and is highly sensitive to, the auxiliary power requirements, so accurately determining  $P_{\text{aux}}$  is crucial and motivates this work. Plasma shaping parameters were determined using exhaust requirements and stability limits. Next, plasma equilibria were examined by solving the Grad-Shafranov equation whilst self-consistently calculating the neoclassical currents using SCENE. The kinetic and auxiliary current profiles were prescribed *a priori*. This allowed for an accurate determination of the total required auxiliary current and by assuming a current drive efficiency,  $\eta_{\text{CD}}$ , it was possible to determine  $P_{\text{aux}}$ . The impact of different plasma temperatures, densities and currents at fixed  $P_{\text{fus}} = 1.1\text{GW}$  was then examined. Imposing the following global limits allowed certain operational regimes to be ruled out;  $H_{98} < 1.6$ ,  $f_{\text{GW}} < 1.0$ ,  $\beta_N < 6.0$  and  $P_{\text{aux}} < 100\text{MW}$ . A baseline scenario was determined within the limits identified and was used in the analysis conducted in the following chapters. Furthermore, the impact of reducing  $\eta_{\text{CD}}$  was explored. A key result is that there is no available operating space when  $\eta_{\text{CD}} \leq 0.2\text{A m}^{-2}\text{W}^{-1}$ , indicating that this current drive efficiency must be exceeded to have

a viable steady state scenario given this  $\beta_N$  limit, regardless of the source. Both NBI and RF methods have demonstrated current drive efficiencies above this suggesting this may be achievable. These empirical restrictions can be added to and refined to more accurately portray the operational limits of BurST.

It was found that a high  $I_p$  regime was generally limited by the  $\eta_{CD}$  and  $P_{aux}$ , and low  $I_p$  operation limited by  $\beta_N$ . A more accurate limit of  $\beta_N$  could be determined using a suitable MHD code which would further refine this operational space. For example, STPP was designed with  $\beta_N = 8.2$ . Furthermore, a higher field superconductor scenario at fixed  $P_{fus}$  was examined where the central conducting column would require a REBCO superconductor rather than the original cryogenic copper (or aluminium) conductor. This reduced the  $\beta_N$  opening up the lower  $I_p$  region. This also allowed for operation at lower  $\eta_{CD}$ , suggesting a solution if a high enough current drive efficiency is not possible.

The approach taken in this thesis was based off of several requirements of BurST, but in principle could be applied when designing any new tokamak. Once the over-arching goals and the relevant operating limits of the tokamak are defined, this analysis could be repeated.

### Auxiliary current drive

A steady state scenario cannot rely on inductive current drive, so non-inductive scenarios must be developed. Chapter 5 examined the feasibility of using NBI to drive all the auxiliary current and some of the reduced models of NBI current drive available were explored. The baseline scenario identified had two regions where current drive was necessary resulting in 2 separate beams; one on the magnetic axis and one off axis near the outer radial edge of the device. On axis, less than 0.2MA is needed to fill the hole left by the bootstrap current, with the remaining 8.1MA being needed off axis. NUBEAM was used to develop a suitable configuration and benchmark two reduced physics models, NBeams and RABBIT.

All 3 codes agreed reasonably well when simulating the on axis beam. Using the different densities (at fixed  $P_{fus} = 1.1GW$ ) examined in Chapter 4, the penetration of a 1MW beam was examined. As the core density increased the penetration of the beam dropped such that the power needed to reach the required current density at the core increased exponentially. Given that most of the current needs to be driven off-axis, the amount of power dedicated for the on-axis beam must be limited. Assuming only 10MW is allocated for the on axis beam leads to an upper density limit of  $\langle n_{e20} \rangle \leq 1.65m^{-3}$ , further limiting the parameter space for operation.

There are several ways to overcome this particular limit; a higher energy beam would provide

one solution, but it seems that 1MeV beams are at the current engineering limits of achievable beam energies. If higher density peaking can be achieved then the beam would be less attenuated at the edge at a given  $\langle n_{e20} \rangle$ , resulting in higher core penetration.

The off-axis current was then examined and it was found with NUBEAM that when the beam was injected within the mid-plane the current drive efficiency was below the required threshold, only reaching a maximum  $\eta_{\text{NBI}} = 0.18 \text{ A m}^{-2} \text{ W}^{-1}$ . This was largely due to the high fraction of trapped fast ions which are unable to contribute to the total current. NBeams is not able to capture this physics of this situation, and whilst RABBIT in principle can, it was found to not agree well with NUBEAM. However, when the beam was angled such that it was aligned with the magnetic field the current drive efficiency increased significantly such that the total amount of power needed to drive the required current was below 100MW. Furthermore, the agreement between the three codes improved in this regime as the trapped particle effect was minimised. A reactor will need to operate with field-aligned beams to maximise  $\eta_{\text{NBI}}$ , so when designing scenarios either NBeams or RABBIT can be used to get a reasonable estimation of the required NBI configuration. This can then be refined with NUBEAM to gain further confidence in the NBI configuration.

### Linear turbulent instabilities

The previous chapters prescribed density and temperature profiles which were examined in the context of confinement scaling laws. Both the ITER98 and Petty scaling laws describe the confinement of existing tokamaks well but when extrapolated to BurST make very different predictions. For example, in the baseline scenario, the required ITER98 confinement factor was  $H_{98} = 1.35$ , but Petty factor was only  $H_{\text{Petty}} = 0.94$ . The actual quality of confinement will be determined by the transport processes, so it is vital to understand what these mechanisms are. Turbulence is often the dominant source of transport and examining the drivers of turbulence will allow for the optimisation of the equilibrium.

The linear turbulent micro-instabilities of the baseline equilibrium were examined with GS2 to determine what modes will be driving the turbulent transport. The dominant instability found in the ion scale region of BurST were KBMs, with MTMs existing sub-dominantly. Additionally, another type of MTM was found in the  $k_y \sim 4$  region. The electron scale region was found to be completely stable due to the large  $\beta'_{e,\text{unit}}$ . The properties of these modes were analysed to determine what equilibrium parameters they were dependent on.

The KBMs and higher  $k_y$  MTMs were very narrow in  $\theta_0$  such that diamagnetic levels of flow shear were sufficient in suppressing them. The low  $k_y$  MTMs were independent of flow shear

but were found to be stabilised by the density gradient. An optimised equilibrium was created with a higher density gradient at fixed  $P_{\text{fus}} = 1.1\text{GW}$  with the volume average temperature and density being similar to the baseline scenario. This stabilised the low  $k_y$  MTMs such that with diamagnetic levels of flow shear the equilibrium is marginally stable to all the micro-instabilities explored at the  $\rho_\psi = 0.5$  surface. These results suggest that BurST could operate at neoclassical levels of heat transport, indicating a high performance regime is possible.

### Quasi-linear models

To determine the power balance for BurST requires reliable calculations of turbulent transport. Nonlinear gyrokinetics is the best tool currently available for turbulence simulations but it is not feasible to use it in a transport solver due to computational costs. The validity of quasi-linear models was examined, as this has proven to be a powerful tool in matching nonlinear turbulence simulations in low  $\beta$  conventional aspect ratio tokamak plasmas.

It was not possible to obtain converged nonlinear BurST simulations due to the extended nature of the MTMs in ballooning space which requires electron-scale radial resolutions. Multi-scale simulations will be necessary to fully resolve these modes and this is crucial for the development of BurST.

It was shown that the MTMs and KBMs prevalent in BurST were not well captured by the TGLF eigensolver. A new quasi-linear model was developed called QLGYRO which combines the linear solver of CGYRO with the TGLF saturation rule. This was then tested in several regimes starting from a GA-STD conventional aspect ratio equilibrium, building up towards a MAST equilibrium, and then a higher  $\beta$  NSTX equilibrium where MTMs were the dominant mode. It was found that the quasi-linear weights are a good approximation for the GA-STD and MAST equilibria where ITGs are the dominant mode. For the NSTX equilibrium the conventional quasi-linear weights did not follow the trend of the nonlinear simulation, but when using the field-independent quasi-linear weights the weights better followed the trend, though it was consistently under-estimated. The cause of the discrepancy was found to be associated with the parallel streaming along perturbed field lines, described by  $A_{\parallel}$  inside the nonlinear interaction term, without which the modified quasi-linear weight agreed with the nonlinear result.

The area that needs the most development is the saturation rule. In the MAST simulations the saturation rule did not capture the electrostatic potential when changing  $a/L_T$ , suggesting an issue in the model. By examining the different components of the saturation rule of TGLF/QLGYRO, the source of the disparity was found to be in the  $\gamma_{\text{eff}}$ , which uses  $c_0$ .

Given that  $c_0$  was fitted from GA-STD like simulations, it is not surprising that this does not perform as well in such a different regime. This may require a more detailed examination to explore what physics is missing to cause the disagreement. Unsurprisingly, the model does not perform well for the NSTX case. Given that MTMs are the dominant source of transport here, it is reasonable to assume that an entirely different mechanism is the cause of saturation compared to ITG dominated regimes.

The formulation of a quasi-linear model valid in a ST MTM dominated regime is a vital element in the development of BurST and this work has taken the initial steps towards such a model. Moreover, a methodology for identifying an available operating space for BurST was created and it was demonstrated that NBI is able to achieve the necessary current drive efficiency to ensure net electricity. Furthermore, a linearly stable equilibrium was identified suggesting that operation at neoclassical levels of heat transport may be possible, illustrating a path towards a net electric ST. A BurST-like approach may help to accelerate the path to fusion whilst reducing fusion's capital costs, which will allow for fusion to make a more significant impact to the global energy-mix. The work conducted in this thesis illustrates that a high performance, net electric ST may be feasible and warrants further investigation.

### **Future work**

The development BurST will require research in many different areas. For example, all of the work in this thesis has assumed a steady state scenario, so research on the ramp-up phase is crucial to identify if a path to these scenarios is possible.

Several limiting factors were examined when determining the available operating space for BurST. However, there will be other issues that need to be accounted for, such as ELMs. ELM mitigation/suppression may be required so a greater understanding of the pedestal is needed. This work assumed an ITER like pedestal but with a more rigorous analysis of the pedestal, the SCENE profiles can be more confidently set and the analysis conducted in Chapter 4 can be repeated. Furthermore, inclusion of fast ions in the equilibrium calculation is a vital next step as it was shown that the fast ion pressure can form a significant fraction of the total pressure and was not included in this work.

The research presented in this thesis suggest that a non-inductive scenario would be possible using only NBI. The viability of RF current drive systems should also be explored for BurST as it has some advantages. Given that a small amount of local current is needed in the core,

EBW could be a promising alternative for the on axis beam given that it does not have a density cut-off. The difficulties in steering EBW would not be an issue as this current would only be needed in one location. Furthermore, operation at higher densities becomes plausible as this was set by the penetration depth of a 1MeV beam which would now only need to drive current at the edge.

The feasibility of a peaked density needs to be examined as this was crucial in stabilising the MTMs. Using an appropriate particle transport model, the amount of core fuelling necessary for these profiles can be determined. There are other considerations to be made with density peaking as it can lead to impurity accumulation which in turn can lead to radiative collapse, so this needs to be examined in further detail.

Linear gyrokinetic simulations including fast ions (from both the NBI and the fusion  $\alpha$ 's) and impurities are the next logical step in examining the linear stability of BurST-like equilibria. Quantifying their impact on the KBMs and MTMs is needed as it may affect the strategy used to design a more stable equilibrium.

Finally, it is critical that the saturation mechanism of MTMs is better understood as any quasi-linear model must be able to account for this source of transport. A potential saturating mechanism was identified for the MTMs in NSTX with  $\gamma_{\text{eff}}^{A_{\parallel}}$  and flow shear possibly playing a crucial role. Further nonlinear MT simulations will help to probe the behaviour of these modes and build a theoretical framework for their saturation. However, the MTMs seen in BurST are unaffected by flow shear so another saturation mechanism must be explored. Obtaining converged nonlinear BurST simulations will be critical in developing these quasi-linear models.

# References

- [1] Janez Sušnik and Pieter van der Zaag. “Correlation and causation between the UN Human Development Index and national and personal wealth and resource exploitation”. In: *Economic research-Ekonomska istraživanja* 30.1 (2017), pp. 1705–1723.
- [2] Daniel M Martinez and Ben W Ebenhack. “Understanding the role of energy consumption in human development through the use of saturation phenomena”. In: *Energy Policy* 36.4 (2008), pp. 1430–1435.
- [3] “Global Energy Review 2019 The latest trends in energy and emissions in 2019”. In: *International energy agency* (2020).
- [4] IPCC. “Special Report on the impacts of global warming of 1.5 C above pre-industrial levels and related global greenhouse gas emission pathways, in the context of strengthening the global response to the threat of climate change, sustainable development, and efforts to eradicate poverty”. In: *Intergovernmental Panel on Climate Change* (2018).
- [5] T Donne, Morris AW, et al. “European research roadmap to the realisation of fusion energy”. In: (2018).
- [6] NJL Cardozo, AGG Lange, and GJ Kramer. “Fusion: expensive and taking forever?” In: *Journal of Fusion Energy* 35.1 (2016), pp. 94–101.
- [7] NJL Cardozo. “Economic aspects of the deployment of fusion energy: the valley of death and the innovation cycle”. In: *Philosophical Transactions of the Royal Society A* 377.2141 (2019), p. 20170444.
- [8] MZ Jacobson et al. “Matching demand with supply at low cost in 139 countries among 20 world regions with 100% intermittent wind, water, and sunlight (WWS) for all purposes”. In: *Renewable Energy* 123 (2018), pp. 236–248.
- [9] W Zappa, M Junginger, and M van den Broek. “Is a 100% renewable European power system feasible by 2050?” In: *Applied energy* 233 (2019), pp. 1027–1050.

- [10] M Ram et al. “Global energy system based on 100% renewable energy—power sector”. In: *Lappeenranta University of Technology and Energy Watch Group: Lappeenranta, Finland* (2017).
- [11] NA Sepulveda et al. “The role of firm low-carbon electricity resources in deep decarbonization of power generation”. In: *Joule* 2.11 (2018), pp. 2403–2420.
- [12] R Herendeen. “Does “100% renewable” trump concern for spatial impacts?” In: *Energy Policy* 130 (2019), pp. 304–310.
- [13] V Smil. “Distributed generation and megacities: Are renewables the answer?” In: *IEEE Power and Energy Magazine* 17.2 (2019), pp. 37–41.
- [14] JD Jenkins, M Luke, and S Thernstrom. “Getting to zero carbon emissions in the electric power sector”. In: *Joule* 2.12 (2018), pp. 2498–2510.
- [15] JD Jenkins et al. “The benefits of nuclear flexibility in power system operations with renewable energy”. In: *Applied energy* 222 (2018), pp. 872–884.
- [16] A Mileva et al. “Power system balancing for deep decarbonization of the electricity sector”. In: *Applied Energy* 162 (2016), pp. 1001–1009.
- [17] S Brick and S Thernstrom. “Renewables and decarbonization: studies of California, Wisconsin and Germany”. In: *The Electricity Journal* 29.3 (2016), pp. 6–12.
- [18] MR Gilbert et al. “Waste implications from minor impurities in European DEMO materials”. In: *Nuclear Fusion* 59.7 (2019), p. 076015.
- [19] G Harris et al. “Cost estimates for nuclear power in the UK”. In: *Energy Policy* 62 (2013), pp. 431–442.
- [20] S Entler et al. “Approximation of the economy of fusion energy”. In: *Energy* 152 (2018), pp. 489–497.
- [21] KH Moon and SS Kim. “An Exploratory Study on a Target Capital Cost and Cost Reduction Methodologies of Innovative SMR in Korea”. In: (2020).
- [22] LM Boldon and P Sabharwall. *Small Modular Reactor: First-of-a-Kind (FOAK) and Nth-of-a-Kind (NOAK) economic analysis*. Tech. rep. Idaho National Lab.(INL), Idaho Falls, ID (United States), 2014.
- [23] TEG Nicholas et al. “Re-examining the role of nuclear fusion in a renewables-based energy mix”. In: *Energy Policy* 149 (2020), p. 112043.

- [24] GR Tynan and A Abdulla. “How might controlled fusion fit into the emerging low-carbon energy system of the mid-twenty-first century?” In: *Philosophical Transactions of the Royal Society A* 378.2184 (2020), p. 20200009.
- [25] Louis N Ridenour. “The hydrogen bomb”. In: *Scientific American* 182.3 (1950), pp. 11–15.
- [26] J Wesson and DJ Campbell. *Tokamaks*. Vol. 149. Oxford university press, 2011.
- [27] EE Salpeter. “Nuclear reactions in the stars. I. Proton-proton chain”. In: *Physical Review* 88.3 (1952), p. 547.
- [28] D Dickinson. “Effects of profiles on microinstabilities in tokamaks”. PhD thesis. University of York, 2012.
- [29] C Gormezano et al. “Internal transport barriers in JET deuterium-tritium plasmas”. In: *Physical review letters* 80.25 (1998), p. 5544.
- [30] Y Kamada et al. “Fusion plasma performance and confinement studies on JT-60 and JT-60U”. In: *Fusion science and technology* 42.2-3 (2002), pp. 185–254.
- [31] AE Costley. “On the fusion triple product and fusion power gain of tokamak pilot plants and reactors”. In: *Nuclear Fusion* 56.6 (2016), p. 066003.
- [32] AJ Creely et al. “Overview of the SPARC tokamak”. In: *Journal of Plasma Physics* 86.5 (2020).
- [33] GM Voss et al. “A conceptual design of a spherical tokamak power plant”. In: *Fusion engineering and design* 51 (2000), pp. 309–318.
- [34] RL Miller et al. “Stable equilibria for bootstrap-current-driven low aspect ratio tokamaks”. In: *Physics of Plasmas* 4.4 (1997), pp. 1062–1068.
- [35] JE Menard et al. “Ideal MHD stability limits of low aspect ratio tokamak plasmas”. In: *Nuclear Fusion* 37.5 (1997), p. 595.
- [36] A Sykes et al. “High beta performance of the START spherical tokamak”. In: *Plasma Phys. Control. Fusion* 39.12B (1997), B247–B260.
- [37] HR Wilson et al. “Integrated plasma physics modelling for the Culham steady state spherical tokamak fusion power plant”. In: *Nuclear fusion* 44.8 (2004), p. 917.
- [38] M Windridge. “Smaller and quicker with spherical tokamaks and high-temperature superconductors”. In: *Philosophical Transactions of the Royal Society A* 377.2141 (2019), p. 20170438.

- [39] YKM Peng and DJ Strickler. “Features of spherical torus plasmas”. In: *Nuclear Fusion* 26.6 (1986), p. 769.
- [40] HR Wilson et al. “STEP - on the pathway to fusion commercialization”. In: *Commercialising Fusion Energy*. 2053-2563. IOP Publishing, 2020, 8-1 to 8-18.
- [41] M Gryaznevich, O Asunta, and Tokamak Energy Ltd Team. “Overview and status of construction of ST40”. In: *Fusion Engineering and Design* 123 (2017), pp. 177–180.
- [42] GT Hoang et al. “A lower hybrid current drive system for ITER”. In: *Nuclear Fusion* 49.7 (2009), p. 075001.
- [43] RA Cairns and CN Lashmore-Davies. “The prospects for electron Bernstein wave heating of spherical tokamaks”. In: *Physics of Plasmas* 7.10 (2000), pp. 4126–4134.
- [44] G Taylor et al. “Efficient generation of noninductive, off-axis, Ohkawa current, driven by electron Bernstein waves in high  $\beta$ , spherical torus plasmas”. In: *Physics of plasmas* 11.10 (2004), pp. 4733–4739.
- [45] W Egbert. “Non-Inductive Current Drive”. In: *Fusion Science and Technology* 61.2T (2012), pp. 312–319. DOI: 10.13182/FST12-A13518. eprint: <https://doi.org/10.13182/FST12-A13518>. URL: <https://doi.org/10.13182/FST12-A13518>.
- [46] MJ Singh et al. “Heating neutral beams for ITER: negative ion sources to tune fusion plasmas”. In: *New Journal of Physics* 19.5 (2017), p. 055004.
- [47] RS Hemsworth et al. “Overview of the design of the ITER heating neutral beam injectors”. In: *New Journal of Physics* 19.2 (2017), p. 025005.
- [48] EDA ITER et al. “Plasma auxiliary heating and current drive”. In: *Nuclear Fusion* 39.12 ITER physics basis (1999), pp. 2495–2539.
- [49] J Garcia et al. “Analysis of DEMO scenarios with the CRONOS suite of codes”. In: *Nuclear fusion* 48.7 (2008), p. 075007.
- [50] E Surrey et al. “The influence of neutral beam optimization for DEMO on injector design”. In: *Fusion Engineering and Design* 87.4 (2012), pp. 373–383.
- [51] C Gormezano et al. “Steady state operation”. In: *Nuclear Fusion* 47.6 (2007), S285.
- [52] RJ Hawryluk. “An empirical approach to tokamak transport”. In: *Physics of plasmas close to thermonuclear conditions*. Elsevier, 1981, pp. 19–46.
- [53] G Cenacchi and A Taroni. *Jetto a free boundary plasma transport code*. Tech. rep. ENEA, 1988.

- [54] J Candy et al. “Tokamak profile prediction using direct gyrokinetic and neoclassical simulation”. In: *Physics of Plasmas* 16.6 (2009), p. 060704.
- [55] Francis Troyon et al. “MHD-limits to plasma confinement”. In: *Plasma physics and controlled fusion* 26.1A (1984), p. 209.
- [56] RJ Buttery et al. “Stability at high performance in the MAST spherical tokamak”. In: *Nuclear fusion* 44.9 (2004), p. 1027.
- [57] RJ Hastie. “Sawtooth instability in tokamak plasmas”. In: *Astrophysics and space science* 256.1-2 (1997), pp. 177–204.
- [58] RJ La Haye. “Neoclassical tearing modes and their control”. In: *Physics of Plasmas* 13.5 (2006), p. 055501.
- [59] HR Wilson et al. “Numerical studies of edge localized instabilities in tokamaks”. In: *Physics of Plasmas* 9.4 (2002), pp. 1277–1286.
- [60] AB Mikhailovskii et al. “Optimization of computational MHD normal-mode analysis for tokamaks”. In: *Plasma Physics Reports* 23.10 (1997), pp. 844–857.
- [61] IT Chapman et al. “Toroidal velocity shear Kelvin–Helmholtz instabilities in strongly rotating tokamak plasmas”. In: *Nuclear Fusion* 52.4 (2012), p. 042005.
- [62] SC Jardin et al. “Physics basis for a reversed shear tokamak power plant”. In: *Fusion Engineering and Design* 38.1-2 (1997), pp. 27–57.
- [63] MS Chu et al. “Resistive interchange modes in negative central shear tokamaks with peaked pressure profiles”. In: *Physical review letters* 77.13 (1996), p. 2710.
- [64] S Günter et al. “MHD phenomena in reversed shear discharges on ASDEX Upgrade”. In: *Nuclear fusion* 40.8 (2000), p. 1541.
- [65] ME Fenstermacher et al. “Pedestal, SOL and divertor plasma properties in DIII-D RMP ELM-suppressed discharges at ITER relevant edge collisionality”. In: *Journal of nuclear materials* 363 (2007), pp. 476–483.
- [66] RD Hazeltine. “Recursive derivation of drift-kinetic equation”. In: *Plasma Physics* 15.1 (1973), p. 77.
- [67] WA Houlberg et al. “Bootstrap current and neoclassical transport in tokamaks of arbitrary collisionality and aspect ratio”. In: *Physics of Plasmas* 4.9 (1997), pp. 3230–3242.

- [68] EA Belli and J Candy. “Kinetic calculation of neoclassical transport including self-consistent electron and impurity dynamics”. In: *Plasma Physics and Controlled Fusion* 50.9 (2008), p. 095010.
- [69] EA Belli et al. “Limitations of bootstrap current models”. In: *Plasma Physics and Controlled Fusion* 56.4 (2014), p. 045006.
- [70] AJ Wootton et al. “Fluctuations and anomalous transport in tokamaks”. In: *Physics of Fluids B: Plasma Physics* 2.12 (1990), pp. 2879–2903.
- [71] JW Conner and HR Wilson. “Survey of theories of anomalous transport”. In: *Plasma physics and controlled fusion* 36.5 (1994), p. 719.
- [72] F Jenko, T Dannert, and C Angioni. “Heat and particle transport in a tokamak: advances in nonlinear gyrokinetics”. In: *Plasma physics and controlled fusion* 47.12B (2005), B195.
- [73] GM Staebler, JE Kinsey, and RE Waltz. “Gyro-Landau fluid equations for trapped and passing particles”. In: *Physics of Plasmas* 12.10 (2005), p. 102508.
- [74] EDA ITER et al. “Plasma confinement and transport”. In: *Nuclear Fusion* 39.12 ITER physics basis (1999), pp. 2175–2249.
- [75] CC Petty. “Sizing up plasmas using dimensionless parameters”. In: *Physics of Plasmas* 15.8 (2008), p. 781.
- [76] A Sykes et al. “Opportunities and challenges for compact fusion energy”. In: *Fusion Science and Technology* 68.2 (2015), pp. 237–244.
- [77] SM Kaye et al. “Confinement and local transport in the National Spherical Torus Experiment (NSTX)”. In: *Nuclear Fusion* 47.7 (2007), p. 499.
- [78] M Valovič et al. “Energy and particle confinement in MAST”. In: *Nuclear fusion* 45.8 (2005), p. 942.
- [79] Y Camenen et al. “Impact of plasma triangularity and collisionality on electron heat transport in TCV L-mode plasmas”. In: *Nuclear fusion* 47.7 (2007), p. 510.
- [80] F Romanelli and JET EFDA Contributors. “Overview of the JET results with the ITER-like wall”. In: *Nuclear Fusion* 53.10 (2013), p. 104002.
- [81] M Artun and WM Tang. “Nonlinear electromagnetic gyrokinetic equations for rotating axisymmetric plasmas”. In: *Physics of plasmas* 1.8 (1994), pp. 2682–2692.

- [82] H Sugama and W Horton. “Nonlinear electromagnetic gyrokinetic equation for plasmas with large mean flows”. In: *Physics of plasmas* 5.7 (1998), pp. 2560–2573.
- [83] CM Roach et al. “Gyrokinetic simulations of spherical tokamaks”. In: *Plasma Physics and Controlled Fusion* 51.12 (2009), p. 124020.
- [84] F Van Wyk. “Subcritical turbulence in the mega ampere spherical tokamak”. In: *arXiv:1703.03397* (2017).
- [85] EG Highcock. “The zero turbulence manifold in fusion plasmas”. In: *arXiv preprint arXiv:1207.4419* (2012).
- [86] Emily Ann Belli. “Studies of numerical algorithms for gyrokinetics and the effects of shaping on plasma turbulence”. PhD thesis. Citeseer, 2006.
- [87] Michael Alan Beer, SC Cowley, and GW Hammett. “Field-aligned coordinates for non-linear simulations of tokamak turbulence”. In: *Physics of Plasmas* 2.7 (1995), pp. 2687–2700.
- [88] JW Connor, RJ Hastie, and John Bryan Taylor. “High mode number stability of an axisymmetric toroidal plasma”. In: *Proceedings of the Royal Society of London. A. Mathematical and Physical Sciences* 365.1720 (1979), pp. 1–17.
- [89] W Dorland and M Kotschenreuther. *Microinstabilities in Axisymmetric Configurations*.
- [90] RJ Akers et al. “Transport studies in the MAST spherical tokamak”. In: *Proc. 22nd IAEA Fusion Energy Conf.(Geneva, Switzerland)*. 2008.
- [91] TS Taylor et al. “Optimized profiles for improved confinement and stability in the DIII-D tokamak”. In: *Plasma physics and controlled fusion* 36.12B (1994), B229.
- [92] TS Hahm et al. “Shearing rate of time-dependent  $E \times B$  flow”. In: *Physics of Plasmas* 6.3 (1999), pp. 922–926.
- [93] DJ Applegate et al. “Microstability in a “MAST-like” high confinement mode spherical tokamak equilibrium”. In: *Physics of plasmas* 11.11 (2004), pp. 5085–5094.
- [94] AG Peeters et al. “The nonlinear gyro-kinetic flux tube code GKW”. In: *Computer Physics Communications* 180.12 (2009), pp. 2650–2672.
- [95] JD Callen. “Drift-wave turbulence effects on magnetic structure and plasma transport in tokamaks”. In: *Physical Review Letters* 39.24 (1977), p. 1540.
- [96] NT Howard et al. “Validation of the gyrokinetic model in ITG and TEM dominated L-mode plasmas”. In: *Nuclear Fusion* 53.12 (2013), p. 123011.

- [97] DR Hatch et al. “A gyrokinetic perspective on the JET-ILW pedestal”. In: *Nuclear Fusion* 57.3 (2017), p. 036020.
- [98] A Casati. “A quasi-linear gyrokinetic transport model for tokamak plasmas”. In: *arXiv preprint arXiv:1204.3254* (2012).
- [99] T Xie, MJ Pueschel, and DR Hatch. “Quasilinear modeling of heat flux from microtearing turbulence”. In: *Physics of Plasmas* 27.8 (2020), p. 082306.
- [100] GM Staebler et al. “Geometry dependence of the fluctuation intensity in gyrokinetic turbulence”. In: *Plasma Physics and Controlled Fusion* 63.1 (2020), p. 015013.
- [101] FJ Casson et al. “Predictive multi-channel flux-driven modelling to optimise ICRH tungsten control and fusion performance in JET”. In: *Nuclear Fusion* 60.6 (2020), p. 066029.
- [102] HR Wilson. *SCENE-simulation of self-consistent equilibria with neoclassical effects*. Tech. rep. UKAEA Government Division, 1994.
- [103] RL Miller et al. “Noncircular, finite aspect ratio, local equilibrium model”. In: *Physics of Plasmas* 5.4 (1998), pp. 973–978.
- [104] PB Snyder et al. “A first-principles predictive model of the pedestal height and width: development, testing and ITER optimization with the EPED model”. In: *Nuclear Fusion* 51.10 (2011), p. 103016.
- [105] SP Hirshman and DJ Sigmar. “Neoclassical transport of impurities in tokamak plasmas”. In: *Nuclear Fusion* 21.9 (1981), p. 1079.
- [106] O Sauter, C Angioni, and YR Lin-Liu. “Neoclassical conductivity and bootstrap current formulas for general axisymmetric equilibria and arbitrary collisionality regime”. In: *Physics of Plasmas* 6.7 (1999), pp. 2834–2839.
- [107] MCR Andrade and GO Ludwig. “Comparison of bootstrap current and plasma conductivity models applied in a self-consistent equilibrium calculation for tokamak plasmas”. In: *Nuclear fusion* 45.1 (2004), p. 48.
- [108] A Pankin et al. “The tokamak Monte Carlo fast ion module NUBEAM in the National Transport Code Collaboration library”. In: *Computer Physics Communications* 159.3 (2004), pp. 157–184.
- [109] J Mandrekas. *Physics models and user’s guide for the neutral beam module of the supercode*. Tech. rep. Georgia Inst. of Tech., Atlanta, GA (United States). Fusion Research Center, 1992.

- [110] M Weiland et al. “RABBIT: Real-time simulation of the NBI fast-ion distribution”. In: *Nuclear Fusion* 58.8 (2018), p. 082032.
- [111] SP Gerhardt et al. “Calculation of the non-inductive current profile in high-performance NSTX plasmas”. In: *Nuclear Fusion* 51.3 (2011), p. 033004.
- [112] Ž Štancar et al. “Generation of a plasma neutron source for Monte Carlo neutron transport calculations in the tokamak JET”. In: *Fusion engineering and design* 136 (2018), pp. 1047–1051.
- [113] DN Hill et al. “DIII-D research towards resolving key issues for ITER and steady-state tokamaks”. In: *Nuclear Fusion* 53.10 (2013), p. 104001.
- [114] William Bell Thompson. *An introduction to plasma physics*. Elsevier, 2013.
- [115] JD Gaffey. “Energetic ion distribution resulting from neutral beam injection in tokamaks”. In: *Journal of Plasma Physics* 16.2 (1976), pp. 149–169.
- [116] JA Rome, JD Callen, and JF Clarke. “Neutral-beam injection into a tokamak, part I: fast-ion spatial distribution for tangential injection”. In: *Nuclear Fusion* 14.2 (1974), p. 141.
- [117] DFH Start and JG Cordey. “Beam-induced currents in toroidal plasmas of arbitrary aspect ratio”. In: *The Physics of Fluids* 23.7 (1980), pp. 1477–1478.
- [118] RV Bravenec et al. “Linear and nonlinear verification of gyrokinetic microstability codes”. In: *Physics of Plasmas* 18.12 (2011), p. 122505.
- [119] J Candy, EA Belli, and RV Bravenec. “A high-accuracy Eulerian gyrokinetic solver for collisional plasmas”. In: *Journal of Computational Physics* 324 (2016), pp. 73–93.
- [120] C Bourdelle et al. “A new gyrokinetic quasilinear transport model applied to particle transport in tokamak plasmas”. In: *Physics of Plasmas* 14.11 (2007), p. 112501.
- [121] GM Staebler et al. “Testing the trapped gyro-landau fluid transport model with data from tokamaks and spherical tori”. In: *Proc. 22nd IAEA Fusion Energy Conf. (Geneva, Switzerland)*. 2008.
- [122] J Candy and GM Staebler. “Crucial role of zonal flows and electromagnetic effects in ITER turbulence simulations near threshold”. In: *26th IAEA Fusion Energy Conference, Kyoto, Japan, 17–22 October 2016*. 2016.
- [123] BS Patel et al. “Optimising TGLF for a Q= 10 Burning Spherical Tokamak”. In: *46th EPS Conference on Plasma Physics*. European Physical Society (EPS). 2019.

- [124] W Dorland and GW Hammett. “Gyrofluid turbulence models with kinetic effects”. In: *Physics of Fluids B: Plasma Physics* 5.3 (1993), pp. 812–835.
- [125] Orso Meneghini et al. “Modeling of transport phenomena in tokamak plasmas with neural networks”. In: *Physics of Plasmas* 21.6 (2014), p. 060702.
- [126] Orso Meneghini et al. “Self-consistent core-pedestal transport simulations with neural network accelerated models”. In: *Nuclear Fusion* 57.8 (2017), p. 086034.
- [127] RE Waltz, GD Kerbel, and J Milovich. “Toroidal gyro-Landau fluid model turbulence simulations in a nonlinear ballooning mode representation with radial modes”. In: *Physics of Plasmas* 1.7 (1994), pp. 2229–2244.
- [128] GM Staebler et al. “The role of zonal flows in the saturation of multi-scale gyrokinetic turbulence”. In: *Physics of Plasmas* 23.6 (2016), p. 062518.
- [129] A Casati et al. “Validating a quasi-linear transport model versus nonlinear simulations”. In: *Nuclear Fusion* 49.8 (2009), p. 085012.
- [130] AM Dimits et al. “Comparisons and physics basis of tokamak transport models and turbulence simulations”. In: *Physics of Plasmas* 7.3 (2000), pp. 969–983.
- [131] GM Voss et al. “Conceptual design of a component test facility based on the spherical tokamak”. In: *Fusion Engineering and Design* 83.10-12 (2008), pp. 1648–1653.
- [132] AW Morris et al. “Spherical tokamaks: present status and role in the development of fusion power”. In: *Fusion engineering and design* 74.1-4 (2005), pp. 67–75.
- [133] YKM Peng et al. “A component test facility based on the spherical tokamak”. In: *Plasma physics and controlled fusion* 47.12B (2005), B263.
- [134] GM Voss et al. “Toroidal field coil design for the spherical tokamak power plant”. In: *Fusion engineering and design* 48.3-4 (2000), pp. 407–418.
- [135] JE Menard et al. “Prospects for pilot plants based on the tokamak, spherical tokamak and stellarator”. In: *Nuclear Fusion* 51.10 (2011), p. 103014.
- [136] JE Menard et al. “Fusion nuclear science facilities and pilot plants based on the spherical tokamak”. In: *Nuclear Fusion* 56.10 (2016), p. 106023.
- [137] H Bolt et al. “Plasma facing and high heat flux materials—needs for ITER and beyond”. In: *Journal of Nuclear Materials* 307 (2002), pp. 43–52.
- [138] M Kotschenreuther et al. “The super X divertor (SXD) and a compact fusion neutron source (CFNS)”. In: *Nuclear Fusion* 50.3 (2010), p. 035003.

- [139] RJ Goldston, ML Reinke, and JA Schwartz. “A new scaling for divertor detachment”. In: *Plasma Physics and Controlled Fusion* 59.5 (2017), p. 055015.
- [140] HR Wilson, G Voss, and JW Ahn. *The spherical tokamak fusion power plant*. Tech. rep. 2003.
- [141] CPC Wong and RD Stambaugh. “Tokamak reactor designs as a function of aspect ratio”. In: *Fusion engineering and design* 51 (2000), pp. 387–393.
- [142] PB Snyder et al. “ELMs and constraints on the H-mode pedestal: peeling–ballooning stability calculation and comparison with experiment”. In: *Nuclear fusion* 44.2 (2004), p. 320.
- [143] S Saarelma et al. “Integrated modelling of H-mode pedestal and confinement in JET-ILW”. In: *Plasma Physics and Controlled Fusion* 60.1 (2017), p. 014042.
- [144] A Diallo et al. “Dynamical evolution of pedestal parameters in ELMy H-mode in the National Spherical Torus Experiment”. In: *Nuclear Fusion* 51.10 (2011), p. 103031.
- [145] L Garzotti et al. “Simulations of density profiles, pellet fuelling and density control in ITER”. In: *Nuclear Fusion* 52.1 (2011), p. 013002.
- [146] W Zwingmann, LG Eriksson, and P Stubberfield. “Equilibrium analysis of tokamak discharges with anisotropic pressure”. In: *Plasma physics and controlled fusion* 43.11 (2001), p. 1441.
- [147] Nikolai N Gorelenkov and Leonid E Zakharov. “Plasma equilibrium with fast ion orbit width, pressure anisotropy, and toroidal flow effects”. In: *Nuclear Fusion* 58.8 (2018), p. 082031.
- [148] MJ Hole and G Dennis. “Energetically resolved multiple-fluid equilibria of tokamak plasmas”. In: *Plasma Physics and Controlled Fusion* 51.3 (2009), p. 035014.
- [149] JE Menard et al. “Physics design of the NSTX upgrade”. In: *37th European Physical Society Conference on Plasma Physics, Dublin, Ireland, online: <http://ocs.ciemat.es/EPS2010PAP/pdf> P. Vol. 2*. 2010.
- [150] M Greenwald et al. “A new look at density limits in tokamaks”. In: *Nuclear Fusion* 28.12 (1988), p. 2199.
- [151] A Sykes et al. “Compact fusion energy based on the spherical tokamak”. In: *Nuclear Fusion* 58.1 (2017), p. 016039.

- [152] BV Kuteev et al. “Development of DEMO-FNS tokamak for fusion and hybrid technologies”. In: *Nuclear Fusion* 55.7 (2015), p. 073035.
- [153] X Yao and Y Shiohara. “Large REBCO single crystals: growth processes and superconducting properties”. In: *Superconductor Science and Technology* 10.5 (1997), p. 249.
- [154] Peter M McIntyre, John S Rogers, and Akhdiyov Sattarov. “Blocks-in-Conduit: REBCO cable for a 20T@ 20K toroid for compact fusion tokamaks”. In: *arXiv preprint arXiv:2101.01754* (2021).
- [155] Franco J Mangiarotti and Joseph V Minervini. “Advances on the design of demountable toroidal field coils with REBCO superconductors for an ARIES-I class fusion reactor”. In: *IEEE Transactions on Applied Superconductivity* 25.3 (2014), pp. 1–5.
- [156] TS Lee et al. “Optimal design of a toroidal field magnet system and cost of electricity implications for a tokamak using high temperature superconductors”. In: *Fusion engineering and design* 98 (2015), pp. 1072–1075.
- [157] DC Van der Laan et al. “Engineering current density in excess of 200 A mm<sup>-2</sup> at 20 T in CORC® magnet cables containing RE-Ba<sub>2</sub>Cu<sub>3</sub>O<sub>7- $\delta$</sub>  tapes with 38  $\mu$ m thick substrates”. In: *Superconductor Science and Technology* 28.12 (2015), p. 124001.
- [158] JE Menard. “Compact steady-state tokamak performance dependence on magnet and core physics limits”. In: *Philosophical Transactions of the Royal Society A* 377.2141 (2019), p. 20170440.
- [159] M Murakami et al. “Off-axis neutral beam current drive for advanced scenario development in DIII-D”. In: *Nuclear Fusion* 49.6 (2009), p. 065031.
- [160] CJ Murphy et al. “Overview of DIII-D off-axis neutral beam project”. In: *2011 IEEE/NPSS 24th Symposium on Fusion Engineering*. IEEE. 2011, pp. 1–6.
- [161] WW Heidbrink et al. “Initial measurements of the DIII-D off-axis neutral beams”. In: *Nuclear Fusion* 52.9 (2012), p. 094005.
- [162] Peter C de Vries et al. “Scaling of rotation and momentum confinement in JET plasmas”. In: *Nuclear Fusion* 48.6 (2008), p. 065006.
- [163] FJ Casson et al. “Anomalous parallel momentum transport due to  $E \times B$  flow shear in a tokamak plasma”. In: *Physics of Plasmas* 16.9 (2009), p. 092303.
- [164] TL Rhodes et al. “L-mode validation studies of gyrokinetic turbulence simulations via multiscale and multifield turbulence measurements on the DIII-D tokamak”. In: *Nuclear Fusion* 51.6 (2011), p. 063022.

- [165] C Holland et al. “Advances in validating gyrokinetic turbulence models against L-and H-mode plasmas”. In: *Physics of Plasmas* 18.5 (2011), p. 056113.
- [166] EA Belli and J Candy. “Fully electromagnetic gyrokinetic eigenmode analysis of high-beta shaped plasmas”. In: *Physics of Plasmas* 17.11 (2010), p. 112314.
- [167] N Joiner, A Hirose, and W Dorland. “Parallel magnetic field perturbations in gyrokinetic simulations”. In: *Physics of Plasmas* 17.7 (2010), p. 072104.
- [168] W Guttenfelder et al. “Scaling of linear microtearing stability for a high collisionality National Spherical Torus Experiment discharge”. In: *Physics of Plasmas* 19.2 (2012), p. 022506.
- [169] AB Hassam. “Fluid theory of tearing instabilities”. In: *The Physics of Fluids* 23.12 (1980), pp. 2493–2497.
- [170] JF Drake and YC Lee. “Kinetic theory of tearing instabilities”. In: *The Physics of Fluids* 20.8 (1977), pp. 1341–1353.
- [171] PJ Catto and MN Rosenbluth. “Trapped electron modifications to tearing modes in the low collision frequency limit”. In: *The Physics of Fluids* 24.2 (1981), pp. 243–255.
- [172] DJ Applegate et al. “Micro-tearing modes in the mega ampere spherical tokamak”. In: *Plasma Physics and Controlled Fusion* 49.8 (2007), p. 1113.
- [173] AK Swamy et al. “Collisionless microtearing modes in hot tokamaks: Effect of trapped electrons”. In: *Physics of Plasmas* 22.7 (2015), p. 072512.
- [174] D Dickinson et al. “Microtearing modes at the top of the pedestal”. In: *Plasma Physics and Controlled Fusion* 55.7 (2013), p. 074006.
- [175] DR Hatch. *Mode analyses of gyrokinetic simulations of plasma microturbulence*. 2010.
- [176] A Ishizawa et al. “Electromagnetic gyrokinetic simulation of turbulence in torus plasmas”. In: *Journal of Plasma Physics* 81.2 (2015).
- [177] CM Roach et al. “Confinement in START beam heated discharges”. In: *Nuclear fusion* 41.1 (2001), p. 11.
- [178] W Guttenfelder et al. “Electromagnetic transport from microtearing mode turbulence”. In: *Physical review letters* 106.15 (2011), p. 155004.
- [179] W Guttenfelder et al. “Progress in simulating turbulent electron thermal transport in NSTX”. In: *Nuclear Fusion* 53.9 (2013), p. 093022.

- [180] DR Hatch et al. “Microtearing turbulence limiting the JET-ILW pedestal”. In: *Nuclear Fusion* 56.10 (2016), p. 104003.
- [181] X Jian et al. “Role of Microtearing Turbulence in DIII-D High Bootstrap Current Fraction Plasmas”. In: *Physical Review Letters* 123.22 (2019), p. 225002.
- [182] N Kumar et al. “Turbulent transport driven by kinetic ballooning modes in the inner core of JET hybrid H-modes”. In: *Nuclear Fusion* (2020).
- [183] H Doerk et al. “Gyrokinetic study of turbulence suppression in a JET-ILW power scan”. In: *Plasma Physics and Controlled Fusion* 58.11 (2016), p. 115005.
- [184] J Garcia et al. “Key impact of finite-beta and fast ions in core and edge tokamak regions for the transition to advanced scenarios”. In: *Nuclear Fusion* 55.5 (2015), p. 053007.
- [185] J Citrin et al. “Electromagnetic stabilization of tokamak microturbulence in a high- $\beta$  regime”. In: *Plasma Physics and Controlled Fusion* 57.1 (2014), p. 014032.
- [186] HS Xie, ZX Lu, and B Li. “Kinetic ballooning mode under steep gradient: High order eigenstates and mode structure parity transition”. In: *Physics of Plasmas* 25.7 (2018), p. 072106.
- [187] D Dickinson et al. “Kinetic instabilities that limit  $\beta$  in the edge of a tokamak plasma: a picture of an H-mode pedestal”. In: *Physical Review Letters* 108.13 (2012), p. 135002.
- [188] M Valovič et al. “Collisionality and safety factor scalings of H-mode energy transport in the MAST spherical tokamak”. In: *Nuclear Fusion* 51.7 (2011), p. 073045.
- [189] RJ Groebner et al. “Limits to the H-mode pedestal pressure gradient in DIII-D”. In: *Nuclear fusion* 50.6 (2010), p. 064002.
- [190] I Predebon and F Sattin. “On the linear stability of collisionless microtearing modes”. In: *Physics of Plasmas* 20.4 (2013), p. 040701.
- [191] CM Roach, JW Connor, and S Janjua. “Trapped particle precession in advanced tokamaks”. In: *Plasma physics and controlled fusion* 37.6 (1995), p. 679.
- [192] F Jenko, W Dorland, and GW Hammett. “Critical gradient formula for toroidal electron temperature gradient modes”. In: *Physics of Plasmas* 8.9 (2001), pp. 4096–4104.
- [193] ASDEX Upgrade Team et al. “Density peaking, anomalous pinch, and collisionality in tokamak plasmas”. In: *Physical review letters* 90.20 (2003), p. 205003.
- [194] C Angioni et al. “Scaling of density peaking in H-mode plasmas based on a combined database of AUG and JET observations”. In: *Nuclear fusion* 47.9 (2007), p. 1326.

- [195] MJ Pueschel, M Kammerer, and F Jenko. “Gyrokinetic turbulence simulations at high plasma beta”. In: *Physics of Plasmas* 15.10 (2008), p. 102310.
- [196] W Guttenfelder et al. “Simulation of microtearing turbulence in national spherical torus experiment”. In: *Physics of Plasmas* 19.5 (2012), p. 056119.
- [197] T Rafiq et al. “Microtearing modes in tokamak discharges”. In: *Physics of Plasmas* 23.6 (2016), p. 062507.
- [198] T Rafiq et al. “Microtearing instabilities and electron thermal transport in low and high collisionality NSTX discharges”. In: *Physics of Plasmas* 28.2 (2021), p. 022504.
- [199] MJ Pueschel et al. “Extreme Heat Fluxes in Gyrokinetic Simulations: A New Critical  $\beta$ ”. In: *Physical review letters* 110.15 (2013), p. 155005.
- [200] PW Terry et al. “Overview of gyrokinetic studies of finite- $\beta$  microturbulence”. In: *Nuclear Fusion* 55.10 (2015), p. 104011.

